ABSTRACT

Title of Dissertation: THERMO-MECHANICAL DURABILITY ASSESSMENT AND MICROSTRUCTURAL CHARACTERIZATION STUDY OF 95.5Pb2Sn2.5Ag HIGH TEMPERATURE SOLDER

Manas Ranjan Dash, Doctor of Philosophy, 2006

Dissertation directed By: Associate Professor F. Patrick McCluskey
Department of Mechanical Engineering

There is an increasing need in the avionics, military, oil exploration and automotive industries for high temperature solders that perform reliably in ever-higher temperature applications. In these applications, solders are often used as large area die attaches and due to the high power involved, they need to dissipate large amounts of heat that can further increase the thermal load on the devices. The mechanical, electrical and thermal behavior of the solder must be understood to ensure devices and package reliability. There is an especially urgent need for characterizing constitutive properties and thermo-mechanical durability of high temperature solders.

A partitioned constitutive model consisting of elastic, plastic and creep models was obtained for the 95.5Pb2Sn2.5Ag solder by implementing the direct local measurement technique. The validity of the assumptions used to generate these models have been demonstrated using microstructural characterization.

The thermo-mechanical durability of the 95.5Pb2Sn2.5Ag solder is investigated using thermal cycling tests and finite element modeling. A high reliability package manufacturing technique has been followed. The extensive detailed two-dimensional viscoplastic FE stress and damage analysis is conducted for five different thermal cycling tests of 95.5Pb2Sn2.5Ag solders. The energy-partitioning durability model of the solder is obtained. It is found that 95.5Pb2Sn2.5Ag solder is creep dominant at high temperatures.

The microstructure characterization study on 95.5Pb2Sn2.5Ag solder reveals that it remains primarily a single phase in the range of temperature under study with very few Ag_3Sn intermetallics. Fatigue cracks due to thermal cycling have been observed.

THERMO-MECHANICAL DURABILITY ASSESSMENT AND MICROSTRUCTURAL CHARACTERIZATION STUDY OF 95.5Pb2Sn2.5Ag HIGH TEMPERATURE SOLDER

By

Manas Ranjan Dash

Dissertation submitted to the Faculty of the Graduate School of the
University of Maryland, College Park, in partial fulfillment
of the requirements for the degree of
Doctor of Philosophy
2006

Advisory Committee:
Associate Professor F. Patrick McCluskey, Chair
Professor Michael Pecht
Associate Professor David Bigio
Associate Professor Peter Sandborn
Associate Professor Isabel K. Lloyd

DEDICATION

To my parents, brothers and sisters for their wisdom, affection, love, encouragement and support and to my lovely wife Devina who stands with me and shares every moment with me. Devina -- without you I would not have been able to do this. This is our degree!

ACKNOWLEDGEMENTS

It has been a privilege to work closely with Dr. F. Patrick McCluskey. I would like to express my most sincere and heartfelt thanks to him for his guidance and continual support. He not only provided me encouragement and instruction but also trained me to be an independent researcher. He is a man of vision and has the engineering sense. His dedication to his graduate students is commendable.

I would like to extend my thanks to my dissertation committee: Dr. Pecht, Dr. Dasgupta, Dr.Bigio, Dr. Sandborn, and Dr. Lloyd for their valuable time and thoughtful input.

I am grateful to Dr. Siegfried Ramminger from Siemens who helped to fund my dissertation research. I do not know what I would do without the benefit of his knowledge. He has masterfully balanced the roles of “critical friend” and motivator.

I would like to acknowledge the significant impact of Dr. Keith Rogers and Bhanu Pratap for their help in laboratory and guidance in failure analysis all throughout the journey. Dan Huff, the CPES packaging lab research manager, at the Virginia Polytechnic Institute and State University deserves special mention for his support in all aspects of packaging during fabrication of the devices, all the intricate processes involved with making industry-quality devices. Michael Khbeis, the Process Engineer at the Laboratory for Physical Sciences was very helpful in dicing work.

I would also like to acknowledge the professors and staff of Mechanical Engineering Department and CALCE Electronic Products and Systems Center who supported me in the project.

Navigating my way through the Ph.D. program was made easier and more enjoyable through my friendship with my colleagues including but not limited to Jyoti, Subrat, Satchi, Sudhir, Satya, Kaushik, Shirish, Anupam, Arindam, Yunqi, Tim, Rui. Special thanks to Ron and Pedro for helping me in my experiments. With kindness and honesty, they all shared their lives with me. I am honored and thankful.

My family and friends, some mentioned above and some not, you have always been the driving force behind my actions and the pages of this dissertation are all imbued with you! Thank you for being there!

TABLE OF CONTENTS

List of Figures

List of Tables

1 Introduction

1.1 Motivation

Electronic devices must perform the electrical functions for which they are designed in addition to maintaining their structural integrity while being subjected to a wide range of environmental and operational loads. Common examples of loads include vibration, shock, impact, bending, radiation, moisture ingress, exposure to chemicals, and exposure to extremes of ambient and operating temperature. All electronic devices are subjected to these loads with few exceptions.

With increasing demands for higher speed and higher integration, chip sizes are becoming larger. As the chip size increases, the thermal expansion driven in-plane displacement between the silicon chip and substrate increases. Furthermore the increasing electrical power results in higher heat flux and, therefore, leads to a higher temperature for chip operation. As a result, thermal expansion difference between the chip and the substrate grows even larger causing mechanical loading on the joints to become more severe. Consequently, thermal fatigue strength of solder, particularly of that used for die bonding, has become of major interest lately. A number of studies have examined thermal fatigue lives of solders, primarily Pb-rich Pb-Sn alloys (e.g., Pb-5%Sn) and the eutectic alloys (e.g., Pb-63 % Sn). Little has been done with other alloys.

1.1.1 Why High Temperature Solder?

Microelectronics assembly has, from its infancy, been based on tin-lead eutectic solder, a mixture of tin and lead that melts at 183 °C. In recent years there has been an increasing need within the avionics, military, telecommunications, oil exploration and automotive industries for solders that perform reliably at ever-higher temperatures, temperatures which approach or exceed the melting point of tin-lead eutectic. Such harsh environment applications require solders with melting points higher than that of tin-lead eutectic in order to achieve the required reliability. Table 1.1 shows the scope and temperature range of high temperature electronic market.

Table 1.1: High Temperature Electronic Markets

Well Logging Instrumentation	
Oil and gas wells	75°C to 225 °C
Steam injection wells	200°C to 300°C
Geothermal wells	200°C to 350°C
Aerospace	
Electronic braking system	Up to 250°C
Engine control/monitoring	Up to 300°C
Automotive	
Engine compartment	Up to 165°C
On-engine and on-transmission	Up to 165°C
Wheel mounted components	Up to 250°C
Others	
Exploration vehicles	Up to 500°C
Space systems	Up to 500°C
Nuclear reactor monitoring	Up to 550°C
Gas Turbine Engines	Up to 1200°C

Solder alloys, with high melting points are typically used in power electronic systems as a large area die attach between the silicon die and the underlying substrate. At such high operating temperatures, the common tin-lead eutectic solder cannot be used, as it would melt before fulfilling service requirements (T_m=183^{o}C). The use of high temperature solders reduce the load on cooling systems. Power-device packages especially require the use of high melting die-attach solders in order that the die stay internally attached to the lead frame while the package is being soldered to a printed wiring board. High-lead solders possess lower shear moduli than the other high temperature alternatives, are cheaper and generally provide much better resistance to thermo-mechanical fatigue than the eutectic gold alloys.

1.1.2 High Temperature Solder Selection

A wide variety of fusible alloys are suitable for soldering. The following areas should be considered when selecting a solder alloy for a specific application:

(a) Metallurgical and morphological considerations

The high temperature performance of solder is actually a complex function of the strain rate, microstructure, fillet geometry, and a host of other parameters. Lower strain rates at high temperatures, for example, permit additional time for creep damage to occur, thereby lessening the high temperature life of solder joints. Microstructure both affects and is affected by high temperature use. When exposed to the thermo-mechanical stresses resulting from temperature cycling in high temperature applications, the solder microstructure will change from a fine grained mixture of lead-rich and tin-rich phases to a more coarse grained structure along a

thin band parallel to the direction of the imposed strain. This occurs as a result of diffusional mass flow at the high temperature portion of the cycle which recovers the damage induced in the form of defects during the low temperature ramp portions of the cycle. This larger grain structure decreases the strength and hardness, but increases the ductility of the solder joints. The individual grains inside the coarsened structure eventually grow to the point at which they can no longer accommodate the deformation, at which time, intergranular cracks form and propagate through the coarsened regions. Fillet geometry also has an effect on high temperature performance because the solder is thin enough that its mechanical properties are not those of the bulk but rather are influenced by interfacial interactions. Thinner solder joints have shorter lives in vibrational fatigue and in high temperature creep. A high temperature solder replacement for eutectic tin-lead is expected to have all the advantages of tin-lead solder such as fast and adherent wetting of most metal surfaces for ease of manufacturing, a narrow melting temperature range, high tensile and shear strength for resistance to overstress failures, high fatigue resistance to inhibit failure in thermal cycling or vibration environments, corrosion resistance, and low cost. In addition, it is expected to also possess the following characteristics: a melting temperature significantly higher than 200°C, high creep resistance to inhibit failure at high steady-state temperatures, high oxidation resistance in the liquid state to minimize dross formation which can impair manufacturability, and low toxicity (i.e., no lead or cadmium, and potentially, no nickel). Other than high lead content, 95.5Pb2Sn2.5Ag solder possesses all the above mentioned characteristics for its selection.

(b) Temperature compatibility

Manufacturing temperature limit: The choice of the solder is usually affected by the maximum temperature that can be tolerated by the assembly. Sometimes a solder with temperature characteristics detrimental to the assembly can be used due to other considerations which outweighs thermal distortion. 95.5Pb2Sn2.5Ag being detrimental to the environment is used in power packaging systems due to its high temperature tolerance. It has got a solidus of 299°C and liquidus of 304°C.

Use temperature limit: As an alloy approaches its melting point, the tensile strength and shear strength fall off. The strength decreases in an asymptotic manner as the melting point is approached. Thus, if the system containing the solder joints has to operate at known elevated ambient temperatures, the selection of the solder must be carefully matched to make sure that the solder joints will have sufficient mechanical strength.

(c) Mechanical properties

Since solder is normally the weakest link in the assembly, the strength of the solder joint is very important. Intrinsic shear strength, creep resistance, fatigue resistance and coefficient of thermal expansion are important properties to the overall performance of solder joints. 95.5Pb2Sn2.5Ag has got much larger shear strength and creep resistance than the lead free ones and other high temperature alternatives.

(d) Alloy-substrate compatibility

Thermodynamically, most tin-based solder alloys are metallurgically reactive to common substrates used for electronic packaging and assembly such as those listed in Table 1.2. The selection of solder alloy depends on the kinetics of the metallurgical

reactions at a given set of process conditions. Because of the metallurgical affinity, the process condition must be controlled to avoid excessive reaction between the solder and substrate.

Table 1.2: Compatibility issues [1]

Solder	Substrate
Sn-based	Cu
Sn-based	Au
Sn-based	Ag
In-based	Cu
Bi-Sn	Pb
Sb-containing	Brass, Zn

(e) Eutectic versus non-eutectic compositions

For a given binary system, the eutectic composition offers the liquid phase with maximum fluidity. High fluidity can be an important attribute for applications requiring penetration into narrow gaps to form joints. Furthermore low fluidity or a more viscous liquid phase, which is offered by a non-eutectic composition with a wide plastic (mushy) range can result in cold solder joints containing high level of incipient microcracks that can cause early failure.

(f) Electrical characteristics

The electrical conductivity or resistivity is an important factor in power devices whenever the solder joint acts as one of the electrodes. It is important to ensure in such applications that enough current-carrying capacity is available in the solder joint to avoid hot spots.

(g) Density

When a solder joint is part of a moving assembly, it is important to be sure that the density of the solder in the joint is similar to that of the material used. Otherwise, particularly in rotating parts, centrifugal force may cause imbalance. The density of the solder is also important in applications where the overall weight of the assembly is a consideration, as with a floating device.

(h) Linear coefficient of thermal expansion

This is especially important when glass-to-metal or ceramic-to-metal joints are soldered, or in surface mount configurations. If the coefficient of thermal expansion of the solder is very different from that of the glass or ceramic material, and the part is subjected to thermal shocks during its service, the stresses and strains that are built up may cause failure. In case of power packaging systems DBC or ceramics are generally used as substrates which have very low CTEs. The CTE of 95.5Pb2Sn2.5Ag solder matches very well with such substrates and silicon dies enhancing the fatigue life of the package.

(i) Effect of intermetallic compound formation

Intermetallic compounds are phases that can form in the solder that have a strong ionic character, fixed stoichiometry and complex crystal structure. These crystals are often brittle and can have poorinterfacial adhesion with other phases and therefore can lead to solder failure. Their presence, as in the case of copper-tin intermetallic, can weaken the joint by acting as crack initiation sites in the bulk or as sites for impact fracture failure when formed at the interface of the materials to be joined. They can also reduce the fluidity of the alloy as it is attempting to spread and wet the

base metal. To avoid the formation of intermetallic compounds it is possible to plate the surfaces of the base metal to be joined with a diffusion barrier. Another way to avoid intermetallics in the joint, is to select an alloy that does not form appreciable amounts of intermetallic-compounds in the bulk or with the base metal at soldering or room temperatures.The slower intermetallic formation is one reason why copper base metal is often plated with nickel. 95.5Pb2Sn2.5Ag solder with its optimum composition of Ag and Sn (as we will see in the dissertation work later) produces very little intermetallics when used with nickel coated dies and substrates.

(j) Repeatability of manufacture / Consistency in melting point

The electronic assembly process is a high volume manufacturing process where repeatability and consistency are required to achieve low defect levels. Alloys whose compositions cannot be repeated lot after lot, or whose melting point varies greatly from lot-to-lot due to compositional shifts, are not acceptable candidates. Alloys with more than 3 elements are prone to macrosegregation and other compositional variations which can result in variable melting points. The more complicated the alloy, the more sensitive the alloy will be to this variability. Global solder manufacturers like Indium, Kester and Amtech have found repeatability in manufacturing 95.5Pb2Sn2.5Ag in all its forms like paste, ribbon, wire etc.

(k) Availability

When attempting to find a solution for the industry, it is critical to select an alloy system whose components are sufficiently available. From a technical standpoint, indium is quite attractive. However, when reviewing the low worldwide availability of indium, it becomes less desirable. Additionally, the industry would prefer a open

alloy system over a patented one. An open alloy would be broadly available and would allow for competitive pricing. A patented alloy would be subject to supply limitation that could increase the price considerably. In case of 95.5Pb2Sn2.5Ag, all the components are widely available and it is a standard alloy sold at a price cheaper than the specialty ones.

(l) Other consideration

Corrosion of the solder alloy must be considered in the intended use environment. This must also take into account the galvanic effect of pairing the solder with different base metals. The issue of cascade soldering must also be addressed where if two consecutive joints are to be made in the same area. The solder chosen for the first joint cannot melt during the formation of the second connection. Here, two soldering alloys are used, and the first alloy must have a solidus temperature above the soldering temperature of the second one.

1.1.3 Die Attach Reliability Concerns

Die attachment in power electronics provides not only a mechanical connection but also the backside electrical connection. The mechanical attachment function is complicated by the fact that at typical operating temperatures solder behaves in a fashion more akin to a very viscous fluid than a typical structural material. It creeps and stress-relaxes readily and can be thought of as having a load-bearing capability on a strictly temporary basis only. Solder die attach subjected to cyclic thermo-mechanical strains and stresses in operation, accumulates fatigue damage which, in time, results in fatigue cracks and eventually in mechanical and electrical failure of the attachment.

Consistent good quality die attachment should result in sufficiently low infant mortality and steady-state failure rates. However, depending on the choice of attachment technology, the design parameters, and the severity of the use environment, wearout failures can become a concern within the intended life of the product.

Die attach can be subjected to considerable cyclic strains during operation caused by the different thermal expansions of the silicon die and the substrate in combination with external temperature variations caused by system load fluctuations or power cycles and by diurnal or seasonal fluctuations. The following appropriate design measures can be employed for improved reliability margins: (a) tailoring the CTE of the substrate to that of the die (b) increasing the attachment compliancy and (c) keeping the solder joint attachment (die) dimensions as small as possible. Failure due to CTE mismatch is stress/strain driven and is compounded by the fact that the highest stress occurs at edge of the die where crack initiation is straight forward.

Assessing the reliability potential of a design and assuring the reliability of an electronic assembly in use requires knowledge of the use environment(s), the resulting loading conditions and the accumulating fatigue damage. It further requires an analytical relationship that relates the accumulating fatigue damage to cyclic fatigue life in general. An empirical model of this relationship based on design-specific characteristics must be developed and then verified using a well-designed accelerated test program. This validated model will provide an acceleration transform that allows valid comparisons of results from different accelerated test conditions and that, more importantly, allows the

extrapolation of these accelerated test results to predict the reliability of the product in use.

Thus, the assurance of die attach integrity warrants the step-by-step evaluation of the following items:

(1) Suitability of solder alloy melting point for required service temperature.

(2) Suitability of solder alloy for required mechanical properties.

(3) Anticipated metallurgical compounds formed between solder and substrates.

(4) Adequacy of solder wetting on substrates.

(5) Design of attach configuration in size, thickness etc.

(6) Optimum die bonding technique including single pass, multiple pass and other parameters like vacuum reflow and ambient atmosphere.

(7) Conditions of storage in relation to aging.

(8) Conditions of actual service in terms of upper temperature, lower temperature, temperature cycling frequency, vibration or other mechanical loading.

(9) Effects from component characteristics including heat dissipation, stress distribution and coplanarity.

(10) Performance requirements under conditions of actual service.

(11) Design of viable accelerated testing conditions that correlate to actual service conditions.

1.1.4 Data Needs for PbSnAg Solder

There are extensive databases of mechanical properties, durability properties (for both mechanical and thermal cycling), and micromechanical characteristics for eutectic Sn-Pb solders. But similar databases are not readily yet available for high lead solders containing tin and silver which are specifically used in high temperature applications. An adequate database of various properties of high lead solders is needed to design robust electronics for both mechanical and thermal environmental stresses. These properties need to be assessed for high lead solders, to enable successful performance in power electronic packaging. These material properties are critical for design and virtual qualification of electronic products with high lead interconnects, because current product development processes rely heavily on modeling and simulation.

1.2 Objectives and Scope of Current Work

Because of the urgent need for constitutive and durability properties of high temperature solders, the primary objective of this study is to characterize the viscoplastic constitutive properties and to assess the cyclic thermo-mechanical durability of 95.5Pb2Sn2.5Ag solders which is one of the most widely used and least characterized. Mechanical constitutive behavior, which describes the deformation of a material in response to an applied load, is a function of stress history and temperature, as well as other secondary factors such as the manufacturing process, aging and annealing histories, and specimen size. Durability is defined here as a material property which quantifies the ability of a material to withstand damage accumulated during cyclic loading. Durability in this study is investigated under temperature cycling.

The primary focus of this thesis is thermo-mechanical durability of 95.5Pb2Sn2.5Ag high temperature solder. The outcome of this research is a set of durability constants using an energy partitioning approach which can be used to predict the time to failure and produce guidelines for reliable die attachment. In addition to finding the durability constants, this research also focuses on the damage propagation in the die attach during temperature cycling and microstructure characterization.

Chapter 1 describes the motivation behind this research and the high temperature solder selection criteria. Different test systems used to measure the constitutive properties of the solder, temperature cycling in different environments and characterization of the temperature cycled samples have been detailed.

Chapter 2 reviews the literature on high temperature solders. This chapter covers in detail the determination of the constitutive behavior of lead-rich 95.5Pb2Sn2.5Ag solder used as a large area die attach in power packaging. Creep model predictions have been done based on the experimental results. A thorough review of the effect of alloying elements like tin and silver on the microstructure and mechanical properties of high temperature solders and 95.5Pb2Sn2.5Ag in particular has been accomplished. Creep-fatigue mechanisms in high temperature solders have been discussed at different temperatures and strain rates. Finally a generic damage model, the Energy Partitioning (E-P) Damage Model, is discussed. This model can be used to predict the durability of lead rich solders under any test or use condition (any combination of plastic and creep deformation).

Chapter 3 covers the complete manufacturing of the packages and discuss the advantages and disadvantages of different processes. It also explains the temperature cycling test procedures. This chapter discusses the quantitative measurement of die-attach degradation using the non-destructive SAM technique. Results of die-attach degradation and crack growth are presented for a variety of packaged samples subjected to accelerated testing. Test data have been analyzed to predict the reliability of the packages in multiple environments. Both destructive and non-destructive failure analysis has been explained. A detailed microstructure study has also been undertaken in this chapter.

Chapter 4 presents the detailed finite element simulation of the packaged structure. The goal is to simulate the packaged sample subjected to temperature cycling and conduct the stress analysis. This chapter starts with an introduction to the finite element analysis tool. A summary of the geometric, material and thermal assumptions is presented to describe the modeling process for the package. The definition of the boundary conditions and application of mesh sizes completes the construction of the FEM model. The FEM results are presented for the two dimensional plane strain model. Finally the energy partitioning constants are derived.

Chapter 5 of the dissertation includes concluding remarks about damage propagation in the large area die attach. The results from simulation and experimental data establish the relationship between time to failure, package dimensions and environmental stresses for the 95.5Pb2Sn2.5Ag solder.

The Appendices contains details of the fabrication of packages and reflow profile, X-Ray results, Microstructure Characterization, Weibull analysis, SAM results and finite element analysis setup. Lastly a number of references have been listed.

1.3 Test Systems

To achieve the goals of the project different test systems are used. This section gives a detailed overview of the test setups and specimens used.

1.3.1 Constitutive Property Measurement

1.3.1.1 MTS TytronTM 250 MicroForce Testing System

Since typical solder interconnects in modern electronics are small, measuring the mechanical behavior is a significant engineering challenge. The die attach height is very small (usually less than 100μm), and shear deformation is dominant. Displacement sensors or gauges, which are easy to use with bulk specimens are often too cumbersome to be used with these miniature specimens. Furthermore due to the small axial displacements recorded in miniature specimens, the large gauge length and poor resolution of typical displacement sensors induce errors in capturing meaningful test data. Such factors contribute towards the choice of testing equipment to be selected for use. A micro-mechanical tester is employed to document the solder deformations. The MTS Tytron^{TM} is a uniaxial micro-tester for miniature specimens. It has a load capacity of 250N and a load resolution of 0.001N. The system consists of the Tytron 250 load unit,

the power amplifier, the Teststar IIs digital software, and the Teststar system software. Figure 1.1 shows the system components.

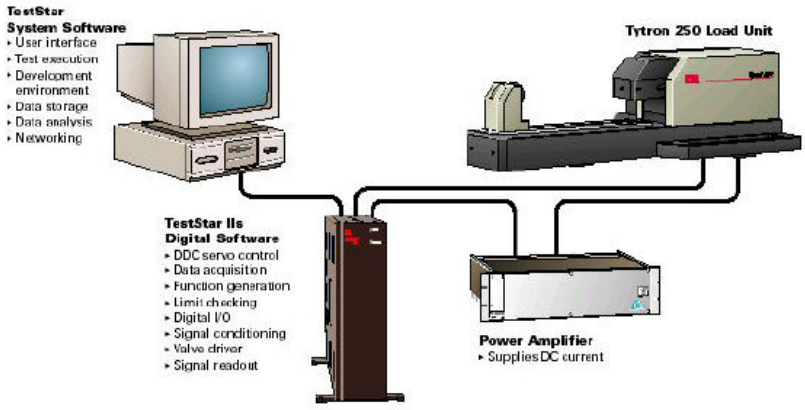

Figure 1.1: The MTS Tytron™ System

The main hardware components of the load unit are the actuator, the reaction fixture, the force transducer, and the measurement devices. A directly coupled linear DC Servomotor drives the actuator, which is capable of speeds ranging from 1µm/hr to 0.5m/sec. It has a stroke of 100mm and is capable of frequencies of up to 50Hz. The force transducer is mounted on the reaction fixture and is stationary. There are two force transducers from which to choose, with load capacities of ±10N (resolution: 0.0003N) and ±250N (resolution: 0.0076N) respectively. There are three displacement measurement devices, namely the linear variable differential transformer (LVDT), the displacement gauge, and the miniature axial extensometer. The various components of the load unit are depicted in Figure 1.2.

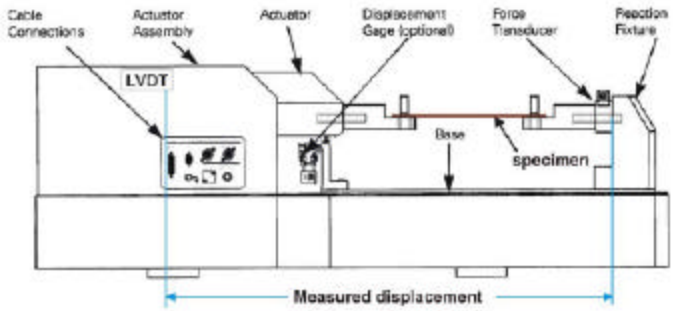

Figure 1.2: MTS Tytron™ Testing System Test Configuration

The LVDT is mounted on the actuator and measures displacement between the actuator and the reaction fixture. It has a resolution of 1.83µm for the ±60mm displacement range, and a resolution of 0.153µm for the ±5mm displacement range. It must be kept in mind that when using the LVDT for measurement, the effect of the compliance of the entire load train must be accounted for and subtracted from the measured displacement. The displacement gauge has a much higher resolution of 0.061µm for a ±2mm displacement range. The third device is the miniature extensometer, which is by far the most accurate and useful since it makes direct strain measurements possible, thus eliminating the compliance effects of the load train. The extensometer (632.29F-20) has a 3mm gauge length and a resolution of 2.44µe (0.0732µm) for the ±8% strain range and a resolution of 0.244µe (0.00732µm) for the ±0.8% strain range. In addition to these components, the TytronTM also has a temperature controller and a temperature chamber. The temperature controller can provide a temperature range of –75^{o}C to 200^{o}C and can control the temperature to within ±1^{o}C.

1.3.1.2 Specimen Configuration

Traditional testing methods involving the use of bulk specimens neglect some fundamental aspects of material behavior that surface when solder alloys are used as permanent interconnects in electronics packaging. The dominant mode of failure in the actual permanent solder interconnect is shear not tensile, due to thermal expansion mismatch between the die and the substrate. Also, the volume of the solder alloy in these electronic assemblies can be much smaller than bulk samples. Also the properties of solder interconnects are strongly dependent upon grain structure, which is governed by the fabrication process and the joint size. Furthermore the displacement of the solder is constrained by the surfaces it is joining. It is desirable therefore that the specimen be fabricated under conditions as similar to the actual manufacturing process as possible, and that its size be on the same order as that of the actual solder joints. For this reason, a conventional tensile test is not suitable for measuring the constitutive properties of solder alloys. Miniature lap shear specimens better simulate the geometrical and loading constraints of the solder interconnects in actual applications. Miniature specimens can have a single joint (single-lap shear), two joints (double-lap shear), or multiple joints (arrayed-lap shear; flip-chip array). Iosipescu [2] has designed a specimen for single in-plane shear of metals or composites utilizing a notched beam type sample, which is loaded so as to produce a zero bending moment across the notch or test section. A typical Iosipescu specimen is shown in Figure 1.3.

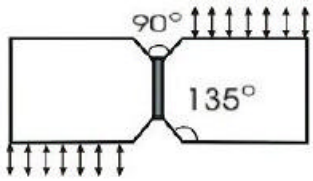

Figure 1.3: Iosipescu Uniform Specimen Configuration

Kwon et al. [3] have improvised the modified Iosipescu micro-shear lap specimen [4] for uniaxial testing purposes. This specimen configuration is shown in Figure 1.4; it retains the characteristic Iosipescu V-notch, which helps minimize stress concentration at the edges and helps maintain a uniform shear stress within the solder, while at the same time permits it to be mounted on a uniaxial test frame. Kwon et al. [3] have used a nominal joint height of 300μm to simulate the geometric and loading constraints present in a solder bump. Smaller heights down to 100 μm have been used to simulate die attach. Nominal solder joint dimensions are: 2.0mm x 1.5mm x 0.3mm.

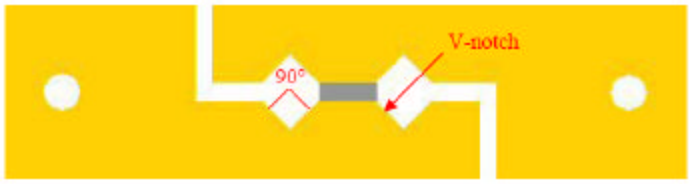

Figure 1.4: Specimen Configuration

1.3.1.3 Specimen Preparation

Good wetting of the solder to the copper requires thorough cleaning of the surfaces to be joined. Use of well-aligned and symmetric specimens with good axial linearity and surface planarity reduces the stress developed simply through installing the specimen into

the test fixture on the Tytron. This simplifies the stress fields throughout the solder thereby producing more uniform test data [5]. Specimens are only produced one at a time. Thus, it is imperative that the procedure be quick, repeatable, and consistent. To this end, specimens are thoroughly cleaned with isopropyl alcohol (IPA) and a special-purpose soldering fixture is designed for reflowing the solder joint as shown in Figure 1.5. Steel shims are wedged between the platens to maintain joint height. The key-shaped platens are made of cold-rolled copper and are obtained via wire cutting (EDM).

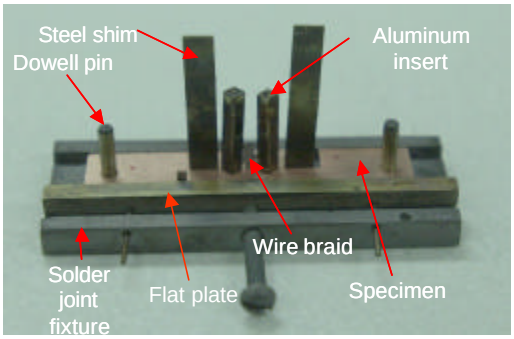

Figure 1.5: Soldering fixture [3]

Cleaning

The active surface of the platen (surface eventually in contact with the solder joint) is made smooth using medium grade sandpaper. The platens are then dipped into flux, and heated to activate the flux. The copper platen is brushed clean with IPA to remove all debris on the surface. This step may be repeated as required.

Reflow Soldering

The platens are then located on the soldering fixture. The active surfaces are again dipped in flux, which is activated as before. The fixture with the two key-shaped platens is then

placed on a hotplate, at 380°C, well above the melting point of the alloy. The solder wire is brought in contact with the active surface, which is at a temperature sufficient to melt the solder on contact and the solder fills the gap by capillary action, creating the joint. The specimen is then gradually brought down to room temperature using a thick aluminum cold plate as a heat sink. Specimens are visually inspected for alignment and solder volume.

Polishing

Specimens are then polished mainly for two reasons: first, to reduce the specimen to the desired thickness, and second, for axial linearity and surface planarity. Two specimens are simultaneously mounted on a special-purpose polishing fixture to increase planarity by increasing the bearing surface, and making it easier to maintain orthogonality of the specimen during polishing. The specimen is polished on both sides using multiple grades of waterproof metallurgical sandpaper (600, 800, and 1200 grit) from coarse grade to remove excess solder to fine grade for a highly polished surface.

Inspection and Measurement of Joint dimensions

The specimen is inspected under an optical microscope for defects such as cracks or surface voids and photographed for documentation purposes. Actual joint dimensions are measured using digital micrometers and an optical microscope.

Pin press-fitting

If the specimen passes the visual inspection, holes in the copper platens are press fitted with pins, which are used for mounting extensions (Please refer to section 1.3.1.3 for details).

Inspection

The specimen is again viewed under the microscope for any evidence of stress-related damage to the joint due to press fitting.

Attaching extensions

The extensions are mounted using room temperature curing high temperature epoxy, after which the epoxy is left to cure for 24 hours. The specimen is now ready for testing.

Due to their small size, the axial stiffness of miniature specimens can be very high compared to bulk specimens, thereby increasing the effect of the compliance of the machine frame and load train on the experimental data. This necessitates local measurement of solder deformation.

1.3.1.4 Direct Local Measurement of Strain Using Axial Extensometer

A shear lap test is performed using a uniaxial testing machine and the measured uniaxial displacements are converted to shear displacements. The total displacement captured by the displacement gage includes displacements of other deformable bodies in the system and they must be compensated to obtain the true deformation of solder. The compensation should include machine compliance, grip compliance and copper compliance. The strain gauge or extensometer is used to measure a displacement over a small gage length in the uniaxial tension test. For a shear lap test, however, gauge cannot be applied directly on the specimen since a relative displacement between the top and bottom of the test coupon is to be measured. An auxiliary device has been developed to cope with the problem. The device (referred to as extension unit) is attached directly to the specimen. An extensometer is mounted on the extension unit and it permits the shear

displacement of the solder to be measured as an equivalent axial displacement by the extensometer. The experimental setup with extensions and an extensometer is shown in Figure 1.6. A high-resolution miniature extensometer (MTS 632.29F-20) is attached to the units by two rubber bands [3].

Figure 1.7 illustrates how the unit is attached to the shear specimen. A pair of dowel pins is inserted in the specimen by press fitting and the units are attached to the other end of the pins using a room temperature curing high temperature epoxy adhesive. With this configuration, the right-hand side unit has a relative horizontal motion with respect to the left-hand side unit. When an extensometer is mounted in such a way that each knife-edge is on each unit, the extensometer effectively measures the relative displacement between the units, which can be related to the shear displacement of the solder joint.

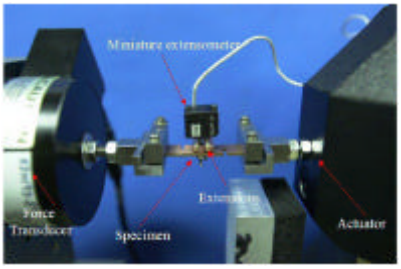

Figure 1.6: Extensions attached to specimen: Set-up

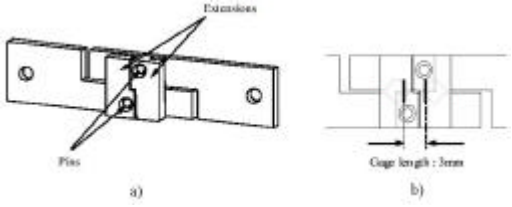

Figure 1.7: Extensions attached to specimen, Schematic

The extensions are designed in such a way that the knife-edges of the extensometer are exactly aligned with the pinholes of the extensions. The reason for this is simple; the two extensions fixed atop the specimen do not come in contact with each other and are free to translate along with the copper platen they are fixed to. In this way, the extensometer is able to measure the deformation between the two pinholes on either platen of the specimen, shown by points B and B' in Figure 1.8.

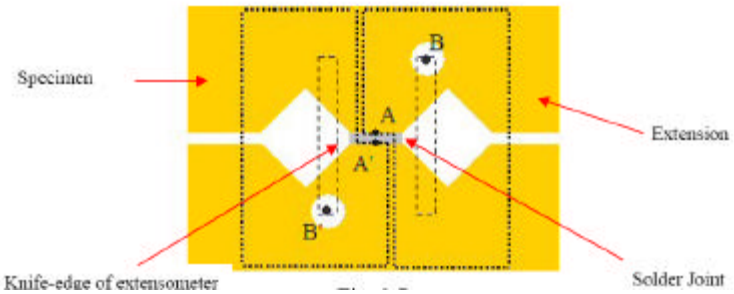

Figure 1.8: Extensions superimposed on specimen B & B' – at location of pins A & A' – at Cu/solder interface

The extensometer measures the deformation between B and B'. But what is actually required is the deformation between A and A', i.e. the actual deformation of the solder joint. To put it simply, the deformation between points A and B, i.e. the deformation of the copper, and for that matter between A' and B' (same), is subtracted from this apparent deformation from the measured deformation to obtain the actual solder deformation [3].

1.3.2 Analytical Measurement

1.3.2.1 SONIX Scanning Acoustic Microscope

Scanning Acoustic Microscopy (SAM) is a failure analysis technique used for detecting disbonds or delaminations between package interfaces, (e.g., the interface between the die and the die attach, the die attach and the substrate in a power module). A scanning acoustic microscope works on the principle of propagation and reflection of acoustic waves at interfaces where a change of acoustic impedance (AI = density x acoustic velocity) occurs. It basically consists of sending a sound wave through the package, and interpreting the interaction of the sound wave with the package. A typical scanning acoustic microscope as shown in Figure 1.9 may employ either pulse echo or through transmission inspection to scan for disbonds or delaminations. Pulse echo inspection consists of interpreting echos sent back by the package while through transmission inspection consists of interpreting the sound wave at the other end of the package, after it has passed through. The ultrasonic wave frequency used ranges from 5 to 200 MHz. The sound wave may be generated by a piezoelectric crystal, or transducer, that has been cut to provide a specific frequency. It is activated by a high voltage pulse from a transmitter, which is also known as the pulser. The activation would cause the transducer to vibrate at the specified frequency, which transmits an ultrasonic wave through the package. This wave travels to the specimen through a medium or couplant, which is usually deionized water since sound waves are severely attenuated in air at the frequencies used. The wave travels through the specimen with a portion of it being reflected back everytime it hits an interface within the specimen.

In the pulse echo method shown in Figure 1.10 (a), the same transducer is used as sender and receiver of the sound waves. Pulses are repeated using repetition rates at which the echoes from one pulse will not interfere with those of another, e.g., 10-20 KHz. The echoes received by the transducer are converted to voltages, amplified, digitized, and presented to the user as an image. In the through transmission technique shown in Figure 1.10 (b), separate transducers are used to send and receive sound waves, both of which are on opposite sides of the specimen. The absence and presence of signals then signifymean bad and good bonding, respectively.

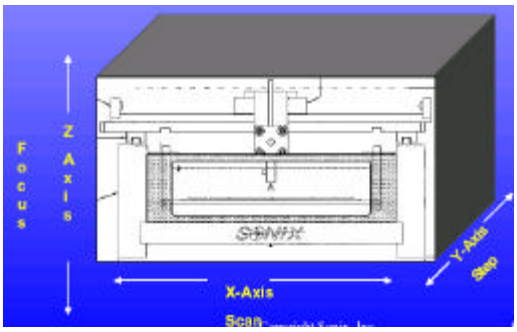

Figure 1.9: SONIX Scanner

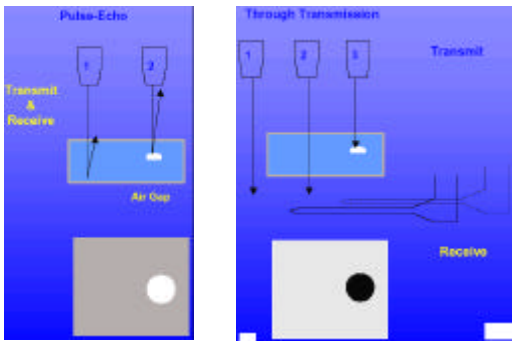

(a) (b)

Figure 1.10: (a) Pulse-Echo, One Transducer (b) Through Transmission, Two Transducers

Acoustic images are generated by raster scanning the transducer across the surface, which receives ultrasonic signals that are then stored as an amplitude plot of the module's interior reflections. The time-amplitude data is called an A-scan, as shown in Figure 1.11. Setting the time of the first reflection as a reference point creates an A-scan; this point is typically the front surface of the object to be scanned. The reflection times after this reference time represent specific depth planes within the part. This depth control is called gating, and is used to generate the amplitude maps. A procedure for generating the A-scan is outlined below.

• Bulk waves are created and then focused towards the section surface.

• Measurements are made starting from the first reflection off the top surface.

• The top surface is used as a reference; subsequent reflections are below this surface.

• Interior sound wave reflections are stored at a user-set time window.

• The entire surface of the section is scanned, storing wave reflection amplitudes relative to the position of the transducer.

• A greyscale map of die-attach interface is reconstructed based on the reflected amplitudes.

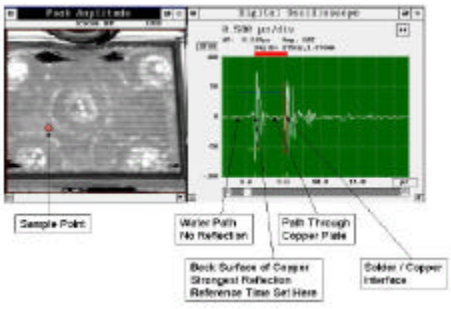

Figure 1.11: Black and white C-scan (left) and A-scan of the backside of a MOSFET (right).

A map of the section can then be built from the stored waveform data. Specific time slices from the waveform data allow the construction of an amplitude map at a specific depth within the section. This amplitude map is called a c-scan. Gaps, such as delaminations and voiding within the bond region, cause a complete reflection of ultrasonic energy. These defects appear as bright areas in the C-scan image acquired in pulse echo mode. They also are significant because they exist due to defects in the die-attach solder. The SAM can be used from the top or bottom of the MOSFET module. The images shown so far assume that the ultrasonic transducer is pointing from the bottom of the device, but images of delaminations can also be taken from the top of the module, as in Figure 1.12.

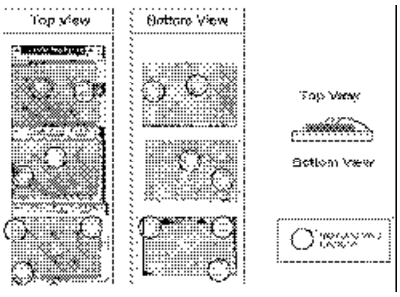

Figure 1.12: Top and bottom mirror images of die-attach delaminations in three different MOSFET devices [6]

Key Issues with Scanning Acoustic Microscopy

The acoustic microscope is a tool that provides a large amount of flexibility in the types of materials and shapes that can be imaged, since it contains transducers with varying frequencies and focal points. Table 1.3 presents an overview of the transducer types and their typical use for imaging power semiconductor devices. Focal points can be changed in many types of transducers; this allows the user to pick a transducer with a short focal

length, which can offer reduced scattering of acoustic energy but does necessitate accurate placement of the desired object within a narrow focal length range, as illustrated in Figure 1.13.

Table 1.3: Transducer frequency and material types imaged in an acoustic microscope

Material to be Imaged	Frequency (MHz)	Notes
DBC Baseplate, Solder Layer	10~15	Low frequency used to penetrate ceramic with minimal scattering
Copper Baseplate, Solder Layer	15	0.5” focal point transducer easily penetrates copper; optimal focal point is easier to find
Solder, Silicon Layer and Wirebonds	15~50	0.5-1.5” focal point resolves wirebond detail around focal point of transducer
Silicon Surface	75~125	High resolution, (10 ~ 5µm objects)
Any Flat Surface	125 and up	Surface wave transducer capable of resolving 2µm objects

Copper-backed power semiconductors are typically the easiest to scan. The homogenous nature of the flat copper substrate provides a good initial reflection and a sharp transition to the solder layer. This makes the images of delaminations readily apparent. Our SAM images of copper substrates use the 110MHz, 8 mm focal point transducer.

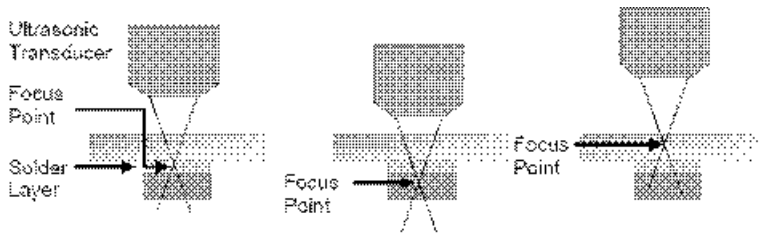

Figure 1.13: Effect of transducer focus on void measurement

Typically, the accepted procedure for focusing is first to define the portion of the A-scan that indicates the desired layer. Next, it is necessary to move the transducer up and down in place, watching the A-scan until the amplitude the waveform in that layer is at its maximum. Great care must be taken during focusing to enhance the repeatability of the process. This careful attention is especially important for devices that are scanned over several periods to track growth of cracks and delaminations. The methods used to ensure repeatability include,

• Using the same transducer for each measurement.

• Maintaining similar focal distance between the transducer and the part, which is accomplished by using the water path distance reported from the edge of the transducer to the top surface of the part.

• Maintaining similar gain amplifier settings; typically, these are stored for recall in the SAM system's parameter memory.

• Defining a similar data gate collection location, also stored in parameter memory.

• Scanning an unaged device along with aged device to be used as a reference.

1.3.2.2 Environmental Scanning Electron Microscopy (E-SEM)

The primary advantages of the ESEM lie in permitting the microscopist to vary the sample environment through a range of pressures, temperatures and gas compositions. The Environmental SEM retains all of the performance advantages of a conventional SEM, but removes the high vacuum constraint on the sample environment. Wet, oily, dirty, non-conductive samples may be examined in their natural state without modification or preparation. The ESEM offers high resolution secondary electron

imaging in a gaseous environment of practically any composition, at pressures as high as 50 Torr, and temperatures as high as 1500 °C.

All SEM's consist of an electron column, that creates a beam of electrons; a sample chamber, where the electron beam interacts with the sample; detectors that monitor a variety of signals resulting from the beam-sample interaction; and a viewing system that constructs an image from the signal. Figure 1.14 shows the schematic of a SEM.

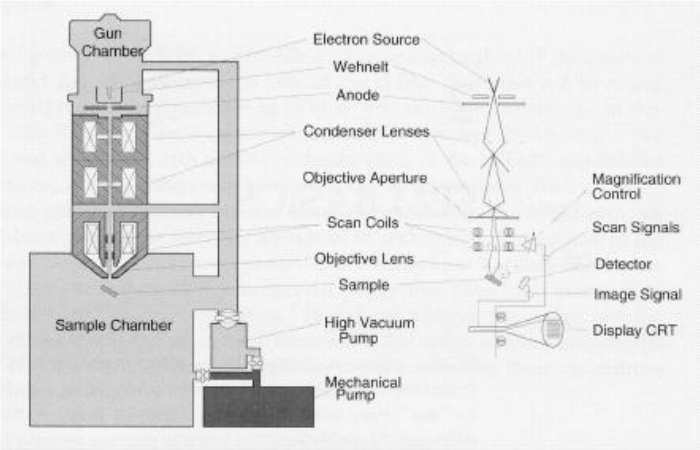

Figure 1.14: A schematic representation of a SEM

High vacuum conditions are required in the electron gas and throughout the column, where gas molecules can scatter electrons and degrade the beam. Instead of using the single pressure limiting aperture typical of conventional SEMs, ESEM uses multiple Pressure Limiting Apertures (PLA's) to separate the sample chamber from the column. The column is still high vacuum, but the chamber may sustain pressures as high as 50 Torr. ESEM uses a proprietary Environmental Secondary Detector (ESD) which can

function in non-vacuum environment instead of the Everhart-Thornley (ET) detector used in SEM.

What can ESEM do?

(1) Gas ionization in the sample chamber eliminates the charging artifacts, typically seen with nonconductive samples. These specimens do not need to be coated with a conductive film. This minimizes sample preparation and limits damage to delicate samples.

(2) The ESEM can image wet, dirty and oily samples. The contaminants do not damage or degrade the image quality.

(3) ESEM can acquire electron images from samples as hot as 1500ºC, because the Environmental Secondary Detector (ESD) is insensitive to heat.

(4) The detector is also insensitive to light. Light from the sample, for example incandescence from heated samples, cathodoluminescence and fluorescence do not interfere with imaging.

(5) ESEM can acquire x-ray data from insulating samples at high accelerating voltage.

(6) Makes it possible to investigate specimens in dynamic processes, such as tension, compression, deformation, crack propagation, adhesion, heating, cooling, freezing, melting, hydration, dehydration and sublimation.

1.3.2.3 X-Ray Tomography and Laminography

X-ray laminography is a nondestructive radiographic process for capturing three-dimensional (3-D) information about the internal structure of an object. It is related to x-ray tomography (commonly known as CAT-scan). In tomography the object is rotated on an axis perpendicular to the x-ray beam, and data is gathered about slices perpendicular to the axis of rotation. In laminography the object is moved in a small diameter orbital path around the center of an inclined x-ray beam. The Phoenix X-Ray machine available in CALCE is shown in Figure 1.15 and the schematic of operation is shown in Figure 1.16.

The system operates by initializing the X-Ray beam and keeping the samples on a rotating horizontal stage. The integrated software controls the X-Ray tube and beam quality. The software also controls the sample positioning in the path of the beam and taking the scanned image for post processing. The machine can be run in 2D mode without changing the system with a maximum resolution of 2 to 3 microns.

Figure 1.15: Phoenix X-Ray Machine (Courtesy: Phoenix X-Ray)

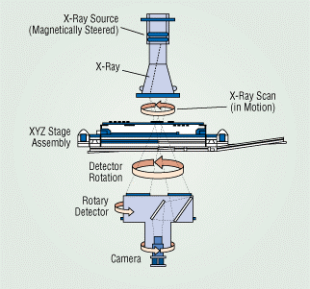

Figure 1.16: A schematic X-Ray Laminography (Courtesy: Phoenix ï X-Ray)

1.3.3 Thermo-mechanical Durability Measurements

1.3.3.1 Environmental Testing Chambers

Environmental testing chambers are used to conduct temperature and power cycling. Temperature cycling tests are used to test the durability of a package undergoing temperature variations over a given period of time. This test exposes the package to mechanical fatigue induced by cycles of thermal expansion. The dwell period is important because it allows the sample load to reach equilibrium and stress relaxation to occur.

1.3.3.2 Vacuum Solder Reflow Chamber

A SST International MV 2200 Programmable Vacuum Reflow Chamber shown in figure 1.17 has been used to fabricate the samples for temperature cycling. It performs flux-less solder reflow in a controlled atmosphere. It is programmed to control temperature, pressure and atmosphere. Performing reflow in vacuum removes oxides from the solder

and keeps the surfaces to be joined clean. The resistive graphite tooling for reflow fixturing provides heat generation. Thermocouples inside the chamber connected to the graphite tooling measure temperature and control current. Forming gas (10% H_2 and 90% N_2) is used as a cover gas during soldering to provide reducing conditions. High pressure nitrogen is fed into the chamber during solidification to reduce void size and speed cooling.

Figure 1.17: Vacuum Reflow Chamber

2 Literature Review

This chapter focuses on characterization of the thermo-mechanical durability of 95.5Pb2Sn2.5Ag solder alloys. In order to assess the durability, viscoplastic constitutive properties of the solder alloys also need to be characterized. Studies related to constitutive and durability properties of 95.5Pb2Sn2.5Ag solder alloy are discussed in this chapter. Microstructure and creep-fatigue mechanisms of relevant high temperature solders having lead, tin and silver are also reviewed.

2.1 Constitutive Properties

In general, temperature fluctuations experienced by electronic products in service cause progressive damage to solder joints; eventually, this damage accumulates beyond certain limits leading to electrical failure. One of the major goals of thermo-mechanical analysis is to be able to simulate the stress/strain responses of the solder joint and then predict its reliability in service. In order to gain accurate simulation and reliable prediction, realistic constitutive relations for solder alloys are warranted.

Mechanical constitutive behavior describes the deformation of a material in response to an applied load. In order to evaluate thermo-mechanical durability of 95.5Pb2Sn2.5Ag solder, constitutive properties need to be characterized. Since the microstructure of 95.5Pb2Sn2.5Ag solders is important to understand various deformation mechanisms (e.g. plastic and creep), the microstructural observations of 95.5Pb2Sn2.5Ag solders are presented in the failure analysis section in next chapter.

Solder materials respond viscoplastically to mechanical loading. In other words, there are multiple competing inelastic deformation mechanisms, each with a different characteristic time scale. Some, like dislocation slip, occur over very short (instantaneous) time scales. Others, like dislocation glide/climb, grainboundary sliding, dislocation pipe diffusion (self diffusion along dislocation cores), grain-boundary diffusion, and intragranular diffusion, occur over much longer time scales and have an Arrhenius dependence on temperature. The fact that most solders are above 0.5 homologous temperature during operation, makes the contribution of each of these rate-dependent mechanisms significant. This multiplicity of deformation mechanisms manifests itself as a combination of recoverable (elastic) deformations as well as irrecoverable (inelastic), nonlinear rate-dependent deformations.

The test results reported in the literature for solder material properties typically display large variabilities and discrepancies across different studies. One reason for this is that the steady state shear strain rates reported by various researchers can span several orders of magnitude. This was seen in data for SnPb eutectic solder at 75°C [5]. Other reasons for the discrepancies include the following: differences in specimen design; differences in alloying compositions; differences in specimen preparation techniques; differences in test methods and stress states generated during testing. The primary issue in specimen design is the characteristic length scale of the specimen. Most solder joints in electronic packages are small enough to be comparable to the grain size of the polycrystalline solder materials. Large bulk specimens thus provide results quite different from those observed in small solder joints. Thus test specimens for material property characterization (both

constitutive and durability properties) should be carefully designed to represent the length scale of real solder joints.

The fabrication process used for solder test specimens is also extremely important as it affects both constitutive and durability behavior. Parameters such as reflow profile affect the void content, average grain size, intermetallic amount and concentrations. Parameters such as flux choice and surface cleanliness can affect the wetting and interfacial strength. Parameters such as choice of plating on the metal terminations can affect local intermetallic compositions, and hence interfacial strength and adhesion. Choice of test method involves deciding what type of loading to use (e.g. cyclic temperature changes, or cyclic mechanical loading or combinations), and what stress state to use (e.g. tensile, shear, combination). The test method therefore also adds to the variability of the test results.

2.1.1 Choice of Constitutive Models

The stress-strain behavior for engineering materials depends on several factors, with temperature and strain (deformation) rate and stress history being the most important. An early concept in developing constitutive equations was the idea that the flow stress was dependent only on the instantaneous values of strain, strain rate, and temperature [7].

$$f(s, \dot{e}, e, T) = 0 \tag{2.1}$$

However it was soon realized that plastic deformation is an irreversible process. The flow stress depends fundamentally on the dislocation structure, which depends on the

metallurgical history of strain, strain rate, and temperature. The general form of a constitutive equation is given by,

$$ds = \{\frac{\partial s}{\partial e}\}_{\dot{e}T} de + \{\frac{\partial s}{\partial \dot{e}}\}_{eT} d\dot{e} + \{\frac{\partial s}{\partial T}\}_{e\dot{e}} dT \tag{2.2}$$

where e is the uniaxial or equivalent strain, s is the equivalent stress, T is temperature, and $\dot{e}$ is the strain rate.

The constitutive models used by the mechanics community for modeling and simulation of mechanical deformations in viscoplastic materials can be broadly grouped into two families: partitioned and unified models. The partitioned constitutive modeling approach partitions the inelastic deformations conceptually into two main groups. Deformations occurring over very short time scales (eg. due to dislocation slip) are idealized as "instantaneous," and hence insensitive to the loading rate. These deformations are termed "plastic" in this discussion. The remaining deformations (those occurring over longer time-scales) are termed "creep." Creep deformation is often further sub-divided into transient (primary) and steady state (secondary) categories, based on whether the strain rate varies with time or not at a constant stress level.

2.1.2 Partitioned Constitutive Model

Since partitioned plastic and creep energies are needed to develop Energy-Partitioning durability models of leaded solders, a partitioned constitutive model is desirable in this study. Considering the viscoplastic deformation characteristics of solder alloys under

complex loading in electronic components, the constitutive model of solder alloys is developed considering three major modes of solder deformation. The total shear strain ε_{tot}, can be constructed as a linear combination from three separate deformation mechanisms: time independent elastic strain, ε_{el}, time independent plastic strain, ε_{pl}, rate dependent creep strain, ε_{cr}.

$$e_{tot} = e_{el} + e_{pl} + e_{cr} \tag{2.3}$$

Elastic deformations of materials result from both expansion (compression) and distortion of the molecular bonds as an external force is applied. They are fully recoverable, compared with non-recoverable inelastic deformations (plastic and creep deformations). Recoverable, in this case, means complete and instantaneous time-independent elastic recovery although certain amount of anelastic i.e. time-dependent elastic recovery does take place as well [8]. However, for all practical purposes elasticity is described by a simple linear relationship between the applied stress and measurable deformation, which is known as Hooke's law:

$$e_{el} = \frac{s}{E(T)} \tag{2.4}$$

where E is the temperature dependent Young's modulus of elasticity, s is the equivalent stress, and e is the uniaxial or equivalent strain.

$$E(T) = E_0 - E_T(T) \tag{2.5}$$

where T is the temperature. For most engineering materials and all solders, the elastic modulus is temperature and strain rate dependent [9].

Modeling the inelastic behavior is far more complex, since it involves plastic and creep deformation interactions. For the sake of convenience, plasticity is modeled as a pseudo-instantaneous phenomenon, i.e. it is assumed to be time-independent, whereas creep is time-dependent. Time-independent plasticity is typically modeled using a power-law expression, commonly known as the Exponential Hardening model:

$$s = K(e_{pl})^{n_p} \tag{2.6}$$

where $\sigma > \sigma_y$, σ_y is the yield stress, K is the pre-exponential strength (hardening) coefficient, and n_p is the plastic strain hardening exponent, which are modeled as temperature dependent constants. Plastic deformations dominate under conditions where there is insufficient time for time-dependent deformation to occur, i.e. at relatively high strain rates. Since creep is a thermally activated process, plastic deformation is also prominent at low temperatures

Since solder alloys are used at high homologous (T/T_m) temperatures - even at room temperature $T>0.5T_m$ (T_m – melting point), - emphasis is placed on creep deformation. A generalized scheme for modeling creep deformation is shown in Figure 2.1. Accumulation of creep deformation can be divided into three steps. The strain rate starts high (primary creep), but decelerates to a lower, steady state value. This is the region where the creep strain rate is saturated and is known as steady state creep strain rate (secondary creep). Eventually, the strain rate begins to increase rapidly leading to failure by creep rupture (tertiary creep). The secondary creep strain region is the one that is most often modeled, and chosen to represent the entire creep process; the reason being that modeling steady state creep eliminates the need for inclusion of strain history.

The secondary (also termed steady state) creep is generally expressed by three major types of relationships:

$$\dot{e}_{cr} = A s_u^{\frac{1}{n_c}} e^{\frac{-Q}{RT}} \tag{2.7a}$$

$$\dot{e}_{cr} = A[\sinh(a s)]^n \exp\left(-\frac{Q}{RT}\right) \tag{2.7b}$$

$$\dot{e}_{cr} = A\left(\frac{s^n}{T}\right)\exp\left(-\frac{Q}{RT}\right) \tag{2.7c}$$

where A is the stress co-efficient, n is the creep strain hardening exponent, Q is the thermal activation energy of creep in J/mol, R is the universal gas constant (= 8.31 J/K mol), T is the absolute temperature in K, $\dot{e}$ is the equivalent creep strain rate, and s_v is the equivalent saturation creep stress. Equation (2.7a) is Weertman's secondary creep law [10], which is used for steady state creep over a wide range of temperature and stress. Equation (2.7b) is the Garofalo, or sinh, creep law [11], which can represent two different creep mechanisms at different stress levels. Equation (2.7c) is Dorn's creep law [12], which considers the temperature dependence of the hardening mechanism.

Various other steady-state creep models employed in the literature include the hyperbolic sine [13, 14], the Norton model [15, 16], variations of the partitioned creep model [17, 18], variations of the Sherby-Dorn model [19]. Other investigators chose to model the primary creep behavior [20], which can be significant in certain conditions. In some cases, plasticity can be represented in a unified manner, using a single expression to

represent both the time-independent and the time-dependent deformation. Examples of this type of modeling scheme are the Bodner-Partom unified creep-plasticity model [21], and the Anand model [22, 23].

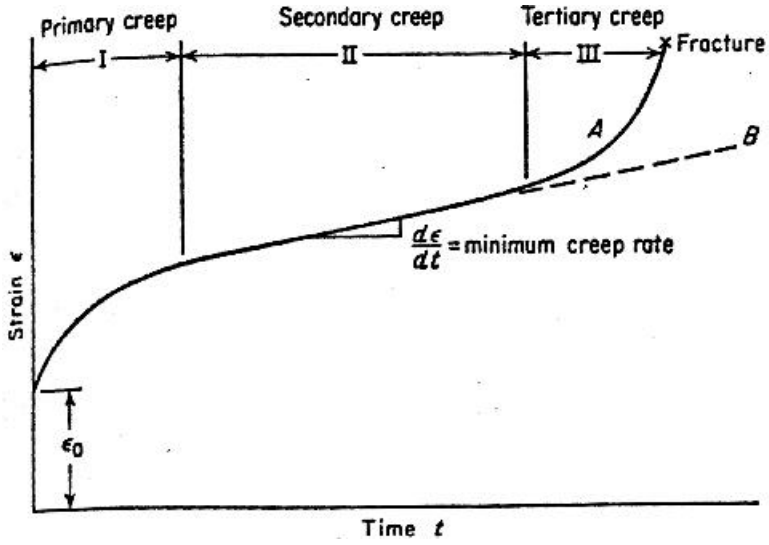

Figure 2.1: Typical constant load creep test

In this study, we choose to express the total equivalent strain, ε, is expressed using the following equation:

$$e_{tot}(t) = \frac{s}{E(T)} + \left(\frac{s}{K(T)}\right)^{\frac{1}{n_p(T)}} + tA(s)^{\frac{1}{n_c}} e^{\frac{-Q}{RT}} \tag{2.8}$$

where s is the equivalent stress.

The values of the material constants in the constitutive model developed above are obtained from literature [24]. Monotonic, isothermal tests have been conducted on 95.5Pb2Sn2.5Ag solder at constant (shear) actual strain rates from $1x10^{-2}s^{-1}$ to $1x10^{-6}s^{-1}$ over a temperature range from 25°C to 150°C (0.5 to 0.75 homologous temperature) in

strain control, to study the effects of strain rate and temperature on the mechanical properties in a systematic manner [24]. The material characterized is highly compliant and the range of strain rates chosen ($1x10^{-2}s^{-1}$ to $1x10^{-6}s^{-1}$) was considered to be wide enough to obtain time-independent plastic and time-dependent creep deformation. The test matrix used in this study is shown in Figure 2.2 below:

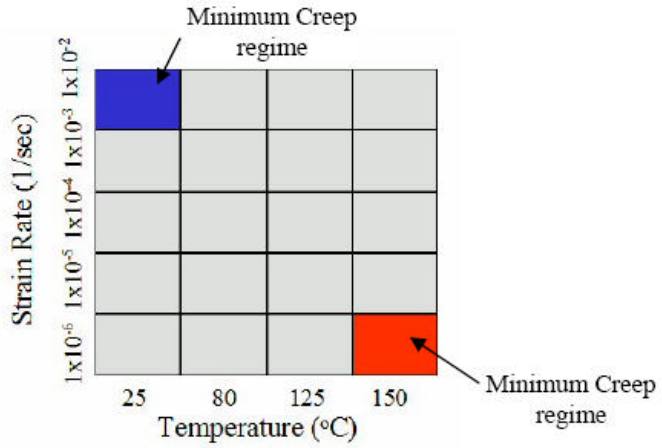

Figure 2.2: Test Matrix [24]

2.1.2.1 Elastic Model

The elastic modulus of solder alloys is a function of strain rate as well as temperature [25]. A shear strain rate ($\dot{g} = 1 \times 10^{-3} s^{-1}$) has been used for modulus tests [24] because it is reasonably close to the actual strain rate of solder in microelectronic packages under normal operating conditions. Modulus tests have been performed for a temperature range designed to simulate field-loading conditions.

Yield stress and Ultimate tensile strength (UTS) were found to decrease with temperature and increase with strain rate [24]. Similar extrapolations [25] have been made from investigations with 63Sn/37Pb eutectic solder. Figures 2.3 and Figure 2.4 show the dependency of yield stress on temperature and strain rate, and Figure 2.5 and Figure 2.6 show the dependencies for ultimate tensile strength of 95.5Pb2Sn2.5Ag solder.

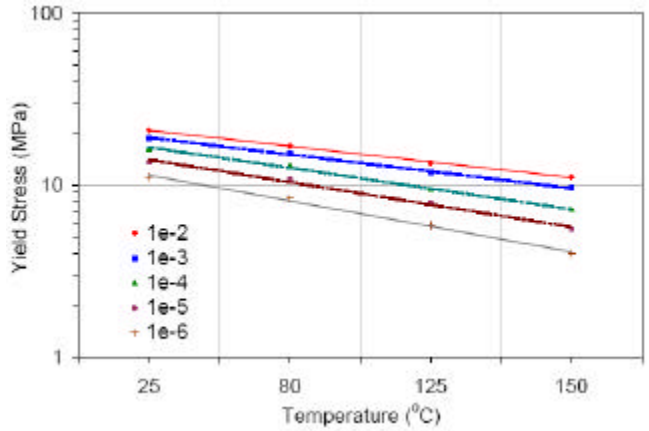

Figure 2.3: Yield Stress of 95.5Pb2Sn2.5Ag as a function of temperature [24]

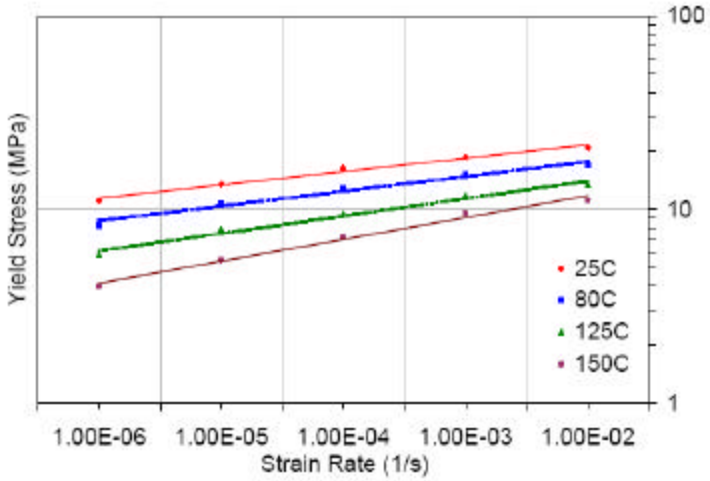

Figure 2.4: Yield Stress of 95.5Pb2Sn2.5Ag as a function of strain rate [24]

The higher the temperature and the lower the strain rate, the greater was the variation in yield stress. This was attributed to the fact that creep deformation makes a larger contribution to the reduction in strength at higher temperatures and lower strain rates.

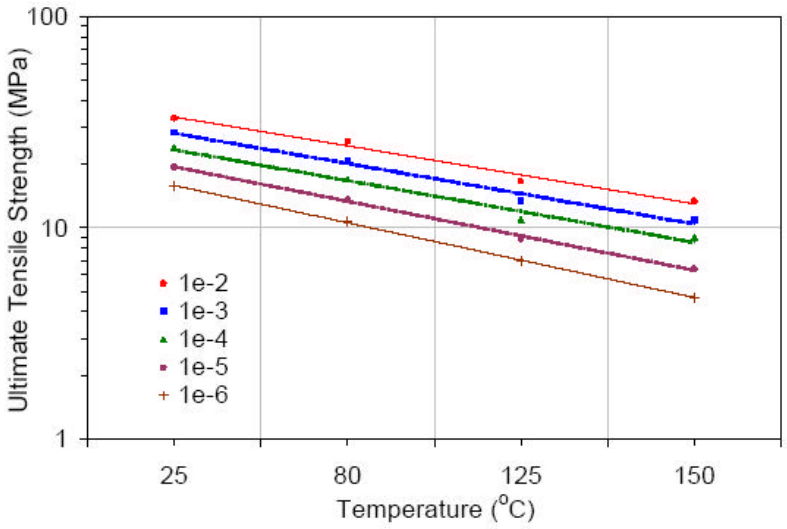

Figure 2.5: Ultimate Tensile Strength of 95.5Pb2Sn2.5Ag as a function of temperature [24]

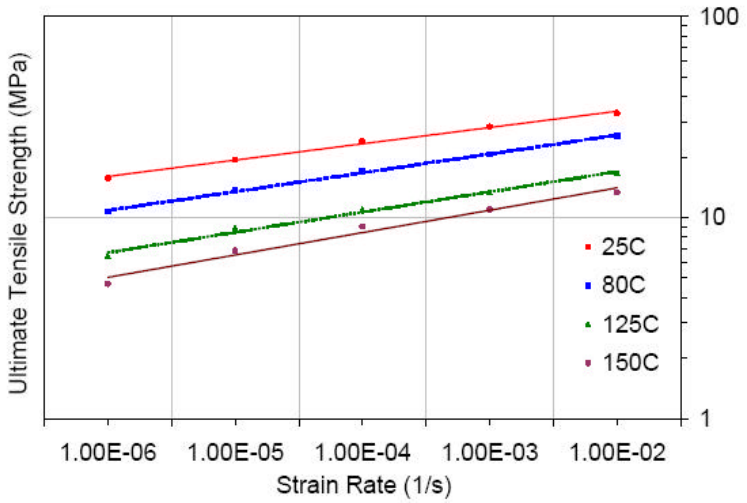

Figure 2.6: Ultimate Tensile Strength of 95.5Pb2Sn2.5Ag as a function of strain rate [24]

The shear modulus was obtained from the ensuing force vs. strain curve [24] and the elastic modulus, E, was then obtained from the relationship,

$$G = \frac{E}{2(1+u)} \tag{2.9}$$

where G is shear modulus calculated from the slope of the force vs. strain plot curve (Figure 2.7), and ? is the Poisson's ratio which was assumded to be 0.4 as is the case for pure lead.

Figure 2.8 shows that Young's modulus decreased with an increase in temperature. The deviation bands are standard deviation. A modulus-temperature relationship for 95.5Pb2Sn2.5Ag solder alloy has been reported [24] for the average value of moduli:

$$E = 30.448 - 0.0585T(K) \tag{2.10}$$

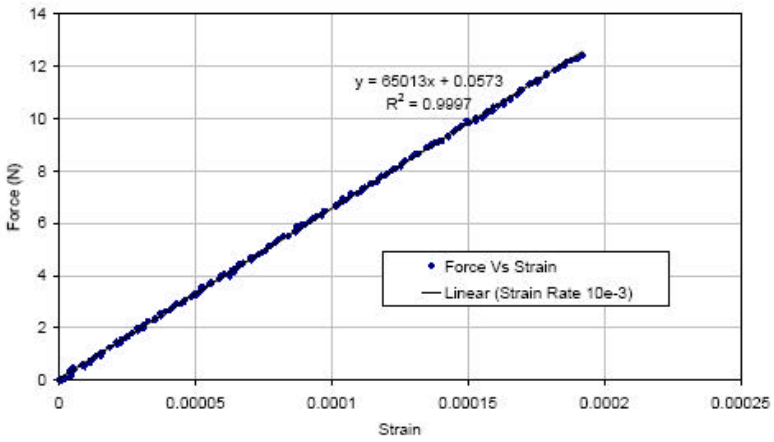

Figure 2.7: Sample force vs. strain curve at 25°C [24]

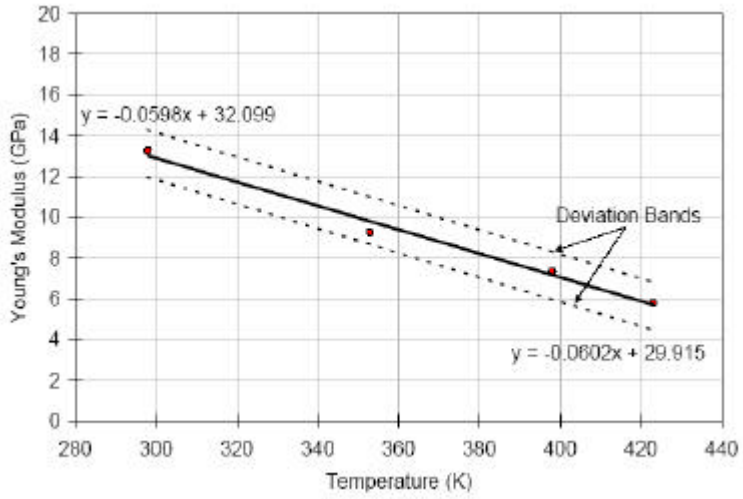

Figure 2.8: Temperature dependence of elastic modulus, E [24]

Figure 2.9 below shows the temperature dependence of Young's Moduli of some high lead solders, in comparison with that of the 95.5Pb2Sn2.5Ag solder.

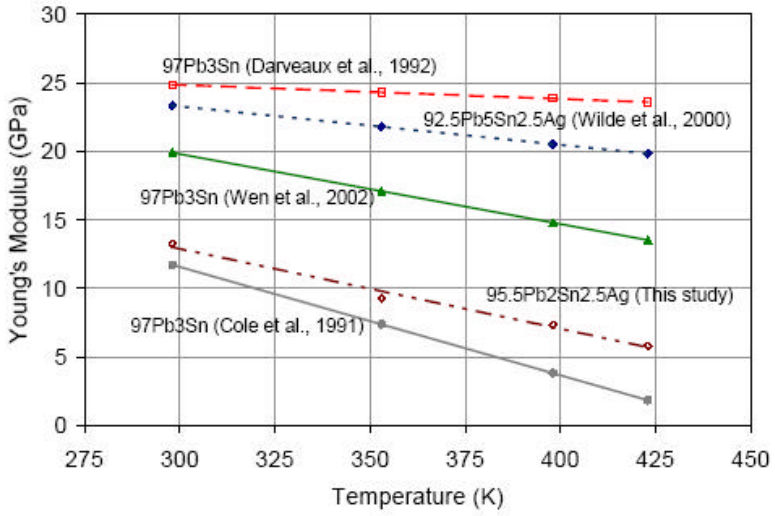

Figure 2.9: Temperature dependence of Young's modulii of some lead-rich solders

It can be seen that the value of Young's moduli reported by different investigators differ even for alloys of the same composition. Several factors influence the measurement of

Young's modulus including the loading rate, creep effects, specimen configuration, and the structural compliance of the load train. Table 2.1 below shows the values of Young's moduli for some lead-rich solders at room temperature as obtained by different investigators, as well as the assumed value of Poisson's ratio.

Table 2.1: Young's Modulii for lead-rich solders obtained from literature

Solder	Specimen Type	Type Modulus at 25°C (GPa)	Assumed Poisson's ratio	Source
92.5Pb5Sn2.5Ag	Cylindrical dog-bone	23.32	0.33	Wilde et.al. 2000
97Pb3Sn	Flip-chip assembly	24.84	0.35	Darveaux et.al 1992
97Pb3Sn	Cylindrical dog-bone	11.73	-	Cole et.al.1991
97Pb3Sn	Cylindrical dog-bone	19.89	-	Wen et.al.2002

2.1.2.2 Plastic Model

Implementing the constant strain rate test has advantages over the creep (constant load) test. With the constant strain rate test, rate-dependent properties as well rate-independent properties can be determined, which can reduce the total number of tests significantly. Another practical advantage is that undesired data can be screened out at the early stage of the tests. If the specimen has defects and thus a crack grows early during the test, a significant load drop is visible in the load-displacement curve very early in the test. Also, since a low strain rate test usually runs for 40~60 hours, it is extremely time-effective if the specimen with defects is detected at the early stage of test.

The tests are conducted for a range of constant strain rates over a range of temperatures. For the constant strain rate tests, the bending effect associated with misalignment of the specimen is not significant because sufficient plastic flow occurs during the test to eliminate the effect [26].

Separating the stress-strain behavior into strain rate-independent and strain rate-dependent flow processes is difficult. One way to get an approximately strain rate-independent curve is to extrapolate the flow stresses vs. strain rate curve at each value of strain to very high strain rates where the increase in the flow stress is minimal for the corresponding increase in strain rate. Defining the extrapolated value of flow stress at a very high strain rate to be the true unrelaxed stress for a given value of strain, and finding such a value for different values of strain allows one to obtain a stress-strain curve (Figure 2.10) that is approximately strain-rate independent [27].

Shear stress can then be converted into an equivalent tensile stress and shear strain to an equivalent tensile strain by applying the Von Mises yield criterion to obtain the relationships [28],

$$s = t\sqrt{3}; e = \frac{1}{\sqrt{3}} g \qquad (2.11)$$

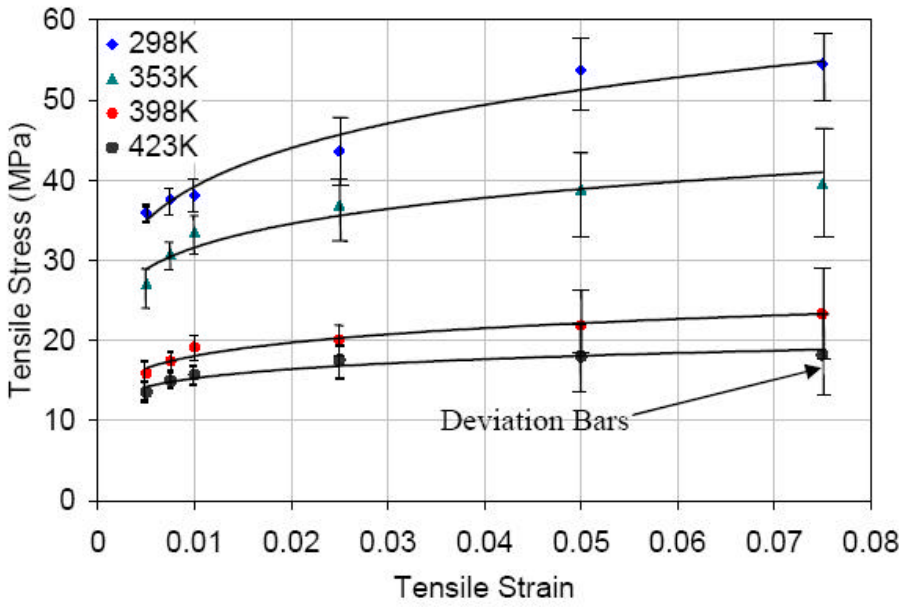

Figure 2.10: Strain rate-independent equivalent tensile stress vs. equivalent tensile strain [24]

The time-independent exponential hardening constant n_p and the pre-exponential co-efficient K can be calculated by curve fitting to the above rate-independent stress vs. strain plot. For the 95.5Pb2Sn2.5Ag solder, reported literature [24] shows the averaged values of the constants as a function of temperature:

$$n_p = 0.2954 - 0.0004T(K) \tag{2.12}$$

$$K = 230.05 - 0.49T(K) \tag{2.13}$$

Their respective temperature dependencies are plotted below in Figure 2.11 and Figure 2.12. The standard deviation in measured parameters is shown as deviation bands.

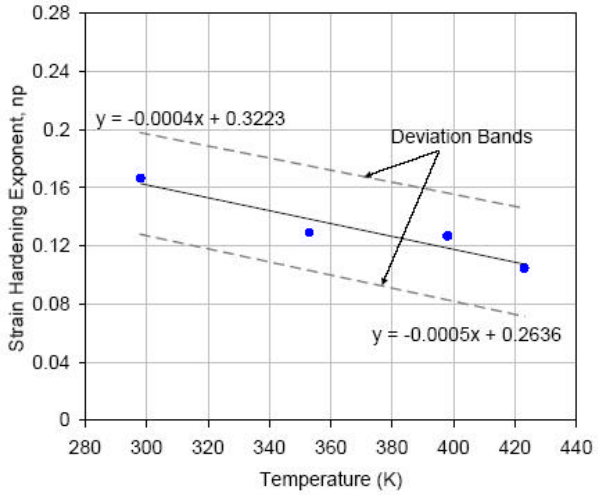

Figure 2.11: Temperature dependence of strain hardening exponent [24]

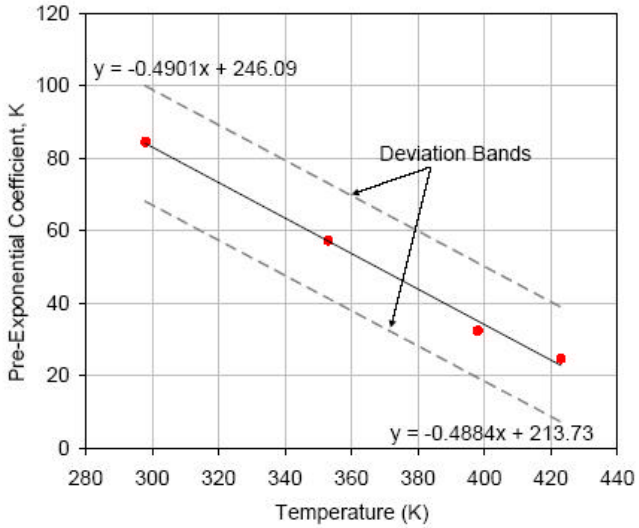

Figure 2.12: Temperature dependence of pre-exponential co-efficient [24]

Both the strain hardening exponent and the pre-exponential coefficient decreased with increasing temperature, since at higher temperatures, thermally activated processes such as creep deformations could induce stress relaxation thereby reducing the strength of the joint.

2.1.2.3 Creep Model

Time-dependent creep behavior can be characterized by a data set consisting of a steady-state strain rate and a saturation stress. The data are usually obtained from creep (constant load) tests. In creep tests, the strain rate is constant in the secondary (steady-state) creep regime, at a constant applied load. In a constant strain rate test, the load increases at a constant strain rate, and eventually the flow stress reaches its steady state saturated value, and is constant. This is analogous to the steady state saturation strain rate for a constant load/stress test [29]. Thus, even from these experiments one can calculate the steady state strain rate and saturation stress pairs. Saturation stress was observed to be temperature and strain rate dependent. After converting the shear components into the equivalent tensile components, saturation stress and strain rate pairs obtained from the constant strain rate tests at different temperatures were plotted on a log-log scale as shown in Figure 2.13. Data from 54 specimens subjected to monotonic, isothermal, constant strain rate tests for a wide range of temperatures of 25^{o}C, 80^{o}C, 125^{o}C, and 150^{o}C, and strain rates of 1x10^{-2}s^{-1}, 1x10^{-3}s^{-1}, 1x10^{-4}s^{-1}, 1x10^{-5}s^{-1}, and 1x10^{-6}s^{-1} were used to model the time dependent inelastic behavior due to creep [24]. The creep exponent, the stress co-efficient, and the thermal activation energy for creep can be calculated as follows,

$$\ln \dot{e}_{cr} = \ln A - \frac{Q}{RT} + \frac{1}{n_c} \ln s_v \qquad (2.14)$$

The slope of the strain rate vs. average saturated stress curves for different temperatures yielded the creep exponent and the intercept yielded the stress co-efficient and the thermal activation energy for creep, according to Equation (2.14). Table 2.2 summarizes the parameters calculated.

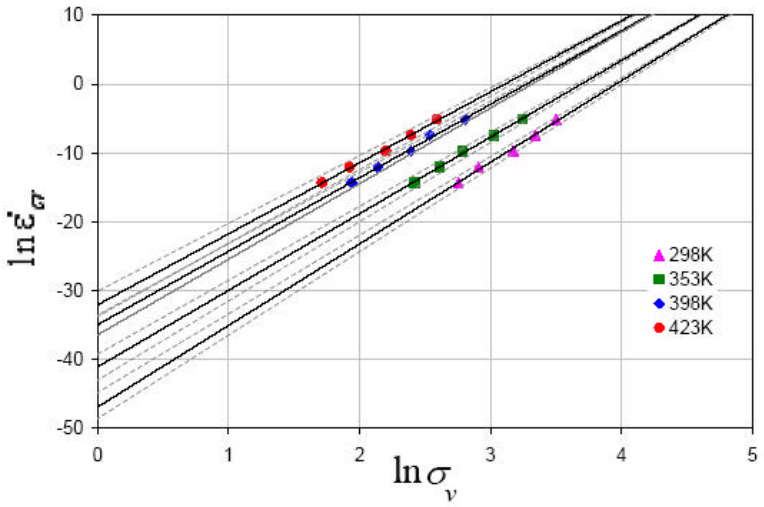

Figure 2.13: Log-log plot of equivalent steady state creep strain rate and equivalent average saturated stress pairs [24]

Table 2.2: Creep model parameters calculated from log-log plot [24]

Temperature	$\frac{1}{n_c}$			$\ln A - \frac{Q}{RT}$		
	Max	Avg	Min	Max	Avg	Min
25°C(298K)	12.312	11.848	11.421	-49.932	-46.910	-43.899
80°C(353K)	11.490	11.123	10.673	-44.657	-41.094	-38.454
125°C(398K)	11.189	10.671	10.113	-37.823	-34.975	-32.720
150°C(423K)	10.823	10.308	9.814	-35.374	-32.061	-29.278

The temperature dependency relationships of creep exponent and stress exponent and thermal activation energy are as follows [24]:

$$\frac{1}{n_c} = 15.425 - 0.0121T(K) \tag{2.15}$$

$$\left(\ln A - \frac{Q}{RT}\right) = 2.4661 - 14903T(K) \tag{2.16}$$

Figure 2.14 and Figure 2.15 show the temperature dependency of creep exponent and stress exponent and thermal activation energy [24]. The standard deviation of measured parameters are shown as deviation bands in the figures.

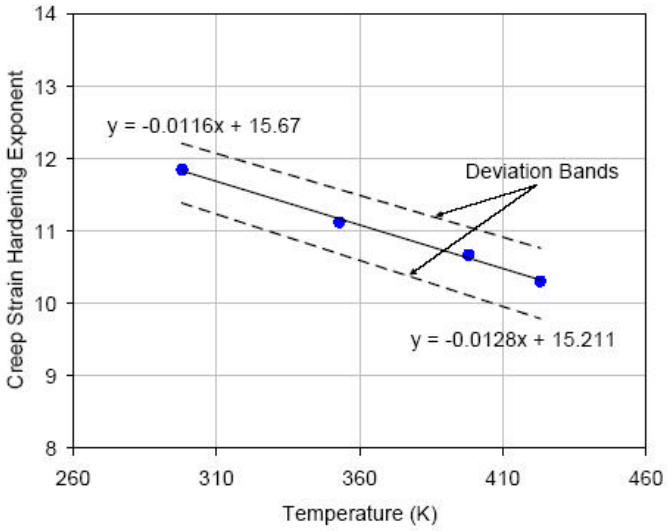

Figure 2.14: Temperature dependence of creep exponent [24]

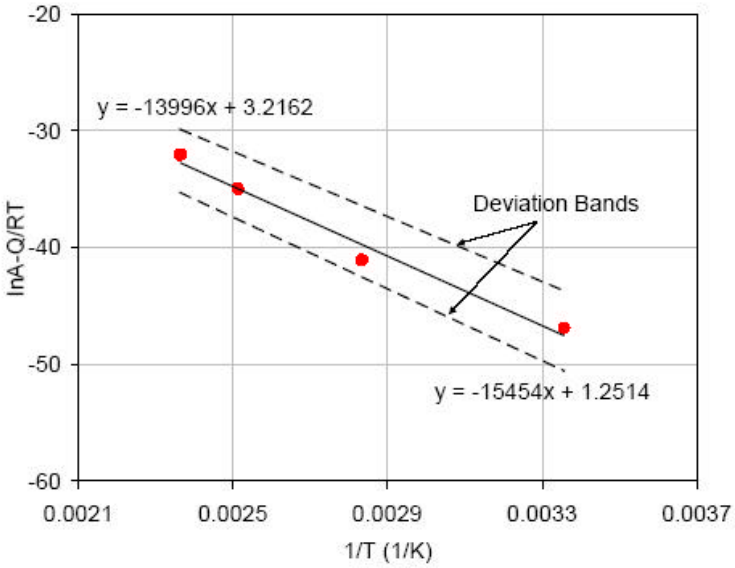

Figure 2.15: Arrhenius plot to determine creep thermal activation energy [24]

The constant term, lnA -Q/RT, can be decomposed into the co-efficient and the activation energy by plotting vs. the inverse of temperature. The y-intercept gives the co-efficient and the slope gives the activation energy.

The stress co-efficient, A, has been calculated [24] from the y-intercept of the average curve in Figure 2.15, and the thermal activation energy, Q, has been calculated from the slope of the same curve. The values are shown in Table 2.3 below:

Table 2.3: Time dependent creep constants [24]

Parameter	Values		
	Max	Avg	Min
A	24.93	11.77	3.49
Q	1.33eV	1.28eV	1.21eV

The average value of the creep stress exponent that was obtained suggested dislocation climb controlled deformation. The average value of activation energy that was obtained is very close to that of dislocation climb in pure lead (1.1eV). And creep tests done [30] on single crystals of pure lead in a helium atmosphere at a constant tensile stress have shown that dislocation climb is the rate controlling step.

2.1.3 Unified Constitutive Model

Both rate-independent plastic and rate-dependent creep deformations are combined as a rate-dependent inelastic deformation in unified constitutive models. Anand and Brown have proposed [31] a simple set of constitutive equations for large, isotropic, viscoplastic deformations. There are two basic features in the Anand model. First, this model needs

no explicit yield condition and no loading/unloading criterion. The plastic strain is assumed to take place at all nonzero stress values, although at low stresses the rate of plastic flow may be immeasurably small. Second, this model employs a single scalar as an internal variable to represent the isotropic resistance to plastic flow offered by the internal state of the material. This internal variable is denoted by *s*, which has the dimensions of stress, and is called the deformation resistance [31].

The internal variable s represents an averaged isotropic resistance to macroscopic plastic flow offered by the underlying isotropic strengthening mechanisms such as dislocation density, solid solution strengthening, subgrain, and grain size effects, etc. The deformation resistance s is consequently proportional to the equivalent stress σ. That is

$$s = c.s; c < 1 \tag{2.17}$$

where c is a material parameter and constant in the constant strain rate test, which is defined as:

$$c = \frac{1}{x}\sinh^{-1}\left[\left(\frac{\dot{e}_p}{A}e^{Q/RT}\right)^m\right] \tag{2.18}$$

where $\dot{e}_p$ is the inelastic strain rate, A is the pre-exponential factor, Q is the activation energy, m is the strain rate sensitivity, ξ is the multiplier of stress, R is the gas constant, and T is the absolute temperature, respectively.

By introducing the internal evolution variable for the physical material state, the unified constitutive model relates steady state inelastic strain rate, $\dot{e}_p$, to stress, temperature and material properties as follows [22]:

$$\dot{e}_p = A\exp\left(-\frac{Q}{RT}\right)\left[\sinh\left(x\frac{s}{s}\right)\right]^{1/m} \tag{2.19}$$

It is to be noted that the internal state variable enters into the flow equation only as a ratio with the equivalent stress. The temperature dependence in Equation. (2.19) is incorporated via a classical Arrhenius term. The stress dependence is a simple modification of the hyperbolic sine form first proposed by Garofalo [32] to model steady-state plastic flow (secondary creep). The evolution equation for the internal variable s is assumed to be of the form as

$$\dot{s} = g(s, s, T)\dot{e}_p \tag{2.20}$$

where the function g(σ, *s*, T) is associated with dynamic process, that is, strain hardening and dynamic recovery. A simple form of evolution equation of Equation (2.20) was given by Anand [31] follows:

$$\dot{s} = \{h_0\left|1-\frac{s}{s^*}\right|^a .sign\left(1-\frac{s}{s^*}\right)\}.\dot{e}_p ; a>1 \tag{2.21}$$

with

$$s^* = \hat{s}\left[\frac{\dot{e}_p}{A}\exp\left(\frac{Q}{RT}\right)\right]^n \tag{2.22}$$

where h_0 is the hardening/softening constant, a is the strain rate sensitivity of hardening/softening. The quantity s^* represents a saturation value of s associated with a

set of given temperature and strain rate as shown in Equation (2.22). $\hat{s}$ is a coefficient, and n is the strain rate sensitivity for the saturation value of deformation resistance, respectively.

When steady-state plastic flow occurs, the stress reaches the saturation value. The saturation stress s^* can be written as

$$s^* = cs^* \tag{2.23}$$

Combining Equations (2.18), (2.22) and (2.23) the saturation stress s* can be described with the following relation:

$$s^* = \frac{\hat{s}}{x}\left(\frac{\dot{e}_p}{A}e^{Q/RT}\right)^n . \sinh^{-1}\left[\left(\frac{\dot{e}_p}{A}e^{Q/RT}\right)^m\right] \tag{2.24}$$

Based on Equation (2.24), the material constants: Q/R, A, $\hat{s}/x$, n and m can be fitted to the strain rate vs. the saturation stress data from a set of experiments. Under isothermal and constant strain rate conditions, for plastic flow not developed fully, i.e., s < s*, the strain hardening data ds/de_p , that is the slope of the stress versus inelastic strain curve, can be represented as

$$\frac{s}{de_p} = ch_0\left(1 - \frac{s}{s^*}\right)a \tag{2.25}$$

Model constants for a few solders have been summarized in Table 2.4.

Table 2.4: Material parameters of viscoplastic Anand model for solders [23, 33]

Material Parameters	60Sn40Pb	62Sn36Pb2Ag	96.5Sn3.5Ag	97.5Pb2.5Sn	92.5Pb5Sn2.5Ag
A(s^{-1})	1.49×10^{7}	2.30×10^{7}	2.23×10^{4}	3.25×10^{12}	1.052×10^{5}
Q/R(°K)	10830	11262	8900	15583	11024.9
ξ	11	11	6	7	7
m	0.303	0.303	0.182	0.143	0.241
$\hat{s}$ (MPa)	80.42	80.79	73.81	72.73	41.63
n	0.0231	0.0212	0.018	0.00437	0.002
h_0 (MPa)	2640.75	4121.31	3321.15	1787.02	1432
a	1.34	1.38	1.82	3.73	1.3
s_0 (MPa)	56.33	42.32	39.09	15.09	33.07

2.1.4 Constitutive Models Used in High Lead Content PbSnAg Solders

Characterizing the deformation behavior of solder joints is an essential part of understanding and predicting thermal fatigue performance in electronic assemblies. One of the major goals of thermo-mechanical analysis in the electronics industry is to be able to simulate the stress/strain responses of the solder joint and then predict its reliability in service. In order to gain accurate simulation and reliable prediction, realistic constitutive relations for solder alloys are warranted. For nonlinear numerical simulation, a constitutive model of solder material must be built. Usually, a viscoplastic constitutive law must be defined as a user-defined subroutine code to represent the nonlinear rate-dependent stress-strain relations in some finite element programs. For high lead solder material the ratio of room temperature to melting temperature is greater than 0.5. Thus, solder operates at a high homologous temperature where creep is a significant factor and

must therefore be included into the constitutive model. There are two major types of constitutive models for solder materials, nonunified and unified. The nonunified model is based on an assumption that creep and plastic deformation are independent and that they can be calculated separately and added together to get the total inelastic deformation. The unified model integrates creep and plastic deformation into one inelastic deformation, which is directly calculated. The constitutive relations for solder alloys range from elastic-plastic models (e.g., Ramberg-Osgood relation) using empirical stress-strain curves to purely phenomenological models where the time-dependent and time-independent deformations are artificially separated. In this section constitutive relations used in some high lead content solders (90Pb10Sn, 97Pb3Sn, 95Pb5Sn, 97.5Pb2.5Sn, 92.5Pb5Sn2.5Ag) have been reviewed.

Data collected using constant displacement rate tests and constant load creep tests on 97Pb3Sn and 95Pb5Sn have shown that at intermediate stresses, the strain rate follows power law with stress. At high stresses, the strain rate is an exponential function of stress [34]. The steady state strain rate is described by [34],

$$\frac{dg_s}{dt} = C_1 \frac{G}{T}\left[\sinh\left(a\frac{t}{G}\right)\right]^n \exp\left(\frac{-Q}{kT}\right) \tag{2.26}$$

where α prescribes the stress level at which the power law dependence breaks down, and C_1 is a constant. Figure 2.16 shows the normalized strain rate plotted versus normalized shear stress for 97Pb3Sn and 95Pb5Sn. It is seen from Figure 2.16 that the power law breakdown is at approximately 10^{-3} τ/G. The stress exponent, n=7.0, suggests dislocation climb controlled deformation.

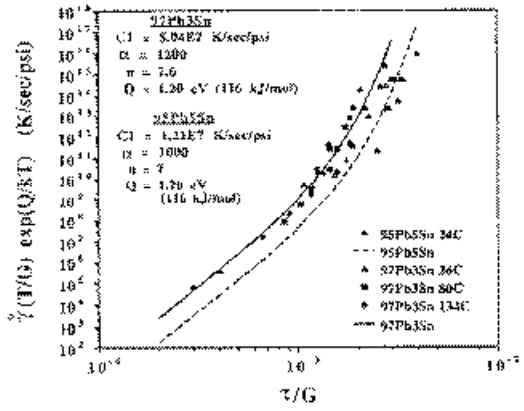

Figure 2.16: 97Pb3Sn and 95Pb5Sn normalized steady state behavior [34]

The transient creep strain given in Equation 2.27, which is the intercept of the linear part of creep strain-time plot is plotted versus the normalized shear stress for 97Pb3Sn and 95Pb5Sn, shown in Figure 2.17. It is seen that 97Pb3Sn undergoes considerable transient creep, with an average value of γ_T = 0.115. This is consistent with dislocation climb controlled deformation. The average value of γ_T for 95Pb5Sn is 0.030.

$$g_T = g_t\left[1-\exp\left(-B\dot{g}_s t\right)\right] \tag{2.27}$$

In Equation 2.27, γ_t is the transient creep strain and B is the transient creep coefficient.

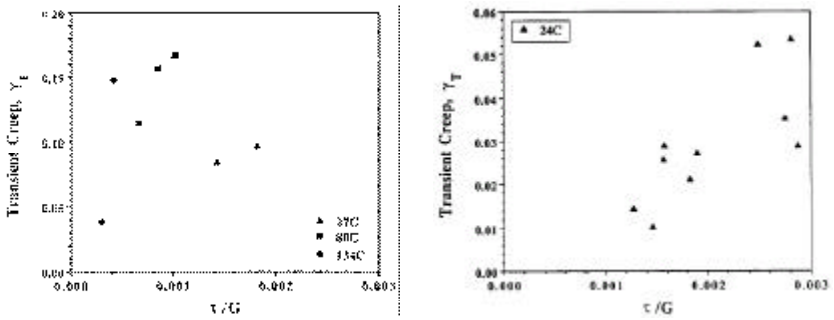

(a) **(b)**

Figure 2.17: Transient creep strain of (a) 97Pb5Sn (b) 95Pb3Sn [34]

An effective and accurate method based on the stress relaxation data at the hold time has been developed by Pao et al. [35] to determine the secondary creep properties of the Pb90Sn10 solder associated with Norton's equation

$$\frac{dg_{crp}}{dt} = B^* \exp\left[\frac{-\Delta H}{kT}\right] t^n \qquad (2.28)$$

where $d\gamma_{crp}/dt$ is the shear creep strain rate, n is the stress exponent, ΔH is the activation energy, *k* is Boltzmann's constant, T is temperature and B^* is a material constant. Table 2.5 shows the creep constants for Norton's relation and the associated mechanisms in a isothermal creep test, for 90Pb10Sn. Figure 2.18(a) and (b) shows the steady state creep rate based on Equation 2.28 versus stress for 40 and 140 °C respectively.

Table 2.5: Creep properties and the associated mechanisms for 90Pb10Sn [36]

Property	90Pb10Sn
B^*	100.6
ΔH, *ev*	0.64
N, 40°C	4.25
n, 140°C	3.03
Deformation mechanism	Dislocation core-diffusion

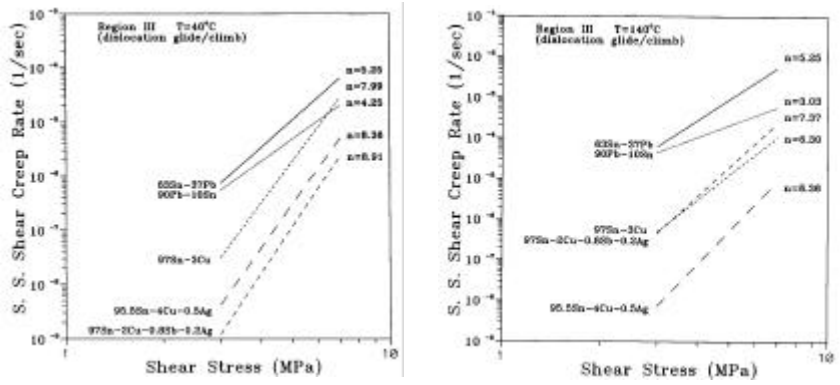

Figure 2.18: Steady-state shear creep rate versus shear stress at (a) 40°C (b) 140°C [36]

Wilde et al. [33] have determined the constants of unified Anand model for 97.5Pb2.5Sn solder (Table 2.4) from separated constitutive relations developed by Darveux & Banerji and concluded that the Anand model can be applied for representing the inelastic deformation behavior at high homologous temperature.

Becker et al. [23] have verified the parameters of Anand model for 92.5Pb5Sn2.5Ag solder to predict its viscoplastic behavior. By conducting a series of constant strain rates tests on cylindrical specimens for a temperature range from 20°C to 250°C, a good agreement between the experimental data and model predictions is achieved (Figure 2.19).

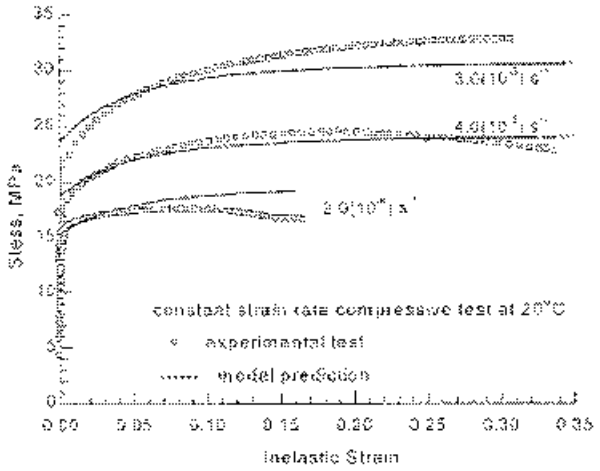

Figure 2.19: Constant strain rate behavior of 92.5Pb5SnPb2.5Ag solder [23]

Figure 2.20 (a) shows verification of steady state creep data of 92.5Pb5Sn2.5Ag solder at temperatures -65°C, 20°C, 100°C, 180°C and 250°C with model predictions. Figure 2.20 (b) shows the independent verification of creep data for this Pb-rich solder at temperatures 35°C and 150°C reported in the work of Solomon [37].

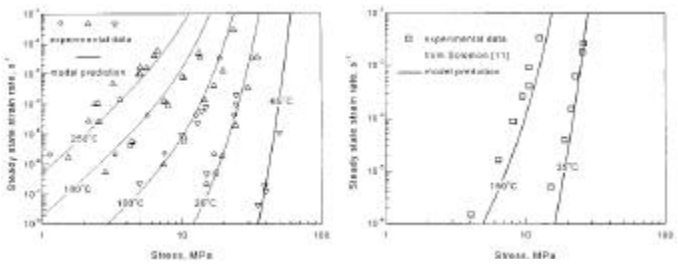

Figure 2.20: Comparisons of (a) experimental data and (b) model prediction for steady state creep behavior. (o: constant strain rate tests; D: constant stress compression tests; and Ñ: constant stress tensile tests in this work) [23]

Steady state creep data collected by Solomon [37] on 92.5Pb5Sn2.5Ag solder have been represented by a power creep law as shown in equation 2.29.

$$dg/dt = At^{h} \tag{2.29}$$

where A and η are constants over a range of applied shear stress, τ. Figure 2.21 shows the forward and reverse steady state creep rate for 92.5Pb5Sn2.5Ag solder where there is a lack of difference between the two. The points generated with creep in the forward direction of loading are the starred points, and the reverse creep data is shown by the "0" data points. At 150°C data curve exhibits a change in η and A which is indicative of a transition from matrix to grain boundary creep.

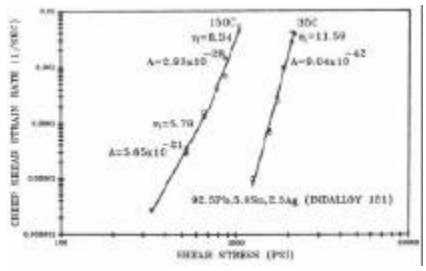

Figure 2.21: Creep shear strain vs. applied shear stress [37]

2.2 Microstructure During Thermal Cycling

Solder joints in electronic devices are often subjected to stresses and strains generated by thermal expansions during thermal cycling. An accurate prediction of the reliability of such joints depends on an understanding of the mechanical behavior and microstructure of the particular solder alloys. Increased solder joint reliability and the development of new more fatigue-resistant solder alloys require a fundamental understanding of the metallurgical mechanisms operative during the fatigue cycle and hence, an understanding of the solder microstructure. Since the solder is mechanically soft and is used at a high homologous temperature, deformation is introduced by plasticity and creep throughout the strain cycle. In addition, the cyclic deformation is affected by the fact that the solder contact is a thin layer bonded to relatively rigid materials with a complex intermetallic layer at the bonding plane. An understanding of the deformation is especially complicated by the inherent complexity of the as-solidified solder microstructure and its instability as it is cycled. The work that is reviewed here concentrates on the role of the solder microstructure and its association with the mechanisms of thermal fatigue. Particular emphasis is placed on a fundamental understanding of the microstructure-property relationship in high lead and Pb-Sn-Ag alloys. It has been observed in various research in the past that in all cases where shear deformation at elevated temperatures is a factor, the solder fails by the same basic mechanism – inhomogeneous deformation of the solder microstructure resulting in inhomogeneous recrystallization and softening leading to eventual joint failure.

Figure 2.22 shows a Pb-Sn phase diagram. Figure 2.23 shows the schematic representations of the equilibrium microstructures for a lead-tin alloy of composition C1 as it is cooled from the liquid-phase region. On cooling from the melt, the off eutectic compositions from 18.3 to 61.9 wt% Sn pass through the Pb-rich (FCC) plus liquid two-phase region. As the temperatures fall inside this phase field, the Pb-rich phase begins to solidify in a dendritic morphology. For compositions like C1 that are less than 18.3 wt% Sn solidification is complete at the solidus temperatures. Further cooling may or may not lead to the precipitation of a Sn-rich phase depending on the final temperature and the exact location of C1. It is even possible that the precipitate may form and dissolve during temperature cycling for some compositions near C1.

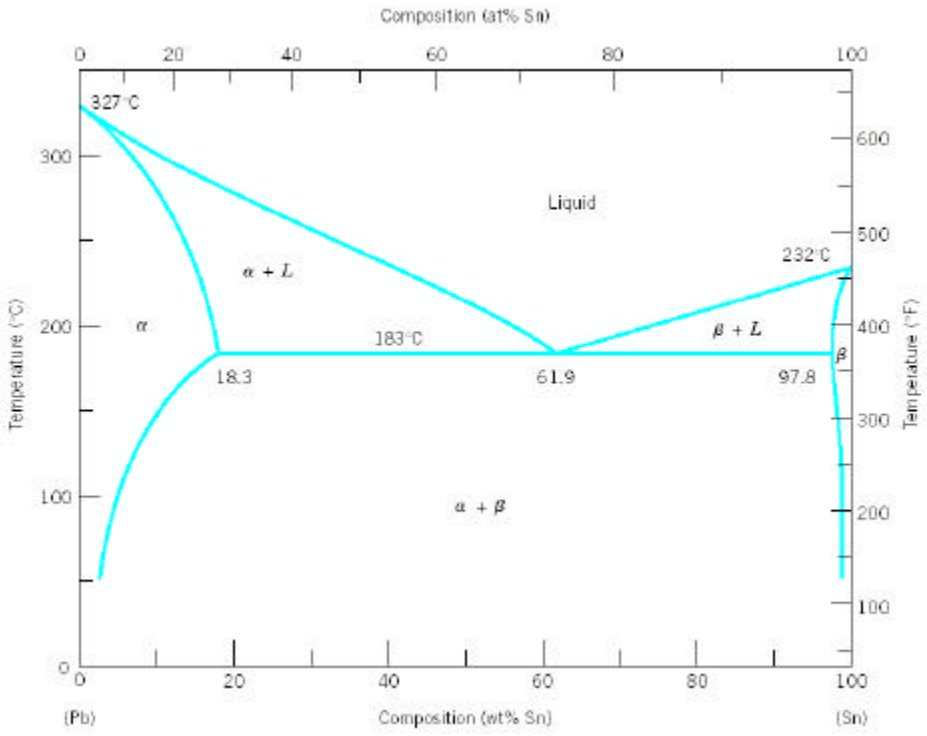

Figure 2.22: Lead –Tin Phase Diagram [38]

The ternary phase diagram for Pb-Sn-Ag is shown in Figure 2.24. In high lead solders the microstructure consists of increasing amounts of the primary Pb-rich phase. In case of 92.5Pb5Sn2.5Ag solders, it is seen that there are dispersed tin-rich phases (dark) in the lead rich matrix [23]. There is evidence of grain boundaries in the lead phase of the microstructure. Also, the crystals of β-SnAg (Ag_3Sn) intermetallic compound appear in the continuous matrix of lead [23]. The β phase is body cube tetragonal in structure. Table 2.6 shows the crystal structure and lattice parameter of the different constituents of high lead solder.

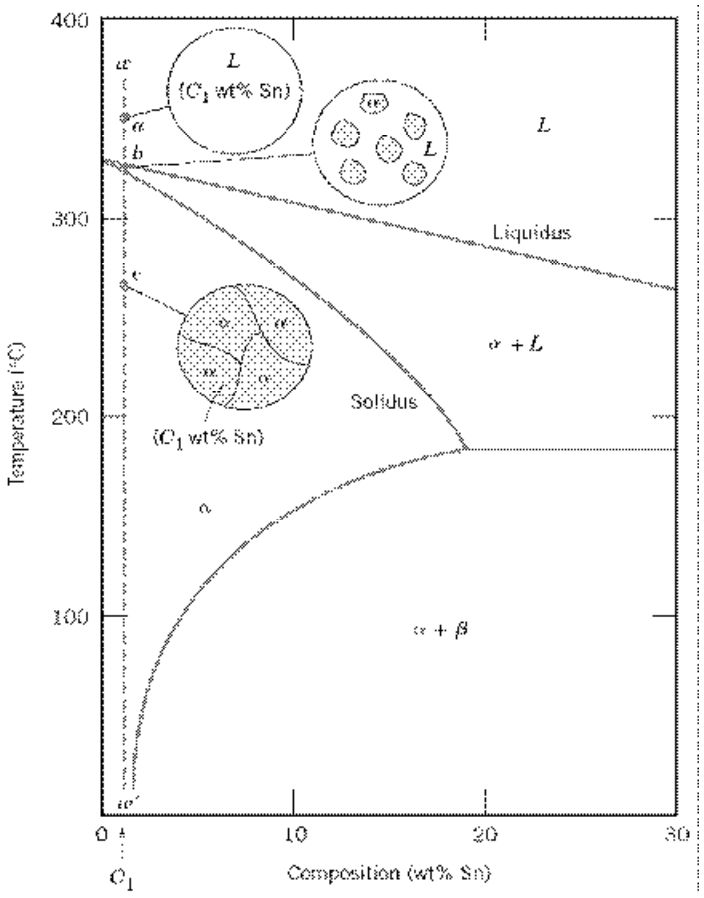

Figure 2.23: Schematic representations of the equilibrium microstructures for a lead–tin alloy [38]

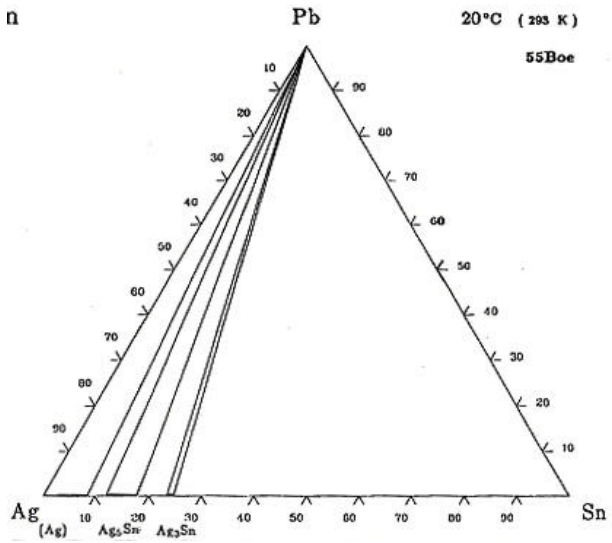

Figure 2.24: Pb-Sn-Ag ternary phase diagram [39]

Table 2.6: Crystal Structure, Lattice Parameter, Density and Unit Cell Volume of Species in High Lead Solder [39]

Species	Crystal Structure	Atomic Radius (Å)	Lattice Parameter (nm)	Density (mg/m^3)
Pb	FCC	1.75	a = 0.49394	11.68
Sn	Tetragonal	1.62	a = 0.58308 c = 0.31810	7.28
Ag	FCC	1.44	a = 0.4086	10.52
Ag_3Sn	Body centered Orthorhombic		a = 0.59689 b = 0.47802 c = 0.51843	10.03

The elements of microstructure that are typically important to mechanical behavior and resistance to failure are the grain size and shape, the size, shape and spacing of second phase particles, and the dislocation density. The strength of eutectic solders is attributed to the large-scale, regular arrangement of lamellae structure and the associated difficulty

of dislocation motion through the aligned two-phase structure. The alloys that exhibit the greatest volume of lamellar aligned eutectic material also exhibit higher shear strengths. In the Pb-rich alloys, the primary Pb-rich phase replaces the classic lamellar eutectic structure. Since the Pb-rich phase is relatively soft, its presence in significant amounts leads to a decreased shear strength in the Pb-rich alloys. An even greater difference in mechanical behavior is exhibited by the recrystallized ternary alloys of Pb, Sn and Ag. Within the homogeneous, fine grained microstructure the strengthening mechanisms associated with the composite nature of the lamellar eutectic are lost and the deformation character is greatly altered. The fine equiaxed grain size and associated large grain boundary area contribute to the exceptional softness and ductility of the recrystallized microstructure.

2.2.1 Microstructure Evolution

Figure 2.25 shows the solid solubility limit of tin in the lead phase as a function of temperature. At higher temperatures, above the solvus temperature, the equilibrium structure is a single-phase solid solution of tin in lead. The solvus temperature varies from about 50°C for 2 wt % Sn to about 125°C for 10 wt % Sn (Figure 2.25). For these alloys, therefore, the temperatures that may be encountered in service or reliability testing are in a range where microstructural changes are expected, particularly the precipitation and dissolution of the tin phase. Upon cooling from the high-temperature single-phase region, the tin phase forms as lamellae by the process of discontinuous or cellular precipitation. The time required for this transformation depends on alloy composition and

temperature. For 10 wt % Sn the transformation is completed within minutes; for 2 wt % Sn the transformation may require several months.

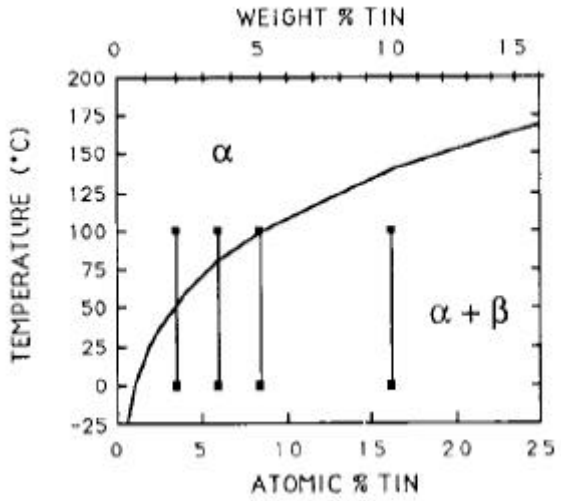

Figure 2.25: Limit of the solid solubility of tin in the lead phase, as a function of Temperature [40]

The cellular precipitation process begins with the nucleation of individual particles of the tin phase on grain boundaries. Groups of particles then grow out into the matrix as cells composed of lamellae of the tin phase, separated by the lead phase. The original grain boundary migrates along as the front of the growing cell, and it provides the fast diffusion path along which the required diffusion of tin is accomplished. The lamellae grow in fixed crystallographic directions on particular habit planes, with a characteristic spacing which is determined by tin concentration and temperature [40]. The cellular precipitation reaction has been studied by microscopic examination of samples quenched from a high temperature solution anneal and aged at various temperatures for various times. Figure 2.26 shows selected micrographs from a typical series.

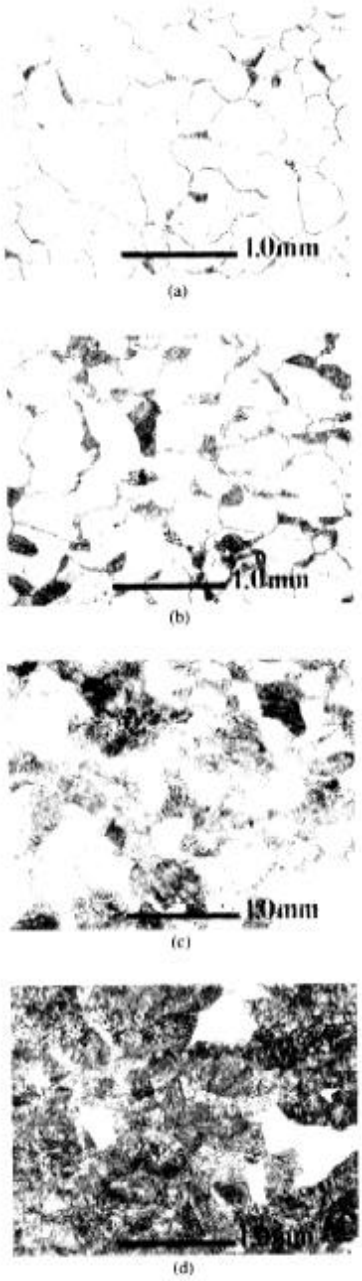

Figure 2.26: Micrographs of Pb-2 wt% Sn alloy aged at 0°C for various times after solution annealing. (a) Aged 16 days; transformed fraction » 3 percent. (b) Aged 49 days; transformed fraction » 20 percent. (c) Aged 79 days, transformed fraction » 50 percent. (d) Aged 190 days; transformed fraction » 90 percent [40]

Since the transformation proceeds by the growth of cells which nucleate at the grain boundaries, the time required to complete the transformation should depend on the initial grain size. It has also been observed that the spacing of the tin lamellae depended on the transformation temperature and alloy composition [40]. As shown in Figures 2.27 and Figure 2.28, the spacing decreased with increasing tin concentration and with decreasing transformation temperature.

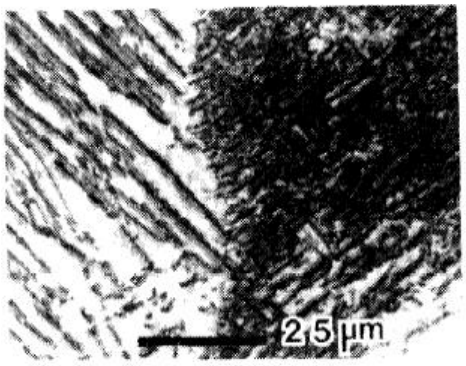

Figure 2.27: Lamellar microstructure of the Pb-3.5 wt % Sn alloy aged partially at » 16°C, followed by aging at 23°C. The fine lamellae formed at the lower temperature, the coarse lamellae at the higher temperature [40]

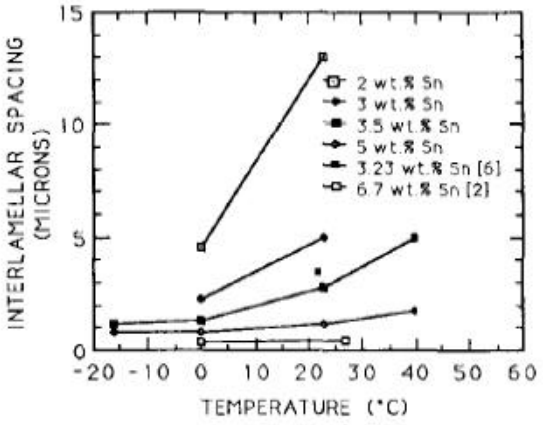

Figure 2.28: Average interlamellar spacings as a function of transformation temperature, for various tin concentrations [40]

For applications with thermal cycling, the rate of dissolution of the precipitate structure is also of interest. For the cellular precipitate structure, dissolution may occur either by direct diffusion of the tin into the lead phase, or by a retraction of the cell boundaries, which provide a fast diffusion path for the tin to disperse. The relative rates of these mechanisms are determined by the relative rates of tin diffusion in the lead lattice and along the grain boundaries. A brief examination of dissolution of the 3 and 5 wt % Sn alloys at 200°C showed no evidence of cell boundary motion, but rather rapid general dissolution directly into the matrix. At temperatures near the solvus, the dissolution was much slower, and it did begin with retraction of cell boundaries [40]. Tu [41] have observed that retraction of the cell boundaries occurs at temperatures slightly below the solvus temperature. This is possible because the surface energy of the interfaces between the lead and the tin phases provides a driving force for the motion of the cell boundary, in addition to the chemical driving force of the transformation. There is, however, a complication with the dissolution process. At the same time as cell boundaries are retracting, there appears to be a coarsening and spheroidization taking place in the lamellae. The spheroidization process can take place by diffusion along the interphase interfaces, which is presumably faster than diffusion in the lead matrix. The instabilities which lead to the break up of the lamellae are the rifts and holes formed during the initial precipitation. Direct diffusion of tin into the lead matrix may contribute to the process because nonuniform thinning of lamellae, or uniform thinning of nonuniform lamellae, will lead to a breakup of the lamellae. Lattice diffusion in the lead matrix is not expected [40] to contribute significantly to the creation of any particles that are larger than the lamellae thickness (above the solvus temperature) because any tin which diffuses into the

lead matrix will have little, if any, driving force to reprecipitate. Below the solvus temperature, the breakup into separate spheres can be followed by further coarsening by lattice diffusion through the lead matrix, though this should be a much slower process. The temperature dependence of the spheroidization process may have components from both lattice diffusion and interface diffusion.

Once the lamellae breakup into individual spherical particles, we expect a significant reduction in the rate at which cell boundary retraction can accomplish the dissolution. The driving force for boundary migration provided by continuous interphase interfaces is gone. There remains some driving force for boundary migration provided by the excess tin present in those individual particles which the boundary intersects. Boundary migration in the neighborhood of such a particle still provides a mechanism for distributing the tin into lead phase, but the boundary will have to jump from one particle to another. At temperatures below the solvus temperature, we expect the retraction of cell boundaries to halt entirely. The combined process of cell boundary retraction and lamella spheroidization is shown by the series of micrographs in Figure 2.29. At the higher magnifications, the breakup of the lamellae is clearly evident.

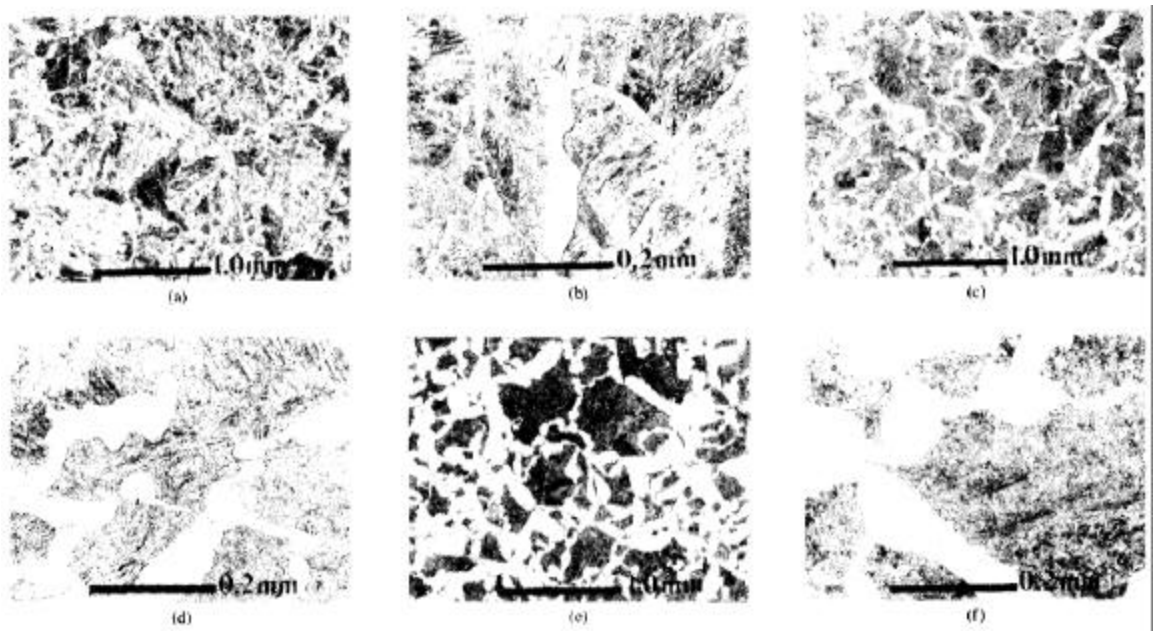

Figure 2.29: Micrographs showing the dissolution of the precipitated structure in the Pb-3.5 wt % Sn alloy at various annealing times at 80°C. The precipitation was formed during aging for 27 days at 0°C. (a), (b) Annealed 18 h. (c), (d) Annealed 73 h. (e), (f) Annealed 138 h [40]

The long duration of creep tests means that precipitation or dissolution reactions may occur during the tests. Furthermore, there is the possibility of coarsening (or overaging) in a precipitated structure during the test. If the phase transformations are sufficiently rapid, then any creep test below the solvus temperature will be in the precipitated state, and any creep test above the solvus temperature will be in the solution annealed state. If the phase transformations are sufficiently slow, then creep tests may be done in either the precipitated or solution-annealed state at any temperature. At intermediate transformation rates, the microstructure will evolve during the test unless the initial structure is the same as the equilibrium structure. In particular, Figure 2.30 shows a clear trend towards lower creep rates for higher tin. The apparent trend of increasing strength with tin content is as expected. This is in direct agreement with the trend of the tensile tests as shown in Figure

2.31. Higher tin concentrations produce finer microstructures and are therefore significantly stronger.

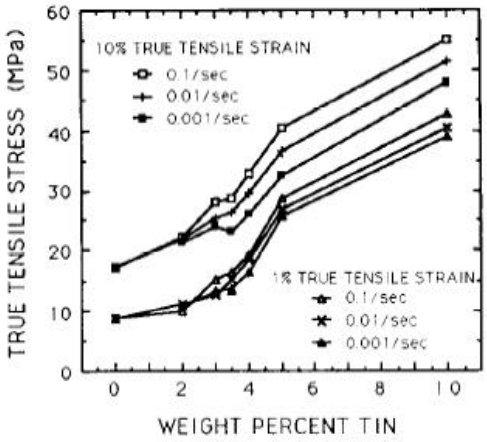

Figure 2.30: Yield stress at 1- and 10-percent true tensile strain as a function of tin content, for three different strain rates. The precipitation transformation was complete for alloys with 3.5 wt % or more tin. The transformation was not complete for the 3 wt % tin alloy at 0.01 and 0.001/s. The 2 wt % tin alloy was in the solution-annealed state [40]

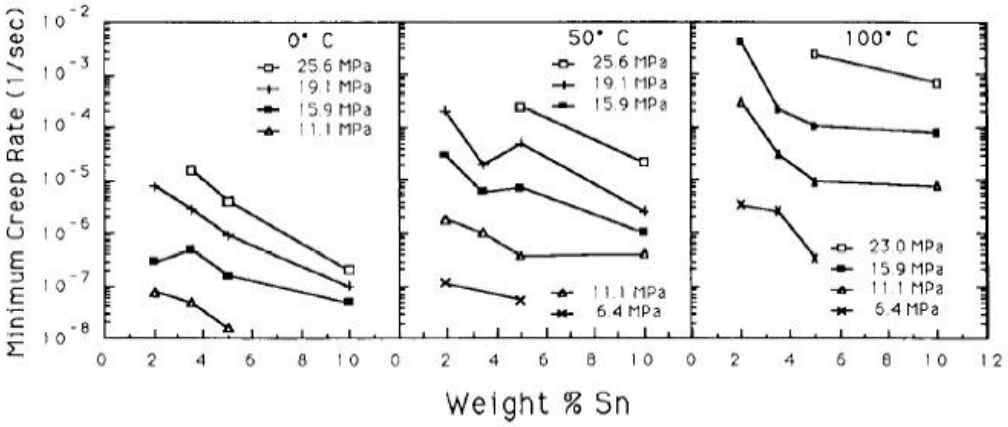

Figure 2.31: Minimum tensile creep rate versus tin concentration for various tensile stresses at three temperatures: 0°C, 50°C, and 100°C. Some values are interpolated. Creep rates decrease with increasing tin concentration [40]

2.2.2 Strain Rate Effect

The strain rates during temperature ramp is calculated as

$$\dot{e} = \frac{e_t}{t_r} \tag{2.30}$$

where $\dot{e}$ is the strain rate, ε_t is the total strain range and t_r is the ramp time. It has been observed [42] that hold is much more destructive than ramp due to lower strain rates operating during hold time. It is also well known that creep-fatigue damage is very sensitive to strain rate. Figure 2.32 shows that for high lead solder, strain to failure is a complex function of strain rate. When strain rate is reduced below 10^{-3} s^{-1}, strain to failure in tests without hold time starts to drop steadily. In hold time tests, strain to failure is very low. It drops very fast and reaches the plateau at hold times over 30s. This drastic difference in the strain rate magnitude explains why hold time has a much stronger effect on the fatigue life of solder than ramp time.

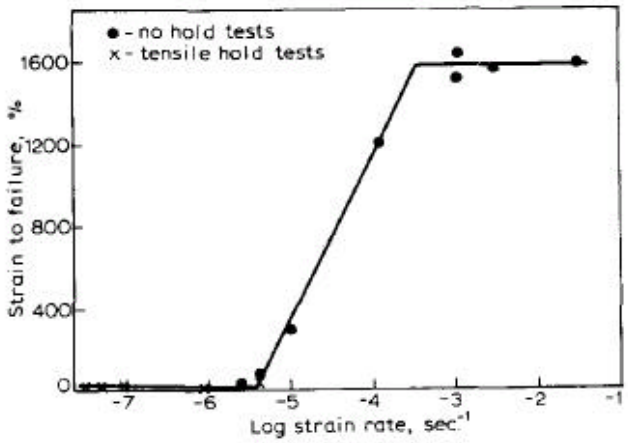

Figure 2.32: Effect of strain rate on strain to failure. Total strain range 0.75 percent, 25°C [42]

It is also indicated that damaging effects of long ramp time and tensile hold time on fatigue life of high lead low-tin solder at 0.75-percent total strain is related to the change

in failure mode from mixed transgranular-intergranular in high frequency continuous wave tests to a predominantly intergranular (creep-controlled) mode of fracture in low-frequency continuous wave tests and in tests with tensile hold in the cycle. Another indication of changes in the mechanisms of solder fatigue was a drop in the values of apparent activation energy from 47 kJ/mole in a fast continuous wave cycle (5 s per cycle) to 24-26 kJ/mole when time per cycle was increased over 1 min [44].

The variation of strain to failure with strain rate for low-tin lead-base solder is depicted in general form in Figure 2.33. Decreasing strain rate leads to reduction in strain to failure from high plateau level via transition region to a low strain to failure level at lower strain rates. This behavior is explained by considering different cavity growth (creep) mechanisms which may operate at various strain rates. At high strain rates, cavity growth occurs by deformation and at these rates an alternative mechanism of fracture, such as transgranular fracture, may operate. Work by Vaynman [42] demonstrated both transgranular and intergranular modes of fracture to be operational in tests with high strain rates. When the strain rate is reduced, the cavity growth mechanism changes from deformation to unconstrained (transition region in Figures 2.32 and Figure 2.33) and constrained cavity growth mechanisms (lower plateau in Figure 2.32 and Figure 2.33). Constrained cavity growth mechanism is considered to be very efficient in converting plastic strain into cavities, i.e., to be the most damaging mechanism during fatigue.

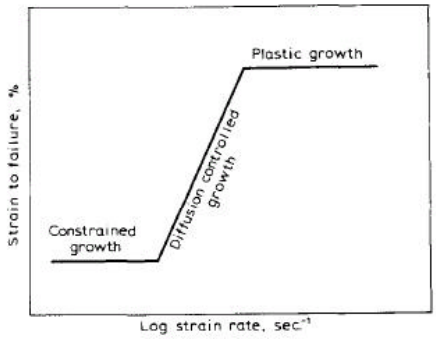

Figure 2.33: Typical strain rate-strain to failure relation for a number of commercial alloys [42]

Work by Liljestrand and Andersson [43] on leadless chip carrier 36Pb-62Sn-2Ag solder joints found that as the cyclic frequency increased, the fatigue life also increased. Their explanation was that stress relaxation and creep cause the most damage and that by increasing the strain rate the creep effects are minimized.

High lead solder does not exhibit a large Bauschinger effect which produces differences between the forward and reverse creep rates. It has been clarified [36] that high lead solder is not viscous, i.e., the flow stress is not just a function of the strain rate, rather it is a function of strain rate and strain. At -50°C it is essentially only a function of the applied stress. Figure 2.34 shows the creep and strain rate sensitivity curves for 92.5Pb5Sn2.5Ag solder. It shows that at high stresses and strain rates, the strain rate is greater than the creep rate, but at lower stresses or strain rates, the reverse is true. The greater the strain rate relative to the creep rate, the less that time dependent deformation (creep) is responsible for the plastic flow. At low stresses, Figure 2.34 shows that the creep rate is greater than the imposed strain rate, so that the deformation should be caused completely by creep. Actually the creep rate cannot be greater than the strain rate, because the more

rapid creep would cause the load to drop until the creep rate was just equal to the imposed creep rate.

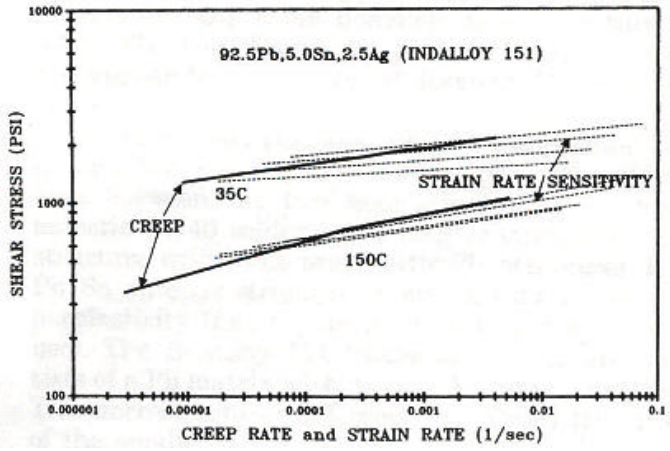

Figure 2.34: Comparison of the creep rate and the strain rate developed at the same stress [37]

The same conclusions have been also verified with the work done by Gupta [24] with the stress-strain curves shown in Figure 2.35a through 2.35d. The flow stresses at corresponding strains were observed to be strong functions of strain rate, with the stresses increasing with the strain rate due to less time for thermally activated processes. Since thermally activated processes occurred faster at higher temperatures, the stresses at corresponding strains were progressively lower at 150°C as compared to 25°C.

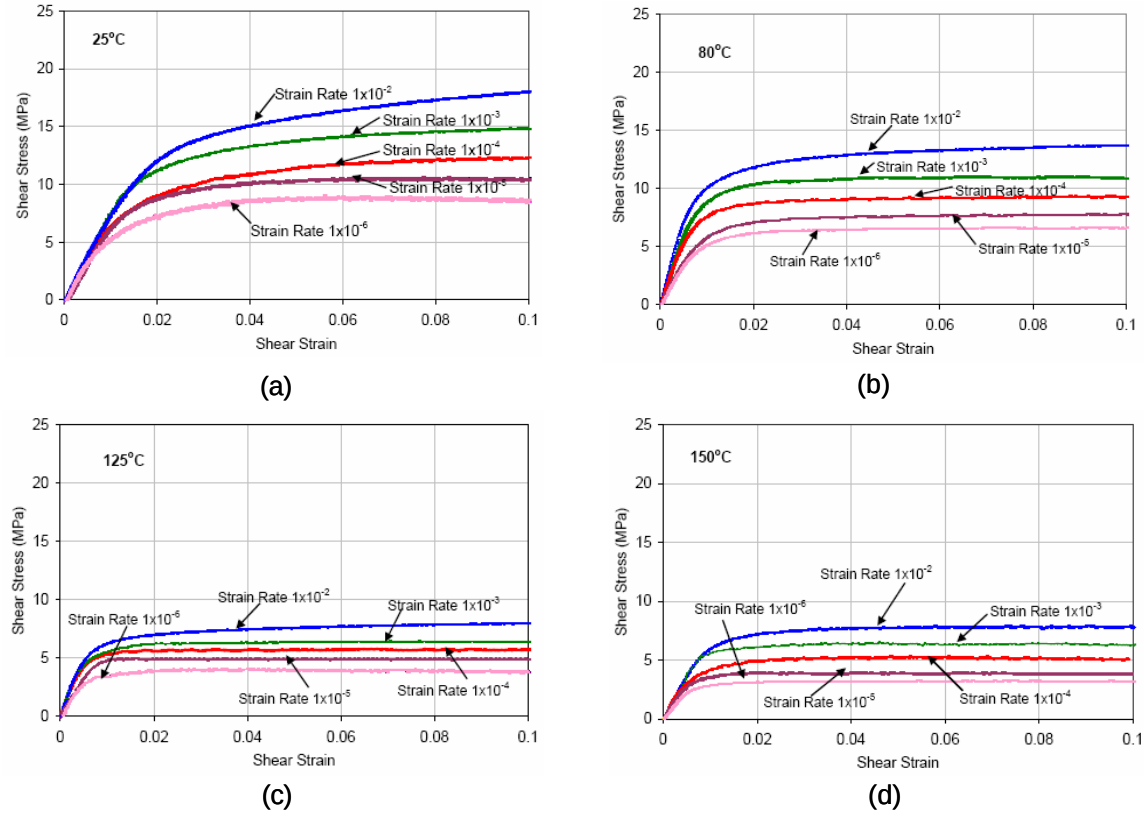

Figure 2.35: Stress-strain curves for 95.5Pb2Sn2.5Ag at (a) 25°C (b) 80°C (c) 125°C (d) 150°C [24]

2.2.3 Effect of Sn Additions

Investigations [44] on different Pb-Sn solders, from Pb-3%Sn to Pb-95%Sn have established the relationship between their composition and thermal fatigue life. Figure 2.36 shows that the most fatigue resistant solder was Pb-50%Sn. Its thermal fatigue life was about nine times that Pb-5%Sn. The second most resistant solder was Pb-75%Sn with a thermal fatigue life of about five times that of Pb-5%Sn. However in our case we are forced to work with solders less than 5% Sn because of the need for the melting point to be greater than 280°C.

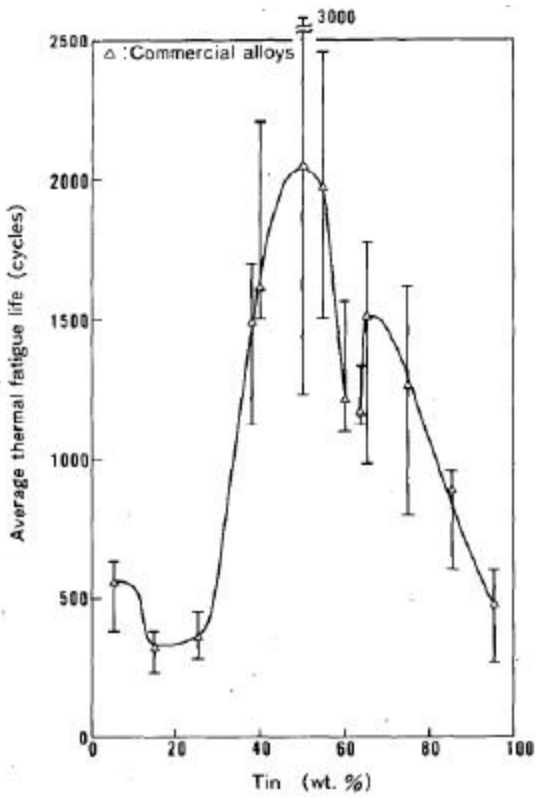

Figure 2.36: Stress Composition of Pb-Sn alloy versus average thermal fatigue life. (Thermal cycle: - 55 to 150°C.) [44]

Investigation of crack propagation in Pb-35%Sn [44] using SEM, has suggested that the cracks propagated selectively in the region, as shown in. Figure 2.37a as Pb-rich (α crystals). Figure 2.37a also shows that there was no relationship between the crack propagating region and the silver distribution. To understand this better, images of Figure 2.37a were traced as given in Figure 2.37b. The trace suggested that the crack which came across the β region, seemed to select the shortest path to return to the α region.

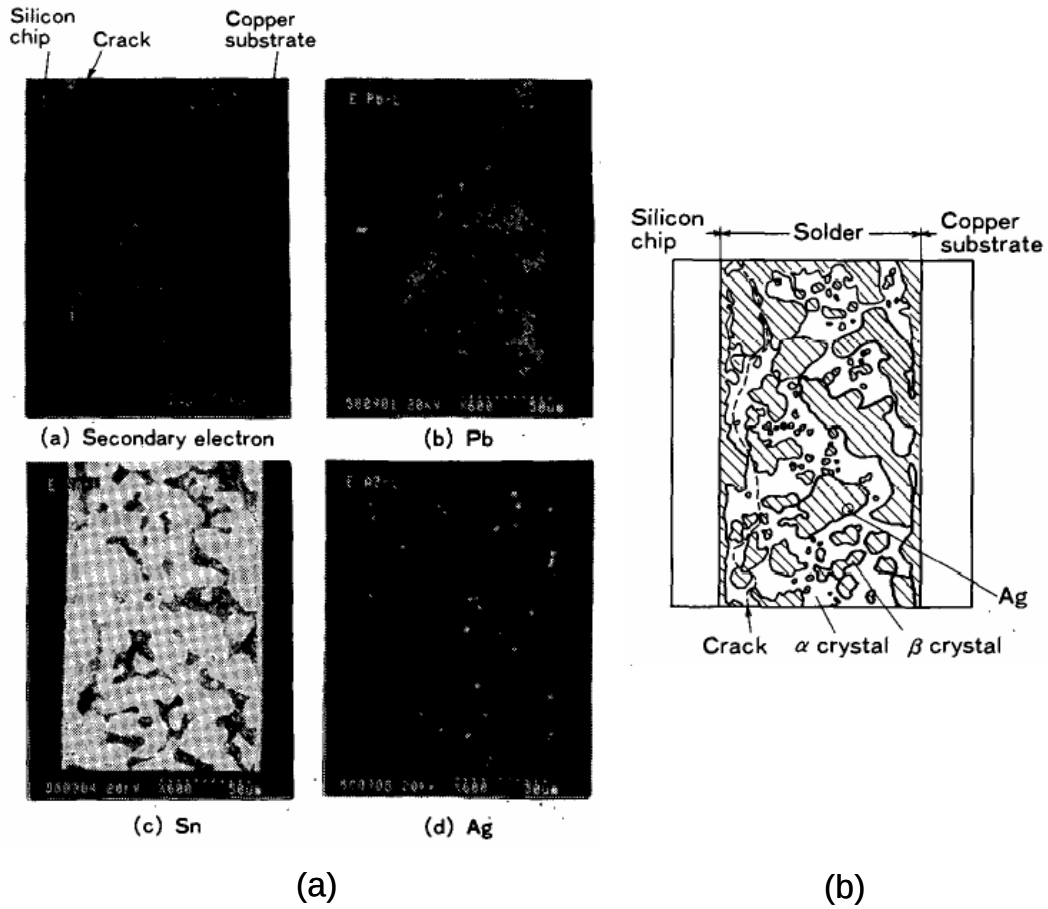

Figure 2.37: (a) Cross sections of soldered region after thermal cycling tests observed by SEM. (Pb-35%Sn, 1500 cycles.) (b) Trace of SEM images [44]

Solomon [37] has addressed that creep rate decreases with increasing tin content under the condition of the same stress and temperature. A numerical study by Hong & Burrell [45] indicates that the increase of the tin content results in an increase in the equivalent creep strain and the Mises stress, while the response of the equivalent plastic strain decreases as the tin content increases, as shown in Figure 2.38 through Figure 2.40.

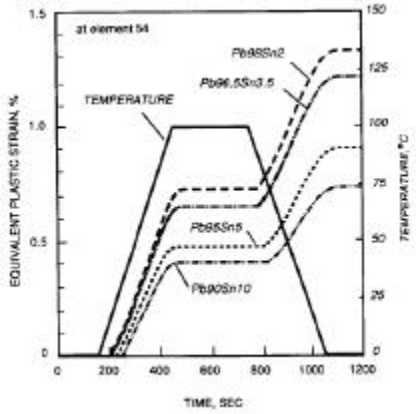

Figure 2.38: The maximum equivalent plastic strain history made among various lead-rich Pb-Sn alloys [45]

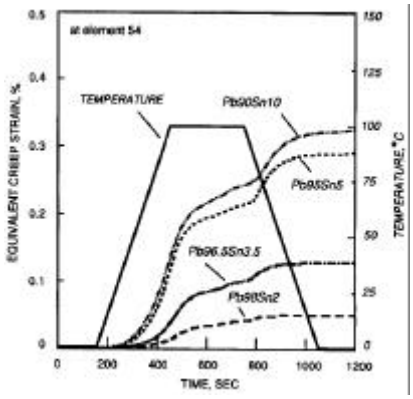

Figure 2.39: The maximum equivalent creep strain history made among various lead-rich Pb-Sn alloys [45]

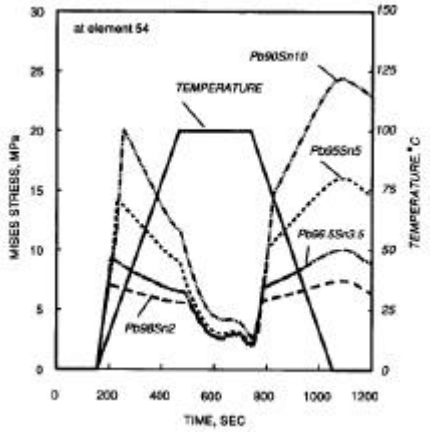

Figure 2.40: The maximum equivalent mises stress history made among various lead-rich Pb-Sn alloys [45]

2.2.4 Effect of Silver Additions

There have been a number of proposed mechanisms by which the addition of Ag acts to increase the fatigue life of near eutectic Sn-Pb solder. One proposal is that fine Ag_3Sn precipitates pin the grain boundaries in the solder, which strengthens the solder (or refines and stabilizes the solder microstructure [43]) making it fatigue resistant. Another hypothesis is that the presence of Ag, either in a fine precipitate form or in solid solution, hardens the solder and it is thought that harder solder have longer fatigue lives [46]. Adding Ag appears to reduce the creep rate, so that with 5 wt% Sn and 2.5 wt% Ag the creep rate is closer to that of a Pb-10 Sn wt% alloy than that of a Pb-5 Sn wt% alloy [37].

2.3 Creep-Fatigue Mechanisms in High Temperature Solders

Since solders are used at relatively high homologous temperatures, study of degradation of mechanical properties by creep and/or fatigue is critical to reliability assessment and can provide a valuable guideline for optimal solder interconnection design.

Damage in solder joints will accumulate from thermally activated, time dependent mechanisms (creep), from athermal cyclic mechanisms (fatigue) and from microstructural changes. These damage mechanisms are expected to interact with one another. In temperature cycling, during dwell at maximum temperature,if the dwell time is too short for the solder to completely relax, the creep damage will dominate and its magnitude will depend on dwell time and temperature. During dwell at the minimum temperatures, the time dependent damage should be small compared to the athermal damage and so dwell time would not be expected to be important. After numerous repetitions, low cycle

fatigue and creep damage occur. Creep-fatigue is a limit state obtained by damage accumulation after repeated loadings at high homologous temperature.

Several metallurgical studies on creep-fatigue interaction in tin-lead solder alloys have been documented in literature. In these studies it was shown that creep deformation is primarily due to dislocation motions in grains at high stresses and to grain boundary sliding at low stresses. Grain boundary sliding results from intergranular decohesion, which permits the nucleation and coalescence of small cavities, leading to the formation of intergranular voids. The intergranular type fracture is also referred to as “ductile hole growth” by Solomon [47]. The final failure is either due to large void coalescence or to surface crack formation and propagation, depending on how the experiment is controlled, in stress or in strain [48].

It is important to note that most of the solder joints produced in electronics have very small dimensions (<1 mm). Accordingly, most creep-fatigue failure models are based on representative solder joint test specimen. Literature reveals that fatigue cracks always propagate near the interface with the substrate, about 5 to 50 μm from the substrate [47].

Schematically, failure occurs in two steps:

- nucleation, growth and coalescence of (intergranular) micro-cracks,
- macro-crack propagation.

Normally, creep-fatigue failure models are suitable to predict the life of the initial crack. Stresses change significantly, when the macro-crack propagates, and methods of rupture mechanics should be then applied [7]. Experimentally, crack formation represents about 10% of the life, and the remaining 90% corresponds to crack propagation until the ultimate limit state. However, methods of rupture mechanics are quite complicated to implement and significant thermal degradation in power devices can result from as little as 10 – 20 % crack growth. In the field of electronics reliability, creep-fatigue failure models usually apply to both the crack initiation and propagation. This is a pragmatic extrapolation that allows predicting the life with a single undamaged mechanical model.

2.3.1 Creep and Stress Relaxation

When a sample's strain is held constant and the stress varies (decreases), the process is called "stress relaxation". When the stress is held constant and the strain changes in time its called "creep". In both cases, there is plastic flow, and similar microstructural changes happen. During temperature cycling, the application of creep-relaxation is of great importance because the number of cycles to failure is often related to the strain range through the "Coffin-Manson" relation, strain range partitioning, damage integral calculations or other theories. A simple linear elastic approximation of strain range is given by Equation 2.31. In Equation 2.31, γ is the shear strain, L is the diagonal half-length of the die, H is the height of the solder, T is the temperature, T_0 of the temperature at which the shear strain is zero, α_c is the CTE of the component and α_s is the CTE of the substrate.

$$g = \frac{L}{H}(T - T_0)(a_s - a_c) \tag{2.31}$$

Figure 2.41a shows the shear strain as a function of temperature. The almost straight line with the triangle data points is the strain expected from the linear elastic approximation of stress given in Equation 2.31. This would be the strain in the solder for complete creep relaxation of the solder as the temperature is changed. At high temperatures, the shear strain for the assembly follows the complete creep-relaxation curve well. That is because the creep relaxation is fast enough to be almost complete as the temperature is changed. The deviation from the complete creep-relaxation line as the temperature is reduced is opposite to that obtained as the temperature is raised. That is because the shear force on the joints is in the opposite direction in the two cases. As the temperature comes down, the deviation from the complete creep-relaxation curve increases as the solder becomes stronger, and at -25°C the slope is close to zero, indicating high rigidity of the solder and little creep-relaxation. During the 2-h dwell as shown in Figure 2.41b, at -25°C, there is little change in the shear since the creep-relaxation is extremely slow at these temperatures. As the temperature is increased again, the shear strain stays almost constant until it reaches the complete creep-relaxation line, at which point the force reverses, creep-relaxation takes over and the curve asymptotically approaches the complete creep-relaxation curve. As the temperature is decreased from 125°C, the force gradually increases in the negative direction, and its slope gradually increases also, as the solder gets “stronger”. As the temperature goes below room temperature, the forces get very large indeed. This puts the largest stress on the metallization and components that are soldered together. At -25°C, the 2-h dwell causes a barely detectable decrease in the

force. As the temperature is increased again, the force increases quite linearly, all the way up to 40°C (Figure 2.41c). This particular part of the cycle is much like a classical bimetallic strip, where there is no shear between the two members, but the force and the bend are linearly related to the temperature. Thus, the temperature can roughly be divided into two regions: (1) above 50°C, the solder creeps-relaxes enough that Equation 2.32 is adequate and (2) below 50°C, the solder is stiff enough that the bimetallic strip analogy holds.

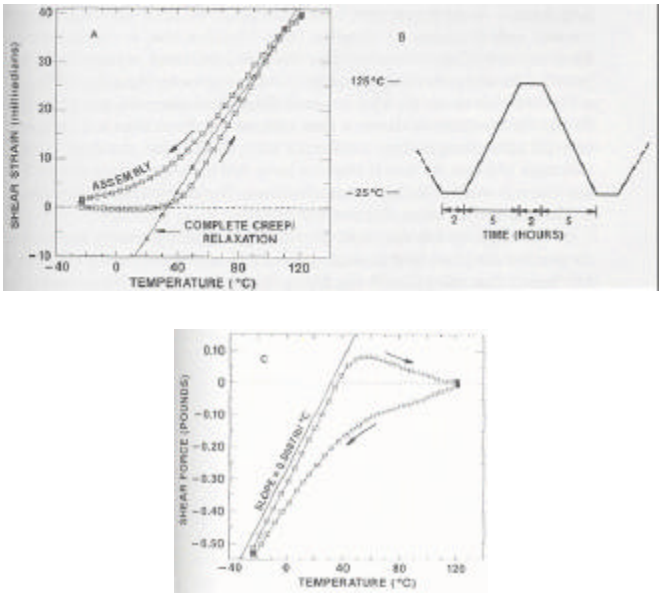

Figure 2.41: Temperature cycling with large D**T [49]**

Creep tests are somewhat unrealistic because real joints are constrained and also creep tests require much time. The mechanistically equivalent stress relaxation tests, on the other hand, can be performed swiftly because the primary information, stress relaxation rate or rate of load drop, occurs “immediately” upon loading. In fact, with solders, the initial strain amplitude must be applied rapidly; otherwise, the load will have

significantly relaxed by the time the desired strain amplitude has been reached, resulting in an unrealistically small recorded peak load. Figure 2.42 shows the correlation between the steady-state creep rate calculated from stress relaxation tests and the data obtained from numerous independent creep tests.

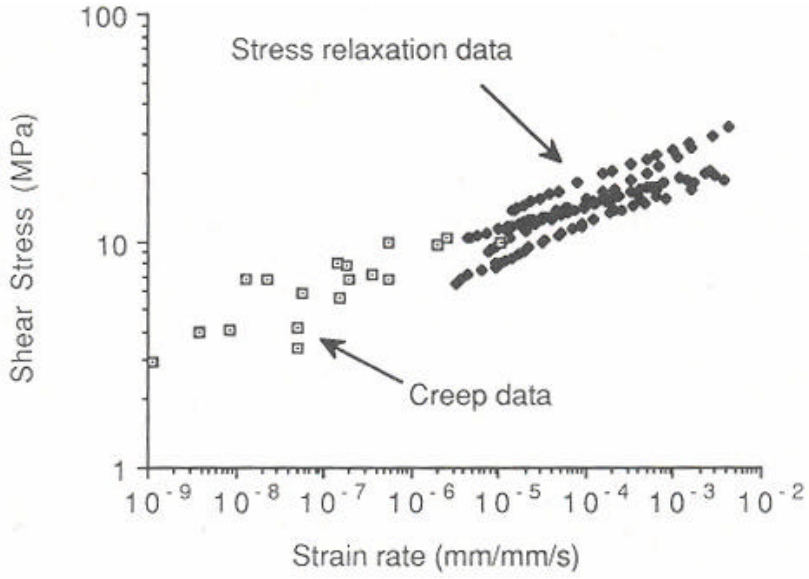

Figure 2.42: Steady-state creep rates for eutectic lead solder at 25°C [49]

2.3.2 Fatigue Models Review

Early solder joint fatigue models were developed based on experimental thermal cycling tests. Most models that address fatigue require stress-strain data in order to predict service life. Early fatigue data was collected experimentally using strain gauges. However, with the decreasing size of the solder joint, experimental collection of stress-strain data is becoming increasingly difficult, and Finite Element Analysis (FEA) is becoming the more practical route for obtaining stress-strain relationships. Rapid thermal cycling of actual parts is still necessary for verifying the life predictions. The necessity to

model the fatigue behavior of solder joints has also been recognized by other investigators; as a result several solder joint fatigue models have been proposed. However, the assumptions and applicability of these models vary, including the manner in which the physical and metallurgical aspects of fatigue are taken into account.

Fatigue models can be divided into empirical and mechanistic categories.

Empirical models: A measurable physical quantity, usually the inelastic strain range, is used as the basis for life prediction. The particular damage mechanisms causing this physical quantity are usually not known. Despite this, empirical models have been successful for several common materials.

Micro-mechanistic models:

Empirical models cannot be easily extrapolated to loadings or microstructures beyond the range of available data because of their empirical nature. For more robust quantification of the damage process the underlying physical mechanisms that drive the failure process must be investigated at the microstructural length scales. Furthermore, it is very important to base the damage model explicitly on the micro-structural state because of the need to assess acceleration factors when micro-structural evolution in short accelerated test environments is significantly different from that encountered over long time scales in the life cycle environment.

From the published literature, fourteen solder joint fatigue models were identified. These were reviewed to determine the bases upon which they were built, the package types that they are suited for, and the material properties required. The models proposed for predicting the fatigue life of solder joints can be divided into five major categories, based on the fundamental mechanism viewed as being responsible for inducing damage. These five categories are (a) stress-based, (b) plastic strain-based, (c) creep strain-based, (d) energy-based, and (e) damage accumulation based, and are tabulated in Table 2.7, along with the researchers who originally proposed or applied these models. Fatigue models that do not fit into one of the five categories listed above, and are empirically based, have been grouped under a separate category labeled `other'. In Table 2.8, the fourteen solder joint fatigue models are summarized and arranged by class.

2.3.2.1 Plastic Strain Fatigue Models

The Coffin-Manson equation can be written as

$$\frac{\Delta e_p}{2} = e_f^{'}(2N_f)^c \tag{2.32}$$

where $\Delta e_p / 2$ =plastic strain amplitude

ε_p=fatigue ductility coefficient

c = fatigue ductility exponent

N_f = total number of cycles to failure

Table 2.7: Fatigue Models and Classification [50]

Fatigue Model	Stress	Strain		Energy	Damage	Other
		Plastic	Creep			
Coffin-Manson		×	×			
Total strain		×	×			
Solomon		×				
Engelmaier		×				
Miner		×	×			
Knecht and Fox			×			
Syed			×	×		
Akay				×		
Liang				×		
Heinrich				×		
Pan				×		
Darveaux				×	×	
Stolkarts					×	
Norris and Landzberg						×

Table 2.8: Summary of solder joint fatigue models [50]

Fatigue Model	Model class	Applicable packages	Required parameters	Coverage
Coffin-Manson	Inelastic strain	All	Plastic strain	Low cycle fatigue
Total strain (Coffin-Manson-Basquin)	Inelastic strain + Elastic strain	All	Strain range	High and low cycle fatigue
Solomon	Plastic shear strain	All	Plastic shear strain	Low cycle fatigue
Engelmaier	Total shear strain	Leaded and leadless TSOP	Total shear strain	Low cycle fatigue
Miner	Superposition (plastic and creep)	PQFP, FCOB w/fill	Plastic failure and creep failure	Plastic shear and matrix creep
Knecht and Fox	Matrix creep	All	Matrix creep shear strain	Matrix creep only
Syed	Accumulation of creep strain energy	PBGA,, SMD, NSMD	grain boundary sliding and matrix creep energy	Implies full coverage
Dasgupta	Total strain energy	LLCC, TSOP	Energy	Joint geometry accounted for
Liang	Stress/strain energy density based	BGA and leadless joints	Energy	Constants from isothermal low cycle fatigue tests
Heinrich	Energy density based	BGA	Energy	Hysteresis curve
Darveaux	Energy density based	Leadless, PBGA	Damage +Energy	Hysteresis curve
Pan	Strain energy density	LCCC	Strain energy density and plastic energy density	Hysteresis curve
Stolkarts	Damage accumulation	All	Damage	Hysteresis curve and damage evolution
Norris and Landzberg	Temperature and frequency	All	Temperature frequency	Test condition versus use conditions

Originally proposed to predict the fatigue life of metals in the aircraft industry, it was found inadequate for modeling in-service thermal fatigue conditions in high temperature alloys. The primary difficulty is the inability to account for variations in waveform. Experimental data are required to determine the constants, and are typically collected by application of strain gauges. Actual fatigue tests, however, are often time consuming and the results are usually applicable only to the specific geometry of the solder joint. Thermal fatigue involves a combination of creep and plastic strains, and each can have a different effect on the component life. The Coffin-Manson equation does not allow differentiation between these two strains, resulting in accurate life predictions.

Because the Coffin-Manson equation considers only plastic deformations, it is commonly combined with Basquin's equation to account for elastic deformation as well. The resulting equation is known as the Total Strain equation, and is shown in Equation 2.33.

$$\frac{\Delta e}{2} = \frac{s_f'}{E}\left(2N_f\right)^b + e_f'\left(2N_f\right)^c \qquad (2.33)$$

$\Delta\varepsilon$ is the strain range, s_f' is the fatigue strength coefficient, E is the elastic modulus, e_f' is the fatigue ductility, b is the fatigue strength exponent (Basquin's exponent), and c is the fatigue ductility exponent. This fatigue model is an improvement over the Coffin-Manson equation in that it also accounts for the elastic contribution to fatigue failure. As can be seen in Figure 2.43, the low cycle region to the left of N_f is governed by the plastic-strain amplitude (Coffin-Manson equation), and the high cycle region to the right of N_f is governed by the elastic-strain amplitude (Basquin's equation).

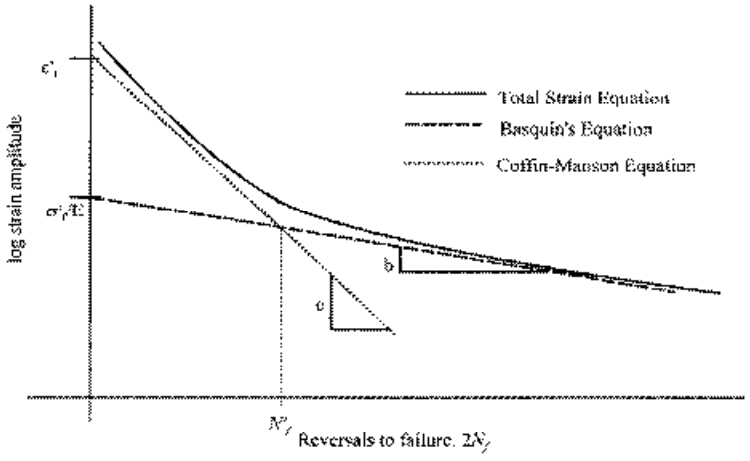

Figure 2.43: Total strain versus life equation [50]

Solomon's low cycle fatigue model relating the plastic shear strain to fatigue life cycles is shown in Equation 2.34 [50].

$$\Delta g_p N_p^a = q \tag{2.34}$$

$\Delta\gamma_p$ is the plastic shear strain range, N_p is the number of cycles to failure, θ is the inverse of the fatigue ductility coefficient, and α is a material constant. This fatigue model relates fatigue behavior to the plastic shear strain imposed on the specimen, and requires data collection or determination of the experimental plastic strain range. However, since this model does not account for creep, it is limited in its practical use for solder joints.

The Engelmaier fatigue model is shown in Equation 2.35. The total number of cycles to failure is related to the total shear strain, $\Delta\gamma_t$, the fatigue ductility coefficient, $e_f^{'}$, and the variable, c, which is a function of frequency and temperature.

$$N_f = \frac{1}{2}\left[\frac{\Delta g_t}{2e_f^{'}}\right]^{1/c} \tag{2.35}$$

where $c= -0.442-6\times10^{-4}T_s+1.74\times10^{-2}\ln(1+f)$. T_s is the mean cyclic solder joint temperature in °C, and f is the cyclic frequency in cycles/day. This fatigue model improves on Solomon's and Coffin-Manson by including cyclic frequency effects, temperature effects, and elastic-plastic strains. It is, however, based on isothermal experimental fatigue data, implying prior testing knowledge of the solder joint of interest and the 'c' provided above is valid only for Sn-Pb eutectic solder.

By applying Miner's linear superposition principle, both plastic and creep strain can be accounted for in a strain-based fatigue model. One example combines the Solomon fatigue model with the Knecht and Fox creep model, using Miner's rule shown in Equation 2.36.

$$\frac{1}{N_f} = \frac{1}{N_p} + \frac{1}{N_c} \tag{2.36}$$

N_p refers to the number of cycles to failure due to plastic fatigue and is obtained directly from Solomon's fatigue model. N_c refers to the number of cycles to failure due to creep fatigue and is obtained from Knecht and Fox's creep fatigue model. This fatigue model is similar to a full method reported by Lau [49] as Strain Range Partitioning (SRP). In SRP, a typical hysteresis loop can be separated into four components: the plastic strain in tension and compression (PP), the creep strain in tension and compression (CC), the creep strain intension-plastic strain in compression (CP) and the plastic strain in tension-creep strain incompression (PC). Equation 2.37 shows the SRP.

$$\frac{1}{N_f} = \frac{F_{pp}}{N_{pp}} + \frac{F_{cc}}{N_{cc}} + \frac{F_{cp}}{N_{cp}} + \frac{F_{pc}}{N_{pc}} \tag{2.37}$$

F_{ij} is the fraction of the total inelastic strain range of the hysteresis loop. The contributions to each part are determined from other fatigue models and from cyclic stress-strain tests.

A lot of work has been done on lead rich solders to calculate the fatigue life. Figure 2.44 shows the room temperature low cycle fatigue S-N curve for 97.5Pb1.5Ag1.0Sn created by performing tests on dog-bone samples with strain control, R= -1.0 and a strain rate of 0.003/sec using a triangle waveform [51]. The Coffin-Manson relation has been used with a failure criterion of 50% drop in shear stress to analyze the data. The high lead alloy 97.5Pb1.5Ag1.0Sn, has the very high strain fatigue resistance in the large strain region ($\Delta\varepsilon > 2.05$). Figure 2.45 shows that the temperature effect is not obvious for 97.5Pb1.5Ag1.0Sn alloy [51].

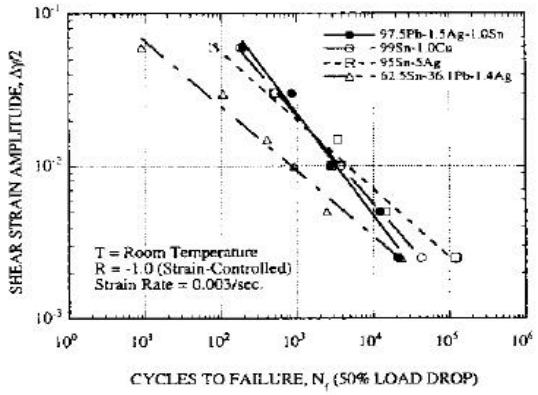

Figure 2.44: Low cycle fatigue S-N curves for four alloys at room temperature [52]

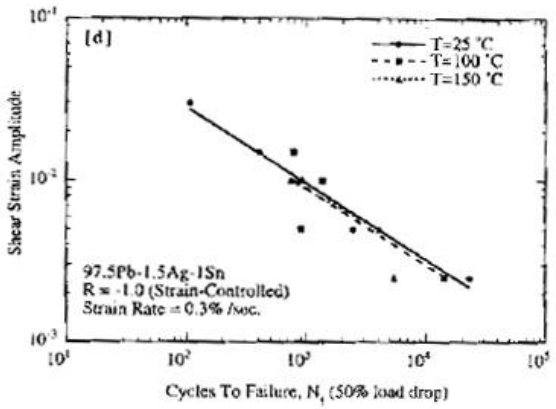

Figure 2.45: Effect of temperature on the low cycle fatigue of 97.5Pb1.5Ag1.0Sn alloy [52]

Vaynman and Zubelewicz [52] have carried out fatigue tests on bulk specimens of Pb-3.5 wt%Sn in strain control mode. They found that the fatigue data could not be extrapolated below 1% by the Coffin-Manson relation due to nonlinearity between fatigue life (log) and strain range (log). Figure 2.46 shows the dependence of the fatigue life of this solder on plastic strain range at temperatures from 5° to 100° C. It is evident that the data for each temperature (except for 5° C) cannot easily be fitted to a single log-log straight line. The data are much better represented by two straight lines with a breakpoint at approximately 0.3% plastic strain. Thus the Coffin-Manson relation cannot be used for extrapolation of experimental fatigue data for this solder from high to low strains. The nonlinearity is due to the change in this solder's failure mode from mixed transgranular-intergranular (fatigue-creep interaction) fracture at high strains to intergranular (creep) fracture at low strains, as shown in Figure 2.47. As can be drawn from Figure 2.46, the change in fatigue life with increasing temperature may be associated in part with complete dissolution of tin precipitates in the matrix above approximately 80°C. No

microstructural changes were observed when the testing temperatures was reduced from 25° to 5° C.

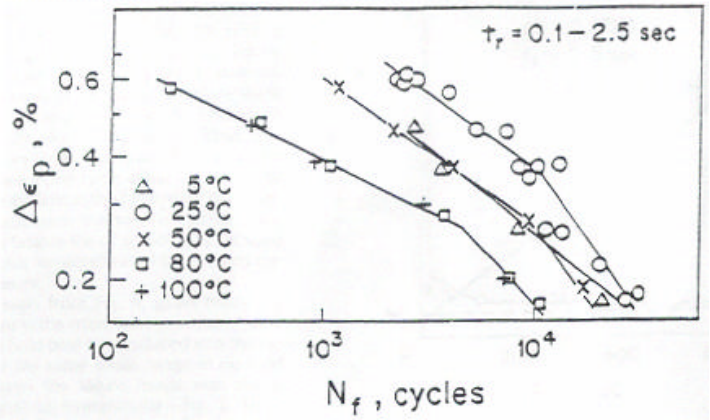

Figure 2.46: Number of cycles to failure vs. plastic strain range. No hold time. [52]

(a) **(b)**

Figure 2.47: Scanning electron micrograph of surface of failed specimen. (a) Total strain range 0.75%, 25°C, ramp time 2.5s. No hold time. (b) Total strain range 0.30%, 25°C, ramp time 2.5s. No hold time. [52]

Figure 2.48 shows the relation between the number of cycles to failure and plastic strain range in tests with and without tensile hold time. It is obvious the Coffin-Manson relation

does not hold in either case. As seen from Figure 2.49, grain boundary fracture is the main failure mode when a tensile hold time is introduced into the cycle.

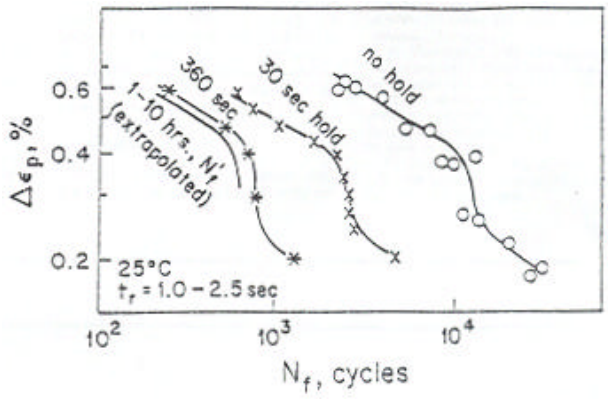

Figure 2.48: Effect of plastic strain range on number of cycles to failure in tests with tensile hold time [52]

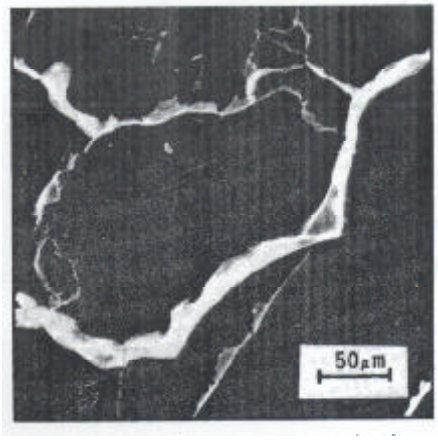

Figure 2.49: Scanning electron micrograph of surface replica. Total strain range 0.75%, 25°C, ramp time 2.5s. Tensile hold time 90s after 60% of fatigue life [52]

2.3.2.2 Creep Strain Fatigue Models

For solder joints, it is commonly accepted that creep may be due to grain boundary sliding and/or matrix creep (dislocation movement). Knecht and Fox have proposed a

simple matrix creep fatigue model relating the solder microstructure and the matrix creep shear strain range as shown in Equation 2.38 [50].

$$N_f = \frac{C}{\Delta g_{mc}} \tag{2.38}$$

The number of cycles to failure, N_f , is related to a constant C, which is dependent on failure criteria and solder microstructure. $\Delta\gamma_{mc}$ is the strain range due to matrix creep. The second creep mechanism, grain boundary sliding, is incorporated with matrix creep into a fatigue model presented by Syed [50]. In this model, creep strain is partitioned into two parts as shown in Equation 2.39 [50].

$$N_f = \left(\left[0.022 D_{gbs}\right] + \left[0.063 D_{mc}\right]\right)^{-1} \tag{2.39}$$

Here, D_{gbs} and D_{mc} are the accumulated equivalent creep strain per cycle for grain boundary sliding and the matrix creep, respectively. One limitation in the Syed fatigue model is the absence of plastic-strain effects, which is described by Syed as being not applicable to solder alloys at high homologous temperatures and slow rates of temperature change.

Solder microstructure also plays a key role in creep strain fatigue because it affects the strength of the solder joint and, hence, the fatigue life. Morris and Reynolds [53] have reported on the effect of microstructure on eutectic solder mechanics. Their conclusions draw attention to the importance of microstructure in fatigue modeling. They emphasize three important points to watch for: (1) the use of engineering data which is not representative of the actual solder joint of interest, (2) analytical models predicting solder

joint behavior without incorporating microstructural effects, and (3) the effect of small impurities on microstructure.

2.3.2.3 Energy-Based Models

Energy based models are used to predict fatigue failure based on a hysteresis energy term or type of volume-weighted average stress-strain history. The energy partitioning method proposed by Dasgupta is discussed in the section 2.4.2. Akay [50] has proposed the following fatigue model, shown in Equation 2.40, based on the total strain energy.

$$N_f = \left(\frac{\Delta W_{total}}{W_0} \right)^{1/k} \tag{2.40}$$

N_f is the mean cycles to failure, ΔW_{total} is the total strain energy, W_0 and k are fatigue coefficients. Liang et.al. [51] have reported a fatigue life prediction methodology that is calculated on an energy-based fatigue failure criterion and is shown in Equation 2.41.

$$N_f = C(W_{ss})^{-m} \tag{2.41}$$

W_{ss} is the stress-strain hysteresis energy density. C and m are temperature-dependent material constants derived from low cycle fatigue tests. It is important to remember that these models calculate the number of cycles to crack initiation, namely, the total energy that must accumulate in the solder joint in order to initiate cracks. Total failure is not addressed. Linking the crack initiation with the actual cycles to failure requires the inclusion of crack propagation.

Gustafsson [50] has reported another energy based fatigue model, based on findings from Darveaux, as depicted in Equation 2.42.

$$N_{aw} = N_{0s} + \frac{a - (N_{0s} - N_{0p})\frac{da_p}{dN}}{\frac{da_s}{dN} + \frac{da_p}{dN}} \tag{2.42}$$

In this equation, the overall time to failure is obtained from a combination of crack initiation and crack propagation. For each of these mechanisms, i.e., initiation and propagation, it is viewed that there are primary and secondary cracks, indicated by the subscripts ‘p’ and ‘s’, respectively. The primary and secondary cracks are thought to initiate and propagate towards each other at different rates. $N_{\alpha w}$ is the number of cycles to failure and *a* is the total possible crack length. N_{0p} and N_{0s} are the primary and secondary crack initiation energy based terms, respectively, and are calculated using Equation 2.43 [50], by first determining the appropriate value of ΔW from the hysteresis curves for each.

$$N_{0p}, N_{0s} = 54.2\Delta W^{-1.00} \tag{2.43}$$

The Darveaux fatigue model shown in Equation 2.42 is an example of an energy-based fatigue model that incorporates crack propagation. The crack propagation terms, da/dN, are dependent on the corresponding values of ΔW, as shown in equation 2.44 for 62Sn36Pb2Ag solder [50].

$$\frac{dA}{dN} = 3.49 \times 10^{-7} \Delta W^{1.13} \tag{2.44}$$

In general, ΔW is the energy density term calculated from the stress-strain hysteresis curve. Pan reports a strain-energy based fatigue model called `critical accumulated strain energy' or CASE. This model is based on the assumption that the strain energy

accumulates during thermal cycling and eventually reaches a critical value, C. This fatigue model is shown in Equation 2.45 [54].

$$N_0 = \frac{(dW/dV)_{cr}^0}{AW_p + BW_c} \tag{2.45}$$

where W_p and W_c are the volume-weighted average plastic and creep strain energy densities per cycle. The parameter $(dW/dV)_{cr}$ represents the critical strain energy density for crack initiation. Crack growth under cyclic loading occurs when the strain energy density of the material along the crack front exceeds the critical strain energy density, $(dW/dV)_c$. This assumption can be interpreted mathematically as Equation 2.46

$$\left(\frac{dW}{dV}\right)_c = \Delta\left(\frac{dW}{dV}\right)\Delta N + \left(\frac{dW}{dV}\right)_{avg} \tag{2.46}$$

where $\Delta(dW/dV)$ is the strain energy density increment per thermal cycle during a number of cycles, ΔN. The average strain energy density, $(dW/dV)_{avg}$, at a distance Δr ahead of the crack front is defined by Equation 2.47.

$$\left(\frac{dW}{dV}\right)_{avg} = \frac{1}{2}\left\{\frac{1}{2}\left[\left(\frac{dW}{dV}\right)_{t_f} + \left(\frac{dW}{dV}\right)_{t_i}\right] + \left(\frac{dW}{dV}\right)_{t_m}\right\} \tag{2.47}$$

in which $(dW/dV)_{tf}$, $(dW/dV)_{ti}$, and $(dW/dV)_{tm}$ represent the strain energy density values at the end (t_f), start (t_i), and middle (t_m) of the thermal cycle, respectively. A typical thermal cycle with definitions of t_f , t_i , and t_m is described in Figure 2.50.

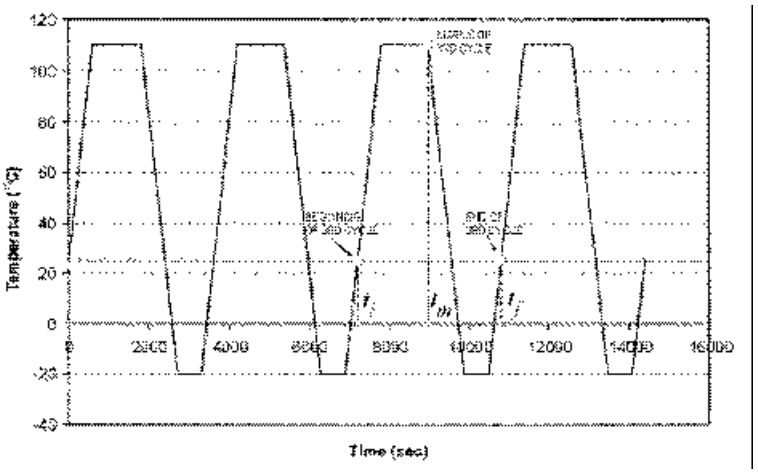

Figure 2.50: Description of the start, middle, and end of a cycle (shown for the third cycle) within the thermal cycle profile used in the simulation [54]

The strain energy density increment per cycle is defined as the difference between the strain energy densities at the end and start of the cycle, as shown in Equation 2.48.

$$\Delta\left(\frac{dW}{dV}\right)=\left(\frac{dW}{dV}\right)_{t_f}-\left(\frac{dW}{dV}\right)_{t_i} \tag{2.48}$$

As illustrated in Figure 2.51, the strain energy density increment per cycle, Δ(dW/dV), can be related to the strain energy density factor increment, ΔS, by Equation 2.49.

$$\Delta\left(\frac{dW}{dV}\right)=\frac{\Delta S}{\Delta r} \tag{2.49}$$

Substituting from this equation into Equation 2.46 results in the crack propagation rate as Equation 2.50.

$$\frac{\Delta r}{\Delta N}=\frac{\Delta S}{\left(\frac{dW}{dV}\right)_c-\left(\frac{dW}{dV}\right)_{avg}} \tag{2.50}$$

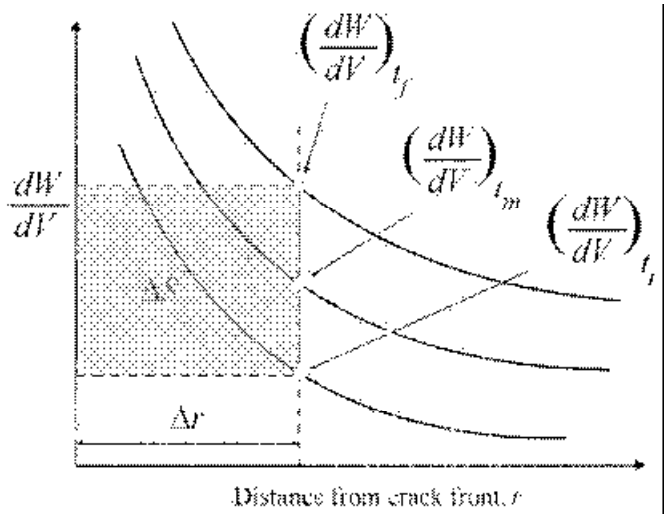

Figure 2.51: Schematic of the variation of dW/dV along the radial distance r from the crack front during the temperature cycle [54]

in which ΔS and $(dW/dV)_{avg}$ are computed by using the stress and strain fields at a distance of Δr from the crack front. The critical value of strain energy density, $(dW/dV)_c$, can be determined experimentally by computing the area underneath the true stress-strain curve of the solder joint at the point of failure. In conjunction with the finite element modeling and simulation, the number of thermal cycles for the specified number of crack growth increments can be obtained from Equation 2.50 in the form of Equation 2.51.

$$N = \sum_{i=1}^{n} \left\{ \frac{\left(\frac{dW}{dV}\right)_c - \left(\frac{dW}{dV}\right)_{avg}}{\Delta S} \Delta r \right\}_i \tag{2.51}$$

in which i denotes the crack growth increment of Δr_i.

The energy based fatigue models predict the accumulated energy required to initiate a crack; it does not predict when fatigue failure will occur - only that a crack will form. The

benefit of an energy-based fatigue model, as compared to the strain-based or creep based fatigue models, is the ability to capture test conditions with more accuracy. For complex waveform stress-strain hysteresis curves, the energy-based fatigue models are better able to capture the accumulated damage. One limitation of the energy-based fatigue models is their inability to predict the actual number of cycles to failure. Only crack initiation is predicted. It was this shortcoming that led to the addition of crack propagation to fatigue modeling.

2.3.2.4 Damage Fatigue Models

Stolkarts [50] has reported successful application of this model over a damage-free model. Equation 2.52 depicts the equation used by Stolkarts in calculating the number of cycles to failure, N_f.

$$N_f \frac{1-\left(1-d_f\right)^{k-1}}{(k+1)L} \tag{2.52}$$

d_f is the amount of damage at failure and is taken as 0.5 for solders. k is defined as a material constant and given a value of 2. L is defined as $L=\int f dt \approx$ constant, where f is 'an initial rate of damage of remaining undamaged material in the representative volume element'. The essential parts of this equation encompass unified creep-plasticity models with an internal damage parameter. The Stolkarts fatigue model has its basis in a constitutive derivation involving creep-plasticity. The introduction of a damage parameter, d, allows calculation of the number of cycles to failure. The stress-strain hysteresis loop is still used in the calculation to determine the amount of damage.

Application of the damage-based fatigue model requires FEA to effectively obtain a solution and any FEA analysis is geometry specific.

2.3.2.5 Cycle Counting Methods

As load fluctuations in actual use environments are hardly ever periodic a cycle counting method is used to convert the actual fluctuations e.g., temperature evolution to periodic cycles. There exist several cycle counting methods. Rainflow cycle counting is the most popular method and empirically the best known. It should be noted, that cycle counting applies to the load – like the temperature – and not to the local stresses or strains. After a Rainflow histogram has been established, cyclic fatigue life criteria can be applied to each single cycle type. Palmgreen-Miner hypothesis of linear damage accumulation should be then applied in order to get the total damage caused by the whole load sequence.

2.3.3 Fatigue Models in Lead Rich Solders - Micromechanical Approach

According to Semiconductor Industry Association's (SIA) roadmap, this solder joint size will decrease from few hundred microns to a few microns or even nanometer scale in future. It is well know that fatigue of such small joints is different from that of the bulk specimen. Therefore, the empirical fatigue formula derived from experimental data of bulk specimens, which are statistically isotropic, may not realistically predict life for such small joints. However, it is very difficult, if not impossible, to conduct fatigue tests on an individual small solder joint to derive an empirical fatigue formula. On the other hand,

even if such tests are performed and an empirical fatigue formula derived as a result, the application of the formula to joints of different sizes is still questionable. A fatigue theory without size limitation is therefore important so that its fatigue parameters can be determined from tests of bulk specimens with the size effect built into the formula.

Wen and Keer [55] carried out strain controlled cyclic loading on 96.5Pb-3.5Sn solder and have developed a theory which is based on fatigue behavior of an individual grain, which is caused by microcracking within its persistent slip bands (PSB). The PSB are formed by motion of slip planes, and these motions can occur only in particular directions, where such motion is related to the magnitude of local resolved shear stress on the slip planes. Their experimental results have shown that PSB form in the material when the device is under cyclic loading at the operating temperature range, and thereafter, microcracks form within PSB due to increment of dislocation density or along grain boundaries because of the impingement of the PSB on the grain boundaries. These microcracks are usually confined to be within the grains or along grain boundaries, and do not coalesce and form one dominant macrocrack that leads to fracture of the solder structure. Instead, the number of grains with such microcracks increases in a percolating manner, and the solder structure deteriorates, not necessarily showing a drop in load carrying ability until some critical point is reached (Figure 2.52). Figure 2.53 shows that the once very smooth surface at the onset of testing becomes full of macrocracks, microcracks, extrusions, and intrusions.

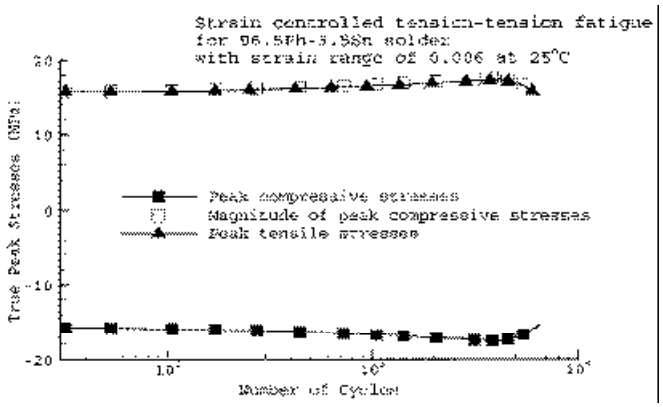

Figure 2.52: Cyclic peak stresses plot for 96.5Pb-3.5Sn solder [55]

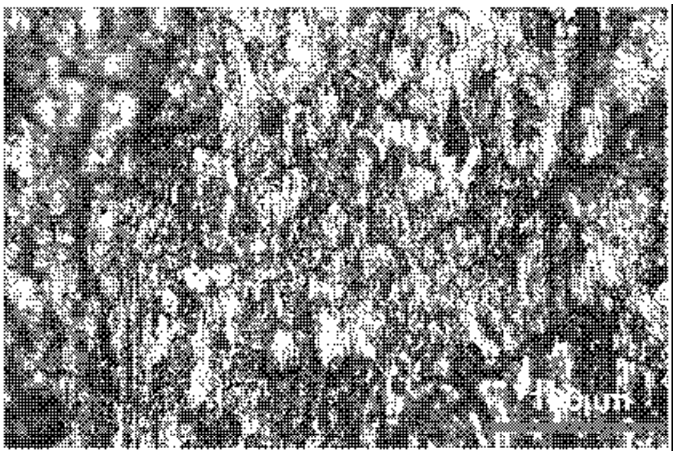

Figure 2.53: Microcracks appeared on the surface of a 96.5Pb-3.5Sn solder specimen after about 6800 cycles under strain-controlled fatigue test (25°C, De=0.006) [55]

Wen and Keer fatigue theory is based on dislocation and percolation damage mechanics. The theory assumes the following: (1) Local resolved shear stress in the crystal slip plane causes PSB and thus the microcracks' formation within the PSB, and the magnitude of the stress differs for grains or cells of different crystallographic orientation; (2) Microcracks do not propagate but rather remain where they appear and fracture the grains or cells locally. The number of failed grains or cells increases within the solder structure;

(3) The portion of such grains or cells reaches a threshold value at which point the entire structure becomes unstable. At this value the failed grains may form a large cluster or macrocrack.

Mura and coworkers [56] have further developed a micromechanical model to quantitatively analyze the microcracking process within the PSB using dislocation theory. In the Mura model, PSB formation results from dislocation density increment in two adjacent but reversely gliding slip layers during the cyclic loading. At the same time, change of the Gibbs' free energy increases as the dislocation energy increases because of the dislocation increment. At a certain point, the Gibbs' free energy change reaches a maximum and microcracking occurs within the PSB. This cycle number is defined as the fatigue point. The Mura model is able to produce the fatigue S-N curve, to capture the grain size effect and to incorporate material properties such as surface energy density, critical friction stresses, and others. Mura model proposes:

$$\Delta G = -W_1 - W_2 + 2cg \tag{2.53}$$

$$\frac{\partial}{\partial n}(\Delta G) = 0 \tag{2.54}$$

where W_1 is the mechanical energy released; W_2 is the energy release from the loss of lattice defects—dislocations—at the nucleation site; γ is the free surface energy; c is the length of the initiated two-dimensional crack; and n is the cycle number. Fine [57] expanded the above theory to a three dimensional penny-shaped mode I crack in the study of fatigue at elevated temperature by rewriting Equation 2.53 as

$$\Delta G = -W_1 - W_2 + 2cA \tag{2.55}$$

where A is the surface area of the initiated three-dimensional crack. For a penny-shaped

three-dimensional microcrack

$$W_1 = \frac{64(1-n^2)\Delta t^2 a^3}{3(2-n)E} \tag{2.56}$$

where E is the Young's modulus, ν is the Poisson's ratio, $\Delta\tau$ is the shear stress range within the crack plane, and a is the radius of the formed microcrack. The energy released from the loss of lattice defects keeps Fine's form [57]:

$$W_2 = 2g_d A \tag{2.57}$$

where γ_d is defined as dislocation energy per unit area and $A=\pi a^2$. Using the total number of dislocations along the diameter of the to-be-nucleated penny-shaped crack and Equations 2.56 through 2.57, the number of cycles at which a microcrack initiates within the PSB or on the grain facets can be calculated as [55]

$$n_{cr} = \frac{(2-n)p(g-g_d)E^2}{32(1-n^2)^2 \bar{d}(\Delta t - 2t_f)\Delta t^2} \tag{2.58}$$

where $\bar{d}$ is the grain size, γ_d is the dislocation energy density and $\Delta\tau$ local resolved shear stress within the cracking plane. Introducing shear strength τ_y into Equation 2.58, it can be rewritten as [55]

$$n_{cr}\left(\frac{\Delta t}{t_y}\right)^3 = \frac{(2-n)p}{32(1-n^2)^2}\frac{(g-g_d)E^2}{d\bar{t}_y^3} \tag{2.59}$$

Making Equation 2.59 more general it can be written as

$$n_{cr}\left(\frac{\Delta t}{t_y}\right)^h = C \tag{2.60}$$

since the right-hand side of Equation 2.59 is a constant and h and C are material constants.

Lin et al. [58], have concluded that the fatigue band is less likely to cross the grain boundary if the orientation of the neighboring grain differs by more than 5 degrees. The bands were actually stopped from crossing the grain boundary when the misorientation was greater than 10 degrees, an angle not uncommon between the grains in a real structure. It is also believed that at high homologous temperature, grain boundaries are obstacles to PSB, and as a result, PSB are confined to be within the grain. If microcracking occurs within the PSB, the newly created microcracks will also be confined to within the grain. If on the other hand a microcrack does not form within the PSB, the strain energy there is not released. Under this condition, the PSB impinge and produce microcracking along grain boundaries. If the grain boundaries are a free surface, then extrusion-intrusion will occur. Figure 2.54 shows the originally smooth surface of a high lead solder at the end of a strain-controlled fatigue test at room temperature (T/T_m=0.5).

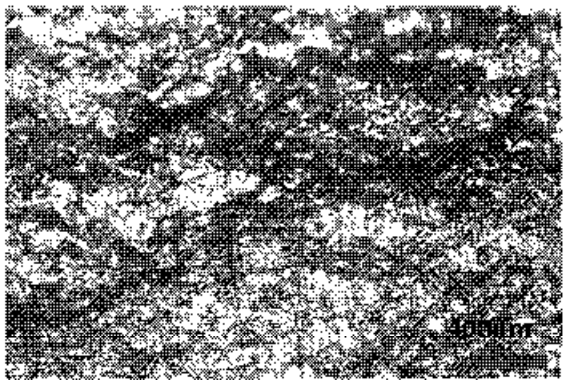

Figure 2.54: The originally smooth surface of 96.5Pb-3.5Sn solder specimen now shows an agglomeration of extrusions, intrusions, striations of PSB and microcracks, with the pattern orienting at roughly 45 deg to the loading axis (vertical) [55]

According to Equation 2.60, the shear stress range has a strong influence on the number of cycles required to initiate a microcrack within the PSB. Under loading σ, the resolved shear stress τ on the system is

$$t = n_s \bullet (S + \frac{1}{3} s_{kk} I) \bullet n_g = n_s \bullet S \bullet n_g = m\|S\| \tag{2.61}$$

where **S** is the deviatoric stress: **S**=s - 1/3tr(s)**I**; *m* is the Schmid factor and $\|o\|$ is a form of norm. Under cyclic loading the number of cycles at which a microcrack initiates is given by

$$n_{cr} m^h = C\left(\frac{\|s_2 - s_1\|}{t_y}\right)^{-h} = C_1 \tag{2.62}$$

where subscripts "1" and "2" correspond to the valley and peak points of cyclic loading respectively [55]. Wen and Keer [55] have defined the fatigue point as the onset point where a sharp peak stress drop begins. According to this fatigue criterion, points N_{fA} , N_{fB}, and N_{fC} are the fatigue points for curves A, B, and C, respectively as shown in Figure 2.55. This criterion has as its physical basis on the percolation damage mechanism. The microcracks developed during cyclic process either appear in the PSB within the grains or along gain boundaries. According to percolation theory, a cluster of microcracked grains or macrocracks may form and the material becomes unstable when the portion of these microcracked grains or the density of microcracks reaches the percolation threshold. The onset of a sharp peak stress drop is the initiation of such an unstable state.

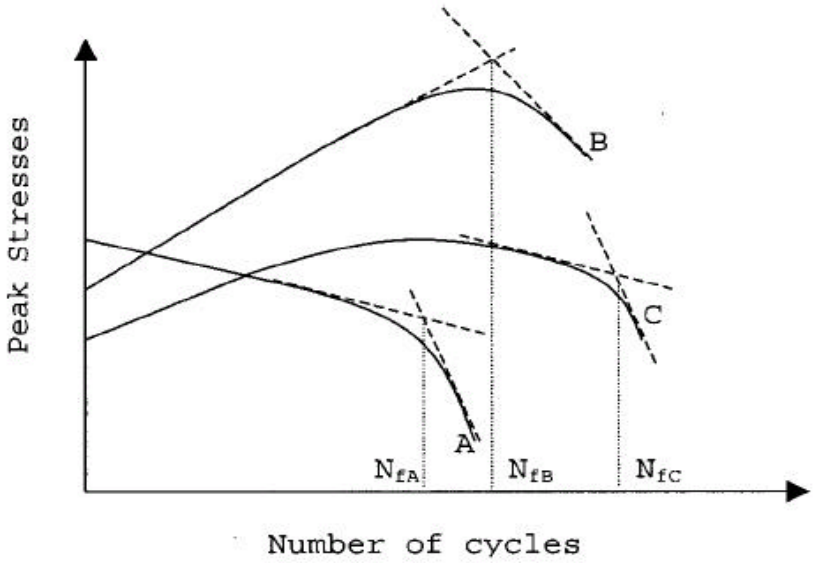

Figure 2.55: Peak stresses evolution during fatigue testing and definition of fatigue point [55]

2.4 Thermal Cycling Durability

Thermal cycling durability of solder joints is affected by a variety of factors such as package type, solder alloy composition, board/component finishes, reflow profile, cycle profile and so on. In this section, major focus is on reviewing the available literature on thermal cycling durability of a few selected high lead content solders for selected package styles.

Luechinger et al. [59] have made extensive study on the reliability of soft solder die attach of multiple die devices by a multiple pass die bonding process. Multiple pass process means a procedure which needs as many die bonder furnace passes as there are different types of die to be bonded into a package. The die used for the investigation have an area of 5.7×4.3 mm^2 and a thickness of 400 μm. Two types of substrates have been used: (1) bare copper with rough surface and 2) Ni/Ni–P plated copper with rough

surface. Soft solder attachment of 50 μm thickness has been carried out in two different ways: (1) single die/multiple pass process (2) multiple die/single pass process. Figure 2.56 through Figure 2.59 shows the rate of delamination in 95.5Pb2Sn2.5Ag and 95.5Pb5Sn solder with number of thermal cycles for samples with pattern dispensing of solder.

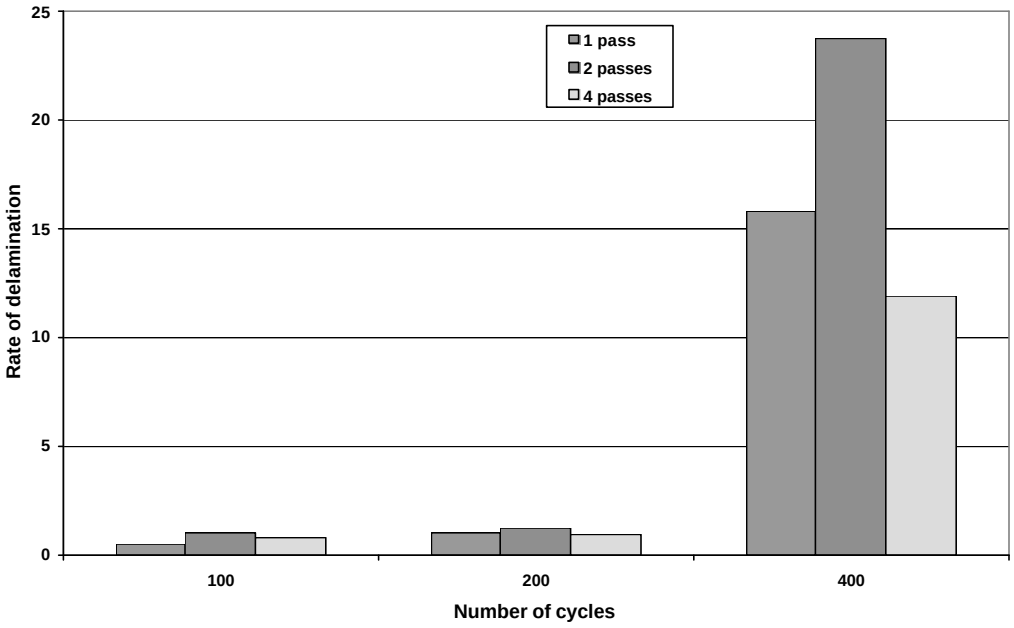

Figure 2.56: Delamination data for 95.5Pb2Sn2.5Ag on bare copper substrate [59]

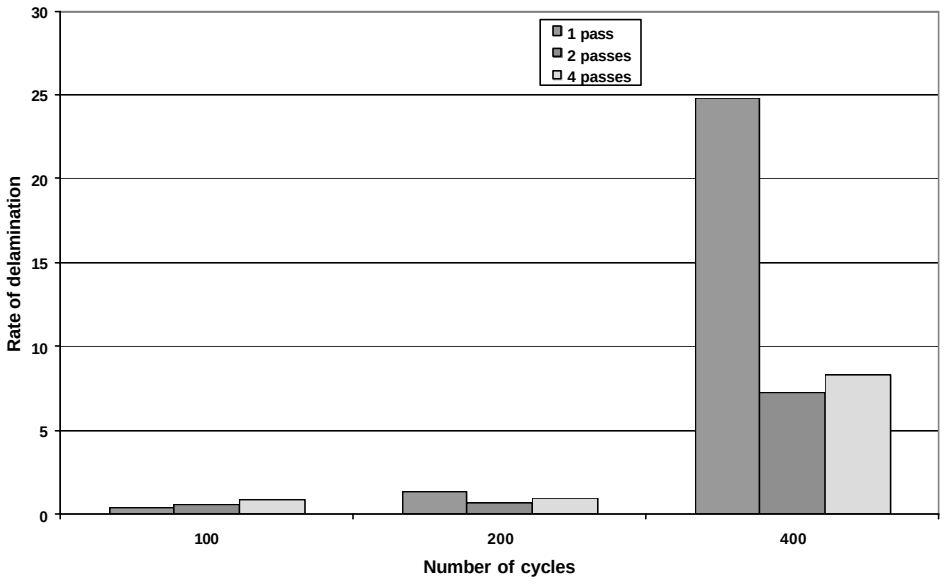

Figure 2.57: Delamination data for 95.5Pb5Sn on bare copper substrate [59]

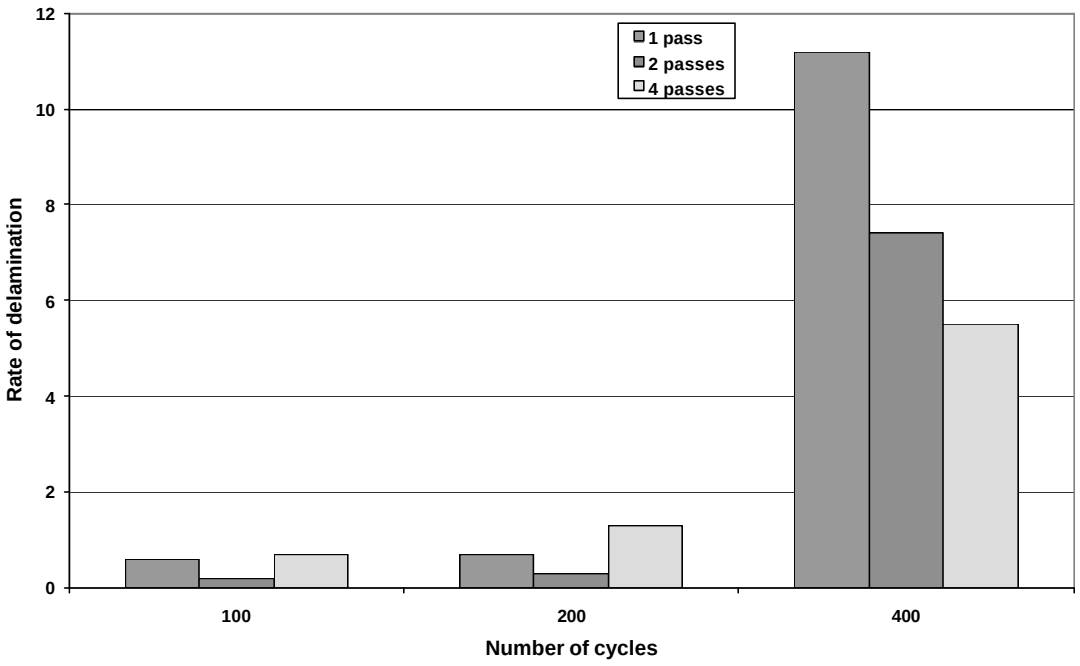

Figure 2.58: Delamination data for 95.5Pb2Sn2.5Ag on Ni/NiP substrate [59]

It is seen from the figures that after 200 cycles there is no significant difference for samples with one, two, and four passes through the furnace. After 400 cycles, with a few exceptions all samples show significant delamination (>5 %). There is no difference between samples for bare copper and nickel plated substrates. For the different material combinations the value of the average delamination after 400 thermal cycles shows strong variations for the samples with a different number of furnace passes. However there is no indication that the reliability of samples with four furnace passes is worse compared to samples with one furnace pass [59].

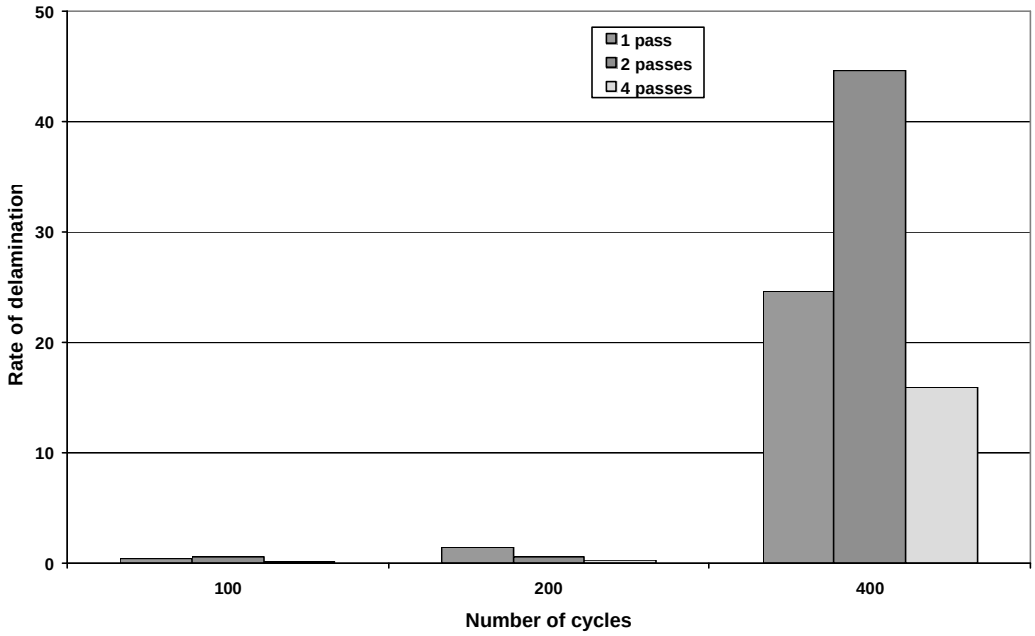

Figure 2.59: Delamination data for 95.5Pb5Sn on Ni/NiP substrate [59]

2.4.1 Durability Modeling

The earliest research examining fatigue phenomena dealt mostly with structural materials and often used stress-based approaches to determining cyclic fatigue life of materials.

The fatigue phenomenon of these structural materials is often referred to as high cycle fatigue since the cyclic loading is in the elastic range. Solder material is subject to large plastic and creep deformations besides elastic deformation, in common application environments because of its rate-independent plastic behavior and its time and temperature dependent creep behavior. The fatigue phenomenon of materials, such as solders, is called low cycle fatigue as the inelastic deformation of materials plays a dominant role.

The Coffin-Manson empirical fatigue model [60, 61] is often used to model the low-cycle fatigue data, by relating total strain range experienced by the material to cycles-to-failure using a power law relationship, as shown in Equation 2.32. This model does not account for the material stress-strain history or mean temperature effects, but can be applied successfully under selected load histories. In order to account for the simultaneous interaction of creep and plasticity in viscoplastic materials, two empirical approaches were developed. The first approach, proposed by Coffin [62], applies a correction factor to the fatigue coefficients and exponents in the Coffin-Manson relationship shown in Equation 2.32. The correction includes the effects of temperature and frequency in the low cycle fatigue model. In the second approach, Manson and Halford [63,64] moved to a strain-range partitioning approach, where the separate effects of plastic and creep strain ranges were correlated to cycles-to-failure, and the damage due to each mechanism combination (i.e. plastic-plastic, plastic-creep, creep-plastic and creep-creep) is superposed to express the aggregate damage condition. These two models have been used to characterize the creep fatigue life of solder due to cyclic loading. Examples of

researchers using strain range approaches in the solder fatigue include Vaynman [65], Enke et al. [66] and Shine and Fox [18]. This approach is more generic and holds greater potential for modeling solder fatigue over a wide range of temperatures and loading frequencies. However, the implementation of this model becomes a complex process if the stresses are not held constant during creep straining.

A widely used variant of Coffin's approach for solder fatigue damage was proposed by Engelmaier [67] on the basis of the Coffin-Manson model, as shown in Equation 2.35. The appropriate time and temperature dependent fatigue constants were obtained from Wild's experimental data [68]. The model has been successfully applied to SnPb solders due to its simplicity and ease of implementation in solder fatigue design. Other approaches relate energy density to cycles-to-failure by Solomon [69]; Darveaux [20]; Vaynman [65]. The Energy-Partitioning (E-P) damage model by Dasgupta et al., [70] is an extension and combination of several of the above approaches. Damage due to elastic strain energy, plastic work and creep work are related individually to damage and then linearly superposed. The E-P model is discussed more extensively in Section 2.4.2.

Rather than attempting to predict the number of cycles to some pre-defined failure condition, several investigators model an effective macro damage propagation rate within the solder joint. The form of such models follows Paris' Law:

$$D = C_{cp}\left(\frac{da}{dN}\right)^{n_{cp}} \tag{2.63}$$

where *da/Dn* is the damage propagation rate, D is the damage metric, and C_{cp} and n_{cp} are the material constants. Damage metric used in such models can be continuum quantities

such as energy [71] or fracture mechanics quantities such as stress intensity or J-integral [71, 72, 73]. Other researchers explicitly model the number of cycles required to initiate a fatigue crack and the damage propagation rate separately, and then predict cycles-to-failure by adding these two quantities together as in Darveaux [20] and Lau, [74].

Fatigue durability of solder is dependent on many factors, including temperature, cycling frequency as given by Solomon and Tolksdorf, [75] as well as the microstructures of the material itself described by Frear [76] and Frost [40]. The definition of failure used also plays a significant role [77]. Failure definitions vary according to the type of test being conducted, and the manner in which the damage is quantified and treated.

2.4.2 Energy Partitioning Damage Model

Durability parameters obtained from experiment can only be used at the same conditions as the test environment because the damage mechanism (creep and plastic damage) change as the test or use conditions changes. An approach to derive a generic damage model (applicable to other test or use conditions) is the Energy Partitioning (E-P) Damage Model. It is a unified approach to creep-fatigue to examine the dependence of solder fatigue behavior on temperature dependent changes in the relative amounts of plastic and creep strains.

2.4.2.1 Approach

Solder material is subject to large plastic and creep deformations in common application environments. The damage mechanisms (creep and plastic damage) change as the test or use condition changes. As test condition changes, specifically temperature, strain rate, and load magnitude, the ratio of plastic deformation to creep deformation changes. Different fatigue curves are thus expected for different test conditions. In order to predict the thermo-mechanical durability of the high lead solder die attach, a generic damage model has to be obtained from these test results. In other words, this model should be able to predict the durability of high lead solders under any test or use condition (any combination of plastic and creep deformation). One such damage model is the energy-partitioning model [70]. The energy-partitioning (E-P) damage model assumes that cyclic fatigue damage is due to a combination of creep deformation mechanisms, plastic deformation mechanisms and elastic deformation mechanisms. This model predicts cyclic creep-fatigue damage based on the deviatoric energy densities: U_e (elastic), W_p (plastic) and W_c (creep) for a typical load cycle. The total damage is determined by using a power law equation and superposing the damage due to all these types of deformations:

$$\text{Total Energy} = U_e + W_p + W_c = U_{e0} N_{fe}^{b} + W_{p0} N_{fp}^{c} + W_{c0} N_{fc}^{d} \tag{2.64}$$

$$\frac{1}{N_f} = \frac{1}{N_{fe}} + \frac{1}{N_{fp}} + \frac{1}{N_{fc}} \tag{2.65}$$

$$U_e = U_{e0} N_{fe}^{b} = \frac{1}{2} G g_e^{2}; W_p = W_{p0} N_{fp}^{c} = \int t dg_p; W_c = W_{co} N_{fc}^{d} = \int t dg_c \tag{2.66}$$

U_{e0}, W_{p0}, W_{c0} represent the intercepts of the elastic, plastic and creep energy density plots vs. cycles-to-failure, on a log-log plot; while the exponents *b*, *c* and *d* are their corresponding slopes. These constants are material properties. The variables N_{fe}, N_{fp} and

N_{fc} represent the cycles-to-failure due to elastic, plastic and creep damage, respectively. The total number of cycles-to-failure N_f is then calculated from an Equation 2.65. Elastic damage is typically very small and negligible, compared with plastic and creep damages in low cycle fatigue. So only plastic and creep terms in Equations (2.64) and Equation (2.65) are considered in this study.

The total damage is computed by summing the inverse of the cycles to failure due to elastic, plastic and creep deformations (using a linear superposition principle for damage). In other words, $D_{total} = (1/N_{fe} + 1/N_{fp} + 1/N_{fc})$. The total number of cycles to failure can also be computed from the inverse of the total damage. It is important to use energy partitioning since plasticity plays an important role in thermal shock tests and the partitioned energies illustrate the contribution of each deformation mechanism to damage.

2.4.2.2 Energy Partitioning Damage Models for Other Lead Solders

Although many energy partitioning models exist in the literature, model constants for high lead solders are almost non-existent. Work done by Zhang [78], Dasgupta [70] and Okura et al. [79] have given E-P model constants for Sn37Pb, shown in Table 2.9.

Table 2.9: Thermo-mechanical Energy-Partitioning model constants for Sn37Pb [78]

E-P Model Constants	Sn37Pb
C	-0.59
W_{p0}	103
D	-1.0
W_{c0}	309

3 Thermo-mechanical Durability

High lead solder interconnects have been extensively used to attach chip to chip carrier in the power electronics industry for many years. These solder interconnects perform three major functions: 1) electrical connection, 2) mechanical attachment, and 3) heat dissipation. Because the coefficients of thermal expansion (CTE) are different between the silicon chip and the substrate, shear strains occur in the solder interconnects when the package is being subjected to ambient thermal loads or when the device is powered on and heat is generated. If the package is operating under cyclic thermal loads heat-induced shear strain within the interconnect layer is also cyclic—causing thermo-mechanical fatigue failure.

Factors affecting the thermo-mechanical durability of large area die attach are as follows:

(a) thermal profile (temperature range, dwell times, dwell temperature and ramp rates)

(b) die attach geometry (thickness, length and width)

(c) defects (voids, cracks, die tilt, delamination)

(d) presence of intermetallics and chemically produced species

(e) solder microstructure (grain size, epitaxy)

(f) die and substrate coatings (metallization, barrier layer)

(g) residual stresses during die bonding and thermal aging

In this chapter, comparison between two different processes for package fabrication is discussed in detail by a description of the accelerated thermal cycling test procedure used for reliability assessment. The packages have been designed, fabricated and tested at the

University of Maryland at College Park in collaboration with Virginia Polytechnic Institute and State University. Package characterization and failure analysis were also conducted at the CALCE center at UMCP. Thermal cycling results are also analyzed and discussed in this section. Finally, comprehensive failure analysis of the failed packages was performed and necessary conclusions were drawn.

3.1 Thermal Cycling Tests

The main objective of the thermal cycling tests in this study is to accelerate potential failure mechanisms in large area die attach packages and to generate failure data to be used in the development of durability models for lead rich solders. The accelerated temperature cycling tests were conducted over a range of design and assembly process variables to assess their effects. Details of the test package, test package characterization, and test profile are discussed below.

3.1.1 Test Package Fabrication

Two different packaging techniques were used to fabricate test samples. These test samples were designed to exhibit different amounts of total mechanical strain during thermal cycling, by using different sizes of die attached to a particular type of substrate. The die were cut from dummy silicon wafers with a constant thickness of 530 μm. The die were backside metallized for good wetting to the solder. The sizes chosen were 6×6 mm^2, 12×12 mm^2 and 20×20 mm^2. Sixteen of each size were then subjected to thermal cycling tests. The substrate was OFHC-grade copper so as to give a high CTE. Copper

substrates were also underplated with sulphamate electroless nickel and overplated with gold flash for better wetting to the lead rich solder.

3.1.1.1 Reflow Belt Oven Soldering

For reflow belt oven soldering, the copper substrates were cleaned with acetone and isopropyl alcohol. The die were placed over the solder performs on the substrates and the stacks were laid on the conveyer belt. A belt oven was used for the reflow process (Figure 3.1). The oven was characterized using thermocouples to create thermal profiles for each solder reflow schedule in coordination with the solder manufacturer's recommendations. Figure 3.2 shows the profile used to reflow the devices [60]. The samples were all cooled in air over a fan-cooled heat sink located at the end of the belt oven. A nitrogen atmosphere was used during the reflow. Figure 3.3 shows the packages fabricated. Table 3.1 contains detailed package configurations.

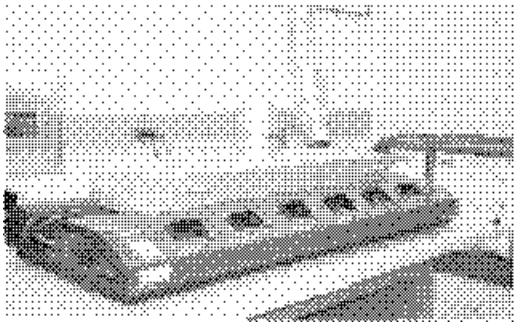

Figure 3.1: Reflow Belt Oven

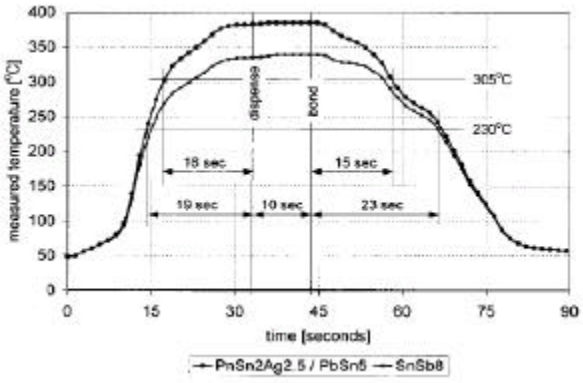

Figure 3.2: Profile used for this research when processing 95.5Pb2Sn2.5Ag soldered devices [60]

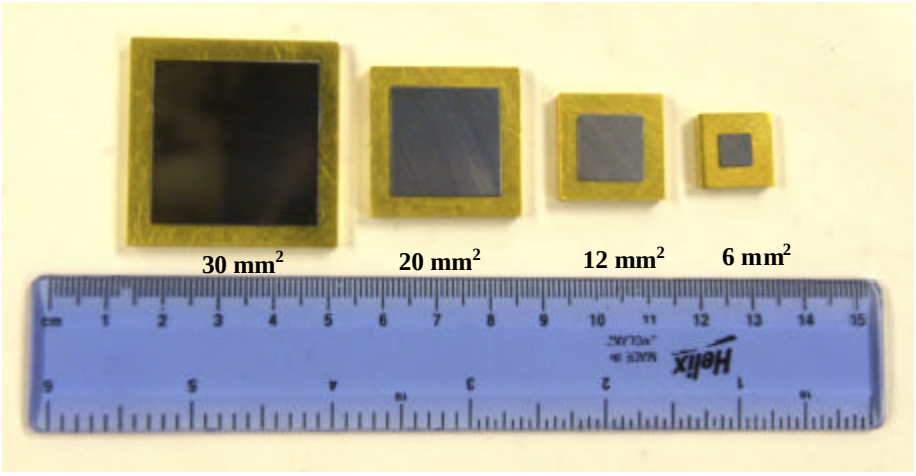

Figure 3.3: Packages subjected to thermal cycling

Table 3.1: Reflow belt oven fabricated package thickness configurations

Characteristic	Package (6×6, 20×20, 30×30 mm^2)			Package (12×12 mm^2)		
Silicon Die	530 µm			530 µm		
Backside metallization	Ti-W = 20 nm	Ni = 2µm	Au = 0.5µm	Ti-W=20 nm	Ni = 2µm	Au = 0.5µm
Die Attach	50 µm			100 µm		
Copper Substrate	3.20 mm			3.20 mm		

3.1.1.2 Vacuum Reflow Soldering

For vacuum reflow soldering, the die were cut from dummy silicon wafers. The die had the dimensions of 6×6 mm^2, 12×12 mm^2 and 20×20 mm^2 and thickness of 525 μm. The die were back metallized with Cr/Ni/Au using a sputtering machine with Argon gas at 0.66 Pa pressure and substrate temperature of 275°C. The wafers were diced using a Disco saw at 30000 rpm and 3mm/s feed with water spray. The OHFC grade copper was plated with 6.096 μm of sulphamate nickel which was overplated with 0.762 μm of gold flash. The solder was procured in form of ribbon preform with thickness 50 μm and cut to a size slightly larger then the die before die bonding using a vacuum reflow oven. Ceramic shims were micro-machined using a Photomachining CO_2 laser system. The substrates and ceramic shims were cleaned with acetone and then with isopropyl alcohol before putting all the components in the graphite tooling.

An exploded view of reflow fixturing is shown in Figure 3.4. Once the graphite fixture is placed in the chamber the heaters are switched on and forming gas is fed into the chamber. Vacuum is created up to 10.665 Pa. The temperature is then raised to 375°C to melt and flow the solder. The solder is kept molten for 1.5 minutes and then N2 is used to pressurize the chamber to eliminate voids and speed cooling. Appendix A describes the solder reflow profile in detail.

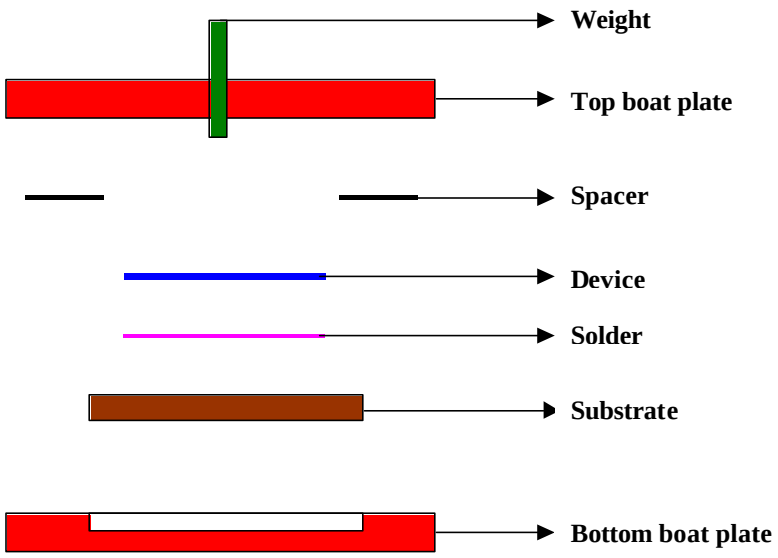

Figure 3.4: Schematic of reflow fixturing exploded view

First a few trial runs were made to optimize the reflow conditions. The packages were observed under a scanning acoustic microscope for delamination. The initial dies while superior to the reflow belt oven samples exhibited some delamination at the die-solder interface although the adherence was very good to the electroplated substrate. A switch from Ti to Cr backside die metallization significantly improved the adherence of the solder to the die. Table 3.2 contains detailed package thickness configurations. Figure 3.5 shows the reflow profile used. The complete fabrication steps are shown in Figure 3.6.

Table 3.2: Package thickness configurations from vacuum reflow soldered samples

Characteristic	Package (6×6, 12×12, 20×20 mm^2)			Package (12×12 mm^2)		
Silicon Die	510 µm			510 µm		
Backside metallization	Cr = 30 nm	Ni = 1µm	Au = 0.3µm	Cr=30 nm	Ni = 1µm	Au = 0.3µm
Die Attach	50 µm			100 µm		
Copper Substrate	3.20 mm			3.20 mm		

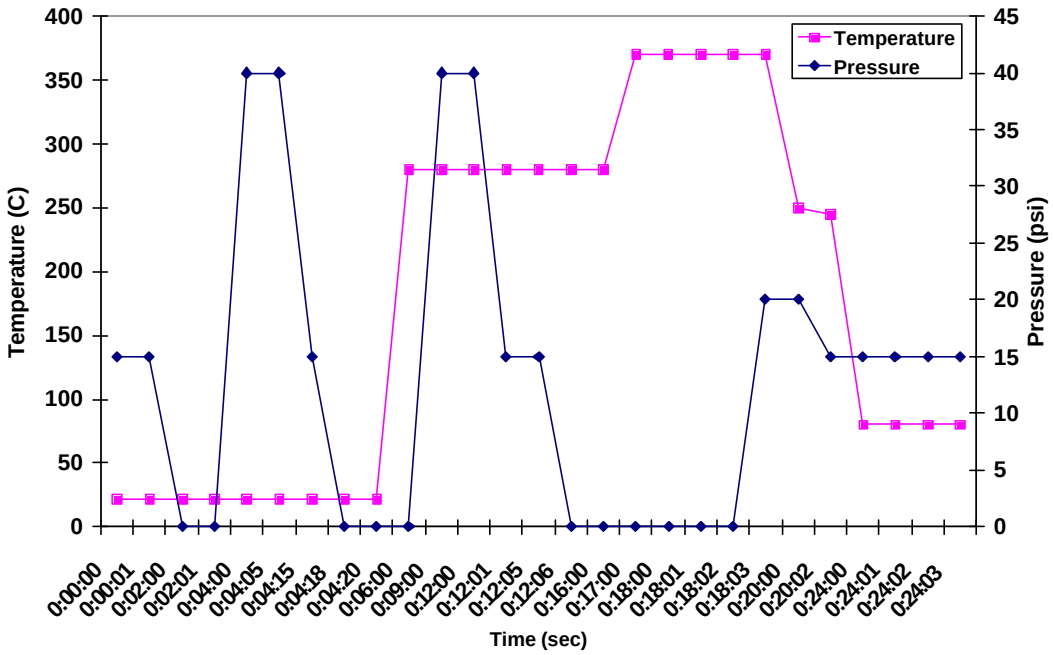

Figure 3.5: Reflow Profile for 95.5Pb2Sn2.5Ag perform

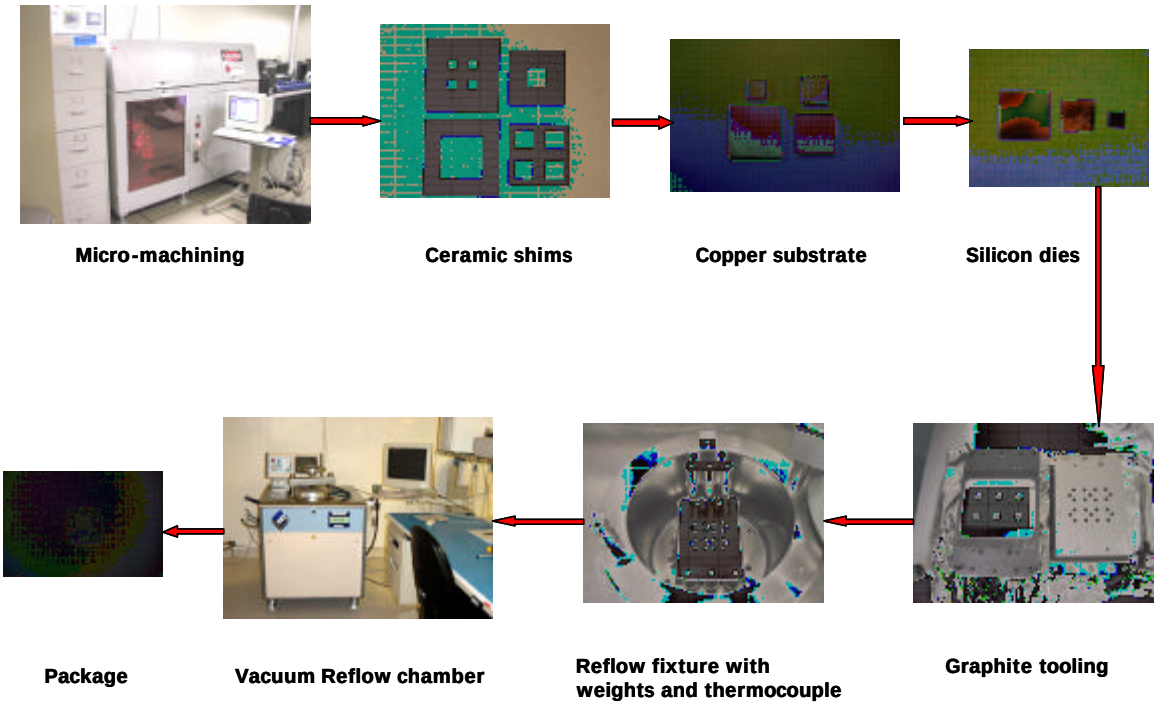

Figure 3.6: Package Fabrication using Vacuum Reflow Chamber

3.1.2 Package Characterization

The major objectives of the package characterization were: (a) to obtain the geometry (thickness) of all assembled packages for finite element analysis (b) to record the microstructures of die attach. The geometry of the die attach in the package was measured by optical microscope after cross sectioning. The thickness dimensions of the 6×6 mm^2 and 12×12 mm^2 size packaged die are shown in Figure 3.7 and Figure 3.8 respectively. Other dimensions, such as substrate thickness and length, and die dimensions, can be found in Figure 3.3, Table 3.1 and Table 3.2. The geometric information is used to build up the 3-D finite element models for these packages.

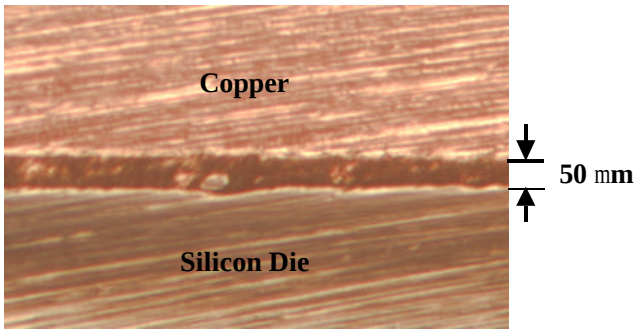

Figure 3.7: Thickness dimensions of die attach and 6 ´ 6 mm^2 die

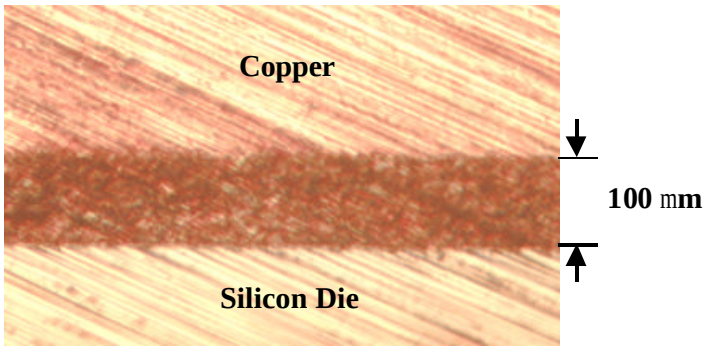

Figure 3.8: Thickness dimensions of die attach and 12 ´ 12 mm^2 die

Most material properties of the die, substrate and die attach found in these packages are collected from component manufacturers and relevant literature. They are summarized in chapter 4.

The packages (with Ti metallization on the backside of die) made by reflow belt oven were revealed by C-SAM and X-Ray to have more than 30% voids in the solder die attach in many cases. Figure 3.9 shows a 6×6 mm^2 die package having more than 23% voids. Packages fabricated by vacuum reflow had less than 1% voids in many cases for both Ti and Cr metallized dies. They are shown in Figure 3.10 for a 6×6 mm^2 die package with Ti metallization and in Figure 3.11 with Cr metallization. Appendix B shows the X-Ray reports of more packages built by vacuum reflow technique.

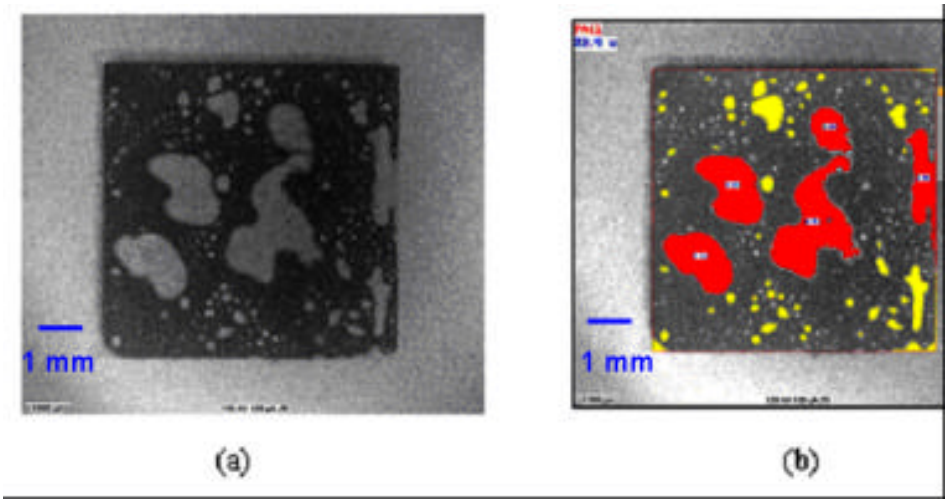

Figure 3.9: (a) X-Ray Laminography showing voids in the die attach (b) 23% voids by reflow belt oven

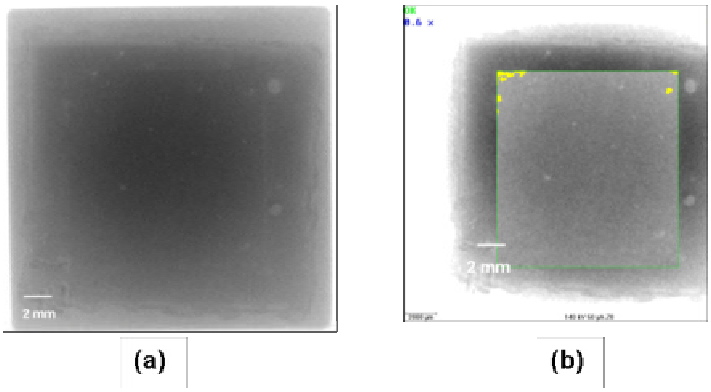

Figure 3.10: (a) X-Ray Laminography showing very few voids in the die attach (b) 0.5% voids (with Ti metallized dies) by vacuum reflow soldering process

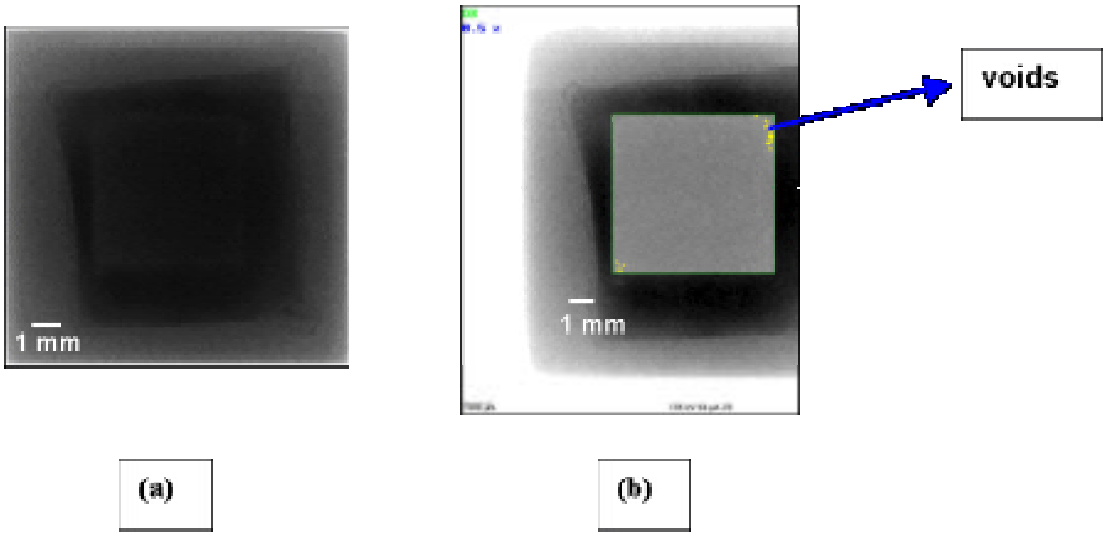

Figure 3.11: (a) X-Ray Laminography showing very few voids in the die attach (b) 0.5% voids (with Cr metallized dies) by vacuum reflow soldering process

Scanning acoustic microscopy of the samples also reveals the cracks and delamination along the interfaces. For the reflow belt oven processed packages, the delamination is all along both the interfaces. This is shown in Figure 3.12 for one of the packages where the white portions signify delaminations. But the vacuum reflow soldered packages have very little delamination as compared to reflow belt oven samples. The packages with Ti

metallization has more delamination (shown in Figure 3.13) then that with Cr metallization shown in Figure 3.14. As vacuum reflow reduced the voiding and the use of Cr metallization reduces the delamination, vacuum reflow fabricated packages with Cr metallization have been chosen for thermo-mechanical study.

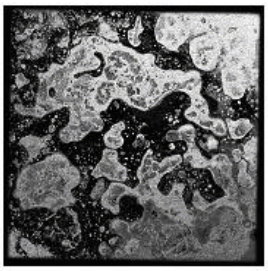

Figure 3.12: C-Scan showing delamination in 6´6 mm^2 package (with Ti metallized died) fabricated by reflow belt oven

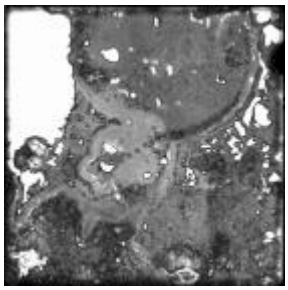

Figure 3.13: C-Scan showing delamination along in 6´6 mm^2 package (with Ti metallized dies) fabricated by vacuum reflow chamber

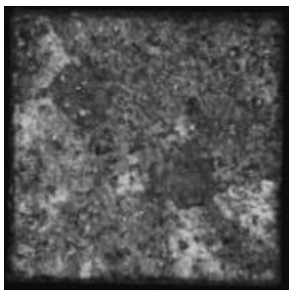

Figure 3.14: C-Scan showing delamination along in 6´6 mm^2 package (with Cr metallized dies) fabricated by vacuum reflow chamber

Die shear testing using the DAGE 2400 precision universal strength testing system also showed that the die packaged using the reflow belt oven process were poorly bonded to the substrate. The average die shear strength of virgin packages was 10.25 KgF, while packages made through vacuum reflow process with Cr metallized dies had an average die shear strengths of more than 21.14 KgF. The testing parameters for the DAGE 2400 were velocity of 200 μm/s; test height of 25 μm; hold time of 10000 ms and fall back of 80%. Table 3.3 shows the die shear strength values of both types of packages.

Table 3.3: Die shear strength of packages made from both the processses

Die shear strength of packages from reflow belt oven (kgf)	Die shear strength of packages from vacuum reflow chamber (kgf)
8.26	> 20.82
9.37	> 21.47
15.72	> 20.96
7.65	> 21.33

3.1.3 Reliability Testing

Two different thermal cycles were performed. Packages of die sizes, 6×6 mm^2 and 20×20 mm^2 that are subjected to thermal cycling with a temperature range varying from -10°C to 100°C (mean temperature of 55°C), ramp rate of 5°C/min, a cooling rate of 8.46°C/min, a high temperature dwell time of 20 minutes and a low temperature dwell time of 5 minutes. Packages of die sizes 6×6 and 12×12 mm^2 were subjected to another thermal cycle loading with a temperature range varying from 0°C to 165°C (mean temperature of 82.5°C), a ramp rate of 6.36°C/min, a cooling rate of 8.25°C/min, a high temperature dwell time of 20 minutes and a low temperature dwell time of 5 minutes. 12×12 mm^2 packages with both 50 μm and 100 μm bondline thickness were subjected to

this thermal cycling from 0 to 165°C. The two thermal profiles are shown in Figure 3.15. The packages were thermal cycled in an Envirotronics chamber using liquid nitrogen for cooling. The set up is shown in Figure 3.16. After every 75 cycles, the packages were taken out for X-Ray examination and scanning acoustic microscopy. Failure was defined as when the cracks and delamination at the corners extended more than 20% of the half diagonal in length.

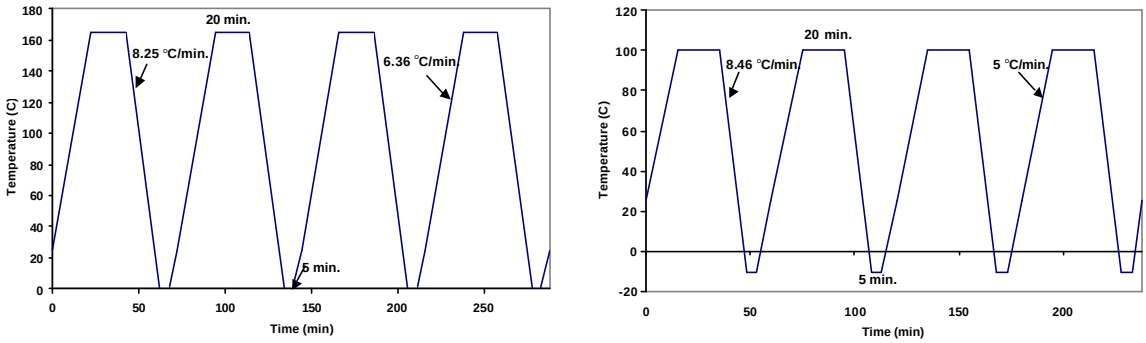

Figure 3.15: Thermal profiles (a) 0 to 165 °C (b) –10 to 100 °C

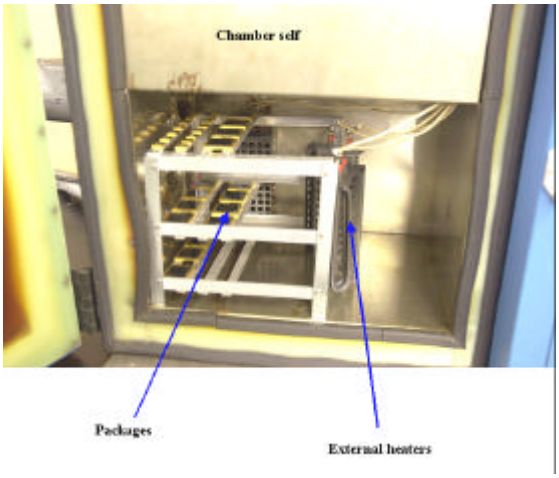

Figure 3.16: Thermal cycling setup for reliability testing

3.2 Thermal Cycling Results and Discussion

After every 75 thermal cycles, the packages are taken out of the chamber and observed using SAM. If any sample has met the failure criterion, it is noted and removed for failure analysis. Unfailed samples are put back inside the chamber for more cycling. Failure data were analyzed using Weibull statistics. Some of the packages were cross-sectioned to observe the crack and delaminations.

3.2.1 Scanning Acoustic Microscopy

Figure 3.17 shows a schematic of the defects in die attach which can affect reliability. Since the bondline is thin, the SAM does not differentiate between thin cracks and delamination. Moreover the resolution capability of SAM limits the clear imaging of hairline cracks. For large area die attach subjected to accelerated cycling, fatigue cracks and delamination progress jointly. So henceforth the cracks and delamination growth will be termed as damage growth in this dissertation. Figure 3.18 shows on the left a C-scan image of the die-solder interface and on the right shows the A-scan image when the acoustic signal is directed at the die side of the package. The A-scan picture shows the depth at which the interface lies for both die-solder and solder-substrate attachment. The value shown at the top of A-scan images matches well with the thickness of layers in the package.

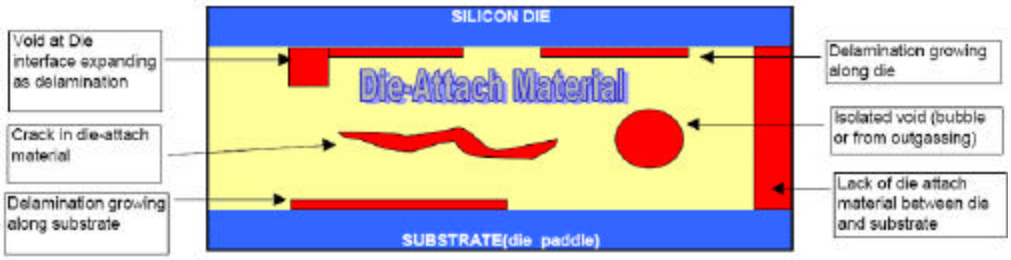

Figure 3.17: Hidden defects revealed by Scanning Acoustic Microscopy

Figure 3.19 shows cracks and delamination growing from the corners and periphery for a 6×6 mm^2 die attach size during –10 to 100°C thermal cycle until failure is declared after 450 cycles. The X-ray image on the leftmost shows that there are very few voids and the white areas in the acoustic images are the cracks and delaminations. So an important observations is made for the samples:

- The damage starts in the corners of the package and
- Propagates towards center of die

This indicates good adhesion and low voiding in the initial sample and strain related crack growth in the solder during cycling.

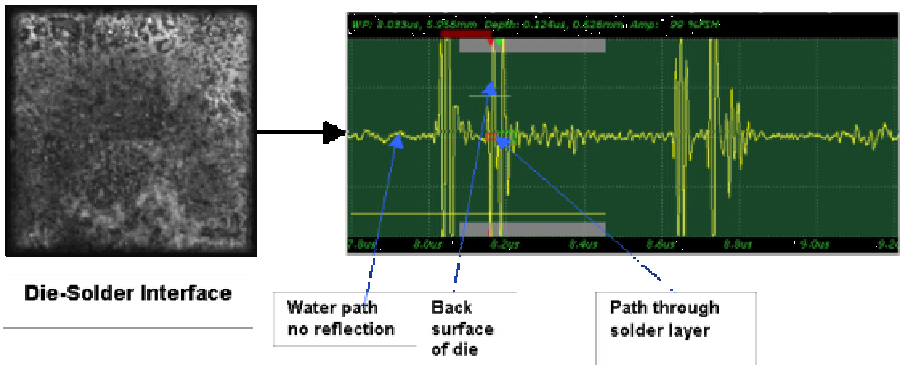

Figure 3.18: Black and white C-scan (left) and A-scan (right) of the package

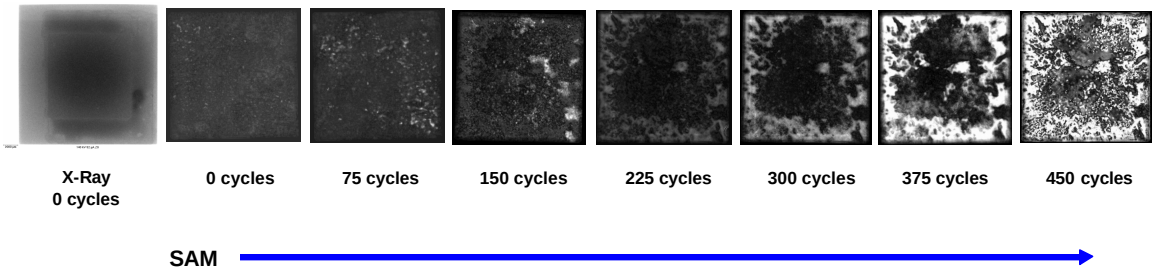

Figure 3.19: Damage growth in a 6´6 mm^2 package during –10 to 100°C

Figure 3.20 shows the acoustic images of another 6×6 mm^2 package during –10 to 100°C thermal cycle. Here after 225 cycles, it can be seen inside the green circle that new cracks are growing towards the center of the die. New voids also appeared during thermal cycling shown inside the red circle. Also towards the end of thermal cycling aggressive cracking and delaminations occurred which is marked in the yellow circle. Failure of this sample occurred at 525 cycles. Figure 3.21 shows a 20×20 mm^2 package size which initially had few delaminations and failed at 375 cycles. More aggressive delamination is shown in Figure 3.22 for a 12×12 mm^2 package during 0 to 165°C thermal cycling. Additional SAM images are shown in Appendix C.

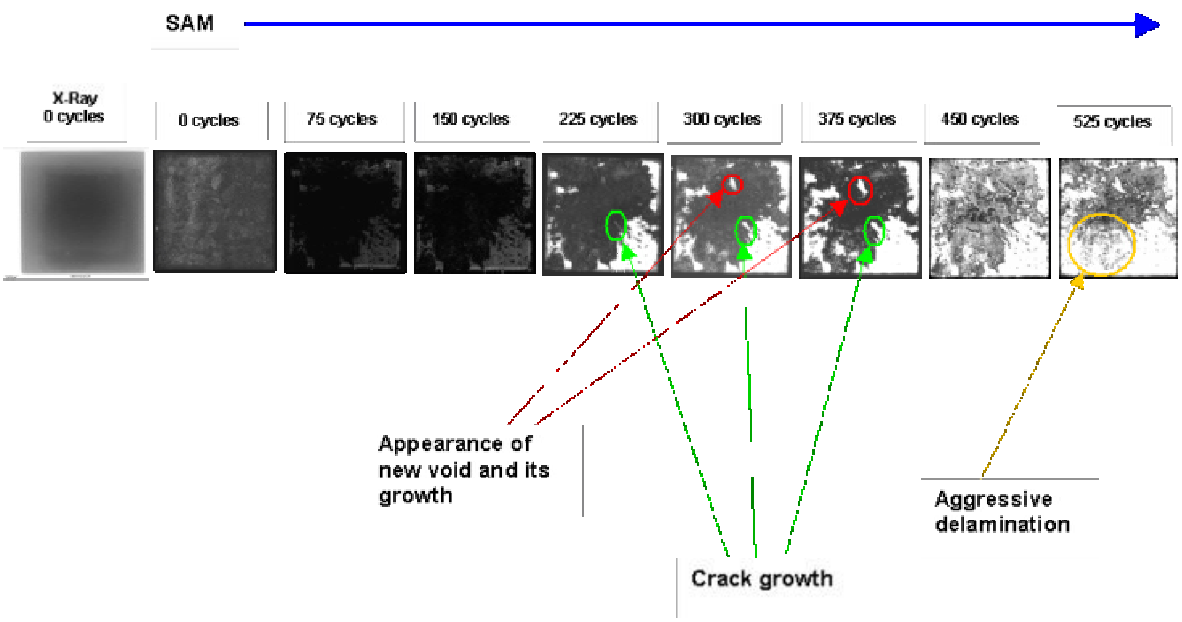

Figure 3.20: Damage growth in a 6´6 mm^2 package during –10 to 100°C

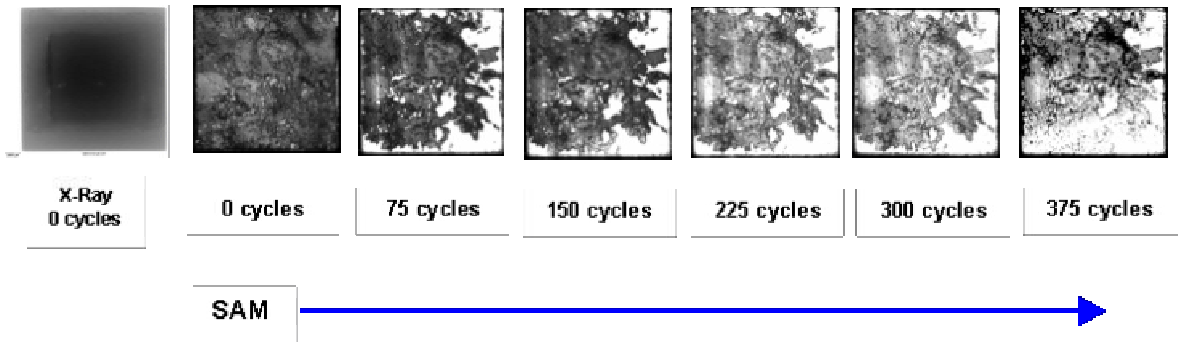

Figure 3.21: Damage growth in a 20´20 mm^2 package with few initial delaminations during –10 to 100°C

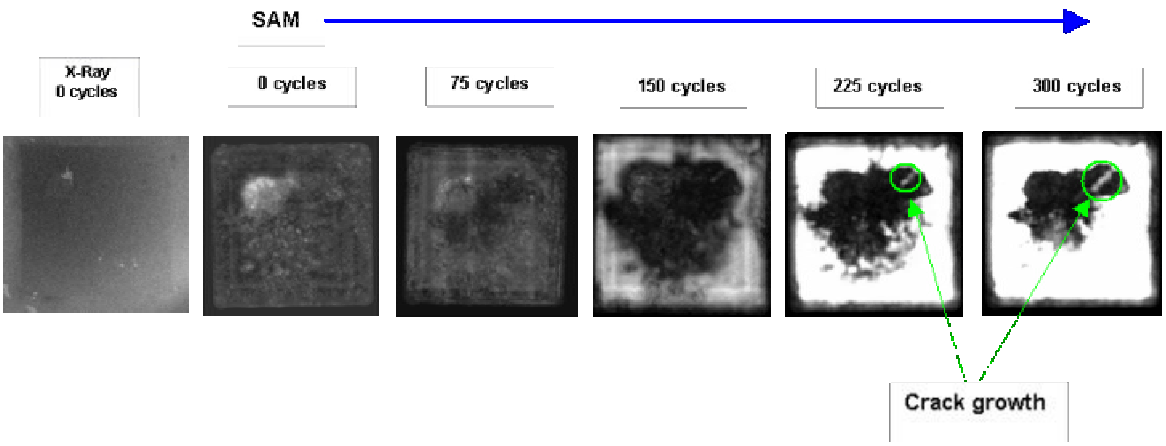

Figure 3.22: Damage growth in a 12´12 mm2 package during 0 to 165°C thermal cycling

Figure 3.23 shows the C-scan and A-scan of a package with 100 µm bondline thickness. Some packages survived through the thermal cycling. SAM images of one such package is shown in Figure 3.24.

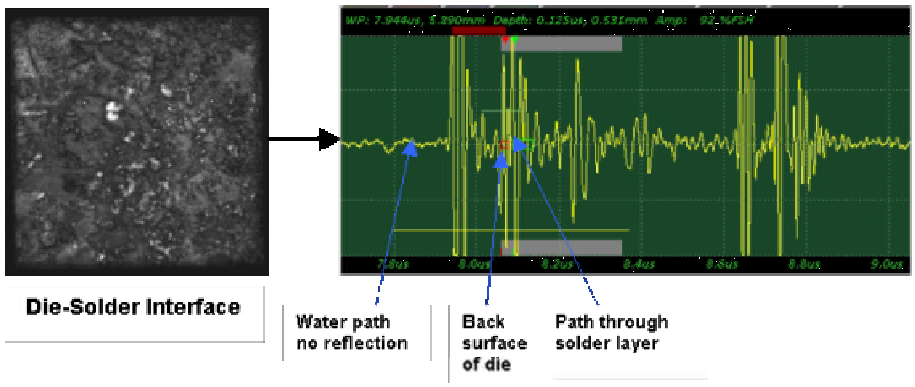

Figure 3.23: Black and white C-scan (left) and A-scan (right) of a package with 100 mm bondline thickness

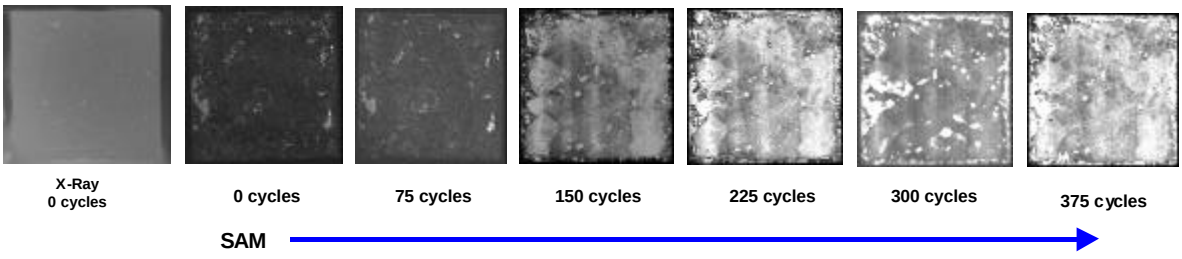

Figure 3.24: SAM showing very slow damage growth during 0 to 165°C cycle in 12 mm^2 package with 100 µm bondline thickness

3.2.2 Weibull Analysis

The Weibull distribution is commonly used in reliability evaluations because it can attain many shapes allowing it to model a large selection of life characteristics. Weibull++ 6 allows one to perform life data analysis for all types of life data. The Weibull technique allows time of failure to be introduced into the analysis. Reliasoft Weibull++ 6 software package was used to estimate the parameters using both the two-parameter Weibull reliability Function and the three-parameter Weibull Reliability Function included in Equations 3.1a and 3.1b.

Two-parameter (2-P) Weibull: $$R(t) = \exp\left\{-\left(\frac{t}{h}\right)^{b}\right\} \quad (3.1a)$$

Three-parameter (3-P) Weibull: $$R(t) = \exp\left\{-\left(\frac{t-g}{h}\right)^{b}\right\} \quad (3.1b)$$

Where: ß = shape parameter (a measure of the variance of the results); ? = scale parameter (characteristic life for 2-P Weibull, when the 63.2% population fail); ? = location parameter (failure free period for 3-P Weibull).

At least 62% of the sample population failed for all the test package configurations. Table 3.4 contains a failure summary for each test configuration. Table 3.5 contains Weibull data of four component types in their test configurations. Failure data used in Weibull technique were grouped together in intervals of time. When a sample failed in an interval the sample identity is noted and fed to the Weibull++6 software. To increase confidence in the calculation and decrease the confidence bounds, the tests were carried out until a large percentage of samples failed.

Table 3.4: Thermal Cycling Tests Results

Package type	Result	0 to 165 °C	-10 to 100 °C
6×6 mm^2 die attach	Failures	12	14
	Survivors	4	2
12×12 mm^2 die attach (50 µm bondline)	Failures	12	
	Survivors	4	
12×12 mm^2 die attach (100 µm bondline)	Failures	11	
	Survivors	5	
20×20 mm^2 die attach	Failures		15
	Survivors		1

Since the failure data is collected in intervals of time it makes more sense to perform a 2-P Weibull than a 3-P Weibull analysis. For the shape parameter, ß, the range for 2-P Weibull is from 1.32 to 1.81.

Table 3.5: Weibull Analysis Results

Test Conditions	6×6 mm^2 die attach			12×12 mm^2 die attach (50 μm bondline)			12×12 mm^2 die attach (100 μm bondline)			20×20 mm^2 die attach		
2-P Weibull	β	η	ρ	β	η	ρ	β	η	ρ	β	η	ρ
0 to 165 °C	1.81	325.43	0.96	1.39	278.79	0.98	1.06	300.15	0.99			
-10 to 100 °C	1.86	436.56	0.94							1.79	300.44	0.99

Figure 3.25 and Figure 3.26 show the effects of die attach size and thickness on characteristic life, ? for 2-P Weibull for both the thermal cycles. Figure 3.27 shows 2-P Weibull plots for 6×6 mm^2 die attach from 0 to 165 °C. Corresponding Weibull plots are shown in Appendix D. The results indicate that 20×20 mm^2 die attach has the worse durability than 6×6 mm^2 attach for the same thermal cycling condition and same attach thickness. Secondly, the durability of 100 μm bondline thickness is better than 50 μm bondline for the same die attach size and same thermal cycle.

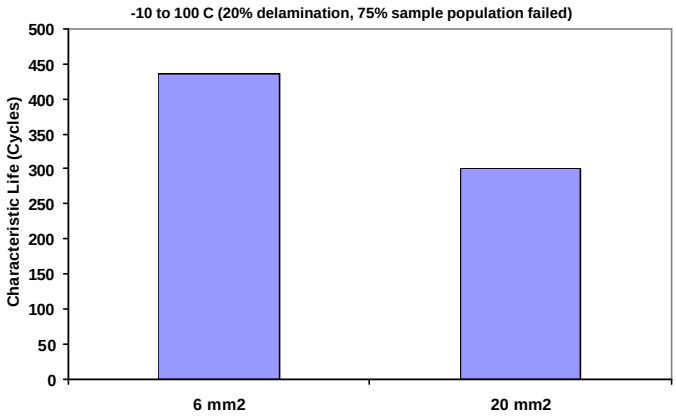

Figure 3.25: Effects of die attach size on characteristic life of the solder attach during –10 to 100°C cycle

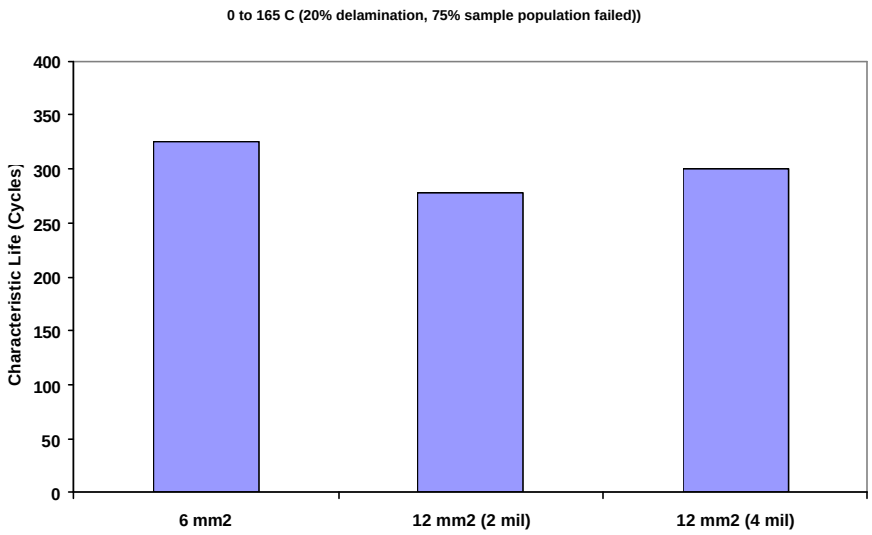

Figure 3.26: Effects of die attach size and thickness on characteristic life of the solder attach during 0 to 165°C cycle

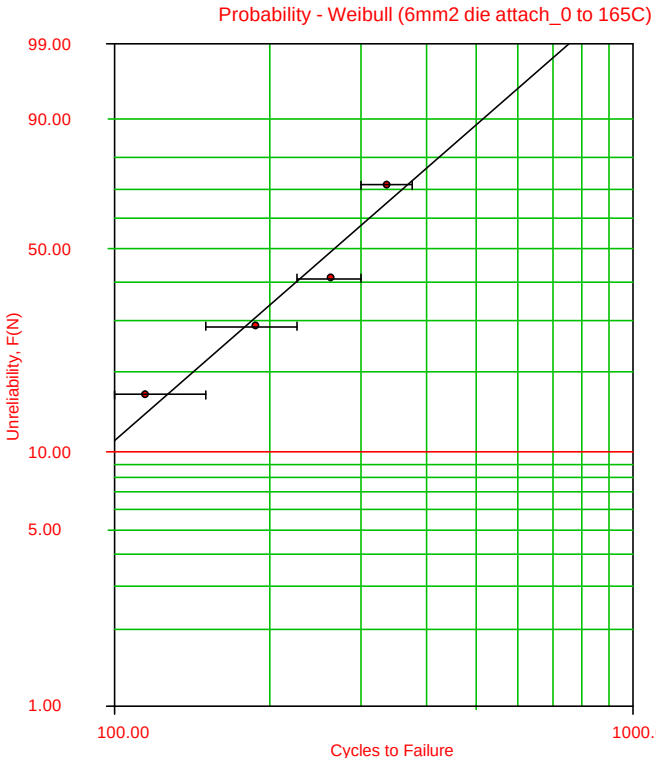

Figure 3.27: 2-P Weibull plot of 6´6 mm^2 package from 0 to 165°C thermal cycle

3.3 Failure Analysis

Failure analysis was conducted to verify the failure modes, failure sites and failure mechanisms of the packages.

3.3.1 Die Shear Testing

Shear testing was carried out on failed samples to reveal the quality of solder attachment to the backside of the die and to the substrate, the effect of delamination, and most importantly the failure mechanism. Figure 3.28 shows the backside of the die and front side of substrate after die shear testing. As is clearly seen, solder is attached to both the surfaces meaning that the package has failed due to fatigue through the bulk solder. The die shear strength value is 5.52 KgF. Figure 3.29 shows the die shear strength values of some failed packages. Comparing this chart with Table 3.3 reveals that the presence of the crack resulting from thermal cycling weakens the strength of the attachment as expected.

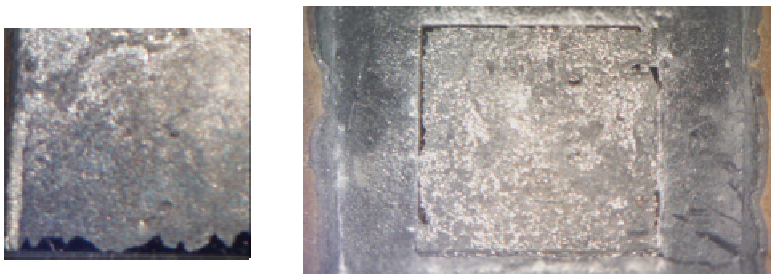

Figure 3.28: (a) Back of die (b) Top view of substrate shows solder attachment

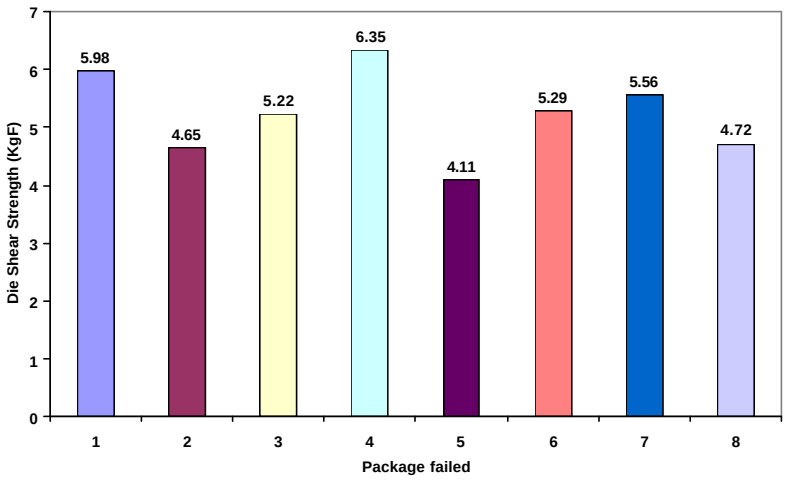

Figure 3.29: Die shear strength values of failed samples

3.3.2 Microstructural Characterization

Microstructure characterization has been done on some failed packages. Figure 3.30 shows the microstructure of 95.5Pb2Sn2.5Ag solder and the X-Ray dot mapping for the elemental spectra shown in Figure 3.31. They reveal together that the metallization elements like Cr, Ni and Au are uniformly distributed and therefore likely dissolved in the solder. Figure 3.32 shows the same solder at a relatively higher magnification.

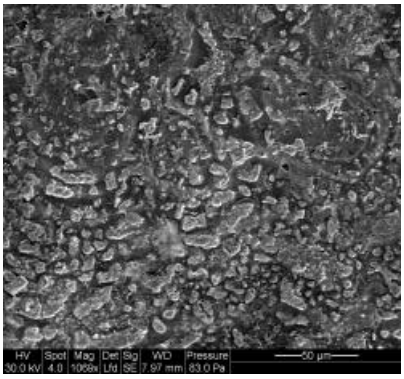

Figure 3.30: Solder microstructure showing a uniform distribution

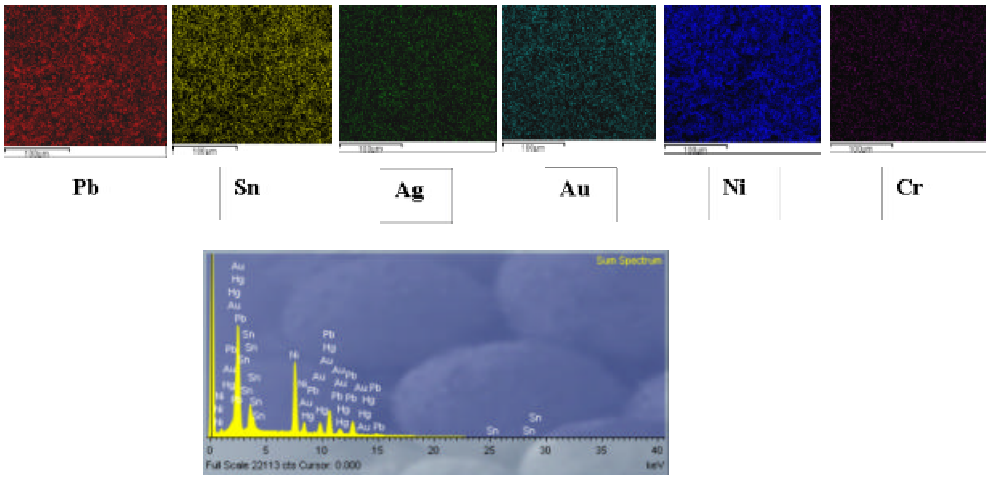

Figure 3.31: Area mapping shows homogeneous distribution of elements

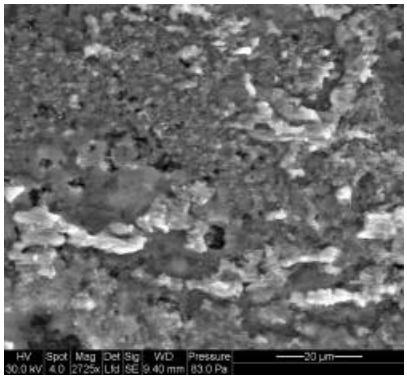

Figure 3.32: Solder microstructure showing homogeneous distribution of elements at 2725X

The cross-sectional view of the package is studied for joint quality and crack propagation. E-SEM is used at higher magnification and EDX was used to observe the metallization layers. Figure 3.33 shows the solder between silicon die and copper substrate. Figure 3.34 shows area mapping which explains that the tin, silver and gold are dissolved in the lead solder.

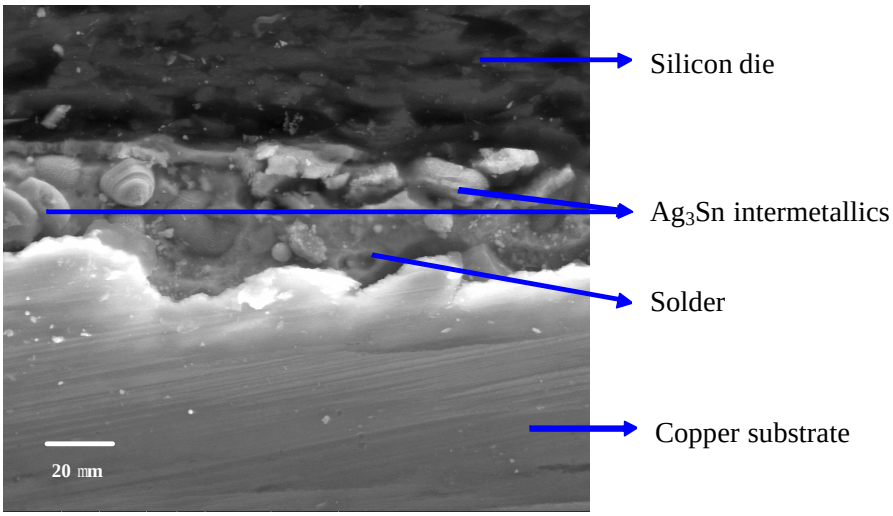

Figure 3.33: Cross sectional view of package at 4336X magnification

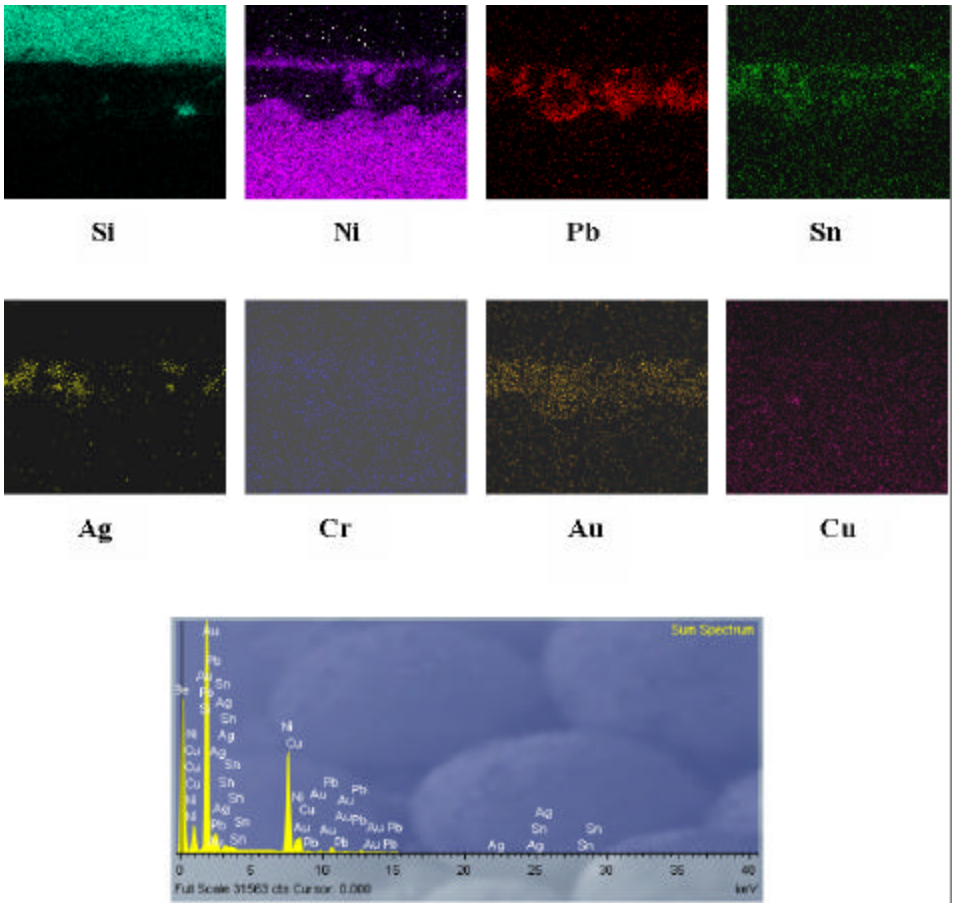

Figure 3.34: Area mapping shows tin, silver and gold dissolved in the lead solder

The solder between the die and substrate gets sheared due to repetitive thermal cycling. This leads to fatigue cracks and delamination from the interfaces. Figure 3.35 through Figure 3.37 shows fatigue cracks inside the 95.5Pb2Sn2.5Ag solder. Cracks developed in the bulk of the solder due to fatigue has been shown in Figure 3.38 and its respective area mapping in Figure 3.39. More microstructures and fatigue crack micrographs are shown in Appendix E.

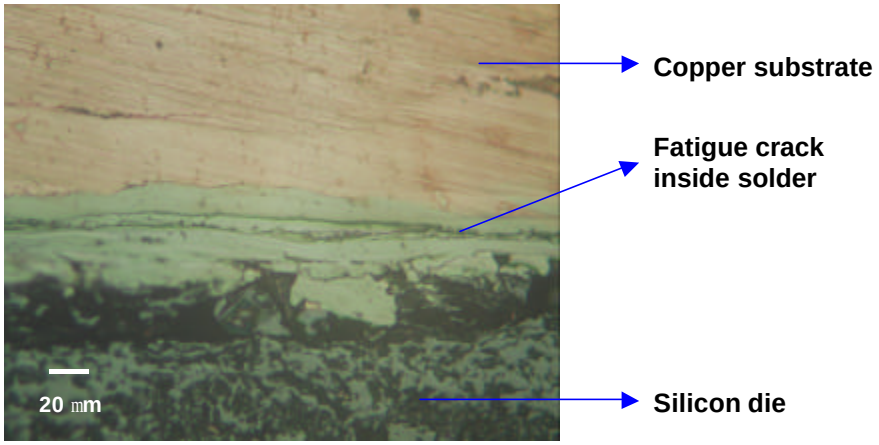

Figure 3.35: Fatigue cracks inside solder at 50X magnification

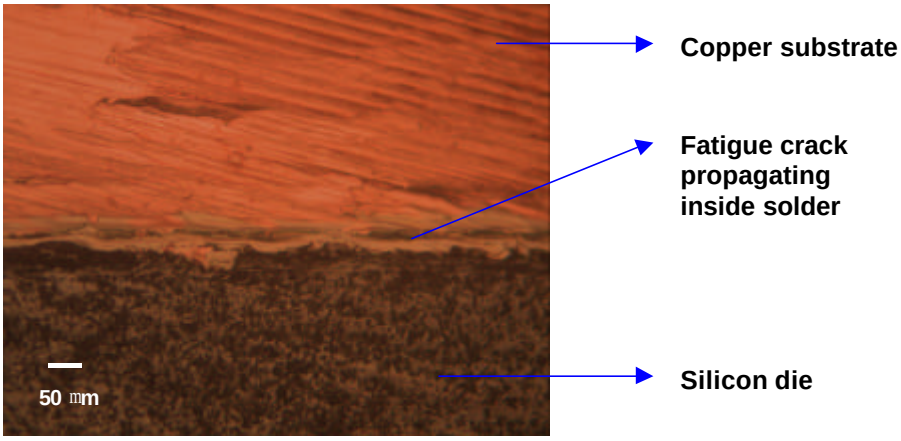

Figure 3.36: Fatigue cracks inside solder at 10X magnification

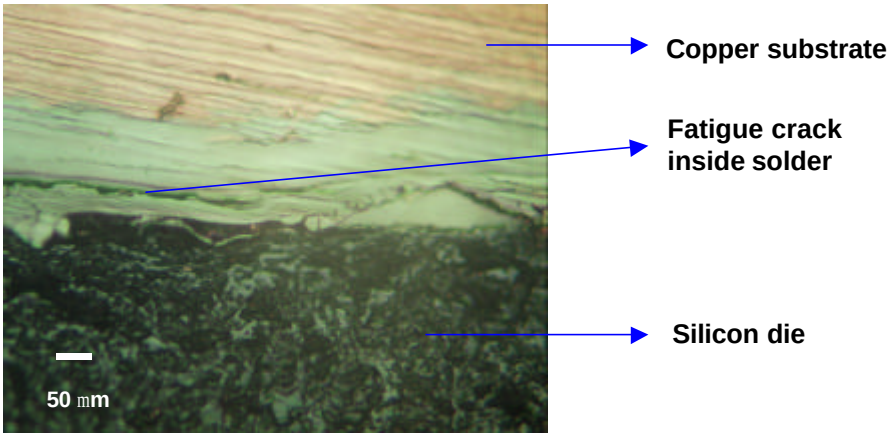

Figure 3.37: Fatigue cracks inside solder at 50X magnification

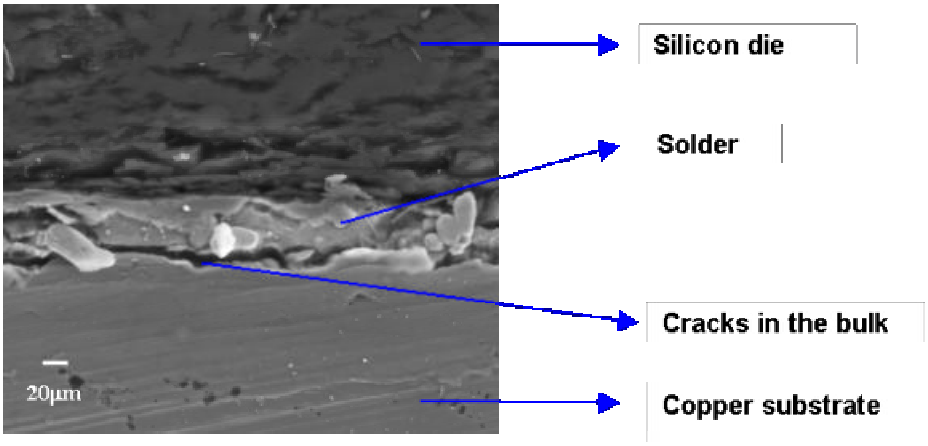

Figure 3.38: Microstructure showing crack propagating at the solder-substrate interface at 2219X magnification

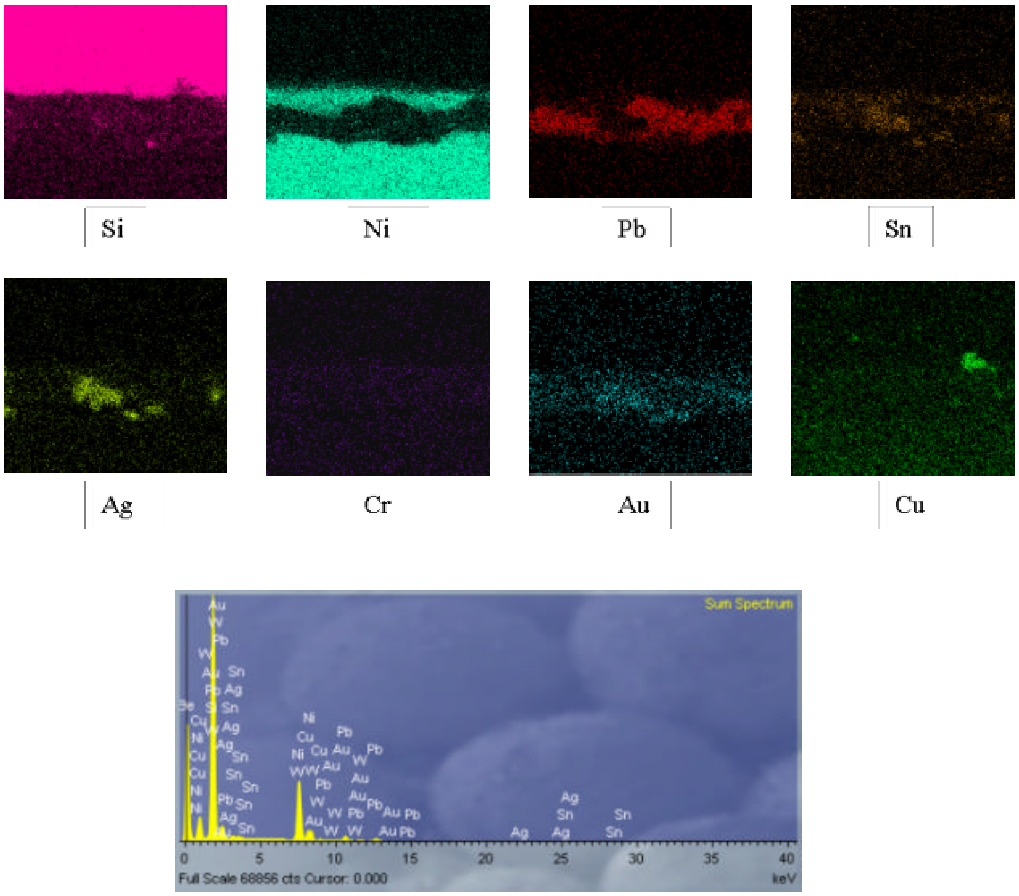

Figure 3.39: Area mapping shows different eleme nts

Microstructural analysis was also conducted. Weertman's creep model used to develop the constitutive relationship for 95.5Pb2Sn2.5Ag is based on a one phase creep model. Presence of a second tin phase would cause a shift in mechanism, but small amounts of Ag_3Sn would simply modify the climb mechanism. In order to validate the use of this model, the microstructure was examined using standard metallographic techniques and E-SEM. The polishing procedure used is explained in Appendix G. Figure 3.40 through Figure 3.43 show the microstructure as it is cooled from 150°C to 0°C. The micrographs do not reveal a second phase microstructure. Lot of Si particles are embedded during

polishing on silicon carbide grit papers since the solder is very soft. The presence of silicon and dissolution of tin and silver is confirmed by area mapping using E-SEM shown in Figure 3.44.

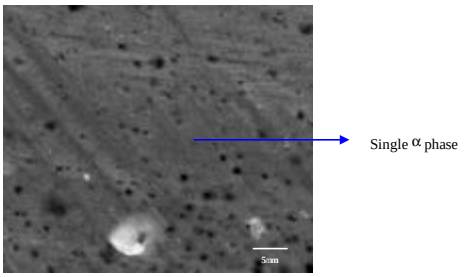

Figure 3.40: At 150°C and 500X

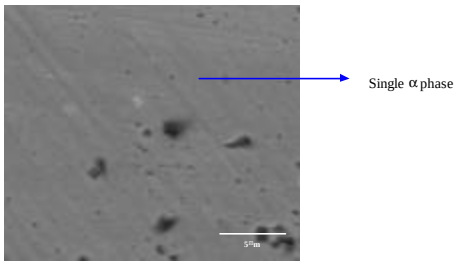

Figure 3.41: At 25°C and 1000X

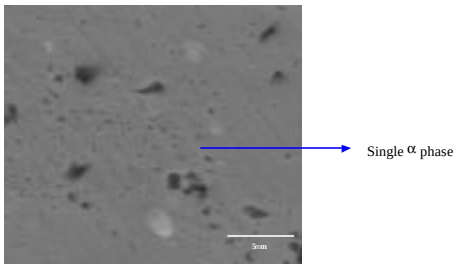

Figure 3.42: At 10°C and 1000X

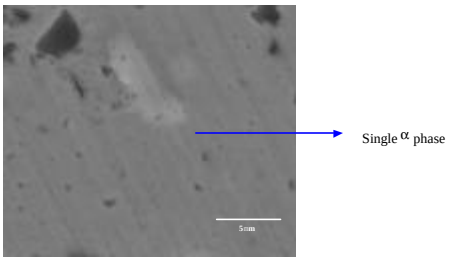

Figure 3.43: At 0°C and 1000X

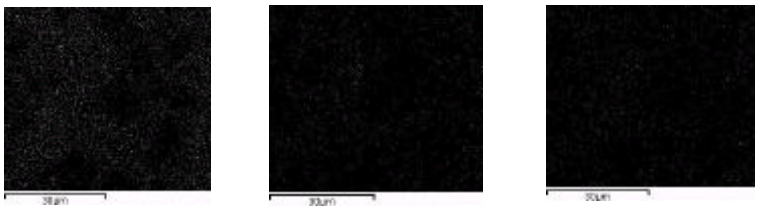

Pb Ag Sn

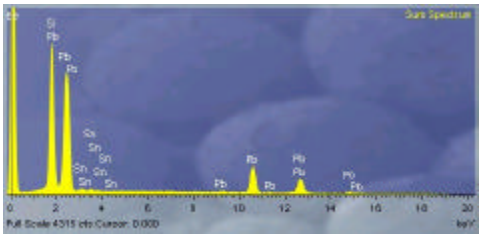

Figure 3.44: Spot mapping of the microstructure shows a lot of silicon particles

Microstructure observation proves the validity of the power law used to establish the constitutive properties of 95.5Pb2Sn2.5Ag high temperature solder. A bit more literature review strengthens the validation further. Work done by Akira Goto *et.al*. [80] on pure lead properties and the creep behavior study by El-Daly *et.al*. [82] along with the this dissertation work have shown that the activation energy based on power law decreases with increasing tin content. Figure 3.45 shows the profile of activation energy. It has been concluded from the plots that the activation energy starts decreasing with tin content with

a slight increase for the 95.5Pb2Sn2.5Ag solder due to the Ag_3Sn intermetallics being formed. As established by Weertman, that dislocation climb controls the creep of pure metals and dilute alloys, with addition of 2.5% silver by weight the activation energy would increase due to intermetallic formation which pins the grain boundary and act as obstacle to dislocation climbing. As the microstructure becomes two phase with the addition of more tin, the creep mechanism changes altogether with different microcreep mechanism playing a role and controlling the creep rate.

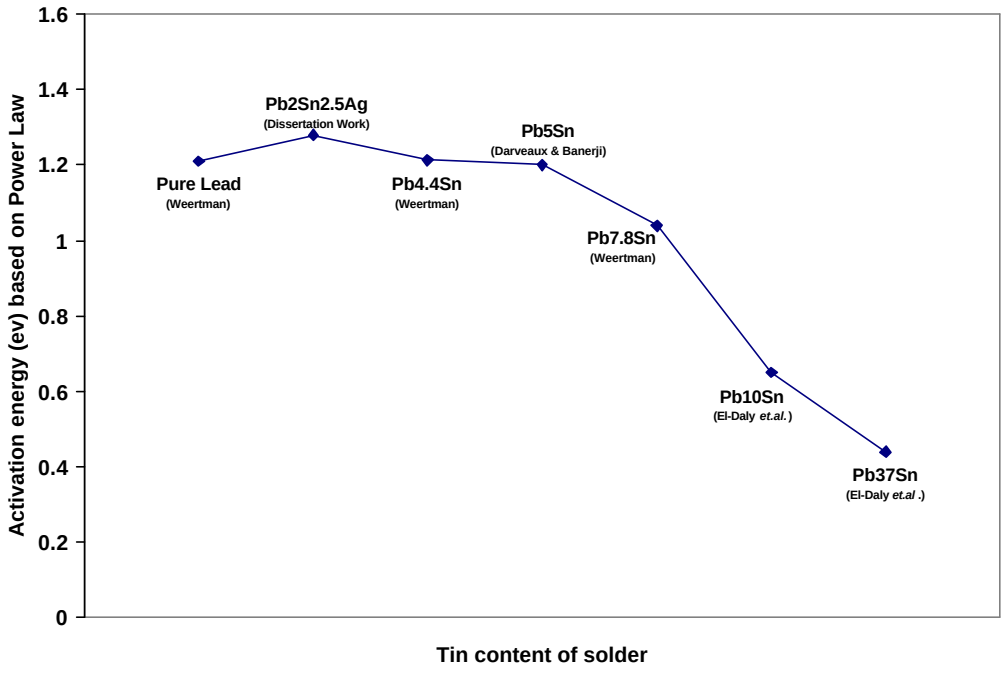

Figure 3.45: Change in activation energy (ev) with tin content

4 Thermo-mechanical Modeling

4.1 Non-Linear Structural Analysis

One of the main objectives of this thesis is to develop a generic thermo-mechanical durability model for 95.5Pb2Sn2.5Ag high temperature solder. Once the model is developed and correlated, it can be used to optimize the design of an assembly or component, and to predict field durability based on accelerated test results. It also reduces experimental costs and product development cycle time as fast and less expensive analytical approaches can be used and far fewer experiments need to be conducted during product design and development.

Figure 4.1 shows the whole approach employed in this study. In order to model the complex viscoplastic behavior of solder materials under thermal cycle loading, constitutive properties are needed as inputs in stress and damage analysis (box 1). Then a general purpose commercial FEA code (ANSYS 7.1 in this study) is used to build up different package geometries and to simulate the thermal cycling tests under investigation (box 2). As shown in box 3, the FE simulations provide stress-strain time history, thus identifying the potential failure site based on maximum accumulated damage. Major outputs of this step are partitioned plastic and creep work densities which are needed to estimate damage based on models such as the E-P durability model [71] of solders. In this study, this scheme is used in an inverse manner to estimate the model constants for the E-P model, for high lead solders. Combining partitioned work densities and cycles-to-failure data from thermal cycling tests, the E-P durability model for solders can be obtained (box 4).

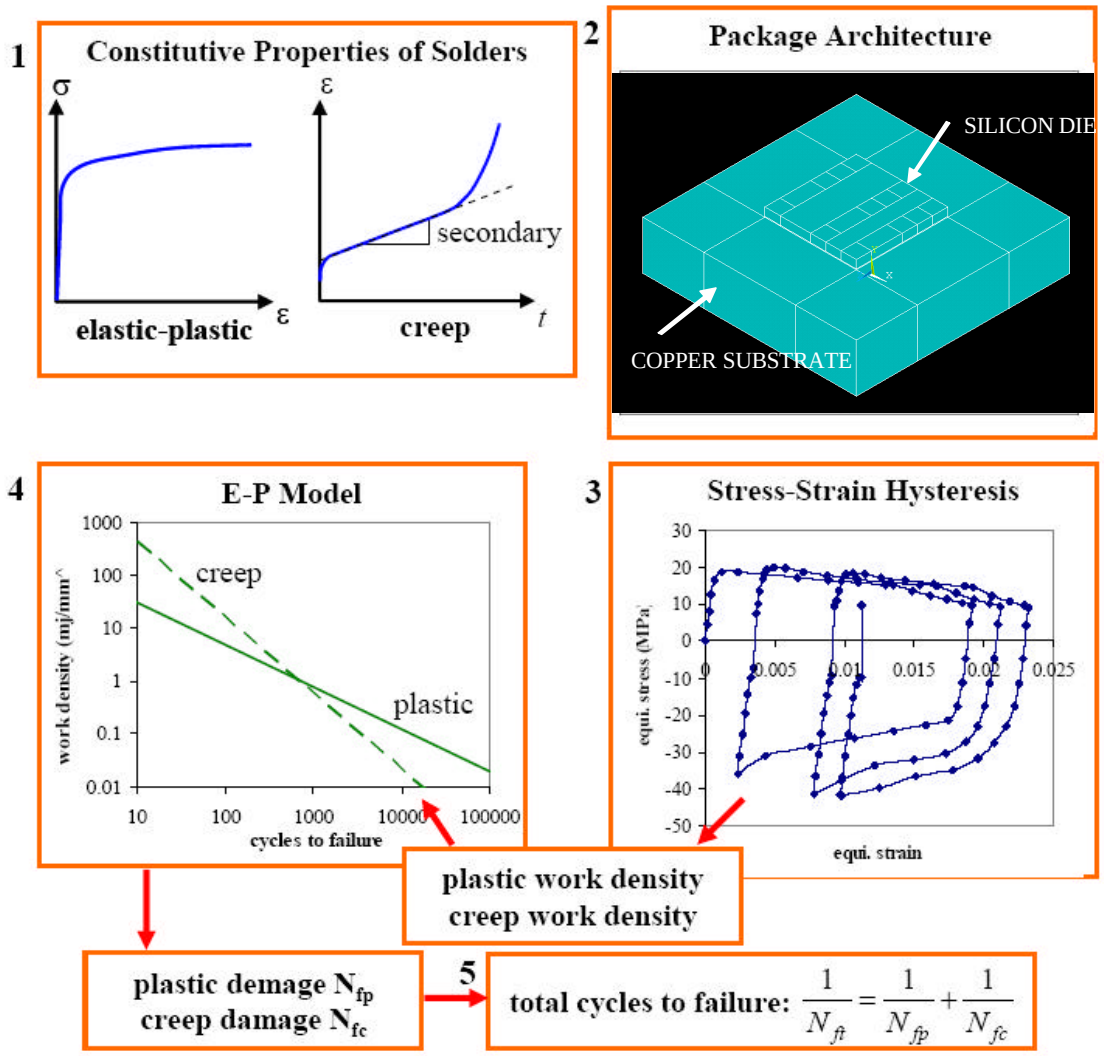

Figure 4.1: Overall approach for thermo-mechanical durability analysis

Implementation of the above approach to large area die attach assemblies of high temperature solders is now presented. First, two-dimensional finite element modeling and stress analysis of two thermal cycling tests for 95.5Pb2Sn2.5Ag solder is presented. Second, based on damage analysis and thermal cycling test results, the thermo-mechanical durability models (E-P model) for high lead solders, i.e., 95.5Pb2Sn2.5Ag are

presented. At the end, the obtained durability model is validated by using a different package assembly.

4.1.1 Finite Element Modeling and Stress Analysis

In order to obtain the E-P damage model, thermal cycling test data from at least four different combinations of component types and thermal profiles are needed (due to four independent E-P model constants). Dummy die bonded to copper substrate packages with different die attach size have been employed in the tests and the corresponding FE models have been developed. Copper has been chosen as the substrate because it has a very large CTE that helps to reduce the testing time. The copper substrate thickness is 3.2 mm and 4 mm clearance is given on all sides. Different thermal profiles have been used so that the effect of the thermal profile can be addressed in the obtained durability models. All five combinations of component type and thermal profiles are summarized in Table 4.1 and in Figure 4.2. It is seen that there are two types of packages of die sizes, 6×6 mm^2 and 20×20 mm^2 that are subjected to one thermal cycle with a temperature range varying from -10°C to 100°C (mean temperature of 55°C), a ramp rate of 5°C/min, a cooling rate of 8.46°C/min, a high temperature dwell time of 20 min. and a low temperature dwell time of 5 min. Two other types of packages of die sizes 6×6, 12×20 mm^2 have been subjected to a different thermal cycle loading with temperature range varying from 0°C to 165°C (mean temperature of 82.5°C), a ramp up rate of 5°C/min, a cooling rate of 8.25°C/min, a high temperature dwell time of 20 min. and a low temperature dwell time of 5 min. The package with 12×12 mm^2 dummy die and 100 μm

bondline thickness is also subjected to thermal cycling from 0 to 165°C for validation of the thermo-mechanical durability modeling as it is a different package.

Table 4.1: Summary of temperature profiles

Profile	Package (die attach mm×mm) Cu substrate	Temp. Range	Ramp rate (°C/min) (Heat/Cool)	Dwell (min) Hot/Cold
TC1	6×6	0 to 165°C	6.36/8.25	20/5
TC1	12×12 (50 µm)	0 to 165°C	6.36/8.25	20/5
TC1	12×12 (100 µm)	0 to 165°C	6.36/8.25	20/5
TC2	6×6	-10 to 100°C	5 / 8.46	20/5
TC2	20×20	-10 to 100°C	5 / 8.46	20/5

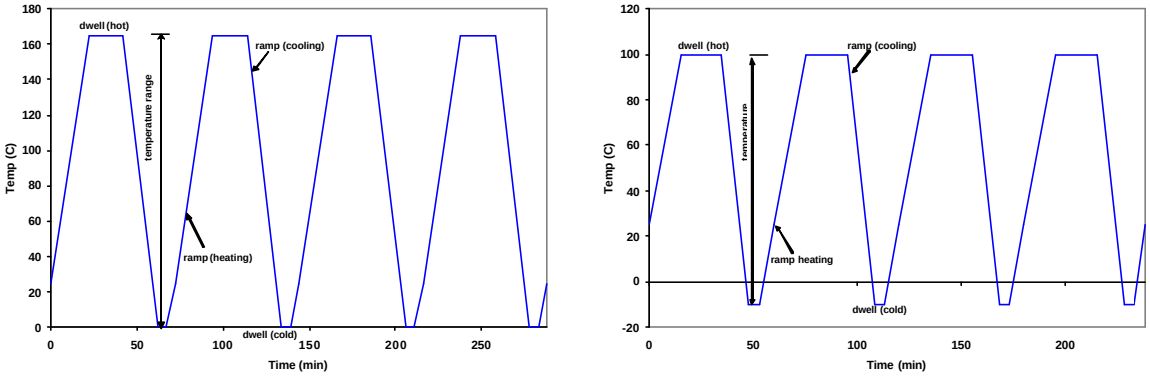

Figure 4.2: Schematic of thermal profile for (a) 0 to 165 °C (b) –10 to 100 °C

Nonlinear finite element analysis is conducted with ANSYS 7.1. Two dimensional plain strain models in the diagonal direction are built up for all the packages in the FE analysis due to the symmetry in geometry. The FE model of 6×6 mm^2 dummy die package is shown in Figure 4.3. Plane 182 elements are used in all FE models. The displacement

boundary conditions are: 1) all nodes on the bottom of copper substrate surface (y=0) are fixed in the y-direction, and 2) symmetric boundary conditions are applied in the surface at x=0 as shown in Figure 4.3. Mesh density sensitivity is studied on the FE model before final analysis is performed. The equivalent creep strain range per cycle is used to evaluate the mesh density sensitivity. The equivalent creep strain range per cycle is the average value of several elements, which enclose ten percent area of the die attach along the diagonal from center to edge of die attach. As shown in Figure 4.4, average equivalent creep strain range per cycle changes as the number of elements increases from 140 to 390 but is stable after 390. Thus the corresponding mesh density for 390 elements is used for the critical die attach for all FE models. Fine meshing is employed for the die attach in the critical crack initiation region located at outer corner along the diagonal. The rest of the components are meshed with far fewer elements in order to reduce the computation time. The total number of elements ranges from 120,000 to 160,000. Parametric modeling is used in the analysis and ANSYS input programs written in APDL (ANSYS Parametric Design Language) are listed in Appendix F for 0 to 165°C thermal profile.

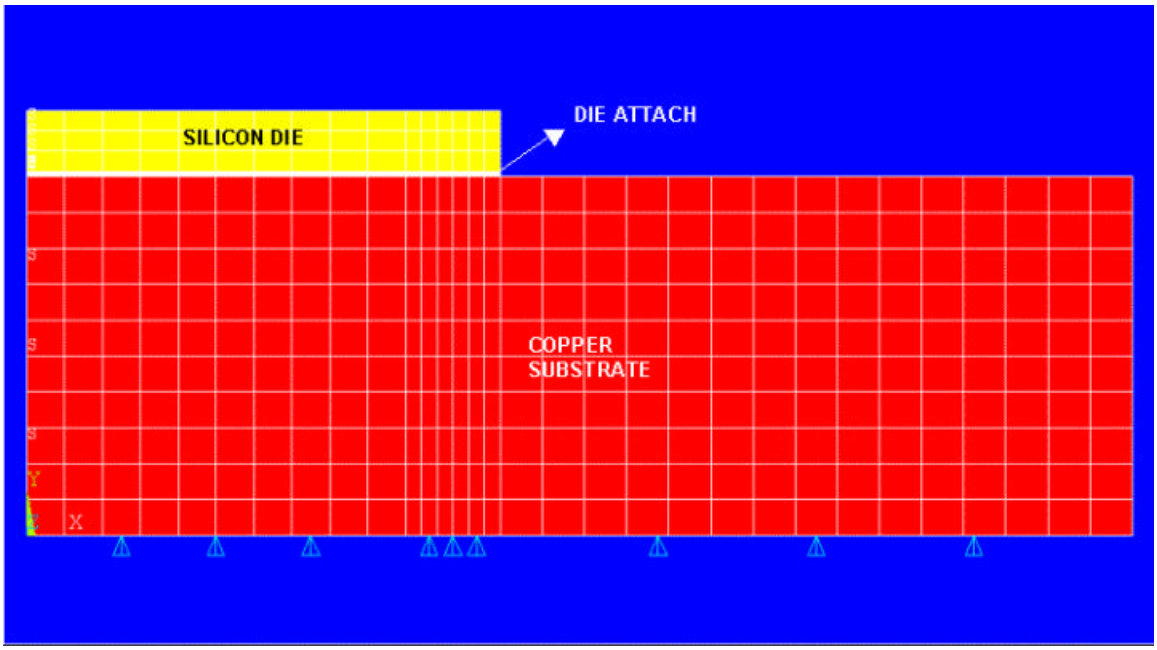

Figure 4.3: Finite element model showing boundary conditions

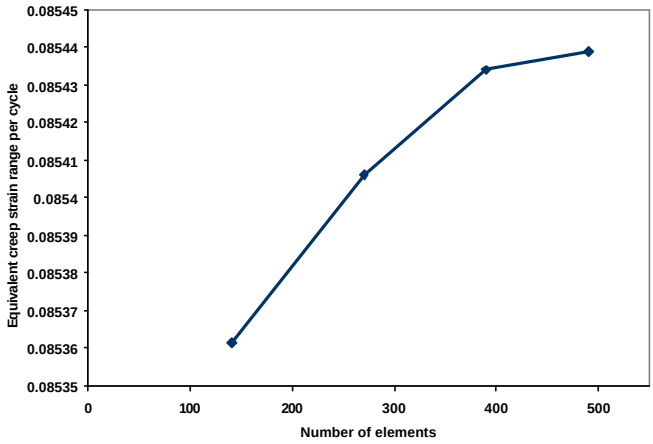

Figure 4.4: Variation of equivalent creep strain range per cycle with mesh density

Temperature profiles shown in Table 4.1 are applied to the assemblies as input loading. In each simulation, four complete thermal cycles are simulated as the hysteresis gets to stabilization which typically occurs at the fourth cycle, as shown in Figure 4.5. Automatic

time stepping is used in the simulation which results in total number of substeps ranging from 520 to 600. The run time of the simulation varies from 12 to 16 hours.

All materials, except solder, are assumed to behave in a linear elastic manner. Their mechanical properties are shown in Table 4.2. All material properties are obtained from the manufacturer, Matweb or Curamik USA.

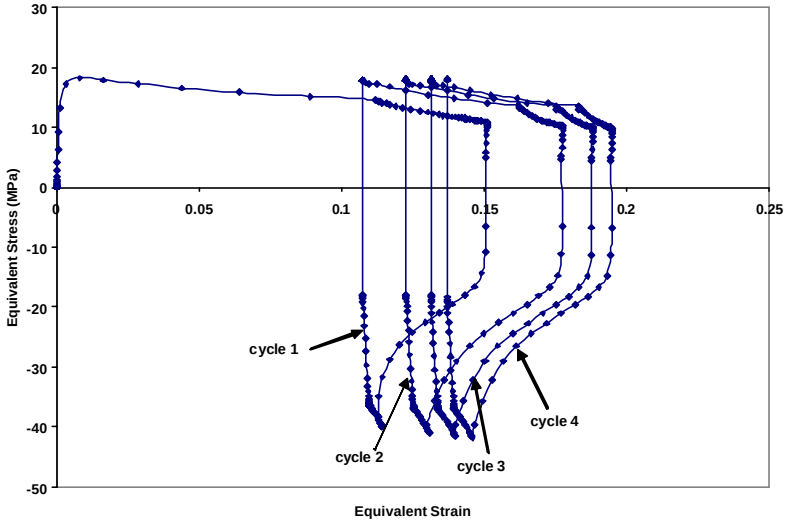

Figure 4.5: Equivalent stress-strain hysteresis loops for 30mm^2 die package subjected to thermal cycling

Table 4.2: Temperature-dependent elastic and plastic properties of the solder

Materials	Young's Modulus (Mpa)	CTE (ppm/°C)	Poisson's Ratio
Silicon die	1.95E05-12.7T(K)	0.0095T(K)-0.5	0.2782
Solder	30.448-0.0585T(K)	29E-06	0.4
Copper	120000	17E-06	0.34

The deformation of solder is much more complex and it deforms elastically, plastically, and viscoplastically under thermal cycling conditions. A partitioned constitutive law is employed in the FE analysis, as given in Equation 2.3. The partitioned temperature-dependent elastic, plastic and steady-state creep properties are used in order to be compatible with the E-P damage model for the 95.5Pb2Sn2.5Ag solder. The individual elastic, plastic and creep model constants have been presented in section 2.1 in terms of tensile strain and tensile stress. The time-independent plastic strain is as shown in Equation 2.6. The time-independent exponential hardening constant n_p and the pre-exponential co-efficient K used are as shown in Equation 2.12 and Equation 2.13 respectively. The steady-state creep strain rate is as described by Equation 2.7a. The temperature dependency relationships of creep exponent and stress exponent and thermal activation energy are as shown in Equations 2.15 and 2.16 respectively. Primary creep is ignored in this study.

4.1.2 FE Analysis Results and Discussion

FE analysis results of all thermal cycling tests shown in Table 4.1 are now presented. In order to obtain damage models of high lead solders, damage criteria (e.g. ISR, total work, or partitioned plastic and creep work) have to be assessed for all tests. It is assumed that the accumulated damage at the potential failure site of die attach is directly related to cycles-to-failure. So the potential failure site for each test case has to be identified. The contour plots at different time are checked for the critical area in order to identify the potential failure site, which has the average accumulated maximum energy density.

For 6×6 mm^2 die attach, the potential failure site is in the solder near the interface of substrate and solder along the outer edge of diagonal as shown in Figure 4.6. The total work density increases at the failure site as thermal cycling continues. At the end of fourth cycle the total work density contour is as shown in Figure 4.7. The effect of increase of die attach size for the same thermal cycling profile can be compared from Figure 4.7 and Figure 4.8. It shows that the total work density at the end of fourth thermal cycle increases with die size as does the area of the potential failure site which has the maximum work density. With an increase in temperature for the same die attach size and thickness, the total work density also increases at the end of fourth thermal cycle. This can be seen from Figure 4.7 and Figure 4.9. The plastic work can also be compared between die attaches of different thickness when subjected to the same thermal cycling. As seen in Figure 4.8 and Figure 4.11, the die attach with higher thickness has less plastic work after stabilization of hysteresis. Comparing Figure 4.12 and Figure 4.13 it can be clearly stated that the higher thickness die attach has lower shear stress in xy direction when measured at the onset of dwell at 165°C before it stress relaxes. The mesh density for this comparison has been kept the same. The crack would initiate at the site with maximum average work density predicted by FE analysis. It would also propagate in the band of high work density.

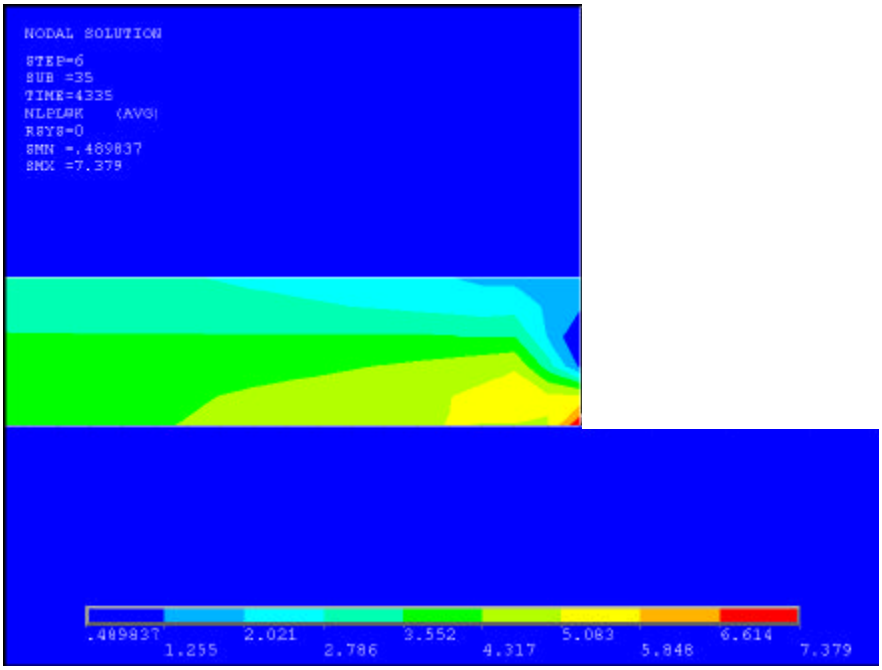

Figure 4.6: Thickness averaged work density contours of 6´6 mm^2 package at the end of first thermal cycle (0 to 165°C)

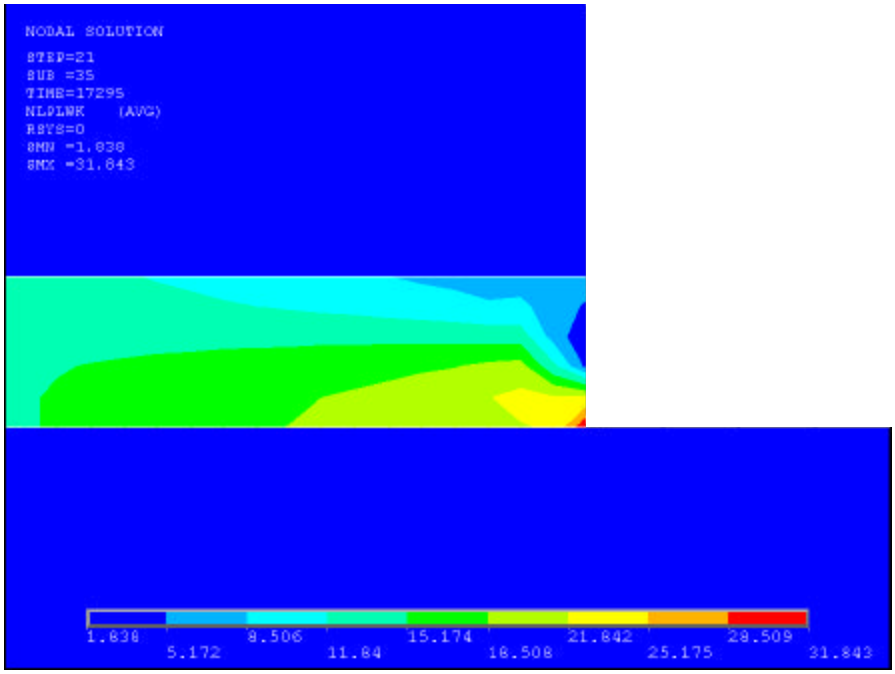

Figure 4.7: Thickness averaged work density contours of 6´6 mm^2 package at the end of fourth thermal cycle (0 to 165°C)

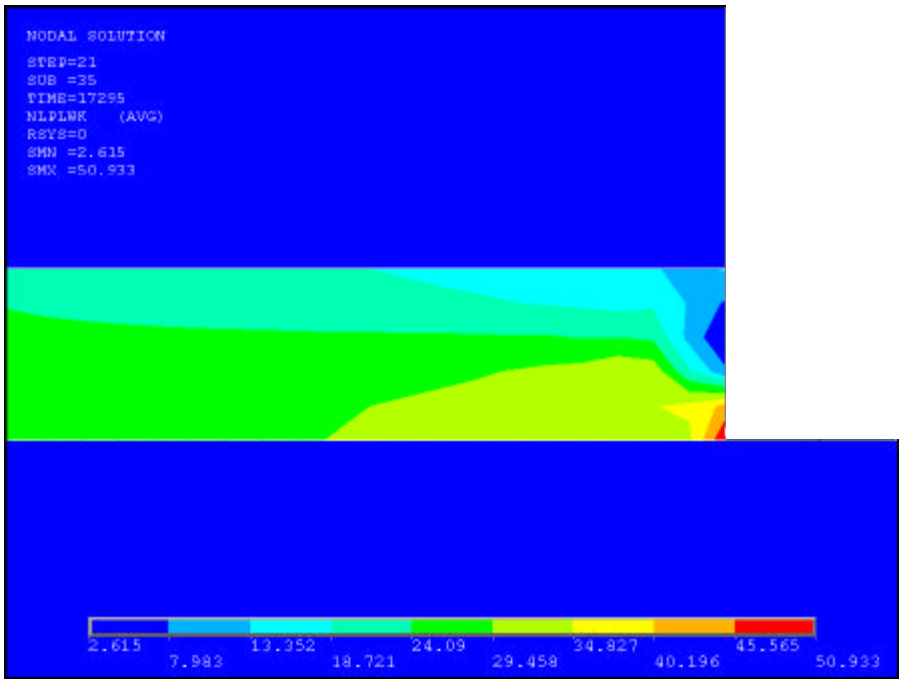

Figure 4.8: Thickness averaged work density contours of 12´12 mm^2 package with 2 mil bondline thickness at the end of fourth thermal cycle (0 to 165°C)

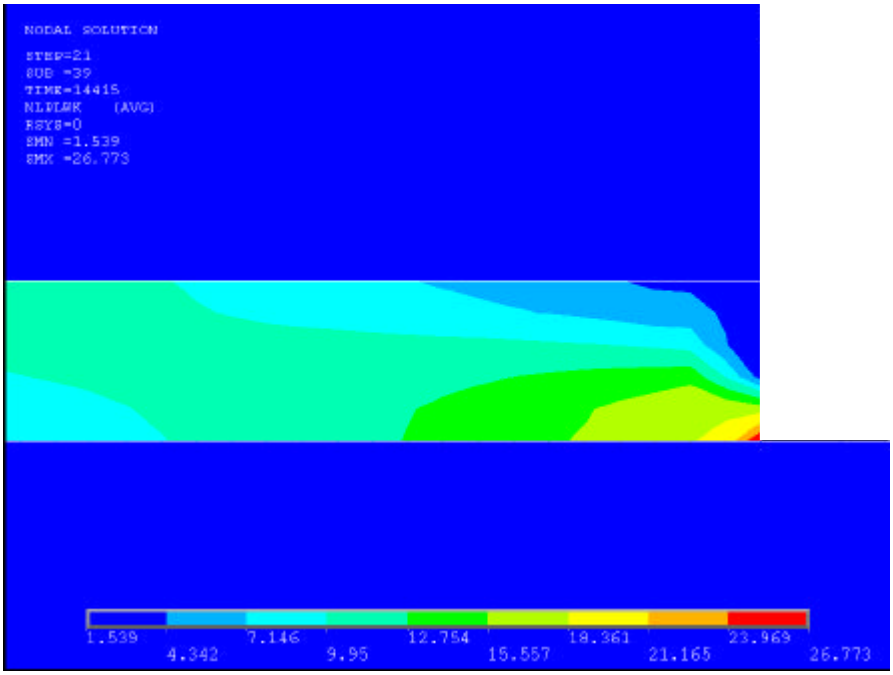

Figure 4.9: Thickness averaged work density contours of 6´6 mm^2 package at the end of fourth thermal cycle (-10 to 100°C)

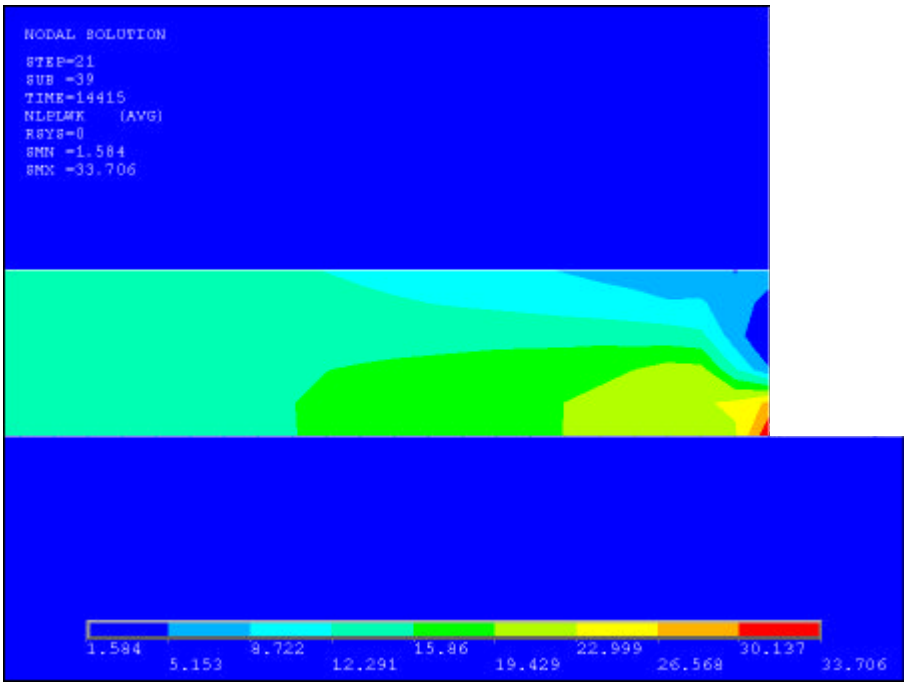

Figure 4.10: Thickness averaged work density contours of 20 ´ 20 mm^2 package at the end of fourth thermal cycle (-10 to 100°C)

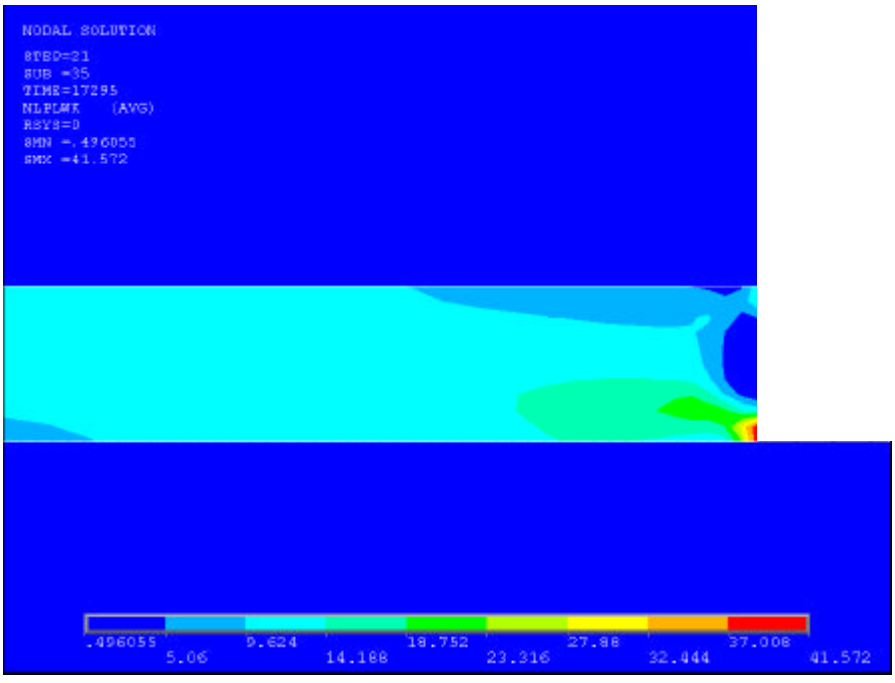

Figure 4.11: Thickness averaged work density contours of 12 ´ 12 mm^2 package with 100 mm bondline thickness at the end of fourth thermal cycle (0 to 165°C)

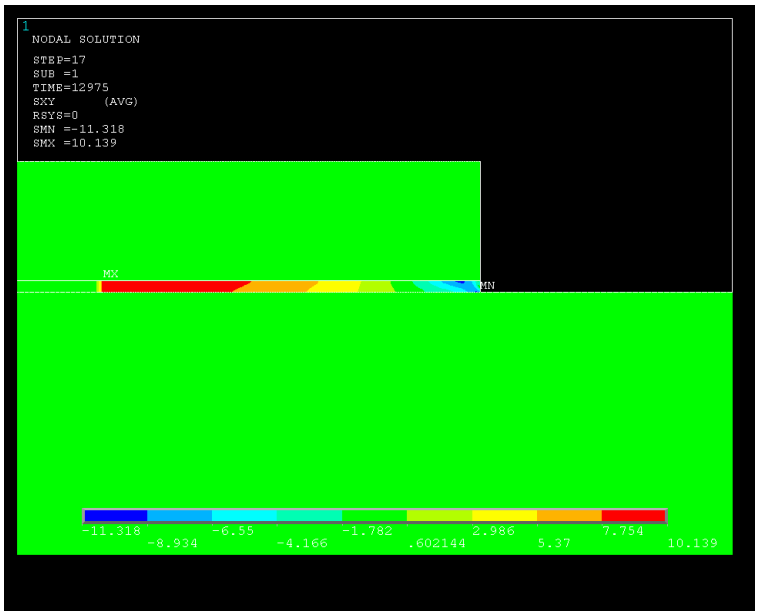

Figure 4.12: Thickness averaged shear stress contour in XY- direction for 12´12 mm^2 package with 50 μm bondline thickness at the onset of dwell at 165°C (0 to 165°C cycle)

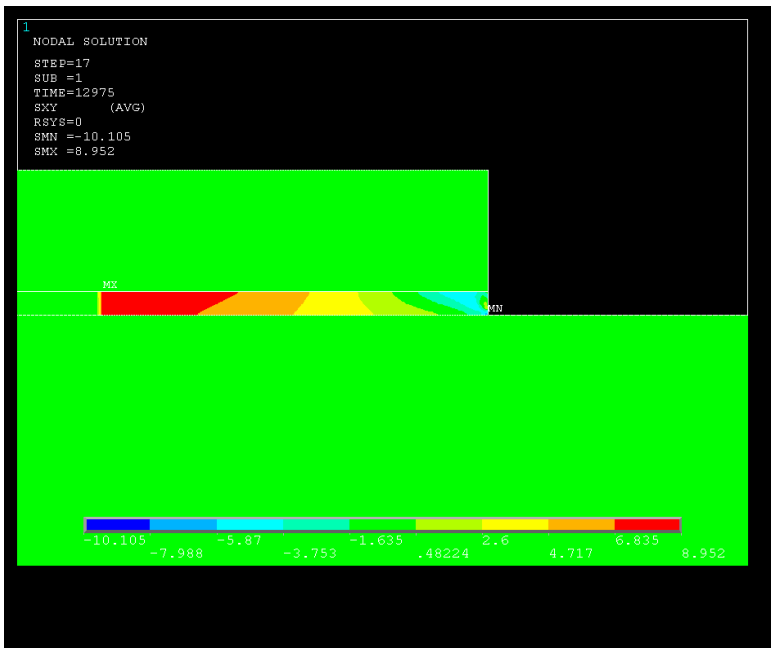

Figure 4.13: Thickness averaged shear stress contour in XY- direction for 12´12 mm^2 package with 100 μm bondline thickness at the onset of dwell at 165°C (0 to 165°C cycle)

The viscoplastic hysteretic response of 95.5Pb2Sn2.5Ag solder in 6×6 mm^2 package to two different thermal cycling profiles is compared for the fourth thermal cycle in Figure 4.14. The von Mises stress is plotted against the equivalent strain. The thermal profile segments are also shown in the figure. The sign of the von Mises stress is arbitrarily assigned to be positive for increasing temperature and negative for decreasing temperature. The two hysteresis loops are different due to different temperature extremes used. There is a larger increase in von Mises stress for the package subjected to 165°C than the one ramped to 100°C. During ramp up to dwell period, the increase in the equivalent strain is larger in the profile ramped to 165°C than that to 100°C. The difference in the two loops results in different accumulated damage for the two thermal profiles such as inelastic strain range (ISR) and total work density (? W). It is also noted that ramping up and down periods have larger effects on the strain range than dwell periods. This conclusion is dependent on the ramp rates used in this study.

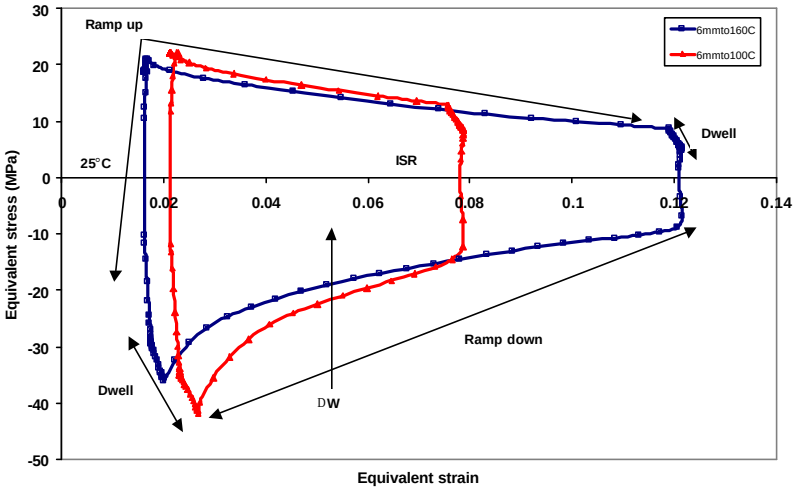

Figure 4.14: Comparison of hysteresis loops during fourth cycle for 6 ´ 6 mm^2 die attach for -10 to 100°C and 0 to 165°C thermal profile

Figure 4.15 and Figure 4.16 shows that for the lead rich 95.5Pb2Sn2.5Ag solder, the creep strain contributes the maximum to the total strain. As dwell temperature increases for the same time period the percentage contribution of creep increases to the total strain. From Figure 4.16 and Figure 4.17 it can be seen that with increase in size for the same thermal profile, the total equivalent strain increases. For higher bondline thickness the equivalent strain range is less than for smaller bondline thickness. Also the equivalent stress range is larger for thinner bondline as the total stress per thickness is higher.

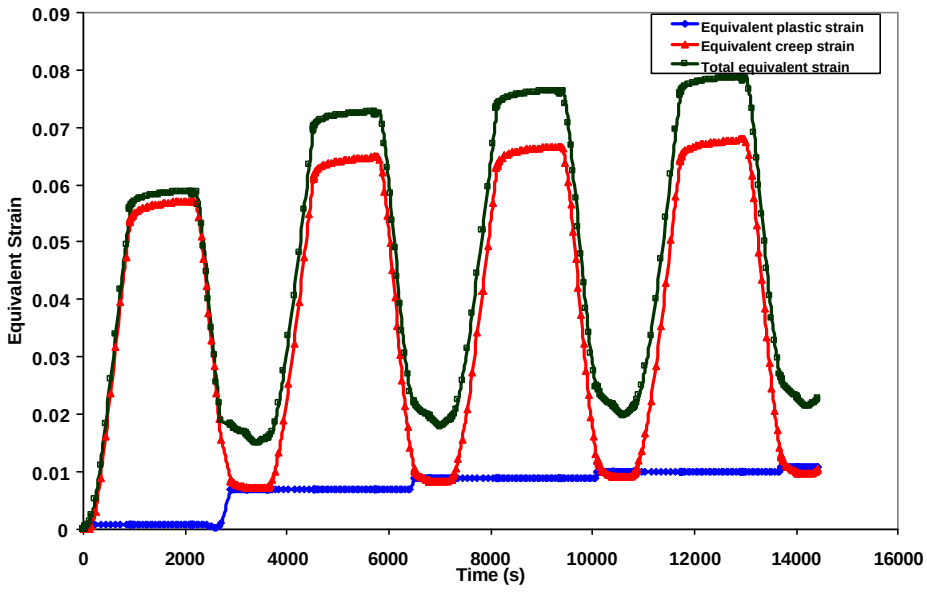

Figure 4.15: Equivalent strain vs. Time for 6´6 mm^2 package for -10 to 100°C thermal profile

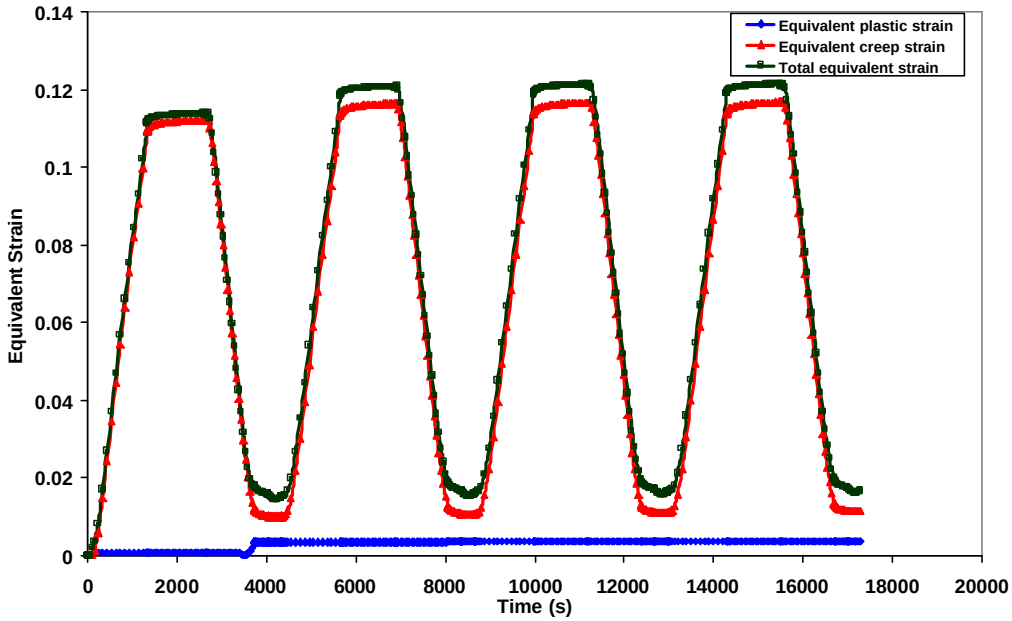

Figure 4.16: Equivalent strain vs. Time for 6´6 mm^2 package for 0 to 165°C thermal profile

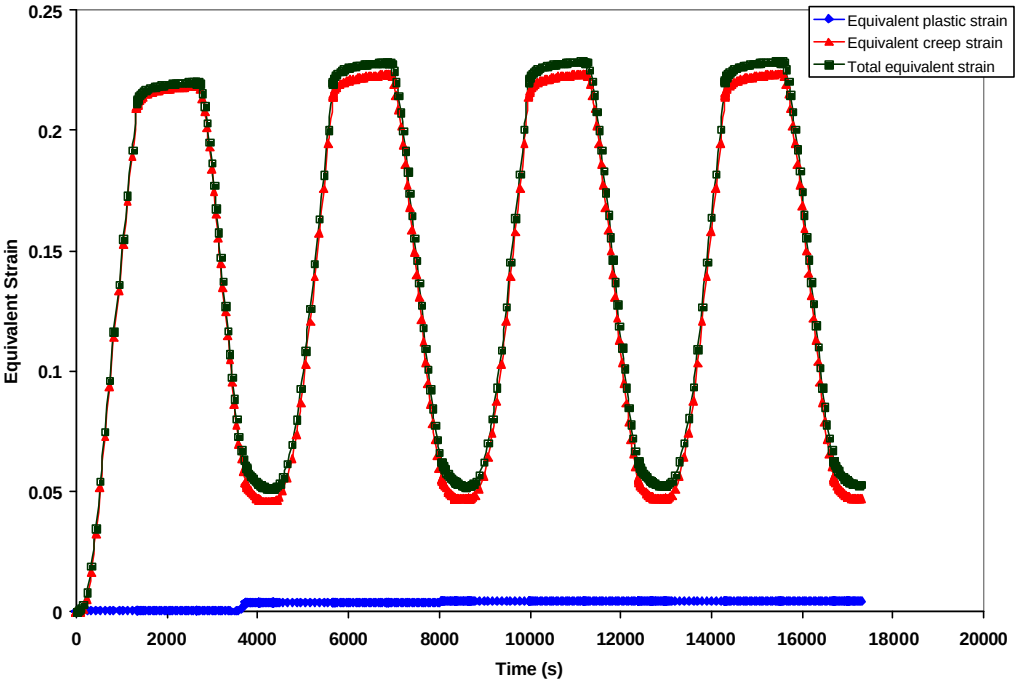

Figure 4.17: Equivalent strain vs. Time for 12´12 mm^2 package with 50 μm bondline thickness for 0 to 165°C thermal profile

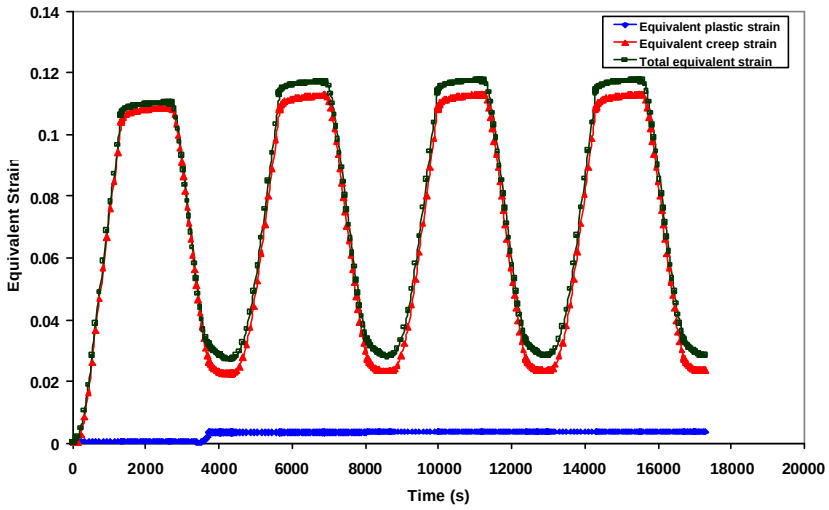

Figure 4.18: Equivalent strain vs. Time for 12 ´ 12 mm^2 package with 100 μm bondline thickness for 0 to 165°C thermal profile

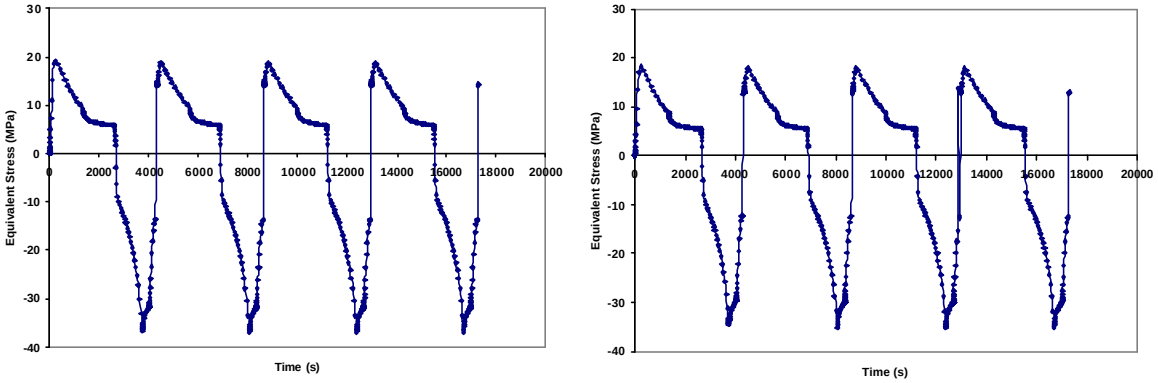

Figure 4.19: Equivalent stress-time plot for (a) 50 μm (b) 100 μm bondline thickness

Figure 4.20 shows the effect of increasing die size on the hysteresis loop for the same thermal profile. It is clearly noticed that as die size increases the inelastic strain range (ISR) and total work density also increase. The same observation holds true for the –10 to 100°C thermal profile as seen in Figure 4.21. Figure 4.22 shows that for 50 μm bondline

thickness the total work density is larger than for 100 μm bondline for same die size and thermal cycling profile.

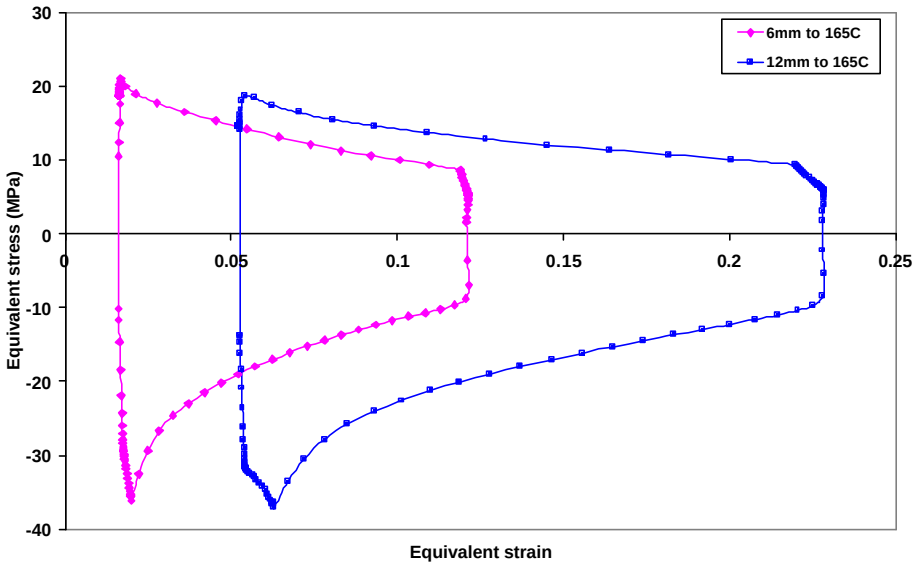

Figure 4.20: Effect of die size on hysteresis loop for 0 to 165°C thermal profile

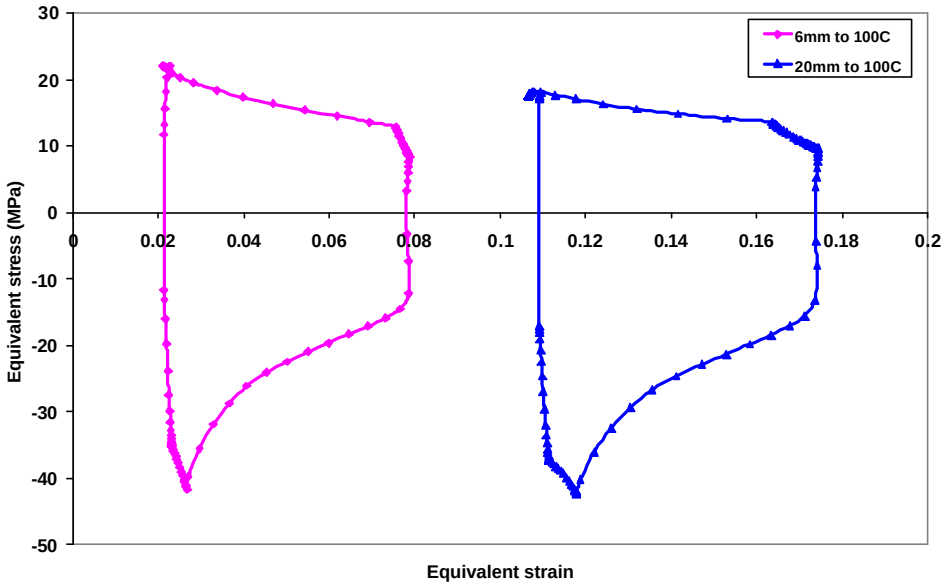

Figure 4.21: Effect of die size on hysteresis loop for -10 to 100°C thermal profile

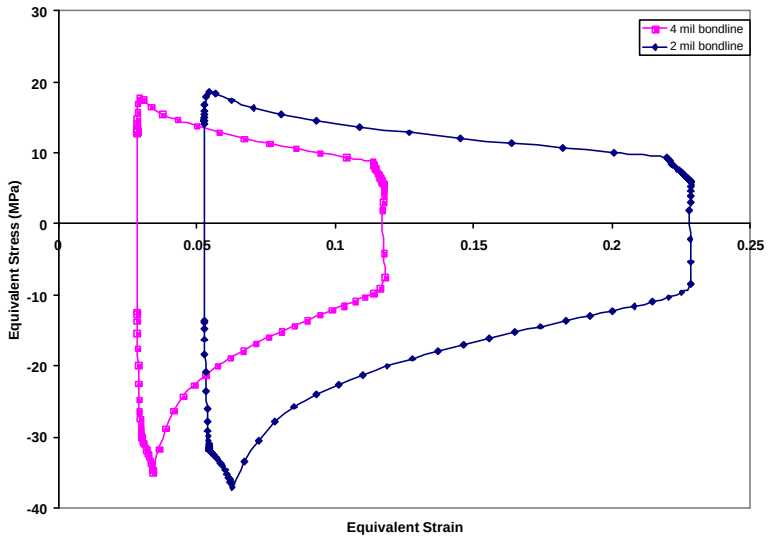

Figure 4.22: Effect of bondline thickness on hysteresis loop for 0 to 165°C thermal profile

4.1.3 Thermo-mechanical Durability Model

Partitioned plastic and creep deformation histories can be obtained from finite element analyses of thermal cycling tests. Consequently, plastic (W_p) and creep (W_c) work densities are partitioned from total work density. Based on thermal cycling life and partitioned plastic and creep work densities, the model constants are obtained for the Energy-Partitioning (E-P) durability model as expressed in the following equations:

$$\text{Total Energy} = W_p + W_c = W_{p0} N_{fp}^{c} + W_{c0} N_{fc}^{d} \tag{4.1}$$

$$\frac{1}{N_f} = \frac{1}{N_{fp}} + \frac{1}{N_{fc}} \tag{4.2}$$

where W_{p0}, W_{c0} represent the intercepts of the plastic and creep energy density plots vs. cycles-to-failure, respectively, on a log-log scale; while the exponents c and d are their corresponding slopes. The variables N_{fp} and N_{fc} represent the cycles-to-failure due to

plastic and creep damage, respectively. The total number of cycles-to-failure N_f is then calculated from Equation 4.2. Elastic terms in Equations (4.1) and (4.2) are ignored in this study because elastic energy has an insignificant effect on the thermo-mechanical durability of solders.

Table 4.3 shows the ratio of plastic work to creep work for all the thermal profiles. It suggests that plastic damage has an important effect on the thermo-mechanical durability of lead rich solders, and hence, ΔW_P should be included in the durability model of lead rich solders. In addition, lower temperature range tests (-10 to 100°C) have a higher ratio of ΔW_P to ΔW_C than higher temperature range tests of 0 to 165°C as the creep deformation in less in these tests.

Table 4.3: Comparison of the ratio ?Wpl/?Wcr for different thermal profiles

Profile	Package (mm×mm) Cu substrate	Temp. Range	Ramp rate (°C/min) (Heat/Cool)	Dwell (min) Hot/Cold	$\Delta W_P/\Delta W_C$ 4th Cycle	$\Delta W_P + \Delta W_C$ (mJ/mm^3)
TC1	6×6	0 to 165°C	6.36/8.25	20/5	1.016	4729.3+4651.7=9381.1
TC1	12×12 (50 μm)	0 to 165°C	6.36/8.25	20/5	1.011	2994.4+2906.2=5900.6
TC1	12×12 (100 μm)	0 to 165°C	6.36/8.25	20/5	1.018	3816.9+3748.8=7565.8
TC2	6×6	-10 to 100°C	5 / 8.46	20/5	1.059	17011.3+16011.1=33022.5
TC2	20×20	-10 to 100°C	5 / 8.46	20/5	1.049	4247.6+4048.4=8296.1

Table 4.4 shows the obtained E-P model constants for 95.5Pb2Sn2.5Ag solder. The thermo-mechanical durability of the solder can be predicted by substituting these model constants into Equation 4.1 and 4.2. The constants have been derived by a least square

optimization method by using the 'fminsearch' function, found in the optimization toolbox, in Matlab. However, the energy minimization could also be performed iteratively using the Levenberg-Marquardt algorithm which also calculates the jacobian matrix. As the iterative method did not converge well, least square optimization method was used.

Table 4.4: Thermo-mechanical Energy Partitioning model constants for 95.5Pb2Sn2.5Ag solder

Model constants	95.5Pb2Sn2.5Ag
c	0.34
W_{p0}	1.40
d	-4.69
W_{c0}	1.17E-8

Separate plastic energy density vs. cycles-to-failure due to plastic damage plot and creep energy density vs. cycles-to-failure due to creep damage plot are shown in Figure 4.31 for 95.5Pb2Sn2.5Ag solder for the package used for validation. The important observation from the plot is that for most of the applied condition creep damage is dominant.

Once the constants are calculated, they need to be validated. The package 12×12 mm^2 has been used for validation study. The constants and work density values of 12×12 mm^2 package upon substituting in the E-P equations, predicts the cycles to failure which is very close to that found during thermal cycling (Weibull Analysis). This validates our Energy Partitioning constants. Figure 4.24 shows the comparison study of cycles to failure for all the package types. It can be concluded from the figure that the E-P constants can be used for any package which uses the 95.5Pb2Sn2.5Ag solder as die attach.

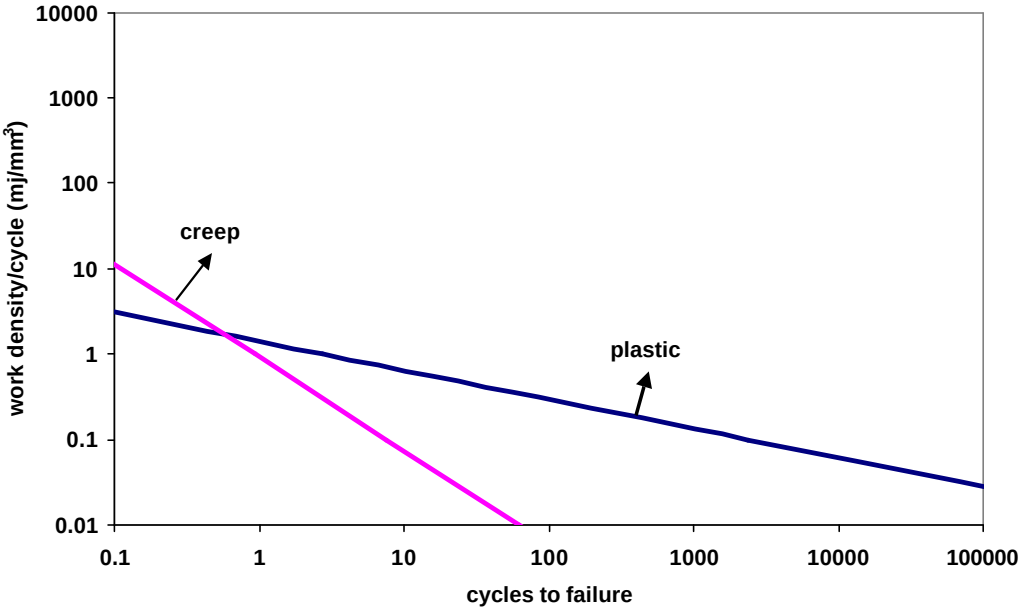

Figure 4.23: Energy-Partitioning model for 95.5Pb2Sn2.5Ag solder

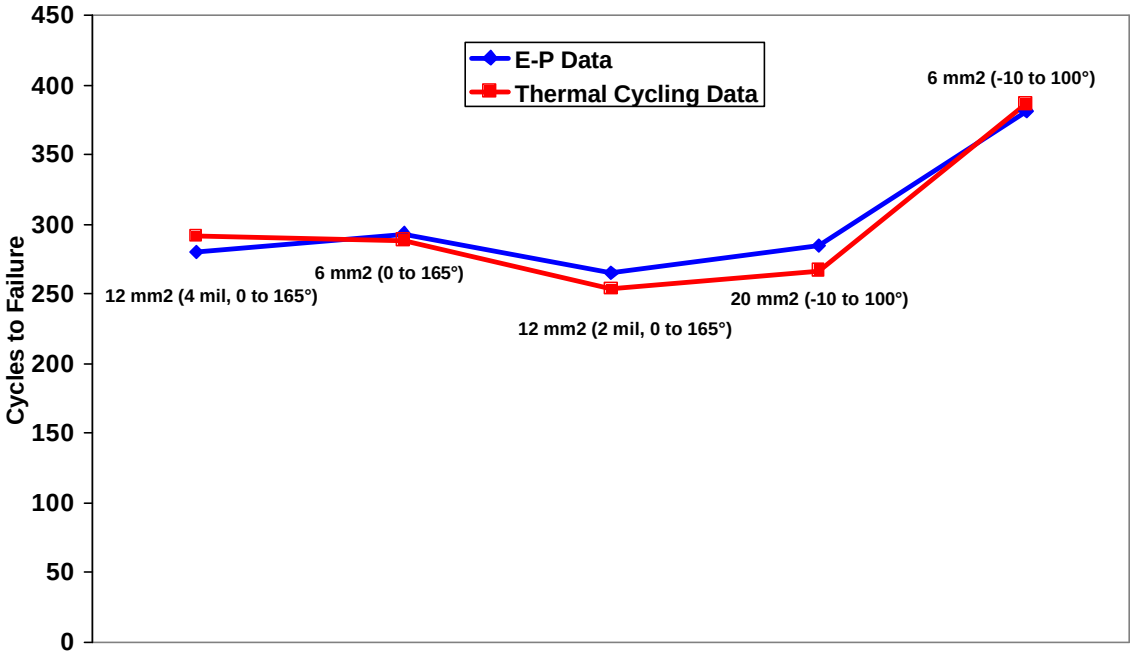

Figure 4.24: Validation of Energy Partitioning Constants

5 Summary, Contributions and Suggestions for Future Work

Although in general, the use of lead in electronics interconnection will be banned globally in the near future, certain alloys are exempted due to the lack of an alternative. This is particularly true of solders for the high temperature application environment. 95.5Pb2Sn2.5Ag is one such solder whose study has been undertaken due to the need in power electronic industry for constitutive properties and thermo-mechanical durability assessment. The study will act as a benchmark to the Pb-free alternative as Pb-free solders for high temperature environment are developed in the future. The results of this study will be crucial for virtual qualification of multichip and power modules during design and development of electronics for harsh environments that contain combined thermal and mechanical loading.

5.1 Summary of Results

A partitioned constitutive model consisting of elastic, plastic and creep terms is presented for the 95.5Pb2Sn2.5Ag solder as derived from isothermal monotonic tests conducted in strain control mode. Constitutive property measurements are needed for quantitative characterization of damage accumulation, the knowledge of which is essential for accurate durability assessment. The direct local strain measurement technique (DLMT) was implemented for constitutive property measurement using the MTS Tytron^{TM} 250 Tester. A miniature modified Iosipescu single-lap, micro-shear specimen has been customized and used for simulating geometrical and loading constraints present in a large area die attach used in power packaging. The specimen preparation procedure has been

improved to obtain optimum solder joint quality before commencement of testing to enhance repeatability of test data.

Microstructural observation of the solder at different temperatures simulating the test and application environments is performed. The observed microstructure validates the assumption used to develop the constitutive relationship presented.

A complete design and fabrication of the test sample packages was carried. Two different die bonding methods: one using an inert atmosphere and the other using vacuum reflow technique, have been employed and their merits and demerits have been discussed from the package quality and reliability perspective. The effects of backside metallization of die, substrate electroplating and reflow temperature have also been addressed.

The thermo-mechanical durability of the 95.5Pb2Sn2.5Ag solder is investigated by a systematic approach combining thermal cycling tests and finite element modeling. Thermal cycle testing, failure analysis, microstructure characterization, and thermo-mechanical analysis were conducted. Thermal cycling results revealed that the 6×6 mm^2 size die attach outperforms the bigger die attach systems under the studied accelerated test condition. Failure analysis and microstructure characterization revealed the failure mechanisms and important factors influencing the die attach cracking. Two-dimensional viscoplastic finite element analysis was conducted for four different package architectures and two different thermal cycling tests. For the lead rich 95.5Pb2Sn2.5Ag solder, the creep strain contributes most to the total strain. As dwell temperature increases

for the same hold time the percentage contribution of creep to the total strain increases. As die attach size increases the inelastic strain range (ISR) and total work density also increases. Also equivalent stress range increases with increasing die attach size. The total work density for a thicker solder is less than a thinner one for the same die attach size. Based on the damage analysis and thermal cycling test results, the thermo-mechanical durability model of the 95.5Pb2Sn2.5Ag solder is obtained.

5.2 Discussion of Results

95.5Pb2Sn2.5Ag solder with a melting point of 304°C is predominantly single α-phase with few Ag_3Sn intermetallics as seen in the microstructures. For single phase metals and alloys, the power law is an established relationship between steady-state strain-rate (or creep rate) and stress. The range of operation being -10 to 165°C (0.45 to 0.75 T_m) suggests the solder is far from power-law breakdown. Generally power-law breakdown occurs when temperatures decrease below 0.5 T_m in which case a hyperbolic sine (sinh) function is often used to describe the transition. Also a hyperbolic sine function is used to describe the creep behavior in case of two or three phase microstructures.

From microstructure observation and literature on work done in the past, a conclusion has been derived on the issue of phases present and how different alloying elements are contributing. In lead (Pb) - tin (Sn) binary eutectic system, the atomic size difference between Pb and Sn is less than 10%. Pb has an FCC crystal structure while Sn has tetragonal structure. This results in limited solid state solubility with the maximum solubility of Sn in the FCC Pb equal to 19.2 wt% Sn while only 2.5wt% of Pb is soluble

in the tetragonal Sn structure. The α-phase is the FCC Pb with some substitutional Sn atoms and the β- phase is tetragonal Sn with only a few substitutional Pb atoms. Silver in the alloy tends to form Ag_3Sn intermetallic because of the restricted solid solubility of Ag in Sn (0.1 wt.% and 0.02 wt.%). Ag_3Sn intermetallics are rod-like with a yield strength of 756 MPa and appear as isolated islands/particles. Because of their high strength the Ag_3Sn particles deform elastically during the tensile flow of the solder. Silver in the α-phase solid solution can contribute to solid-solution strengthening and Ag_3Sn precipitate makes the solder resistant to grain coarsening and dislocation climb thereby increasing the fatigue life. The gold flash coating used to protect nickel from oxidation is found to be dissolved uniformly in the solder.

5.3 Contributions of the Dissertation

The main contributions of this dissertation are the comprehensive experimental and numerical study of constitutive properties and thermo-mechanical durability of the high temperature solder alongwith its microstructural characterization and improved package design and fabrication methods. Some of the contributions are scientific and facilitate further academia research. There are also technical contributions made by this work which will facilitate the use of this high temperature solder in power packaging industry. They are as follows:

1. One of the scientific contribution of this dissertation is the validation of the assumptions used to derive the partitioned constitutive model for 95.5Pb2Sn2.5Ag solder. The model is based on constitutive equations that assume a one-phase microstructure as modified by a small amount of intermetallics. This is the type of

microstructure that was seen here and it is in accord with the phase diagram and previous studies. Furthermore, the activation energy for the creep portion of the model is in line with that found for similar alloys in previous work.

2. An important technical contribution is that the thesis compares two industry standard fabrication methods for 95.5Pb2Sn2.5Ag soldering and establishes that vacuum reflow produces packages, with fewer delaminations and voids. Cr/Ni/Au metallization with an optimum thickness on the backside of die and nickel electroplating on the copper substrate play a great role in wetting of the high lead solder and are superior to approaches involving Ti backside die metallization.
3. Another scientific contribution is that this is the first study to calibrate the energy partitioning constants for 95.5Pb2Sn2.5Ag solder. No high temperature solders have previously been calibrated in this way. The constants have been validated through the prediction of time to failure by 95.5Pb2Sn2.5Ag solder fatigue in other package architectures and by extensive failure analyses of test packages that verify that the failure mode is fatigue crack initiation and propagation in the solder die attach.
4. This study validates through failure analysis that the crack inititation takes place at the corner of die attach along the diagonal of the die as predicted by detailed two-dimensional viscoplastic finite element stress and damage analyses. This finding will always prove to be beneficial not only to the scientific community but also to the power packaging industry.

6 Appendices

Appendix A: Solder Reflow Profile

Table 6.1: Solder reflow profile

Line	Time (h:m:s)	Event	Temp (deg. C)	Pressure (PSI)	Comment
1	0:00:00	Beep	22	15	
2	0:00:01	Vac On	22	15	Evacuate chamber
3	0:02:00	Vac Off	22	0	
4	0:02:01	Gas2 On	22	0	Purge chamber
5	0:04:00	Gas2 Off	22	40	
6	0:04:05	Exhaust On	22	40	Vent
7	0:04:15	Exhaust Off	22	15	
8	0:04:18	Vac On	22	0	Start vacuum bake
9	0:04:20	Heat On	22	0	
10	0:06:00	280	280	0	Ramp to280 deg C in 1 min., 20 sec.
11	0:09:00	Gas1 On	280	40	End 5 min. vacuum bake, Start FG Bake
12	0:12:00	Gas1 Off	280	40	
13	0:12:01	Exhaust On	280	15	End 5 min. FG bake
14	0:12:05	Exhaust Off	280	15	
15	0:12:06	Vac On	280	0	Start reflow vacuum
16	0:16:00	280	280	0	End Pre-Reflow Bake
17	0:17:00	370	370	0	Ramp to 370 deg C in 60 sec.
18	0:18:00	370	370	0	Reflow at 370 deg C
19	0:18:01	Vac Off	370	0	End reflow vacuum
20	0:18:02	Gas 2 On	370	0	Start reflow FG/pressure
21	0:18:03	Heat Off	370	20	End reflow
22	0:20:00	Exhaust On	250	20	Start Cool-Down
23	0:20:02	Gas 3 On	245	15	Start Forced Cool-Down
24	0:24:00	Gas 2 Off	80	15	
25	0:24:01	Gas 3 Off	80	15	
26	0:24:02	Exhaust Off	80	15	
27	0:24:03	Beep	80	15	End of Cycle

Appendix B: X-Ray Laminography

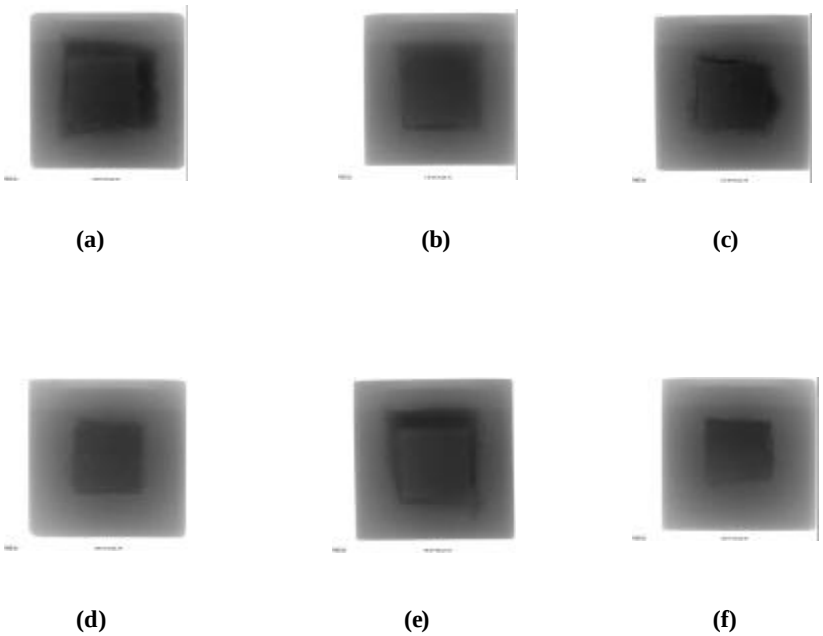

(a) (b) (c)

(d) (e) (f)

Figure 6.1: X-Ray report of 6 ´ 6 mm^2 package

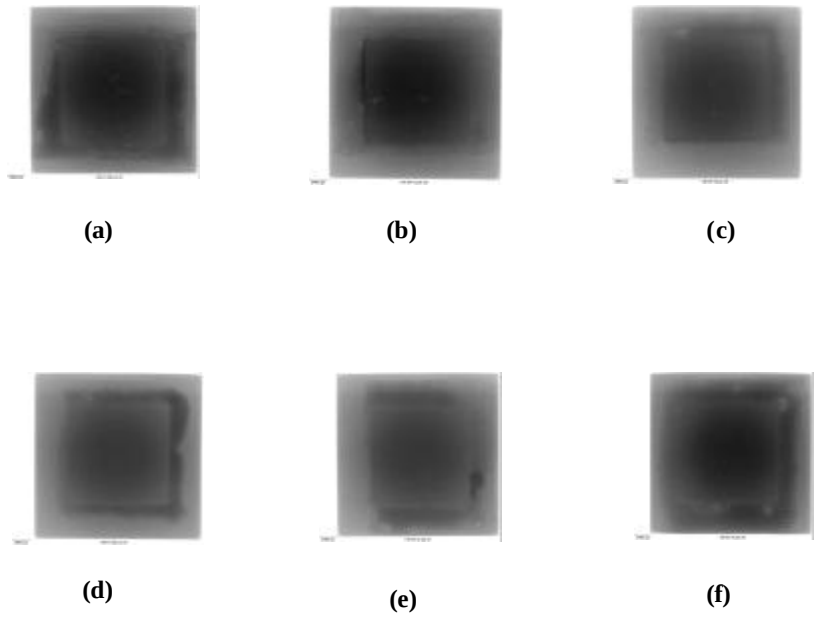

(a) (b) (c)

(d) (e) (f)

Figure 6.2: X-Ray report of 12 ´ 12 mm^2 package

Appendix C: C-SAM Results

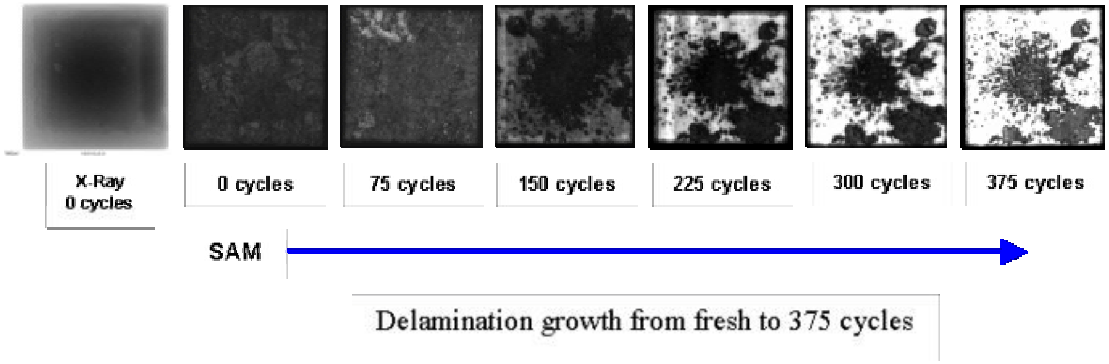

Figure 6.3: SAM showing delamination (white areas) growth during –10 to 100°C cycle in 20 mm^2 package

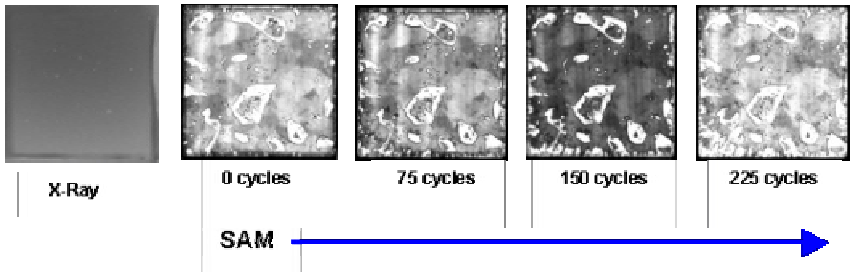

Figure 6.4: SAM showing survival of a 12 mm^2 package with 100 μm bondline thickness

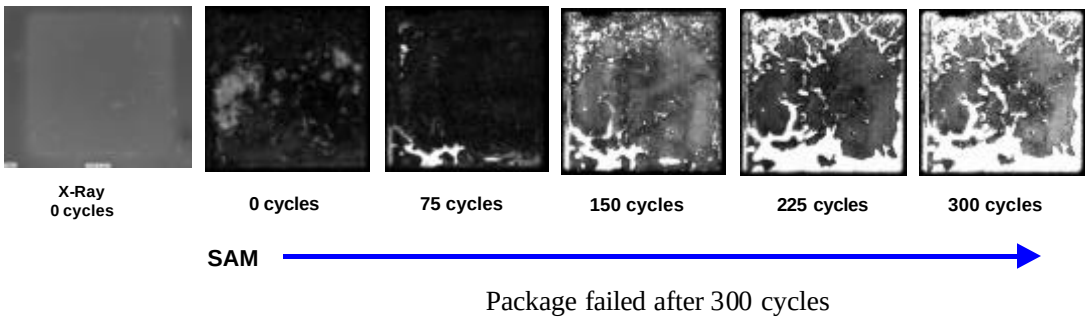

Figure 6.5: SAM showing delamination growth during 0 to 165°C cycle in 12 mm^2 package with 100 μm bondline thickness

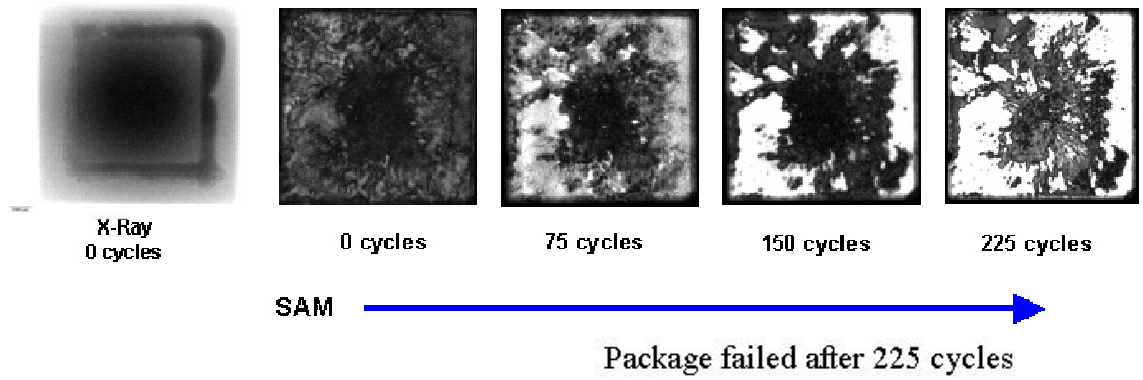

Figure 6.6: SAM showing fast delamination growth during 0 to 165°C cycle in 6 mm^2 package

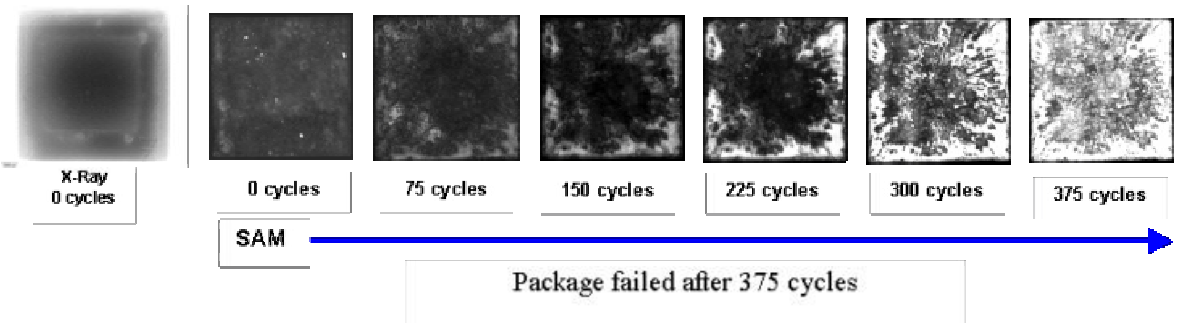

Figure 6.7: SAM showing delamination growth during 0 to 165°C cycle in 12 mm^2 package

Appendix D: Weibull Plots

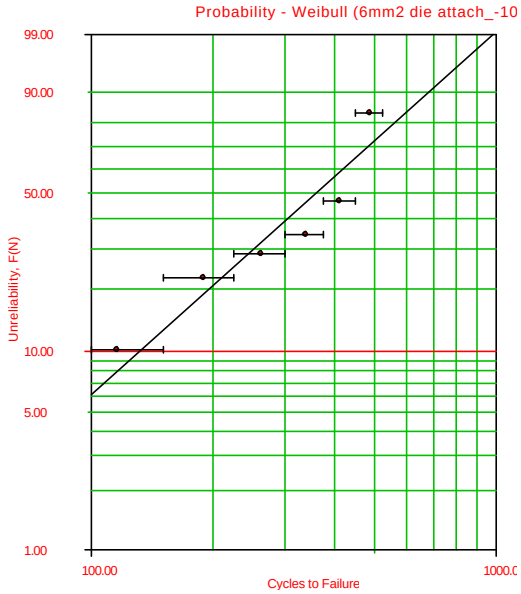

Figure 6.8: 2-P Weibull plot of 6´6 mm^2 package from -10 to 100°C thermal cycle

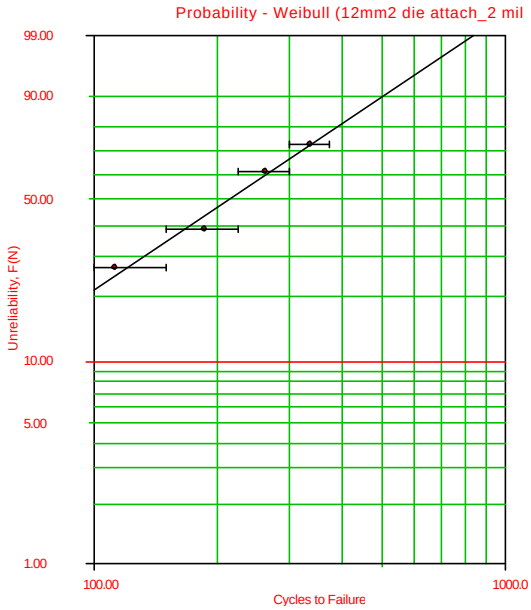

Figure 6.9: 2-P Weibull plot of 12´12 mm^2 package (50 μm bondline) from 0 to 165°C thermal cycle

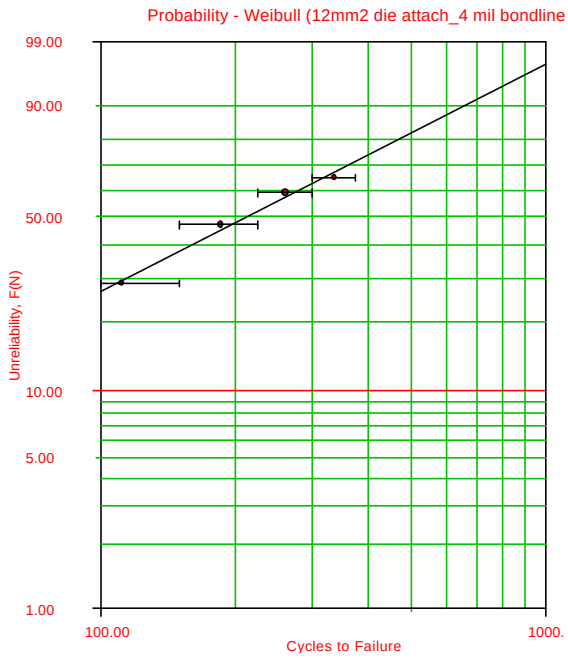

Figure 6.10: 2-P Weibull plot of 12´12 mm^2 package (100 μm bondline) from 0 to 165°C thermal cycle

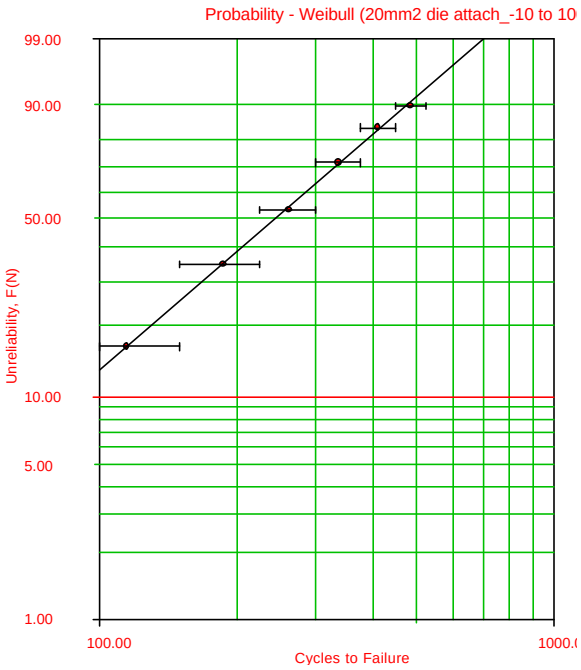

Figure 6.11: 2-P Weibull plot of 20´20 mm^2 package from -10 to 100°C thermal cycle

Appendix E: Microstructure Characterization

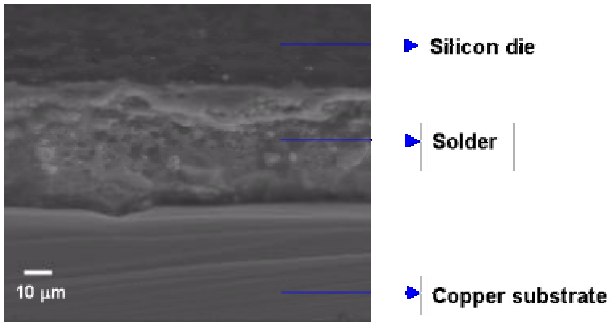

Figure 6.12: Good Solder attachment at 3879X magnification

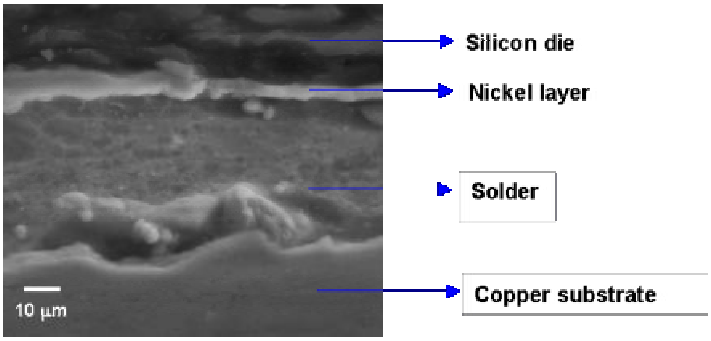

Figure 6.13: Good Solder attachment at 4963X magnification

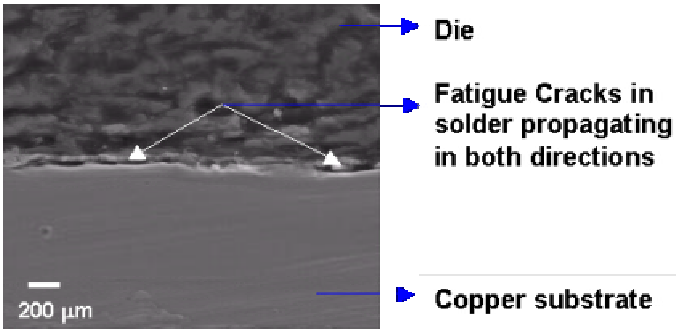

Figure 6.14: Cracks propagating in 100 mm die attach at 1156X magnification

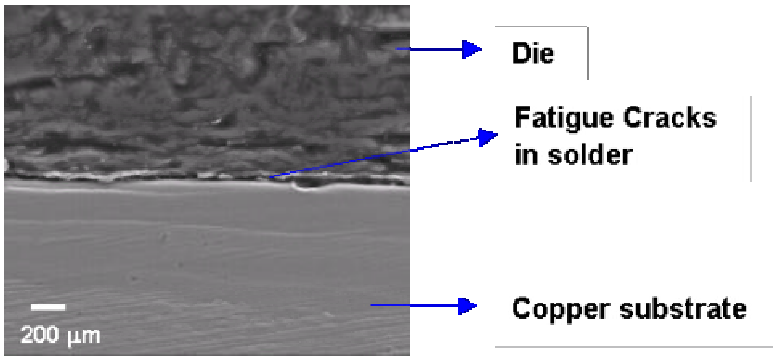

Figure 6.15: Cracks propagating in 100 mm die attach at 1256X magnification

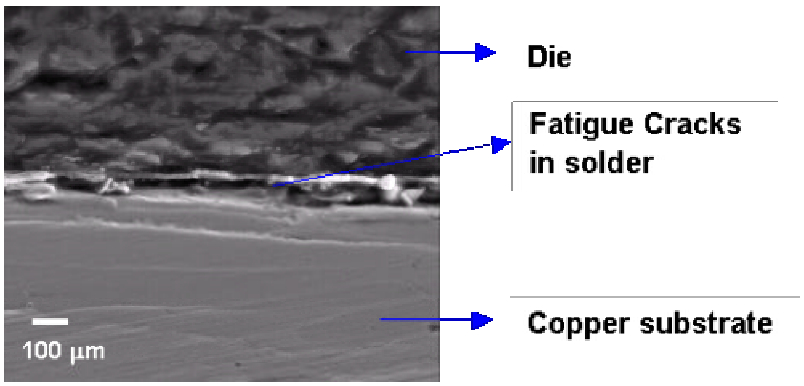

Figure 6.16: Cracks propagating in 100 mm die attach at 2841X magnification

Appendix F: Ansys Input Files for 6´6 mm^2 die attach for 0 to 165°C thermal profile

Ansys input files used in this study are presented in this Appendix.

Appendix F1: Ansys Input File for Parametric Modeling

```
/NOPR
/PMETH,OFF,0
KEYW,PR_SET,1
KEYW,PR_STRUC,1
KEYW,PR_THERM,0
KEYW,PR_FLUID,0
KEYW,PR_ELMAG,0
KEYW,MAGNOD,0
KEYW,MAGEDG,0
KEYW,MAGHFE,0
KEYW,MAGELC,0
KEYW,PR_MULTI,0
KEYW,PR_CFD,0
/GO
!*
/COM,
/COM,Preferences for GUI filtering have been set to display:
/COM,  Structural
!*
!50.8 MICRONS BONDLINE THICKNESS USED


/PREP7
K,1,0,0,0,
K,2,3.3941,0,0,
K,3,4.2426,0,0,
K,4,9.8994,0,0,
K,5,9.8994,3.2,0,
K,6,4.2426,3.2,0,
K,7,3.3941,3.2,0,
K,8,0,3.2,0,
K,9,0,3.2508,0,
K,10,3.3941,3.2508,0,
K,11,4.2426,3.2508,0,
K,12,4.2426,3.7858,0,
K,13,3.3941,3.7858,0,
K,14,0,3.7858,0,

LSTR,      1,      2
LSTR,      2,      3
LSTR,      3,      4
LSTR,      4,      5
LSTR,      5,      6
LSTR,      6,      7
LSTR,      7,      8
LSTR,      8,      1
LSTR,      2,      7
LSTR,      3,      6
LSTR,      8,      9
LSTR,      9,     10
LSTR,     10,     11
LSTR,     11,      6
LSTR,      7,     10
LSTR,      9,     14
LSTR,     14,     13
LSTR,     13,     12
LSTR,     12,     11
LSTR,     13,     10

FLST,2,4,4
FITEM,2,1
FITEM,2,9
FITEM,2,7
FITEM,2,8
AL,P51X
FLST,2,4,4
FITEM,2,2
FITEM,2,10
FITEM,2,6
FITEM,2,9
AL,P51X
FLST,2,4,4
FITEM,2,7
FITEM,2,15
FITEM,2,12
```

```
FITEM,2,11
AL,P51X
FLST,2,4,4
FITEM,2,6
FITEM,2,14
FITEM,2,13
FITEM,2,15
AL,P51X
FLST,2,4,4
FITEM,2,12
FITEM,2,20
FITEM,2,17
FITEM,2,16
AL,P51X
FLST,2,4,4
FITEM,2,13
FITEM,2,19
FITEM,2,18
FITEM,2,20
AL,P51X
FLST,2,4,4
FITEM,2,10
FITEM,2,3
FITEM,2,4
FITEM,2,5
AL,P51X

! PLANE STRAIN ELEMENT
ET,1,PLANE182
!*
KEYOPT,1,1,0
KEYOPT,1,3,2
KEYOPT,1,4,0
KEYOPT,1,6,0
KEYOPT,1,10,0
!*

!MATERIAL PROPERTY
!
MPTEMP,,,,,,,,
MPTEMP,1,263
MPTEMP,2, 273
MPTEMP,3,298
MPTEMP,4,323
MPTEMP,5,353
MPTEMP,6,373
MPTEMP,7,398
MPTEMP,8,423
MPDATA,EX,1,,191659.9
MPDATA,EX,1,,191532.9
MPDATA,EX,1,,191215.4
MPDATA,EX,1,,190897.9
MPDATA,EX,1,,190516.9
MPDATA,EX,1,,190262.9
MPDATA,EX,1,,189945.4
MPDATA,EX,1,,189627.9
MPDATA,PRXY,1,,0.2782
MPDATA,PRXY,1,,0.2782
MPDATA,PRXY,1,,0.2782
MPDATA,PRXY,1,,0.2782
MPDATA,PRXY,1,,0.2782
MPDATA,PRXY,1,,0.2782
MPDATA,PRXY,1,,0.2782
MPDATA,PRXY,1,,0.2782
MPTEMP,,,,,,,,
MPTEMP,1,263
MPTEMP,2,273
MPTEMP,3,298
MPTEMP,4,323
MPTEMP,5,353
MPTEMP,6,373
MPTEMP,7,398
MPTEMP,8,423
UIMP,1,REFT,,,298
MPDE,ALPX,1
MPDE,ALPY,1
MPDE,ALPZ,1
MPDATA,ALPX,1,,1.9985E-6
MPDATA,ALPX,1,,2.0935E-6
MPDATA,ALPX,1,,2.331E-6
MPDATA,ALPX,1,,2.5685E-6
MPDATA,ALPX,1,,2.8535E-6
MPDATA,ALPX,1,,3.0435E-6
MPDATA,ALPX,1,,3.281E-6
MPDATA,ALPX,1,,3.5185E-6

MPTEMP,,,,,,,,
MPTEMP,1,298
MPTEMP,2,353
MPTEMP,3,398
MPTEMP,4,423
MPDATA,EX,2,,13280
MPDATA,EX,2,,9270
```

MPDATA,EX,2,,7340
MPDATA,EX,2,,5810
MPDATA,PRXY,2,,0.4
MPDATA,PRXY,2,,0.4
MPDATA,PRXY,2,,0.4
MPDATA,PRXY,2,,0.4
MPTEMP,,,,,,,
MPTEMP,1,0
UIMP,2,REFT,,,298
MPDE,ALPX,2
MPDE,ALPY,2
MPDE,ALPZ,2
MPDATA,ALPX,2,,29E-6
TB,MISO,2,4,42,
TBTEMP,298

TBPT,,0.001,13.28
TBPT,,0.002,19
TBPT,,0.00356,25
TBPT,,0.005,30
TBPT,,0.008,36.5
TBPT,,0.01,39.21252
TBPT,,0.015,41.95116
TBPT,,0.02,44.00948
TBPT,,0.025,45.67534
TBPT,,0.03,47.08314
TBPT,,0.035,48.30723
TBPT,,0.04,49.39327
TBPT,,0.045,50.37147
TBPT,,0.05,51.26291
TBPT,,0.055,52.0829
TBPT,,0.06,52.84294
TBPT,,0.065,53.55189
TBPT,,0.07,54.21676
TBPT,,0.075,54.84316
TBPT,,0.08,55.43566
TBPT,,0.085,55.99806
TBPT,,0.09,56.53353
TBPT,,0.095,57.04475
TBPT,,0.1,57.53402
TBPT,,0.15,61.5522
TBPT,,0.2,64.57230119
TBPT,,0.25,67.01650591
TBPT,,0.3,69.08208845
TBPT,,0.35,70.8781052
TBPT,,0.4,72.47158473
TBPT,,0.45,73.90684329
TBPT,,0.5,75.21479484
TBPT,,0.55,76.41791028
TBPT,,0.6,77.53306502
TBPT,,0.65,78.57327285
TBPT,,0.7,79.54879277
TBPT,,0.75,80.46786338
TBPT,,0.8,81.33720645
TBPT,,0.85,82.16238183
TBPT,,0.9,82.94804361
TBPT,,0.95,83.698129
TBPT,,1,84.416
TBTEMP,353
TBPT,,0.001,9.27
TBPT,,0.002,15.8
TBPT,,0.00356,22
TBPT,,0.005,26
TBPT,,0.008,30
TBPT,,0.01,31.61175
TBPT,,0.015,33.31056
TBPT,,0.02,34.57096
TBPT,,0.025,35.58136
TBPT,,0.03,36.4288
TBPT,,0.035,37.16102
TBPT,,0.04,37.80719
TBPT,,0.045,38.38648
TBPT,,0.05,38.91218
TBPT,,0.055,39.39393
TBPT,,0.06,39.83894
TBPT,,0.065,40.25276
TBPT,,0.07,40.63972
TBPT,,0.075,41.00331
TBPT,,0.08,41.34637
TBPT,,0.085,41.67124
TBPT,,0.09,41.97988
TBPT,,0.095,42.27392
TBPT,,0.1,42.55479
TBPT,,0.15,44.84168052
TBPT,,0.2,46.53840247
TBPT,,0.25,47.89857065
TBPT,,0.3,49.03936666
TBPT,,0.35,50.02506749
TBPT,,0.4,50.89492088
TBPT,,0.45,51.67473215
TBPT,,0.5,52.38241612
TBPT,,0.55,53.03093958
TBPT,,0.6,53.63000347

TBPT,,0.65,54.18706308
TBPT,,0.7,54.70797699
TBPT,,0.75,55.1974364
TBPT,,0.8,55.65925846
TBPT,,0.85,56.09659256
TBPT,,0.9,56.51206884
TBPT,,0.95,56.90790739
TBPT,,1,57.286
TBTEMP,398
TBPT,,0.001,7.34
TBPT,,0.002,11.5
TBPT,,0.00356,13.9
TBPT,,0.005,15.4
TBPT,,0.008,17.3
TBPT,,0.01,18.07113
TBPT,,0.015,19.02451
TBPT,,0.02,19.73131
TBPT,,0.025,20.29757
TBPT,,0.03,20.77228
TBPT,,0.035,21.1823
TBPT,,0.04,21.544
TBPT,,0.045,21.86818
TBPT,,0.05,22.16229
TBPT,,0.055,22.43175
TBPT,,0.06,22.68061
TBPT,,0.065,22.91198
TBPT,,0.07,23.1283
TBPT,,0.075,23.33152
TBPT,,0.08,23.52323
TBPT,,0.085,23.70475
TBPT,,0.09,23.87718
TBPT,,0.095,24.04144
TBPT,,0.1,24.19832
TBPT,,0.15,25.47496479
TBPT,,0.2,26.42139989
TBPT,,0.25,27.17965964
TBPT,,0.3,27.81532866
TBPT,,0.35,28.36436392
TBPT,,0.4,28.84871197
TBPT,,0.45,29.28279772
TBPT,,0.5,29.67663241
TBPT,,0.55,30.0374603
TBPT,,0.6,30.37069982
TBPT,,0.65,30.68051423
TBPT,,0.7,30.97017449
TBPT,,0.75,31.24229933
TBPT,,0.8,31.4990192
TBPT,,0.85,31.7420916
TBPT,,0.9,31.97298405
TBPT,,0.95,32.19293509
TBPT,,1,32.403
TBTEMP,423
TBPT,,0.001,5.81
TBPT,,0.002,10
TBPT,,0.00356,12.5
TBPT,,0.005,13.7
TBPT,,0.008,14.8
TBPT,,0.01,15.27726
TBPT,,0.015,15.94042
TBPT,,0.02,16.42833
TBPT,,0.025,16.81704
TBPT,,0.03,17.14146
TBPT,,0.035,17.42062
TBPT,,0.04,17.66612
TBPT,,0.045,17.88554
TBPT,,0.05,18.08412
TBPT,,0.055,18.26566
TBPT,,0.06,18.43298
TBPT,,0.065,18.58826
TBPT,,0.07,18.73319
TBPT,,0.075,18.86913
TBPT,,0.08,18.99718
TBPT,,0.085,19.11826
TBPT,,0.09,19.23313
TBPT,,0.095,19.34242
TBPT,,0.1,19.44667
TBPT,,0.15,20.29082712
TBPT,,0.2,20.91189214
TBPT,,0.25,21.406689
TBPT,,0.3,21.81964569
TBPT,,0.35,22.17500455
TBPT,,0.4,22.48750504
TBPT,,0.45,22.76680344
TBPT,,0.5,23.01958252
TBPT,,0.55,23.25066595
TBPT,,0.6,23.46365356
TBPT,,0.65,23.66130569
TBPT,,0.7,23.84578705
TBPT,,0.75,24.01882772
TBPT,,0.8,24.18183298
TBPT,,0.85,24.3359604
TBPT,,0.9,24.4821752
TBPT,,0.95,24.62129096

```
TBPT,,1,24.754
TB,CREE,2,4,3,10
TBTEMP,298
TBDATA,,11.776,11.848,14903,,,
TBTEMP,353
TBDATA,,11.776,11.123,14903,,,
TBTEMP,398
TBDATA,,11.776,10.671,14903,,,
TBTEMP,423
TBDATA,,11.776,10.308,14903,,,
!*

MPTEMP,,,,,,,,
MPTEMP,1,0
MPDATA,EX,3,,120000
MPDATA,PRXY,3,,0.34
MPTEMP,,,,,,,,
MPTEMP,1,293
MPTEMP,2,373
UIMP,3,REFT,,,298
MPDE,ALPX,3
MPDE,ALPY,3
MPDE,ALPZ,3
MPDATA,ALPX,3,,17E-6
MPDATA,ALPX,3,,17.3E-6


!MATERIAL ATTRIBUTES
!
FLST,5,3,5,ORDE,3
FITEM,5,1
FITEM,5,-2
FITEM,5,7
CM,_Y,AREA
ASEL, , , ,P51X
CM,_Y1,AREA
CMSEL,S,_Y
!*
CMSEL,S,_Y1
AATT,      3, ,   1,      0,
CMSEL,S,_Y
CMDELE,_Y
CMDELE,_Y1
!*
FLST,5,2,5,ORDE,2
FITEM,5,3
FITEM,5,-4
CM,_Y,AREA
ASEL, , , ,P51X
CM,_Y1,AREA
CMSEL,S,_Y
!*
CMSEL,S,_Y1
AATT,      2, ,   1,      0,
CMSEL,S,_Y
CMDELE,_Y
CMDELE,_Y1
!*
FLST,5,2,5,ORDE,2
FITEM,5,5
FITEM,5,-6
CM,_Y,AREA
ASEL, , , ,P51X
CM,_Y1,AREA
CMSEL,S,_Y
!*
CMSEL,S,_Y1
AATT,      1, ,   1,      0,
CMSEL,S,_Y
CMDELE,_Y
CMDELE,_Y1
!*

!MESHING

!MESHING THE THICKNESS OF DIE ATTACH
FLST,5,3,4,ORDE,3
FITEM,5,11
FITEM,5,14
FITEM,5,-15
CM,_Y,LINE
LSEL, , , ,P51X
CM,_Y1,LINE
CMSEL,,_Y
!*
LESIZE,_Y1, , ,5, , , , ,0
!*
!MESHING THE HORIZONTAL LENGTH OF REGION OF INTEREST
FLST,5,4,4,ORDE,4
FITEM,5,2
FITEM,5,6
FITEM,5,13
FITEM,5,18
```

```
CM,_Y,LINE
LSEL, , , ,P51X
CM,_Y1,LINE
CMSEL,,_Y
!*
LESIZE,_Y1, , ,76, , , , ,0
!*
!MESHING THE HORIZONTAL LENGTH TILL REGION OF INTEREST
FLST,5,4,4,ORDE,4
FITEM,5,1
FITEM,5,7
FITEM,5,12
FITEM,5,17
CM,_Y,LINE
LSEL, , , ,P51X
CM,_Y1,LINE
CMSEL,,_Y
!*
LESIZE,_Y1, , ,300, , , , ,0
!*
!MESHING THE VERTICAL HEIGHT OF COPPER
FLST,5,4,4,ORDE,3
FITEM,5,4
FITEM,5,8
FITEM,5,-10
CM,_Y,LINE
LSEL, , , ,P51X
CM,_Y1,LINE
CMSEL,,_Y
!*
LESIZE,_Y1, , ,190, , , , ,0
!*
!MESHING THE THICKNESS OF DIE
FLST,5,3,4,ORDE,3
FITEM,5,16
FITEM,5,19
FITEM,5,-20
CM,_Y,LINE
LSEL, , , ,P51X
CM,_Y1,LINE
CMSEL,,_Y
!*
LESIZE,_Y1, , ,30, , , , ,0
!*
!MESHING THE HORIZONTAL LENGTH OF COPPER SUBSTRATE OUTSIDE REGION OF INTEREST
FLST,5,2,4,ORDE,2
FITEM,5,3
FITEM,5,5
CM,_Y,LINE
LSEL, , , ,P51X
CM,_Y1,LINE
CMSEL,,_Y
!*
LESIZE,_Y1, , ,220, , , , ,0
!*

AMAP,1,8,7,2,1
AMAP,2,7,6,3,2
AMAP,3,9,10,7,8
AMAP,4,10,11,6,7
AMAP,5,14,13,10,9
AMAP,6,13,12,11,10
AMAP,7,6,5,4,3
EPLOT

!76 elements in x-direction constitutes 20% length

FLST,5,380,2,ORDE,2
FITEM,5,72941
FITEM,5,-73320
ESEL,S, , ,P51X
CM,ATTACH,ELEM
ALLSEL,ALL
EPLOT
```

Appendix F2: Ansys Input File for Thermal Profile

```
/SOL
FLST,2,3,4,ORDE,2
FITEM,2,1
FITEM,2,-3
!*
/GO
```

```
DL,P51X, ,UY,0.0
FLST,2,3,4,ORDE,3
FITEM,2,8
FITEM,2,11
FITEM,2,16
DL,P51X, ,SYMM

OUTRES,ERASE
ANTYPE,0
TREF,298,
TUNIF,298,
TIMINT,OFF
TOFFST,0,
LSWRITE,INIT


!STEP 1                 !DWELL FOR 15 SECONDS AT 298 K
TIME,15
TUNIF,298,
NLGEOM,1
RATE,1
AUTOTS,ON
SOLCONTROL,ON,0,
CUTCONTROL,CRPLIMIT,,1
NSUBST,,100000,
DELTIM,1,1E-15,3,ON
KBC,1
OUTRES,ALL,NONE
OUTRES,ESOL,ALL,ATTACH
LSWRITE


!STEP 2                 !RAMP UP TO 438 k
TIME,1335
TUNIF,438,
NLGEOM,1
RATE,1
AUTOTS,ON
SOLCONTROL,ON,0,
CUTCONTROL,CRPLIMIT,,1
NSUBST,,10000000,
DELTIM,1E-5,1E-15,100,ON
KBC,0
OUTRES,ALL,NONE
OUTRES,ESOL,ALL,ATTACH
LSWRITE

!STEP 3                 !DWELL FOR 1200 SECONDS AT 438 K
TIME,2635
TUNIF,438,
NLGEOM,1
RATE,1
AUTOTS,ON
SOLCONTROL,ON,0,
CUTCONTROL,CRPLIMIT,,1
NSUBST,,100000,
DELTIM,2,1E-15,50,ON
KBC,1
OUTRES,ALL,NONE
OUTRES,ESOL,ALL,ATTACH
LSWRITE

!STEP 4                 !COOL DOWN TO 273 K
TIME,3735
TUNIF,273,
NLGEOM,1
RATE,1
AUTOTS,ON
SOLCONTROL,ON,0,
CUTCONTROL,CRPLIMIT,,1
NSUBST,,100000,
DELTIM,2,1E-15,50,ON
KBC,0
OUTRES,ALL,NONE
OUTRES,ESOL,ALL,ATTACH
LSWRITE

!STEP 5                 !DWELL AT 273 K FOR 300 SECONDS
TIME,4035
TUNIF,273,
NLGEOM,1
RATE,1
AUTOTS,ON
SOLCONTROL,ON,0,
CUTCONTROL,CRPLIMIT,,1
NSUBST,,100000,
DELTIM,2,1E-15,30,ON
KBC,1
OUTRES,ALL,NONE
OUTRES,ESOL,ALL,ATTACH
LSWRITE

!STEP 6                 !RAMP UP TO 298 K
```

```
TIME,4335
TUNIF,298,
NLGEOM,1
RATE,1
AUTOTS,ON
SOLCONTROL,ON,0,
CUTCONTROL,CRPLIMIT,,1
NSUBST,,10000000,
DELTIM,1E-3,1E-15,30,ON
KBC,0
OUTRES,ALL,NONE
OUTRES,ESOL,ALL,ATTACH
LSWRITE

!STEP 7                 !RAMP UP TO 438 k
TIME,5655
TUNIF,438,
NLGEOM,1
RATE,1
AUTOTS,ON
SOLCONTROL,ON,0,
CUTCONTROL,CRPLIMIT,,1
NSUBST,,10000000,
DELTIM,1E-5,1E-15,100,ON
KBC,0
OUTRES,ALL,NONE
OUTRES,ESOL,ALL,ATTACH
LSWRITE

!STEP 8                 !DWELL FOR 1200 SECONDS AT 438 K
TIME,6855
TUNIF,438,
NLGEOM,1
RATE,1
AUTOTS,ON
SOLCONTROL,ON,0,
CUTCONTROL,CRPLIMIT,,1
NSUBST,,100000,
DELTIM,2,1E-15,50,ON
KBC,1
OUTRES,ALL,NONE
OUTRES,ESOL,ALL,ATTACH
LSWRITE


!STEP 9                 !COOL DOWN TO 273 K
TIME,8055
TUNIF,273,
NLGEOM,1
RATE,1
AUTOTS,ON
SOLCONTROL,ON,0,
CUTCONTROL,CRPLIMIT,,1
NSUBST,,100000,
DELTIM,2,1E-15,50,ON
KBC,0
OUTRES,ALL,NONE
OUTRES,ESOL,ALL,ATTACH
LSWRITE

!STEP 10                !DWELL AT 273 K FOR 300 SECONDS
TIME,8355
TUNIF,273,
NLGEOM,1
RATE,1
AUTOTS,ON
SOLCONTROL,ON,0,
CUTCONTROL,CRPLIMIT,,1
NSUBST,,100000,
DELTIM,2,1E-15,30,ON
KBC,1
OUTRES,ALL,NONE
OUTRES,ESOL,ALL,ATTACH
LSWRITE

!STEP 11                !RAMP UP TO 298 K
TIME,8655
TUNIF,298,
NLGEOM,1
RATE,1
AUTOTS,ON
SOLCONTROL,ON,0,
CUTCONTROL,CRPLIMIT,,1
NSUBST,,10000000,
DELTIM,1E-3,1E-15,30,ON
KBC,0
OUTRES,ALL,NONE
OUTRES,ESOL,ALL,ATTACH
LSWRITE


!STEP 12                !RAMP UP TO 438 k
TIME,9975
```

```
TUNIF,438,
NLGEOM,1
RATE,1
AUTOTS,ON
SOLCONTROL,ON,0,
CUTCONTROL,CRPLIMIT,,1
NSUBST,,10000000,
DELTIM,1E-5,1E-15,100,ON
KBC,0
OUTRES,ALL,NONE
OUTRES,ESOL,ALL,ATTACH
LSWRITE

!STEP 13                !DWELL FOR 1200 SECONDS AT 438 K
TIME,11175
TUNIF,438,
NLGEOM,1
RATE,1
AUTOTS,ON
SOLCONTROL,ON,0,
CUTCONTROL,CRPLIMIT,,1
NSUBST,,100000,
DELTIM,2,1E-15,50,ON
KBC,1
OUTRES,ALL,NONE
OUTRES,ESOL,ALL,ATTACH
LSWRITE


!STEP 14                !COOL DOWN TO 273 K
TIME,12375
TUNIF,273,
NLGEOM,1
RATE,1
AUTOTS,ON
SOLCONTROL,ON,0,
CUTCONTROL,CRPLIMIT,,1
NSUBST,,100000,
DELTIM,2,1E-15,50,ON
KBC,0
OUTRES,ALL,NONE
OUTRES,ESOL,ALL,ATTACH
LSWRITE

!STEP 15                !DWELL AT 273 K FOR 300 SECONDS
TIME,12675
TUNIF,273,
NLGEOM,1
RATE,1
AUTOTS,ON
SOLCONTROL,ON,0,
CUTCONTROL,CRPLIMIT,,1
NSUBST,,100000,
DELTIM,2,1E-15,30,ON
KBC,1
OUTRES,ALL,NONE
OUTRES,ESOL,ALL,ATTACH
LSWRITE

!STEP 16                !RAMP UP TO 298 K
TIME,12975
TUNIF,298,
NLGEOM,1
RATE,1
AUTOTS,ON
SOLCONTROL,ON,0,
CUTCONTROL,CRPLIMIT,,1
NSUBST,,10000000,
DELTIM,1E-3,1E-15,30,ON
KBC,0
OUTRES,ALL,NONE
OUTRES,ESOL,ALL,ATTACH
LSWRITE


!STEP 17                !RAMP UP TO 438 k
TIME,14295
TUNIF,438,
NLGEOM,1
RATE,1
AUTOTS,ON
SOLCONTROL,ON,0,
CUTCONTROL,CRPLIMIT,,1
NSUBST,,10000000,
DELTIM,1E-5,1E-15,100,ON
KBC,0
OUTRES,ALL,NONE
OUTRES,ESOL,ALL,ATTACH
LSWRITE

!STEP 18                !DWELL FOR 1200 SECONDS AT 438 K
TIME,15495
TUNIF,438,
```

```
NLGEOM,1
RATE,1
AUTOTS,ON
SOLCONTROL,ON,0,
CUTCONTROL,CRPLIMIT,,1
NSUBST,,100000,
DELTIM,2,1E-15,50,ON
KBC,1
OUTRES,ALL,NONE
OUTRES,ESOL,ALL,ATTACH
LSWRITE


!STEP 19                    !COOL DOWN TO 273 K
TIME,16695
TUNIF,273,
NLGEOM,1
RATE,1
AUTOTS,ON
SOLCONTROL,ON,0,
CUTCONTROL,CRPLIMIT,,1
NSUBST,,100000,
DELTIM,2,1E-15,50,ON
KBC,0
OUTRES,ALL,NONE
OUTRES,ESOL,ALL,ATTACH
LSWRITE

!STEP 20                    !DWELL AT 273 K FOR 300 SECONDS
TIME,16995
TUNIF,273,
NLGEOM,1
RATE,1
AUTOTS,ON
SOLCONTROL,ON,0,
CUTCONTROL,CRPLIMIT,,1
NSUBST,,100000,
DELTIM,2,1E-15,30,ON
KBC,1
OUTRES,ALL,NONE
OUTRES,ESOL,ALL,ATTACH
LSWRITE

!STEP 21                    !RAMP UP TO 298 K
TIME,17295
TUNIF,298,
NLGEOM,1
RATE,1
AUTOTS,ON
SOLCONTROL,ON,0,
CUTCONTROL,CRPLIMIT,,1
NSUBST,,10000000,
DELTIM,1E-3,1E-15,30,ON
KBC,0
OUTRES,ALL,NONE
OUTRES,ESOL,ALL,ATTACH
LSWRITE

LSSOLVE,1,21,1
FINISH
SAVE
```

Appendix F3: Ansys Input File for Post Processing

```
/POST26
RESET
ALLSEL,ALL


XMIN1=4.1577
XMAX1=4.2426
YMIN1=3.2
YMAX1=3.2508

ESEL,S,MAT,,2

!GET ALL THE ELEMENTS IN THE DIE ATTACH LAYER

*GET,NETOTAL,ELEM,0,COUNT
*GET,NE_MAX,ELEM,0,NUM,MAX
*GET,NE_MIN,ELEM,0,NUM,MIN

*DIM,TLIST,ARRAY,NETOTAL

!GET ALL THE ELEMENTS (ELIST) WHOSE CENTER LOCATED IN THE CRITICAL AREA
```

```
KK=0
*DO,i,NE_MIN,NE_MAX
 XA=CENTRX(i)
 YA=CENTRY(i)
 *IF,XA,LT,XMAX1,THEN
   *IF,XA,GT,XMIN1,THEN
      *IF,YA,LT,YMAX1,THEN
         *IF,YA,GT,YMIN1,THEN
           KK=KK+1
           TLIST(KK+1)=i
         *ENDIF
      *ENDIF
   *ENDIF
 *ENDIF
*ENDDO

KLIST=KK+1

*DIM,ELIST,ARRAY,KK+1
*DO,i,2,KLIST
  ELIST(i)=TLIST(i)
*ENDDO

NSTEP=668
NUMVAR,KLIST


!GET THE CORRESPONDING AREA FOR ELEMENTS IN THE CRITICAL AREA
*DIM,ELEMA,ARRAY,KLIST
*DO,i,2,KLIST
 *GET,ELEMA(i),ELEM,ELIST(i),AREA
*ENDDO




!GET THE CORRESPONDING ELASTIC STRAIN ENERGY DENSITY FOR ELEMENTS IN THE CRITICAL AREA
!FIRST COLUMN OF ELIST IS FOR TIME
*DIM,EDEL,,ARRAY,NSTEP,KLIST
*DO,i,2,KLIST
ESOL,i,ELIST(i),,SEND,ELASTIC
STORE,MERGE
VGET,EDEL(1,i),i
*ENDDO


!GET THE CORRESPONDING PLASTIC STRAIN ENERGY DENSITY FOR ELEMENTS IN THE CRITICAL AREA
!FIRST COLUMN OF ELIST IS FOR TIME
*DIM,EDPL,ARRAY,NSTEP,KLIST
*DO,i,2,KLIST
ESOL,i,ELIST(i),,SEND,PLASTIC
STORE,MERGE
VGET,EDPL(1,i),i
*ENDDO


!GET THE CORRESPONDING CREEP STRAIN ENERGY DENSITY FOR ELEMENTS IN THE CRITICAL AREA
!FIRST COLUMN OF ELIST IS FOR TIME
*DIM,EDCR,ARRAY,NSTEP,KLIST
*DO,i,2,KLIST
ESOL,i,ELIST(i),,SEND,CREEP
STORE,MERGE
VGET,EDCR(1,i),i
*ENDDO




!GET THE CORRESPONDING X-COMPONENT OF STRESS FOR ELEMENTS IN THE CRITICAL AREA
!FIRST COLUMN OF ELIST IS FOR TIME
*DIM,XSTS,ARRAY,NSTEP,KLIST
*DO,i,2,KLIST
ESOL,i,ELIST(i),,S,X
STORE,MERGE
VGET,XSTS(1,i),i
*ENDDO


!GET THE CORRESPONDING X-COMPONENT OF ELASTIC STRAIN FOR ELEMENTS IN THE CRITICAL AREA
!FIRST COLUMN OF ELIST IS FOR TIME
*DIM,XELN,ARRAY,NSTEP,KLIST
*DO,i,2,KLIST
ESOL,i,ELIST(i),,EPEL,X
STORE,MERGE
VGET,XELN(1,i),i
*ENDDO


!GET THE CORRESPONDING X-COMPONENT OF PLASTIC STRAIN FOR ELEMENTS IN THE CRITICAL AREA
```

```
!FIRST COLUMN OF ELIST IS FOR TIME
*DIM,XPLN,ARRAY,NSTEP,KLIST
*DO,i,2,KLIST
ESOL,i,ELIST(i),,EPPL,X
STORE,MERGE
VGET,XPLN(1,i),i
*ENDDO


!GET THE CORRESPONDING X-COMPONENT OF CREEP STRAIN FOR ELEMENTS IN THE CRITICAL AREA
!FIRST COLUMN OF ELIST IS FOR TIME
*DIM,XCRN,ARRAY,NSTEP,KLIST
*DO,i,2,KLIST
ESOL,i,ELIST(i),,EPCR,X
STORE,MERGE
VGET,XCRN(1,i),i
*ENDDO




!GET THE CORRESPONDING VON-MISES STRESS FOR ELEMENTS IN THE CRITICAL AREA
!FIRST COLUMN OF ELIST IS FOR TIME
*DIM,VMSTS,ARRAY,NSTEP,KLIST
*DO,i,2,KLIST
ESOL,i,ELIST(i),,S,EQV
STORE,MERGE
VGET,VMSTS(1,i),i
*ENDDO


!GET THE CORRESPONDING VON-MISES ELASTIC STRAIN FOR ELEMENTS IN THE CRITICAL AREA
!FIRST COLUMN OF ELIST IS FOR TIME
*DIM,VMELN,ARRAY,NSTEP,KLIST
*DO,i,2,KLIST
ESOL,i,ELIST(i),,EPEL,EQV
STORE,MERGE
VGET,VMELN(1,i),i
*ENDDO


!GET THE CORRESPONDING VON-MISES PLASTIC STRAIN FOR ELEMENTS IN THE CRITICAL AREA
!FIRST COLUMN OF ELIST IS FOR TIME
*DIM,VMPLN,ARRAY,NSTEP,KLIST
*DO,i,2,KLIST
ESOL,i,ELIST(i),,EPPL,EQV
STORE, MERGE
VGET,VMPLN(1,i),i
*ENDDO


!GET THE CORRESPONDING VON-MISES CREEP STRAIN FOR ELEMENTS IN THE CRITICAL AREA
!FIRST COLUMN OF ELIST IS FOR TIME
*DIM,VMCRN,ARRAY,NSTEP,KLIST
*DO,i,2,KLIST
ESOL,i,ELIST(i),,EPCR,EQV
STORE,MERGE
VGET,VMCRN(1,i),i
*ENDDO


!GET THE CORRESPONDING PLASTIC WORK PER VOLUME FOR ELEMENTS IN THE CRITICAL AREA
!FIRST COLUMN OF ELIST IS FOR TIME
*DIM,ENPLWK,ARRAY,NSTEP,KLIST
*DO,i,2,KLIST
ESOL,i,ELIST(i),,NL,PLWK
STORE,MERGE
VGET,ENPLWK(1,i),i
*ENDDO



*DIM,AEDEL,ARRAY,NSTEP
*DIM,AEDPL,ARRAY,NSTEP
*DIM,AEDCR,ARRAY,NSTEP
*DIM,AXSTS,ARRAY,NSTEP
*DIM,AXELN,ARRAY,NSTEP
*DIM,AXPLN,ARRAY,NSTEP
*DIM,AXCRN,ARRAY,NSTEP
*DIM,AVMSTS,ARRAY,NSTEP
*DIM,AVMELN,ARRAY,NSTEP
*DIM,AVMPLN,ARRAY,NSTEP
*DIM,AVMCRN,ARRAY,NSTEP
*DIM,AENPLWK,ARRAY,NSTEP


!CALCULATE TOTAL CRITICAL AREA
SAREA=0
*DO,i,2,KLIST
SAREA=SAREA+ELEMA(i)
```

```
*ENDDO


!CALCULATE AVERAGE ELASTIC STRAIN ENERGY DENSITY OVER CRITICAL AREA
*DO,i,1,NSTEP
AEDEL(i)=0
  *DO,j,2,KLIST
    AEDEL(i)=AEDEL(i)+EDEL(i,j)*ELEMA(j)
  *ENDDO
AEDEL(i)=AEDEL(i)/SAREA
*ENDDO


!CALCULATE AVERAGE PLASTIC STRAIN ENERGY DENSITY OVER CRITICAL AREA
*DO,i,1,NSTEP
AEDPL(i)=0
  *DO,j,2,KLIST
    AEDPL(i)=AEDPL(i)+EDPL(i,j)*ELEMA(j)
  *ENDDO
AEDPL(i)=AEDPL(i)/SAREA
*ENDDO


!CALCULATE AVERAGE CREEP STRAIN ENERGY DENSITY OVER CRITICAL AREA
*DO,i,1,NSTEP
AEDCR(i)=0
  *DO,j,2,KLIST
    AEDCR(i)=AEDCR(i)+EDCR(i,j)*ELEMA(j)
  *ENDDO
AEDCR(i)=AEDCR(i)/SAREA
*ENDDO


!CALCULATE AVERAGE X-COMPONENT OF STRESS OVER CRITICAL AREA
*DO,i,1,NSTEP
AXSTS(i)=0
  *DO,j,2,KLIST
    AXSTS(i)=AXSTS(i)+XSTS(i,j)*ELEMA(j)
  *ENDDO
AXSTS(i)=AXSTS(i)/SAREA
*ENDDO


!CALCULATE AVERAGE X-COMPONENT OF ELASTIC STRAIN OVER CRITICAL AREA
*DO,i,1,NSTEP
AXELN(i)=0
  *DO,j,2,KLIST
    AXELN(i)=AXELN(i)+XELN(i,j)*ELEMA(j)
  *ENDDO
AXELN(i)=AXELN(i)/SAREA
*ENDDO


!CALCULATE AVERAGE X-COMPONENT OF PLASTIC STRAIN OVER CRITICAL AREA
*DO,i,1,NSTEP
AXPLN(i)=0
  *DO,j,2,KLIST
    AXPLN(i)=AXPLN(i)+XPLN(i,j)*ELEMA(j)
  *ENDDO
AXPLN(i)=AXPLN(i)/SAREA
*ENDDO


!CALCULATE AVERAGE X-COMPONENT OF CREEP STRAIN OVER CRITICAL AREA
*DO,i,1,NSTEP
AXCRN(i)=0
  *DO,j,2,KLIST
    AXCRN(i)=AXCRN(i)+XCRN(i,j)*ELEMA(j)
  *ENDDO
AXCRN(i)=AXCRN(i)/SAREA
*ENDDO


!CALCULATE AVERAGE VON-MISES STRESS OVER CRITICAL AREA
*DO,i,1,NSTEP
AVMSTS(i)=0
  *DO,j,2,KLIST
    AVMSTS(i)=AVMSTS(i)+VMSTS(i,j)*ELEMA(j)
  *ENDDO
AVMSTS(i)=AVMSTS(i)/SAREA
*ENDDO


!CALCULATE AVERAGE VON-MISES ELASTIC STRAIN OVER CRITICAL AREA
*DO,i,1,NSTEP
AVMELN(i)=0
  *DO,j,2,KLIST
    AVMELN(i)=AVMELN(i)+VMELN(i,j)*ELEMA(j)
```

```
  *ENDDO
AVMELN(i)=AVMELN(i)/SAREA
*ENDDO


!CALCULATE AVERAGE VON-MISES PLASTIC STRAIN OVER CRITICAL AREA
*DO,i,1,NSTEP
AVMPLN(i)=0
  *DO,j,2,KLIST
    AVMPLN(i)=AVMPLN(i)+VMPLN(i,j)*ELEMA(j)
  *ENDDO
AVMPLN(i)=AVMPLN(i)/SAREA
*ENDDO


!CALCULATE AVERAGE VON-MISES CREEP STRAIN OVER CRITICAL AREA
*DO,i,1,NSTEP
AVMCRN(i)=0
  *DO,j,2,KLIST
    AVMCRN(i)=AVMCRN(i)+VMCRN(i,j)*ELEMA(j)
  *ENDDO
AVMCRN(i)=AVMCRN(i)/SAREA
*ENDDO


!CALCULATE AVERAGE PLASTIC WORK OVER CRITICAL AREA
*DO,i,1,NSTEP
AENPLWK(i)=0
  *DO,j,2,KLIST
  AENPLWK(i)=AENPLWK(i)+ENPLWK(i,j)*ELEMA(j)
  *ENDDO
AENPLWK(i)=AENPLWK(i)/SAREA
*ENDDO
```

Appendix F4: Ansys Input File for Data Output

```
MM=KLIST-1

*cfopen,6mmto165_1st_aavg,csv

*VWRITE,MM
('NUMBER OF ELEMENTS IN THE CRITICAL AREA:',f5.0)


*VWRITE
('AVGELDEN',3x,'AVGPLDEN',3x,'AVGCRDEN',3x,'AVGXSTRS',3x,'AVGXELSTN',3x,'AVGXPLSTN',3x,'AVGXCRSTN',3x,'AVGVONSTS',3x,'AVGVONELSTN',3x,'AV
GVONPLSTN',3X,'AVGVONCRSTN',3X,'AVGPLASWOK',3X)

*VWRITE,AEDEL(1),AEDPL(1),AEDCR(1),AXSTS(1),AXELN(1),AXPLN(1),AXCRN(1),AVMSTS(1),AVMELN(1),AVMPLN(1),AVMCRN(1),AENPLWK(1)
(f12.6,3x,f12.3,3x,f12.3,3x,f10.3,3x,f12.6,3x,f12.6,3x,f12.6,3x,f10.3,3x,f12.6,3x,f12.6,3x,f12.6,3x,f12.3)

*vwrite
('element #',1x)

*cfclose
finish
```

Appendix G: Polishing Procedure Developed

Table 6.2: Polishing Procedure Developed

Step	1	2	3	4	5
Abrasive	600 grit	2500 Fine grit	3 μm Polycrystalline Suspension	1 μm Polycrystalline Suspension	0.05 Colloidal
Type Carrier	SiC	SiC	Diamond	Diamond	Silica
	Grinding Disc	Grinding Disc	Glycol	Glycol	Suspension
Polishing Cloth			White Label	Final B	Chem-Pol
Coolant	Water	Water	RedLube	RedLube	Water
Platen Speed	250 RPM	100 RPM	250 RPM	250 RPM	250 RPM
Platen Direction	CCW	CCW	CCW	CCW	CCW
Pressure	Medium	Medium	Medium – High	Low	Low
Time	1:00 min	1:00 min	3-4 min	1:00 min	45 sec

7 References

1. S. Hwang, “Modern Solder Technology for Competitive Electronics Manufacturing”, McGraw-Hill, 1996.
2. N. Iosipescu, “New Accurate Procedure for Single Shear Testing of Metals, Journal of Materials”, Vol. 2, No. 3, September 1967, pp. 537-566.
3. S. Kwon, Y. Lee, B. Han, “Advanced Micro Shear Testing for Solder Alloy Using Direct Local Measurement”, Proceedings of IPACK'03, InterPACK2003-35325, Maui, Hawaii, (July 2003).
4. T. Reinikainen and W. Ren, “An optimized shear test sample for assessing solder deformation properties”, Proceedings of EuroSimE 2001, Paris, April 2001.
5. P. Haswell, “Durability assessment and microstructural observations of selected solder alloys”, Ph.D. Dissertation, Dept. of Mechanical Engineering, University of Maryland, College Park, MD, 2001.
6. Katsis, D.C., “Thermal Characterization of Die-Attach Degradation in the Power MOSFET”, Ph.D. Dissertation, Electrical and Computer Engineering, Virginia Polytechnic Institute and State University, Blacksburg, VA, 2003.
7. Dieter, G.E., Mechanical Metallurgy, McGraw-Hill, Inc., Third Edition, 1986.
8. R. Arrowood, A. Mukherjee, W. Jones, “Hot deformation of two-phase mixtures, Solder Mechanics: A state of the art assessment”, Frear, Jones, Kinsman (eds.), The Minerals, Metals, and Materials Society, 1991.
9. J. H. Lau and D. W. Rice, “Thermal life prediction of flip-chip solder joints by fracture mechanics method”, AME Advances in Electronic Packaging, 1992, pp. 385-392.

10. D. Tribula, J. W. Morris Jr., “Creep in shear of experimental solder joints”, Journal of Electronics Packaging, Vol. 112, 1990, pp. 87-93.
11. R. Darveaux, “Crack initiation and growth in surface mount solder joints”, Proc. of ISHM, 1993, pp. 86-97.
12. B. P. Kashyap, G. S. Murty, “Experimental constitutive relations for the high temperature deformation of a Pb-Sn eutectic alloy”, Materials Science and Engineering, Vol. 50, 1981, pp. 205-213.
13. J. Wang, Z. Qian, D. Zou, S. Liu, “Creep behavior of a flip-chip package by both FEM modeling and real-time moiré interferometry”, ASME Journal of Electronics Packaging, Vol. 120, 1998, pp. 179-185.
14. D. H. Frear, “The mechanical behavior of interconnect materials for electronic packaging”, Journal of Metals, Vol. 48, No. 5, 1996, pp. 46-53.
15. M. Mukai, T. Kawakami, Y. Hiruta, K. Takahashi, K. Kishimoto, T. Shibuya, “Fatigue life estimation of solder joints in SMT-PGA packages”, ASME Journal of Electronic Packaging, June 1998, pp. 207-212.
16. P. M. Hall, “Creep and stress relaxation in solder joints of surface-mounted chip carriers”, IEEE Trans. CHMT, Vol. 12, No. 4, 1987, pp. 556-565.
17. B. Wong, D. Helling, R. W. Clark, “A creep-rupture model for two phase eutectic solders”, IEEE Trans. on CHMT, Vol. 11, 1988, pp. 305-325.
18. M. C. Shine, L. R. Fox, “Fatigue of solder joints in surface mount devices, Low Cycle Fatigue”, Solomon, Halford, Kaisand, Leis (eds.), ASTM STP 942, 1988.
19. T. G. Langdon, F. A. Mohamed, “The activation energies of superplasticity, Scripta Metallurgica”, Vol. 11, 1977, pp. 575-579.

20. Darveaux, R., “Solder joint fatigue life modeling, Design and Reliability of solders and solder interconnections”, The Minerals, Metals, and Materials Society, 1997, pp. 213-218.
21. Skipor, A.F., Harren, S.V., Botsis, J., “On the constitutive response of 63/37 Sn/Pb eutectic solder”, ASME Journal of engineering materials and technology, Vol. 118, 1996, pp. 1-11.
22. Anand, L., “Constitutive Equations for the Rate-dependent Deformation of Metals at Elevated Temperatures”, ASME Journal of Engineering Materials & Technology, Vol. 104, pp. 12-17, 1982.
23. J. Wilde, K. Becker, M. Thoben, W. Blum, T. Jupitz, G. Wang, Z. Cheng, “Rate dependent constitutive relations based on Anand model for 92.5Pb5Sn2.5Ag solder”, IEEE Transactions on Advanced Packaging., Vol. 23, No. 3, August 2000, pp. 408-414.
24. S. A. Gupta, “Temperature and Rate Dependent Partitioned Constitutive Relationships for 95.5Pb2Sn2.5Ag Solder Alloy”, M.S. Thesis, 2003, University of Maryland, College Park, MD.
25. Shi, X. Q., Pang, H. L. J., Zhou, W., Wang, Z. P., “Temperature and Strain Rate Effect on Mechanical Properties of 63Sn/37Pb Solder Alloy”, WWP-Vol. 26-1, Advances in Electronic Packaging, Volume 1, ASME 1999.
26. ASTM Standard E1012-99, Standard Practice for Verification of Specimen Alignment under Tensile Loading.

27. Mavoori, H, Chin, J, Vaynman, S, Moran, B, Keer, L, Fine, M, Creep, Stress Relaxation, and Plastic Deformation in Sn-Ag and Sn-Zn Eutectic Solders, Journal of Electronics Materials, Vol. 26, No. 7, 1997.
28. Meyers, M. A., Chawla, K. K., Mechanical metallurgy, principles and applications, Prentice-Hall, 1984.
29. Zhang, Q., Dasgupta, A., Haswell, P., "Viscoplastic constitutive properties and energy-partitioning model of lead-free Sn3.9Ag0.6Cu solder alloy," Proc. of the 53rd Electronic Components and Technology Conference, 2003. May 27-30, 2003, Page(s): 1862 -1868.
30. Weertman, J., "Creep of Indium, Lead and Some of Their Alloys with Various Metals," Transactions of the Metallurgical Society of AIME, Vol. 218, April 1960, pp.207 – 218.
31. Anand, L., 1985, ''Constitutive Equations for Hot Working of Metals,'' J. Plasticity, 1, pp. 213–231.
32. Garofalo, F., 1963, ''An Empirical Relation Defining the Stress Dependence of Minimum Creep Rate in Metals,'' Transactions of AIME, 227, pp. 351–362.
33. Wang, G., Cheng, Z., Becker, K., Wilde, J., "Applying Anand Model to Represent the Viscoplastic Deformation Behavior of Solder Alloys", ASME Journal of Electronic Packaging, Vol. 123, September 2001, pp. 247-253.
34. Darveaux, R. and Banerji, K., "Constitutive Relations for Tin-Based-Solder Joints", Electronic Components and Technology Conference, 1992 Proceedings, 42nd ,18-20 May 1992, pp. 538 – 551.

35. Pao, Y.H., Govila, R. and Badgley, S., Thermal Fatigue Fracture of 90Pb/10Sn Solder Joints", Advances in Electronic Packaging 1992, Proceedings of the 1992 Joint ASME/JSME Conference on Electronic Packaging, pp. 291-300.
36. Pao, Y.H., Govila, R., Badgley, S., and Jih, E., "Thermomechanical and Fatigue Behavior of High-Temperature Lead and Lead-Free Solder Joints", Fatigue of electronic Materials, ASTM STP 1153, S.A. Schroeder and M.R.Mitchell, Eds., ASTM, Philadelphia, 1994, pp. 60-81.
37. Solomon, H.D., "The Creep and Strain Rate Sensitivity of a High Pb Content Solder with Comparisons to 60Sn/40Pb Solder", Journal of Electronic Materials, Vol.19, No.9, 1990, pp.929-936.
38. Callister, W.D., Materials Science and Engineering An Introduction, John Wiley & Sons, Inc., Sixth Edition, 2003.
39. Metals Handbook, ASM
40. Frost, H.J., Howard, R.T., Lavery, P.R., Lutender, S.D., "Creep and Tensile Behavior of Lead-Rich Lead-Tin Solder Alloys", IEEE Transactions On Components, Hybrids and Manufacturing Technology, Vol. 11, No. 4, December 1988, pp. 371-379.
41. Tu, K. N., "The cellular reaction in Pb-Sn alloys," Met. Trans., vol. 3, pp. 2769-2775, 1972.
42. Vaynman, S., "Effect of Strain Rate on Fatigue of Low-Tin Lead-Base Solder", IEEE Transactions On Components, Hybrids and Manufacturing Technology, Vol.12, No.4, December 1989, pp.469-472.

43. Liljestrand, L.G. and Andersson, L.O., “Accelerated thermal fatigue cycling of surface mounted PWB assemblies in telecom equipment,” Circuit World, Vol.14, p.73, 1988.
44. Inoue, H., Kurihara, Y., Hachino, H., “Pb-Sn Solder for Die Bonding of Silicon Chips”, IEEE Transactions On Components, Hybrids & Manufacturing Technology, Vol.CHMT-9, No.2, June 1986, pp.190-194.
45. Hong, B.Z., Burrell, L.G., “Nonlinear Finite Element Simulation of Thermoviscoplastic Deformation of C4 Solder Joints in High Density Packaging Under Thermal Cycling”, IEEE Transactions on Components Packaging & Manufacturing Technology - Part A, Vol.18, No.3, September 1995, pp.585-591.
46. Marshall, J.L., “Characterization of solder fatigue in electronic packaging”, Brazing Soldering, No.15, pp.4-9, 1998.
47. Solomon, H.D., “Low-Frequency, High Temperature Low Cycle Fatigue of 60Sn-40Pb Solder”, Proceedings of the Symposium on Low Cycle Fatigue, ASTM Publication Code Number (PCN) 04-94200030, October 1985, pp.342-370.
48. Kuo, Chih-Wei G., Sastry, Shankar M.L., and Jerina, Kenneth L., “Creep-Fatigue Interactions in Eutectic Tin-Lead Solder Alloys”, Proceedings of the Symposium on Fatigue of Electronic Materials, STP 1153, ASTM Publication Code Number (PCN) 04-011530-30, December 1994, pp. 22-41.
49. Lau, J.H., Solder Joint Reliability, Theory and Applications, Van Nostrand Reinhold.
50. Lee, W. W., Nguyen, L. T., and Selvaduray, G. S., ‘‘Solder Joint Fatigue Models: Review and Applicability to Chip Scale Packages,’’ Microelectronic Reliability, 40, pp. 231–244, 2000.

51. Liang, J., Gollhardt, N., Lee, P.S., Schroeder, S.A. and Morris, W.L., “A Study of Fatigue and Creep Behavior of Four High Temperature Solders”, Fatigue and Fracture of Engineering Materials & Structures, Vol.19, No.11, 1996, pp.1401-1409.
52. Vaynman, S. and Zubelewicz, A., “Fatigue Life Prediction for Low-Tin Lead-Based Solder at Low Strains”, Welding Journal, vol.69, 1990, pp. S395-S398.
53. Morris, J.W. and Reynolds, H.L. “The influence of microstructure on the mechanics of eutectic solders”, Advances in Electronic Packaging 1997, Proceedings of the Pacific Rim/ASME International Intersociety Electronic and Photonic Packaging Conference INTERpack'97, vol. 2. 1997, pp. 1529-34.
54. Guven, I., Kradinov, V., Tor, J.L. and Madenci, E., “Strain Energy Density Criterion for Reliability Life Prediction of Solder Joints in Electronic Packaging”, Transactions of ASME, Vol. 126, September 2004, pp. 398 – 405.
55. Wen, S. and Keer, L.M., “A Theory of Fatigue: A Physical Approach with Application to Lead-Rich Solder”, Journal of Applied Mechanics, Vol.69, January 2002, pp.1-10.
56. Mura, T., and Nakasone, Y., ‘‘A Theory of Fatigue Crack Initiation in Solids,’’ ASME Journal of Applied Mechanics, Vol.57, 1990, pp. 1–6.
57. Fine, M. E., 2000, ‘‘Phase Transformation Theory Applied to Elevated Temperature Fatigue,’’ Scripta Materialia., 42, pp. 1007–1012.
58. Lin, T. H., Wong, K. K. F., Teng, N. J., and Lin, S. R., 1998, ‘‘Micromechanic Analysis of Fatigue Band Crossing Grain Boundary,’’ Mater. Sci. Eng., A, 246, pp. 169–179.

59. Radeck, S., Kellenberger, D., and Luechinger, C., “Soft Solder Die Bonding of Multiple Die Devices”, IEEE Transactions on Components and Packaging Technologies , Vol. 23, No.4, December 2000, pp. 646 – 656.
60. Coffin, L.F., Transactions of ASME, Vol.76, 1954, pp. 931-950.
61. Manson, S.S., Experimental Mechanics, Vol.5, No.7, 1965, pp. 193-226.
62. Coffin, L.F., “Fatigue at High Temperature”, ASTM STP 520, 1973, PA.
63. Halford, G. R., Hirschberg, M. H., and Manson, S. S., “Temperature Effects on the Strain-Range Partitioning Approach for Creep Fatigue Analysis,” ASTM STP 520, 1973, pp. 658-667, PA.
64. Manson, S. S., Halford, G. R., and Hirschberg, M H., “Creep-Fatigue Analysis by Strain-Range Partitioning,” ASME Symposium on Design for Elevated Temp-Environment, San Francisco, CA, 1971.
65. Vaynman, S., “Effect of Temperature on Isothermal Fatigue of Solders,” IEEE Transactions on Components, Hybrids and Manufacturing Technology, Vol.13, No. 4, 1990, pp. 909-913.
66. Enke, N.F., Kilinski, T.J., Schroeder, S.A., and Lesniak, J.R., "Mechanical Behaviors of 60/40 Tin-lead Solder Lap Joints," IEEE Transactions CHMT, Vol. 12, No. 4, 1989, pp.459-468.
67. Engelmaier W., “Test Method Considerations for SMT Solder Joint Durability,” IEPS, 1984, pp. 360-369.
68. Wild, R. N., “ Some Fatigue Properties of Solder and Solder Joints,” IBM Rep. No. 74Z000481, also INTERNEPSON, Brighton, England, 1975.

69. Solomon, H.K., “Low Cycle Fatigue of Surface Mounted Chip Carrier/Printed Wiring Board Joints,” Proceedings IEEE 39th ECC, 1989, pp. 277-292.

70. Dasgupta, A., Oyan, C., Barker, D., and Pecht, M., “Solder Creep-Fatigue Analysis by an Energy-Partitioning Approach,” ASME Journal of Electronic Packaging, Vol. 114, No. 2, 1992, pp. 152-160.

71. Guo, Z. and Conrad, H., "Fatigue Crack Growth Rate in 63Sn37Pb Solder Joints," ASME Trans. J. Electronic Packaging, Vol. 115, No. 2, 1993, pp. 159-164.

72. Ju, S. H., Sandor, B. I., Plesha, M. E., Dec. “Life Prediction of Solder Joints by Damage and Fracture Mechanics,” ASME, Journal of Electronic Packaging, Vol. 118, 1996, pp. 193-200.

73. Rafanelli, A. J., “The Validation and Evaluation of the J-Integral for 63-37 Tin Lead Solder,” ASME Mechanics and Materials for Electronic Packaging: Volume 2-Thermal and Mechanical Behavior and Modeling, AMD Vol. 187, 1994, pp. 91-99.

74. Lau, J. H., “Solder Joint Reliability of a Low Cost Chip Scale Package - NuCSP,” Proceedings of ISHM 1997, Philadelphia, PA.

75. Solomon, H.D. and Tolksdorf, E.D., “Energy Approach to the Fatigue of 60/40 Solder: Part I–Influence of Temperature and Cycle Frequency,” ASME, Journal of Electronic Packaging, Vol. 117, 1995, pp 130-135.

76. Frear, D.R., “Microstructural Evolution During Thermomechanical Fatigue of 62Sn36Pb2Ag and 60Sn40P Solder Joints”, IEEE Transactions on Components, Hybrids and Manufacturing Technology, Vol.13, No.4, December 1990, pp.718-726.

77. Cutiongco, E. C., Vaynman, S., Fine, M. E., Jeannotte, D. A., “Isothermal Fatigue of 63Sn-37Pb Solder,” ASME, Journal of Electronic Packaging, Vol.112, No. 2, 1990, pp. 110-114.
78. Zhang, Qian., “Isothermal Mechanical and Thermomechanical Durability Characterization of Selected Pb-Free Solders”, 2004, Ph.D. Dissertation, University of Maryland, College Park, MD.
79. Okura, J.H., Darbha, K., Shetty, S., Dasgupta, A., Caers, J.F.J.M., “Guidelines to Select Underfills for Flip Chip on Board Assemblies”, IEEE, Electronic Components and Technology Conference, 1999, pp. 589-594.
80. Goto, Akira., Oikawa, Hiroshi., Karashima, Seiichi., “Effects of Temperature and Stress on Work-Hardening and Recovery Rates during Steady-State Deformation of Lead”, Transaction of Japan Institute of Metals, 1980, Vol.21, pp. 15-19.
81. El-Daly, A.A., Abdel-Daiem, A.M., Abdel-Rahman, A.N., Mohammed, S.M., “Effect of Zn-addition and Structural Transformation on the Creep Behavior of Pb-10wt% Sn Alloy”, Materials Chemistry and Physics, Vol.85, 2004, pp. 163-170.